

**AN EXPERIMENTAL AND NUMERICAL INVESTIGATION OF
LAMINAR AND TURBULENT NATURAL CONVECTION IN
VERTICAL PARALLEL-PLATE CHANNELS**

by

TURGUT YILMAZ B.Sc., M.Sc.

A thesis submitted for the degree of Doctor of Philosophy

**University of Strathclyde
Department of Mechanical Engineering
Glasgow, U.K.**

September 1997

Copyright Declaration

The copyright of this thesis belongs to the author under the terms of the United Kingdom Copyright Acts as qualified by University of Strathclyde Regulation 3.49. Due acknowledgment must always be made of the use of any material contained in, or derived from, this thesis.

Dedicated to
YILMAZ family

ABSTRACT

Laminar and turbulent natural convection heat transfer and fluid flow processes in asymmetrically heated vertical parallel flat plate channels have been investigated both experimentally and numerically. The experimental part of the investigation was carried out using a fibre optic Laser-Doppler Anemometer (LDA) together with a temperature probe and data acquisition system. The numerical analysis was done using the computational fluid dynamics (CFD) code PHOENICS. The laminar natural convection flow case was examined for a uniform heat flux (UHF) heating mode while the turbulent flow case was examined considering both UHF and uniform wall temperature (UWT) heating modes.

Small and large scale channels were constructed to perform laminar and turbulent flow experiments respectively. The channels were formed by a heated wall, an opposing unheated perspex or glass wall and side walls. Velocity profile and time history data along the channel and temperature profiles at channel exit were recorded for the laminar flow case. In the turbulent flow case of UWT heating mode mean and turbulent velocity data and mean temperature data at the channel exit were collected. For the UHF heating mode turbulent flow case, however, both mean and turbulent velocity and temperature data were recorded. The main objective of the experiments was to obtain data by which the numerical analysis could be supported since not enough experimental data is available, especially for the turbulent flow case. The numerical analysis of the laminar flow situation was performed with the standard features of PHOENICS. The turbulent flow case was examined by building into PHOENICS the codes for four different Low Reynolds Number k - ϵ turbulence models. The grid pattern was optimised for a test case and employed for final computations. Due to the lack of experimental data regarding the location of transition to turbulent flow, computations were done by introducing a level of turbulence at the inlet and solving the governing equations for turbulent flow throughout the channel. The results of measurements justified this approach.

The results of numerical and experimental analysis of laminar flow showed good agreement confirming that the numerical method was capable of predicting the flow with good accuracy. Turbulent flow experiments exhibited the characteristics of a developing turbulent channel flow. Low amplitude, high frequency velocity fluctuations were observed close to the channel inlet with higher amplitudes downstream and almost similar fluctuation patterns in the uppermost region of the channel suggesting fully developed turbulence. The temperature data indicated intermittent bursts of high frequency temperature fluctuations near the inlet and continuous high frequency temperature fluctuations of increasing amplitude downstream. Numerical results of the turbulent flow case have produced good agreement with experiments. The solutions were most sensitive to the level of turbulence introduced at the channel inlet. Reasonable grid independent solutions were obtained for grids greater than 60x60 for most of the turbulence models considered.

Velocity and temperature profiles obtained from experiments and numerical analysis are presented for both flow cases. Typical time histories of velocity and temperature at different channel heights and cross-stream locations are presented. From the numerical and experimental results correlations were produced for Nusselt number, and Reynolds number as functions of Rayleigh number, for the UWT heating mode of turbulent flow.

ACKNOWLEDGEMENT

The author wishes to express his sincere appreciation to his supervisor Dr. A. Gilchrist for his valuable guidance and encouragement during the course of this study. The author also would like to thank Prof. S. M. Fraser for his valuable help in the CFD part of the study. Thanks are also due to Dr. C. Carey, Dr. S. Baskaya, Dr. T. Comlekci, Dr. İ. Horuz and Dr. G. Ozmen for their support. The author is grateful to E. Duncan and P. M^cGuinness for their help in the setting up of experimental rig.

The author also would like to thank his family for their continuous courage and care.

Finally thanks are due to Istanbul Technical University, Faculty of Mechanical Engineering, TURKEY, for the financial support.

CONTENTS

ABSTRACT.....	i
ACKNOWLEDGEMENT.....	iii
CONTENTS.....	iv
LIST OF FIGURES.....	ix
LIST OF TABLES.....	xiii
ABBREVIATIONS.....	xiv
NOMENCLATURE.....	xv

CHAPTER 1. INTRODUCTION

1.1 Introduction.....	1
1.2 Present Project and Objectives.....	3

CHAPTER 2. LITERATURE REVIEW

2.1 Introduction.....	5
2.2 Laminar Natural Convection in Parallel Plate Vertical Channels.....	5
2.3 Turbulent Natural Convection in Parallel Plate Vertical Channels.....	11
2.4 Turbulence Models for Natural Convection.....	13

CHAPTER 3. PROBLEM FORMULATION AND FLOW EQUATIONS

3.1 Description of the Physical Models.....	16
3.1.1 Laminar Flow Channel.....	16
3.1.2 Turbulent Flow Channel.....	18
3.2 Mathematical Formulation.....	18
3.2.1 Laminar Flow Equations.....	19
3.2.2 Turbulent Flow Equations and K- ϵ Turbulence Models.....	20
3.2.3 Dimensional and Dimensionless Parameters.....	24

CHAPTER 4. NUMERICAL SOLUTION METHOD AND MODELLING

4.1 Introduction.....	26
4.2 PHOENICS CFD Code.....	26
4.2.1 The Overall Structure of PHOENICS.....	27
4.2.2 The General Transport Equation Solved by PHOENICS.....	28
4.2.3 Modelling of Fluid Flow and Heat Transfer within PHOENICS.....	28
4.2.3.1 Derivation of Finite-Volume Discretisation Equations.....	29
4.2.3.2 Finite-Volume Equation Solved by PHOENICS.....	32
4.2.3.3 Staggered Grid Approach.....	32
4.2.3.4 Boundary Conditions and Source Terms.....	33
4.2.3.5 Solution of Finite-Volume Equations.....	34
4.3 Modelling of Natural Convection Channel Flows by PHOENICS.....	35
4.3.1 Laminar Natural Convection Channel Flow.....	35
4.3.2 Turbulent Natural Convection Channel Flow.....	36
4.3.2.1 PHOENICS Implementation of Turbulent Transport.....	36
4.3.2.2 The LRN k- ϵ Turbulence Modelling of Natural Convection by PHOENICS.....	36
4.3.2.3 The Q1 File for the LRN k- ϵ Turbulence Models.....	41

CHAPTER 5. EXPERIMENTAL SETUP AND MEASUREMENT METHODS

5.1 Introduction.....	43
5.2 Laminar Flow.....	43
5.2.1 The Flow Channel.....	43
5.2.2 Instrumentation.....	46
5.2.2.1 He-Ne Fibre Flow LDA System.....	46
5.2.2.2 Flow Seeding Arrangement.....	47
5.2.2.3 Temperature Measurements.....	48

5.2.2.4 Traversing Mechanisms.....	49
5.2.3 Experimental Procedure.....	50
5.3 Turbulent Flow.....	52
5.3.1 The Flow Channels.....	52
5.3.1.1 The Flow Channel Used for the UWT Heating Mode.....	52
5.3.1.2 The Flow Channel Used for the UHF Heating Mode.....	53
5.3.2 Instrumentation.....	54
5.3.2.1 Ar-Ion Fibre Flow LDA System.....	54
5.3.2.2 Flow Seeding Arrangement.....	58
5.3.2.3 Temperature Measurements.....	58
5.3.2.3.1 Surface Temperature Measurements.....	58
5.3.2.3.1 Air Temperature Measuring System.....	59
5.3.2.4 Traversing Mechanisms.....	61
5.3.2.4.1 LDA Probe Traverse Mechanism.....	61
5.3.2.4.1 Temperature Probe Traversing Mechanism.....	61
5.3.2.5. Closed Circuit TV.....	63
5.3.3 Experiments and Experimental Procedure.....	63
5.3.3.1 The UWT Heating Mode.....	63
5.3.3.2 The UHF Heating.....	65

CHAPTER 6. PRESENTATION AND DISCUSSION OF EXPERIMENTAL RESULTS

6.1 Introduction.....	66
6.2 Laminar Flow Experiments.....	67
6.2.1 Velocity Profiles.....	69
6.2.2 Temperature Profiles.....	74
6.2.3 Time Histories of Velocity.....	76
6.2.4 Summary and Conclusions.....	78
6.3 Turbulent Flow Experiments.....	78
6.3.1 Mean Velocity Profiles.....	81

6.3.2	Mean Temperature Profiles.....	86
6.3.3	Turbulent Kinetic energy and Reynolds Stress Profiles.....	88
6.3.4	Time Histories of Velocity and Temperature.....	95
6.3.5	Summary and Conclusions.....	106
6.4	Uncertainty of Experimental Data.....	106

CHAPTER 7. NUMERICAL ANALYSIS AND COMPARISON OF NUMERICAL AND EXPERIMENTAL RESULTS

7.1	Introduction.....	107
7.2	Laminar Flow.....	107
7.2.1	Boundary Conditions.....	107
7.2.2	Convergence Criteria.....	108
7.2.3	Selection of Grid Pattern and Grid Size.....	108
7.2.4	Comparison of Numerical solution with Experimental Results.....	111
7.2.4.1	Comparisons of Experimental and Numerical Heat Transfer and Mass Flow Rates.....	112
7.2.4.2	Comparisons of Velocity and Temperature Profiles of Selected Cases with Experimental Results.....	112
7.2.4.3	The Effect of Three Dimensionality.....	116
7.2.4.4	The Effect of Different Boundary Conditions.....	116
7.2.5	Summary and Conclusions.....	118
7.3	Turbulent Flow.....	119
7.3.1	Boundary Conditions.....	119
7.3.2	Convergence Criteria.....	120
7.3.3	Selection of Grid Pattern and Size.....	120
7.3.4	The Effect of Inlet Boundary Condition of k	123
7.3.5	Comparison of Numerical Solution with Experimental Results.....	124
7.3.5.1	Comparisons of Experimental and Numerical Heat Transfer and Mass Flow Rates.....	124

7.3.5.2 Comparisons of Experimental wall Temperatures with Numerical Predictions for UHF Heating mode.....	125
7.3.5.3 Comparisons of Mean Velocity and Temperature Profiles for Selected Cases with Experimental Results.....	126
7.3.5.4 Comparisons of Turbulent Kinetic Energy Profiles of Selected Cases with Experimental Results.....	135
7.3.6 Summary and Conclusions.....	135
7.4 Correlating Equations.....	136

CHAPTER 8. CONCLUSIONS AND RECOMMENDATIONS FOR FUTURE STUDY

8.1 Conclusions.....	140
8.2 Recommendation for Future Study.....	141

REFERENCES.....	142
------------------------	------------

APPENDICES

A Governing Equations.....	150
B Turbulence Model Files.....	160
C Calibration Data and Uncertainty of Experimental Data.....	204
D Specifications of Temperature Measuring Device.....	219
E Specifications of Data Acquisition Board.....	220
F Data Acquisition and Traversing Software.....	221
G Laminar Flow Channel Surface Temperatures.....	230

EXPERIMENTAL DATA:

An internal Departmental report entitled “An Experimental and Numerical Investigation of Laminar and Turbulent Natural Convection in Vertical Parallel-Plate Channels - Experimental Data Report” and computer discs with all the experimental data can be obtained from Mechanical Engineering Department, Strathclyde University.

LIST of FIGURES

3.1	Laminar flow channel model for numerical analysis.....	17
3.2	Turbulent flow channel model for numerical analysis.....	17
4.1	The layout of PHOENICS code.....	27
4.2	Space-time domain and a computational cell in PHOENICS.....	29
4.3	One dimensional cell cluster.....	30
4.4	The cell structure of PHOENICS for scalars and velocity.....	33
4.5	Laminar flow boundary cell in PHOENICS.....	33
5.1	Schematic diagram of the laminar flow channel.....	44
5.2	Photograph of the laminar flow channel.....	44
5.3	Layout of the He-Ne LDA system and the experimental channel.....	46
5.4	Photograph of seeding generator.....	49
5.5	Schematic diagram of the UWT turbulent flow channel.....	55
5.6	Schematic diagram of the UHF turbulent flow channel.....	55
5.7	Layout of Ar-Ion LDA system with the UWT experimental channel.....	56
5.8	Partial photograph of the Ar-Ion LDA system.....	57
5.9	Photograph of the air temperature probe.....	62
5.10	Photograph of the optical probe and traversing mechanism.....	62
6.1	Laminar flow velocity profiles, Case 1, $b/H=1/32$	70
6.2	Laminar flow velocity profiles, Case 2, $b/H=1/32$	71
6.3	Laminar flow velocity profiles, Case 3, $b/H=1/16$	71
6.4	Laminar flow velocity profiles, Case 4, $b/H=1/16$	74
6.5	Laminar flow velocity profiles, Case 5, $b/H=1/16$	72
6.6	Laminar flow velocity profiles, Case 6, $b/H=5/32$	73
6.7	Laminar flow velocity profiles, Case 7, $b/H=5/32$	73
6.8	Laminar flow temperature profiles, Case 3, $b/H=1/16$	74
6.9	Laminar flow temperature profiles, Case 4, $b/H=1/16$	75
6.10	Laminar flow temperature profiles, Case 5, $b/H=1/16$	75
6.11	Laminar flow velocity time history, Case 2, $b/H=1/32$	76
6.12	Laminar flow velocity time history, Case 5, $b/H=1/16$	77

6.13	Laminar flow velocity time history, Case 7, $b/H=5/32$	77
6.14	UHF turbulent flow heated wall temperature distributions.....	80
6.15	UWT turbulent flow mean velocity profiles, Case 1 $T_w = 60$ C.....	82
6.16	UWT turbulent flow mean velocity profiles, Case 2 $T_w = 75$ C.....	82
6.17	UWT turbulent flow mean velocity profiles, Case 3 $T_w = 90$ C.....	83
6.18	UWT turbulent flow mean velocity profiles, Case 4 $T_w = 100$ C.....	83
6.19	UWT turbulent flow mean velocity profiles, Case 5 $T_w = 130$ C.....	84
6.20	UHF turbulent flow mean velocity profiles, Case 1.....	84
6.21	UHF turbulent flow mean velocity profiles, Case 2.....	85
6.22	UHF turbulent flow mean velocity profiles, Case 3.....	85
6.23	UWT turbulent flow mean temperature profiles, at the channel exit.....	86
6.24	UHF turbulent flow mean temperature profiles, Case 1.....	87
6.25	UHF turbulent flow mean temperature profiles, Case 2.....	87
6.26	UHF turbulent flow mean temperature profiles, Case 3.....	90
6.27	UWT turbulent flow turbulent kinetic energy profiles, Case 4.....	90
6.28	UWT turbulent flow x-comp. normal Reynolds stress profiles, Case 4.....	91
6.29	UWT turbulent flow y-comp. normal Reynolds stress profiles, Case 4.....	91
6.30	UHF turbulent flow turbulent kinetic energy profiles, Case 3.....	92
6.31	UHF turbulent flow x-comp. normal Reynolds stress profiles, Case 3.....	92
6.32	UHF turbulent flow y-comp. normal Reynolds stress profiles, Case 3.....	93
6.33	UHF turbulent flow Reynolds stress ($\overline{u'v'}$) profiles, Case 1.....	93
6.34	UHF turbulent flow Reynolds stress ($\overline{u'v'}$) profiles, Case 2.....	94
6.35	UHF turbulent flow Reynolds stress ($\overline{u'v'}$) profiles, Case 3.....	94
6.36	Time history of velocity, Case 1, $X=0.033$	96
6.37	Time history of velocity, Case 1, $X=0.033$	96
6.38	Time history of velocity, Case 1, $X=0.033$	97
6.39	Time history of velocity, Case 1, $X=0.033$	97
6.40	Time history of temperature, Case 1, $X=0.033$	98
6.41	Time history of temperature, Case 1, $X=0.033$	98
6.42	Time history of temperature, Case 1, $X=0.033$	99
6.43	Time history of temperature, Case 1, $X=0.033$	99

6.44	Time history of velocity, Case 1, $X=0.983$	100
6.45	Time history of velocity, Case 1, $X=0.983$	100
6.46	Time history of velocity, Case 1, $X=0.983$	101
6.47	Time history of velocity, Case 1, $X=0.983$	101
6.48	Time history of temperature, Case 1, $X=0.983$	102
6.49	Time history of temperature, Case 1, $X=0.983$	102
6.50	Time history of temperature, Case 1, $X=0.983$	103
6.51	Time history of temperature, Case 1, $X=0.983$	103
6.52	Time history of velocity and temperature, Case 1, $X=0.983$	104
6.53	Time history of velocity and temperature, Case 1, $X=0.983$	104
7.1	The grid used in laminar natural convection calculations.....	110
7.2	Comparison of experimental and numerical velocity profiles, Case 2.....	113
7.3	Comparison of experimental and numerical velocity profiles, Case 5.....	114
7.4	Comparison of experimental and numerical velocity profiles, Case 7.....	114
7.5	Comparison of experimental and numerical temperature profiles, Case 5.....	115
7.6	Comparison of velocity profiles for diff. boun. conditions, $X=0.38$, Case 5.....	117
7.7	Comparison of velocity profiles for diff. boun. conditions, $X=0.98$, Case 5.....	117
7.8	The grid used in turbulent natural convection calculations.....	122
7.9	Experimental and numerical wall temperature distribution, UHF case 3.....	126
7.10	Experimental and numerical velocity profiles, UWT Case 4, TH model.....	127
7.11	Experimental and numerical velocity profiles, UWT Case 4, DA model.....	128
7.12	Experimental and numerical velocity profiles, UWT Case 4, LB model.....	128
7.13	Experimental and numerical temperature profiles at exit, UWT Case 4.....	129
7.14	Experimental and numerical velocity profiles, UHF Case 3, TH model.....	129
7.15	Experimental and numerical velocity profiles, UHF Case 3, DA model.....	130
7.16	Experimental and numerical velocity profiles, UHF Case 3, LB model.....	130
7.17	Experimental and numerical temp. profiles, UHF Case 3, TH model.....	131
7.18	Experimental and numerical temp. profiles, UHF Case 3, DA model.....	131
7.19	Experimental and numerical temp. profiles, UHF Case 3, LB model.....	132
7.20	Experimental and numerical k profiles, UWT Case 4, TH model.....	132
7.21	Experimental and numerical k profiles, UWT Case 4, DA model.....	133

7.22	Experimental and numerical k profiles, UWT Case 4, LB model.....	133
7.23	Experimental and numerical k profiles, UHF Case 3, TH model.....	134
7.24	Experimental and numerical k profiles, UHF Case 3, DA model.....	134
7.25	Experimental and numerical Re/GR as function of $GrPr(b/H)$	137
7.26	Numerical and experimental Nu as function of $GrPr(b/H)$	138
A-1	The buoyancy force due to density variation in a quiescent ambient.....	152
C.1	Thermocouple locations on the laminar flow channel.....	207
C.2	Calibration curves of TCs attached to laminar flow channel.....	209
C.3	Thermocouple locations on the turbulent flow channel, UWT heating mode...209	
C.4	Calibration curves of TCs attached to turbulent flow channel, UWT heating mode.....	211
C.5	Thermocouple locations on the turbulent flow channel, UHF heating mode....	211
C.6	Calibration curves of TCs attached to turbulent flow channel, UHFheating mode.....	213
C.7	Calibration curve of air temperature measurement probe, laminar flow.....	214
C.8	Calibration curve of air temperature measurement probe, turbulent flow.....	214

LIST of TABLES

3.1	The functions of the Low Reynolds Number k- ϵ turbulence models.....	24
6.1	List of laminar flow experiments.	68
6.2	List of the ratio of surface temperatures for the laminar flow channels.....	68
6.3	List of turbulent flow experiments, UWT.....	79
6.4	List of turbulent flow experiments, UHF.....	80
7.1	Grid dependence of numerical solutions.....	109
7.2	Comparison of experimental results with numerical solutions.....	112
7.3	Grid dependence of numerical solutions.....	121
7.4	The Effect of Inlet Boundary Condition of Turbulent kinetic energy.....	123
7.5	Comparison of experimental results with numerical solutions.	125
C.1	Results of uncertainty analysis from the calibration data of TCs attached to laminar flow channel.....	208
C.2	Results of uncertainty analysis from the calibration data of TCs attached to turbulent flow channel, UWT heating mode.....	210
C.3	Results of uncertainty analysis from the calibration data of TCs attached to turbulent flow channel, UHF heating mode.....	212
C.4	Results of uncertainty analysis from the calibration data of air temperature measurement probes.....	213
C.5	Results of uncertainty analysis of velocity measurements.....	215
C.6	Results of uncertainty analysis heat and mass flow rates.....	217

ABBREVIATIONS

BC	: Boundary Condition
CFD	: Computational Fluid Dynamics
Cr-Al	: Chromel-Alumel
DA	: Davidson (Turbulence Model)
UHF	: Uniform wall heat flux
UWT	: Uniform wall temperature
LDA	: Laser-Doppler Anemometry
LRN	: Low Reynolds Number
NX	: Number of cells in X direction
NY	: Number of cells in Y direction
PHOENICS	: The PHOENICS CFD Code
TC	: Thermocouple
TH	: To and Humphrey (Turbulence Model)
LB	: Lam and Bremhorst (Turbulence Model)
LS	: Launder and Sharma (Turbulence Model)
ST	: Standard k- ϵ (Turbulence Model)

NOMENCLATURE

B	: Buoyancy force eq. (A.7)
b	: Channel width
$C_{\mu}, C_{\varepsilon 1}, C_{\varepsilon 2}$: LRN k- ε model constants
c_p	: Specific heat
D	: LRN k- ε model function eq. (3.11)
E	: LRN k- ε model function eq. (3.12)
f_{μ}, f_1, f_2	: LRN k- ε model functions
g	: Gravity
G	: Production of k due to buoyancy eq. (3.14)
Gr	: Grashof number eq. (3.28)
h	: heat transfer coefficient eq. (3.31)
H	: Turbulent flow channel height
L	: Laminar flow channel heated section
k	: Turbulent kinetic energy eq. (B.13)
m	: Flow rate
M	: Dimensionless flow rate eq. (3.34)
Nu	: Nusselt number eq. (3.30)
p	: Static pressure eq. (A.10)
p_h	: Hydrostatic pressure eq. (A.10)
p_m	: Motion pressure eq. (A.10)
P	: Production of k due to shearing eq. (3.13)
Pr	: Prandtl number eq. (3.26)
q	: Heat flux applied to the heated wall [W/m ²]
q_c	: Convected heat transfer from the walls along the channel [watt/m ²]
$q_{w,h}$: Wall heat flux at the hot wall [W/m ²]
$q_{w,c}$: Wall heat flux at the cold wall [W/m ²]
\dot{q}	: Volumetric heat production

Ra	: Rayleigh number eq. (3.29)
Re	: Reynolds number eq. (3.27)
Re_t	: Turbulent Reynolds number eq. (3.24)
Re_y	: Turbulent Reynolds number eq. (3.25)
t	: time
T	: Temperature
Tu	: Turbulence intensity eq. (3.30)
u,v,w	: x,y,z components of velocity
x,y,z	: Cartesian coordinates
X,Y,Z	: Cartesian coordinates

Greek letters:

α	: Thermal diffusivity eq. (3.25)
β	: Thermal expansion coefficient
δ	: Unit tensor
ε	: Dissipation of turbulent kinetic energy eq. (B.9)
κ	: Von Karman coefficient
λ	: Thermal conductivity
μ	: Dynamic viscosity
μ_t	: Dynamic turbulent viscosity eq. (3.10)
ν	: Kinematic viscosity
ν_t	: Kinematic turbulent viscosity
ρ	: Density
σ_t	: Turbulent Prandtl number
σ_k	: Prandtl number of k
σ_ε	: Prandtl number of ε
ϕ	: Computed dependent variable
Φ	: Viscous dissipation eq. (A.4)

Subscripts:

- ave** : Averaged quantity
- c** : Convective or convected, channel, case
- exp** : Experimental value
- i,j** : Tensor indices (x,y,z, or 1,2,3)
- m** : Maximum value
- num** : Numerical value
- w** : Quantity at the wall
- 0** : Quantity at the inlet
- ∞ : Reference quantity
- ε : Quantity referring to the dissipation of turbulent kinetic energy
- k** : Quantity referring to turbulent kinetic energy
- t** : Quantity referring to turbulence

Superscript:

- : Fluctuating quantity
- : Time averaged quantity

CHAPTER 1. INTRODUCTION

1.1 Introduction

Most of the fluid flow and transport processes that occur in our near and far environment are driven by buoyancy forces. The buoyancy force arises from density differences that result from inhomogeneous spatial distribution of temperature and / or concentration of chemical species, material phase changes, and many other effects. The buoyancy force acting on a fluid induces a flow in the direction such that equilibrium can be re-established. The most widely used term for the buoyancy driven fluid flow and transport processes is “**natural convection**”. The term “**free convection**” is also commonly used. Many kinds of natural convection flow can be found because of different geometric configurations, different boundary conditions, and some other effects. In all natural convection flows the velocity and temperature fields are coupled and must be considered together and, compared with forced convection flows, the velocities are of small magnitude and the momentum and viscous effects are commonly of similar order.

Natural convection is employed in many technological and industrial applications due to its simplicity, reliability, and cost effectiveness. The natural convection heat transfer and fluid flow processes in a vertical parallel flat plate channel are relevant to the cooling of electronic equipment, solar collectors and dryers, passive solar heating and ventilation of buildings, Trombe Wall applications, heat exchange applications in nuclear technology, and some other applications [1]. Electronic circuit boards are positioned vertically in a cabinet forming parallel plate channels through which a coolant, usually air, is passed. Solar energy is collected by a conventional flat plate collector or a Trombe Wall to be utilised for active or passive heating, active and passive heating and ventilation of buildings. In nuclear technology natural convection in a vertical parallel flat plate channel is applied to the safe storage of used fuel assemblies and, more recently, to the reactor vessel auxiliary cooling system

(RVACS) which is employed by a new nuclear reactor design [2]. In the latter, the reactor guard vessel is surrounded by a duct wall forming a vertical channel. Under abnormal operating conditions, the guard vessel is heated by decay energy released from the reactor core. Consequently an upward flow is induced inside the channel because of buoyancy effects. The air drawn from the surroundings at the bottom of the channel is convected along it and the decay energy is removed from the surface by natural convection.

Natural convection heat transfer and fluid flow processes in small scale applications, such as electronic equipment cooling, usually fall into the category of the laminar flow regime as the geometric sizes and temperature differences or heat fluxes involved are relatively small. Although the flow may have large amplitude low frequency fluctuations, the flow field can still be successfully predicted by the tools of laminar flow analysis as reported by Carey et al. [3]. The processes in solar collectors, Trombe Walls, and nuclear technology heat exchange applications will usually involve either transition and/or turbulent flow regimes depending upon the sizes and thermal parameters. In both laminar and turbulent regimes, the flow along the channel is a developing flow. Induced flow rate and the convective heat transfer coefficient are the most important quantities that need to be accurately predicted in the evaluation of natural convection in vertical flat plate channels. The predictive methods and tools for the laminar flow case are well established. But this is not the case for the turbulent flows, and empirical relationships are still heavily relied on. Thus the availability of reliable experimental data is very important in order to tune the numerical models. Laminar natural convection in a vertical parallel flat plate channel has been extensively investigated both numerically and experimentally. The parameters affecting the above mentioned two quantities have been identified. However, experimental data on the flow and temperature fields inside the channel and on the behaviour of the flow is rather limited. The case of turbulent natural convection in a vertical channel has hardly been investigated despite its practical importance. Some work has been reported on the uniform wall heat flux (UHF) heating mode, but none for the uniform wall temperature (UWT) heating mode.

1.2 Present Project and Objectives

The present work deals with the experimental and numerical study of natural convection in vertical parallel flat plate channels heated asymmetrically. The channel considered is formed by a heated wall and an opposing unheated (or passively heated by the former). The investigation is undertaken for a small scale and a large scale channel. The geometric sizes and heating levels employed for the small and large scale channels, coupled with the experimental results obtained during this study, make it justifiable to refer to the small scale channel as a laminar flow channel and the large scale channel as a turbulent flow channel. In the turbulent flow channel, the flow starts as essentially laminar, undergoes a transition, and becomes turbulent depending upon the geometric and thermal parameters. As explained in later chapters, slightly different channel geometries are employed for laminar and turbulent flow cases. The laminar flow channel is formed by a heated central wall and two parallel outer walls passively heated by the former. The central wall is one third shorter than the outer walls and level with them at the channel outlet. This gives two identical channels one on each side of the central heated wall. The turbulent flow channel is formed by a heated wall and an opposing adiabatic wall. The heated and adiabatic walls are level both at the inlet and outlet. The laminar natural convection flow case is examined for the constant wall heat flux heating mode while the turbulent flow case is examined considering both UHF and UWT heating modes. The experimental work involves the simultaneous measurement of velocity and temperature profiles inside the channel using a Laser-Doppler Anemometry (LDA) system and a thermocouple temperature probe. Numerical analyses are carried out with the commercial Computational Fluid Dynamics (CFD) code PHOENICS. The numerical investigation of laminar channel flow is carried out with the standard features of PHOENICS. For the turbulent flow case, however, some Low Reynolds Number (LRN) k - ϵ turbulence models have been programmed into the CFD coding using the GROUND facility available within PHOENICS.

The main objectives of the present project are;

- 1) To measure flow and temperature fields inside the channel for both laminar and turbulent flow cases,
- 2) To model numerically and solve the natural convection processes for both laminar and turbulent flow cases using PHOENICS,
- 3) To assess how accurately the flow and temperature fields can be predicted by numerical solution by comparing numerical results and measurements for both laminar and turbulent flow cases,
- 4) To compare different k- ϵ turbulence models and select the most appropriate,
- 5) To provide correlations for the induced flow rate and heat transfer rate.

CHAPTER 2. LITERATURE REVIEW

2.1 Introduction

A survey of the literature has indicated that the case of laminar natural convection between parallel flat plates and parallel flat plate channels has been the subject of many research studies. This case has been investigated in many aspects ranging from geometric parameters to variable fluid properties. The turbulent channel case, however, has attracted little interest despite its importance. In the following sections a brief review of the literature on the laminar and turbulent channel flows, and on the application of LRN k - ϵ turbulence models to natural convection is presented. The section devoted to turbulent channel flows also includes references to studies of turbulent natural convection on single vertical flat plates due to the similarities of boundary layers on the channel walls to that on a single plate even though the cases are not exactly similar.

2.2 Laminar Natural Convection in Vertical Parallel Flat Plate Channels

The laminar natural convection heat transfer and fluid flow within vertical parallel flat plate channels has been extensively investigated by experimental, analytical, and numerical methods. The investigations covered a wide range of geometrical and thermo-physical aspects of the problem. These can be summarised as open and closed edged channels, effect of convection-radiation interaction, effect of obstruction near the inlet and outlet of channel, effect of channel inclination, effect of channel aspect ratio, effect of a vent on the channel wall, and effect of channel wall conductivity.

The first and most widely quoted detailed study is that of Elenbaas [4]. He reported heat transfer measurements on an experimental system made up of isothermal square vertical parallel flat plates. He developed an approximate simplified mathematical model by fitting a modified parabolic velocity profile and a modified exponential temperature profile for the region between the plates. When corrected for the finite

size of the plates, the result of the measurements agreed with the results of his mathematical model. Ostrach [5] carried out the first detailed analytical study of natural convection between parallel flat plates with uniform wall temperatures. Ostrach [5] gave particular attention to the case of fully developed flow, but did not present any correlations for the induced flow rate and heat transfer rate. Bodoia and Osterle [6] performed the first numerical study of the development of natural convection between symmetrically heated isothermal parallel plates and successfully compared their results with those of Elenbaas [4]. They used a finite difference method to discretise the transport equations and employed a uniform velocity profile at the channel inlet. Engel and Mueller [7] used an integral technique to solve the equations governing natural convection in vertical channels analytically. Their results agreed well with the results of [6] except for the velocity and temperature profiles close to the channel inlet. Engel and Mueller [7] claimed that their approach is applicable for $0 < Ra < \infty$ provided Gr is sufficiently large.

Aung et al. [8] conducted an experimental and numerical study of developing natural convection in vertical parallel plate channels for both UHF and UWT heating modes. Numerical solutions of the developing flow have been found to approach asymptotically the closed form solution for fully developed flow, Aung [9]. However, they neglected the Bernoulli pressure defect at the inlet associated with the acceleration of fluid from rest to the induced velocity. Their numerical solutions and experimental results produced reasonable agreement except for high Rayleigh numbers. Carpenter et. al. [10], and Sparrow et al. [11] performed numerical investigation of interacting radiation and developing laminar natural convection in vertical parallel plate channels. The results they obtained indicated that radiation can increase the overall heat transfer rate by 50 to 75 percent and reduce the wall temperature by as much as 50 percent compared with the non-radiation case. Dalbert et al. [12] have numerically studied the developing laminar natural convection between vertical parallel plates under UHF heating mode. They have calculated the wall temperatures and heat transfer parameters employing a Bernoulli pressure defect boundary condition at the channel inlet. Wirtz and Stutzman [13] reported

experiments on natural convection of air between parallel plates with uniform and symmetric wall heat fluxes. They have presented a correlation that allows for the calculation of the maximum temperature variation of plates for a given heat flux and channel geometry. The correlation equation has been shown to be accurate to ± 5 percent.

Flow reversal near the outlet of a vertical parallel flat plate channel has been reported by Sparrow et al. [14]. Their experiments which were carried out on a channel formed by an isothermal plate and an unheated opposing plate, for the first time revealed the existence of a pocket of downflow and recirculation adjacent to the unheated wall in the upper part of the channel. They found, however, that previous theoretical approaches, without consideration of flow reversal, could still be used although flow reversal exist close to the channel outlet. Aung and Worku [15, 16] performed a detailed study of flow reversal for the case of asymmetric isothermal parallel plates. They presented criteria for the occurrence of flow reversal based on an analytical solution of fully developed flow.

O'Meara and Poulikakos [17] investigated natural convection in an array of vertical heated plates with a 'floor' below and a 'ceiling' above them, their interest being in the temperature distribution of the plates in their multi-channel assembly.

Recent experimental studies concerning some other aspects of laminar natural convection in vertical parallel flat plate channels have been reported by Sparrow and Bahrami [18], Sparrow and Azevedo [19], Azevedo and Sparrow [20, 21], Papple and Tarasuk [22], Guo et al. [23], Li et al. [24], and Webb and Hill [25].

Sparrow and Bahrami [18], carried out experiments using a mass transfer measurement technique in order to eliminate the radiation, conduction and variable property effects. Their experiments were an elaborate scrutiny of the work of Elenbaas [4]. They examined open, one-side open, closed edged channels and the effect of channel aspect ratio. Their results agreed with [4] within a limit of 15-20

percent for relatively high channel aspect ratios, but the discrepancies were substantial for small channel aspect ratios. They attributed this to the effect of property variations and the massive corrections of [4] to account for the heat losses.

Sparrow and Azevedo [19] reported the experimental and computational investigation of the effect of channel aspect ratio ranging from fully developed channel flow to effectively single plate condition. The experiments were performed in water and the channel was formed by an isothermal plate and a parallel unheated wall. Their computational study took conduction in the plate into account. The results indicated that the effectively single flat plate did not form an upper bound for the channel heat transfer, and that the channel heat transfer was particularly sensitive to the channel width for small aspect ratios and small temperature differences.

The effect of channel inclination on natural convection in parallel flat plate channels has been investigated by Azevedo and Sparrow [20], and Papple and Tarasuk [22]. Azevedo and Sparrow [20] carried out experiments on an inclined channel in water changing the channel aspect ratio, inclination angle and heating conditions. The heating conditions considered were, symmetric isothermal walls, isothermal upper wall, and isothermal lower wall. They observed recirculation zones on the unheated wall for the single-sided heating conditions and secondary flows in the form of longitudinal vortices for lower isothermal wall conditions. A correlation has been given for the Nusselt number, which has represented all of the results within ± 10 percent. Papple and Tarasuk [22] performed experiments on inclined square cross section isothermal ducts using Mach-Zehnder interferometer. They considered the inclination angles of 0 and 45 degrees. Their result indicated a 5 percent increase in the average heat transfer in the case of inclined channel. The most significant effect of inclination was increased heat transfer from the lower wall and decreased heat transfer from the upper wall.

Azevedo and Sparrow [21], and more recently Moutsoglou et al. [26] investigated vented vertical channels. In [21] a channel formed by an isothermal wall and an

opposing vented unheated wall was examined experimentally and numerically. Both experimental and numerical results indicated that the average heat transfer rate was insensitive to vent size and location. The induced flow rate at the channel inlet was found to decrease with the existence of vent, but the overall flow rate was hardly affected. In [26], natural convection-radiation cooling of a similar channel was examined numerically for UHF heating mode. Moutsoglou et al. [26] reported that the heated wall temperature increased upstream of the uppermost vent location and decreased for low positioned vents compared to the unvented channel case.

Guo et al. [23] examined the natural convection heat transfer and fluid flow between isothermal parallel plates using Laser Speckle Photography. They presented a correlation of the experimental data to allow calculation of the local heat transfer rate. Li et al. [24] investigated the edge effect on a similar experimental set-up to [23]. They examined the entrainment of air from the edges qualitatively by flow visualisation. They also measured velocity profiles between the plates using LDA, but produced no correlation.

Webb and Hill [25] reported the results of an experimental study of natural convection in a vertical parallel plate channel heated asymmetrically. The importance of this work is its coverage of high Rayleigh numbers and an unheated channel section at the inlet. They have presented correlations of local Nusselt numbers as well as average Nusselt numbers.

Aihara and Maruyama [27] have explored numerically the effects of variable fluid properties for symmetric UHF and UWT heating modes. Air and transformer oil have been considered as convecting fluids. The results have indicated a decrease in the local heat transfer rates for air and an increase for oil with respect to constant property solutions. The differences of heat transfer characteristics for UHF heating mode between the constant property and variable property solution have been found to be smaller than for the UWT heating mode.

Effects of conducting walls have been investigated numerically by Sparrow and Tao [28], Burch et al. [29], and Kim et al. [30]. In [28] a pair of channels formed by two asymmetrically heated isothermal plates and a conducting plate in between has been studied. Variations of dimensionless channel height, dimensionless temperature difference of two outer walls and dimensionless position of the inner wall have been considered. The results presented have indicated the attainment of a fully developed flow regime for sufficiently tall channels. As for the surface temperature of the intermediate wall, it has been shown to increase with developing channel flow and to level off when fully developed conditions are reached. Burch et al. [29] have performed a numerical study of laminar natural convection between finitely conducting isothermal parallel vertical plates. They have considered different channel aspect ratios, plate thickness to channel width ratios, and plate to fluid conductivity ratios. Their results have indicated a non-uniform interface temperature, an increase in the heat transfer and induced flow rate with increasing plate conductivity. Kim et al. [30] have carried out a similar study to that of [29] with emphasis on asymmetric UHF heating mode and with air as the fluid. They have reported a maximum flow rate increase of 30 percent due to wall conduction for symmetric heating, and a more significant effect of wall conduction at low Grashof numbers than at high Grashof numbers.

The effect of channel inlet boundary condition treatment in numerical solutions has been analysed by Chappidi and Eno [31], and Naylor et al. [32]. Chappidi and Eno [31] examined the effects of uniform and parabolic velocity profiles at the inlet and the Bernoulli pressure defect boundary condition in the developing laminar natural convection channel flows for both UHF and UWT heating modes. The results have indicated little influence of inlet conditions on the thermal performance of channels at low Rayleigh numbers, and only a moderate influence at high Rayleigh numbers. The Bernoulli pressure defect boundary condition resulted in lower Nusselt numbers. Comparing the results of different boundary conditions with the experimental data, they concluded that there is not a single 'best type' of inlet boundary condition. The study of Naylor et al. [32] of an isothermal channel with an extended calculation

domain at the inlet has indicated the necessity of elliptic solution of the transport equations.

2.3 Turbulent Natural Convection in Vertical Parallel flat Plate Channels

As mentioned before, the reported work on the basic aspects of turbulent natural convection in vertical parallel flat plate channels is very limited. Thus it will be worthwhile to mention some of the studies of turbulent natural convection on single vertical flat plates due to the similarity of the boundary layers to those on the channel walls. The pioneering work on turbulent natural convection on a single vertical flat plate is by Griffith and Davies [33]. They measured velocity and temperature profiles and local heat transfer rates. In two later studies, Warner and Arpaci [34] measured mean temperature, and Cheesewright [35] measured mean velocity and temperature profiles. The measurements of Cheesewright [35] showed remarkably good agreement with the measurements of Griffith and Davies [33]. All of the above studies dealt with isothermal plates. Vliet and Liu [36] conducted experiments to investigate the development of a turbulent natural convection boundary layer on a uniformly heated plate in water. They measured mean temperature and velocity profiles as well as surface temperature distribution, and presented data for laminar, transition and turbulent flow regimes. An extensive experimental study of turbulent natural convection boundary layers is due to Smith [37] who measured the probability density distribution of temperature and streamwise velocity, and the power spectra of these quantities. He concluded that the fully developed flow had a spectral structure similar to that of forced convection flow, that is, a viscous sublayer where molecular transport conditions prevail, a buffer layer that includes the maximum of the mean velocity profile, and a turbulent layer where the spectra of temperature and velocity contain an inertial subrange. George and Capp [38], citing some previous works [39, 40], claimed that the heat flux, not the wall shear stress characterizes the flow region close to the wall. They proposed a boundary layer consisting of an inner flow region where mean convection terms are negligible, and an outer flow region where viscous

and conductive terms are negligible. The inner region, referred to as constant heat flux region, was also divided into a viscous sublayer, a buoyant sublayer and a buffer layer between. George and Capp [38] correlated existing data in conjunction with their proposed boundary layer structure, and presented universal velocity and temperature profiles for the inner and outer layers. Cheesewright [41], however, challenged the approach by George and Cap [38], that wall shear stress is not the main parameter in the correlation of natural convection boundary layers. Cheesewright and Mirzai [42] checked the arguments of George and Capp [38] with their measurements, and concluded that the wall shear stress is expected to be a parameter in the correlation of the temperature profiles at Grashof numbers above 10^{13} , and the velocity profiles can only be correlated when wall shear stress is included as a parameter. Several studies have been carried out on the stability and transition to turbulence of natural convection boundary layers. These and other aspects of natural convection are well presented in the reference book by Gebhart et al. [43].

The pioneering experimental work of Miyamoto et al. [44] is an important contribution to the understanding of turbulent natural convection phenomena in vertical parallel flat plate channels. They conducted experiments, with air on a channel formed by a uniformly heated plate and an opposing adiabatic plate, to measure turbulence properties of the flow and surface temperature distribution on the channel walls. They presented a correlation of their data that can be used to predict the heat transfer coefficient in the fully developed turbulent flow region of the channel.

Al Azzawi [1] carried out experiments with air in a similar but smaller scale channel arrangement of [44] measuring mean velocity and temperature profiles for both UHF and UWT heating modes. He made a numerical study with the assumption of laminar flow using PHOENICS. Experimental and numerical results were not in good agreement. Al Azzawi [1] presented correlations for induced flow rate and heat transfer coefficient.

Pederson et al. [45] performed experiments on an asymmetrically heated channel with unheated inlet and insulated outlet sections. They measured induced flow rate and wall temperature distribution. The heat fluxes considered were much higher than that of [1] and [44].

The most recent experimental study of turbulent natural convection in a vertical flat plate channel was carried out by La Pica et al. [46]. They employed a channel similar to the arrangements of [1] and [44] but with horizontal inlet and outlet sections. Measurements of wall temperature distribution, mean temperature profiles at different sections of channel and velocity profile at the channel inlet were conducted. La Pica et al. [46] produced correlations as given below for average Nusselt number, and Reynolds number based on the average inlet velocity and channel width.

$$\text{Nu} = \frac{hb}{k} = 0.9282\text{Ra}^{0.2035} \left(\frac{b}{H}\right)^{0.8972} \quad (2.1)$$

$$\text{Re} = \frac{\bar{U}_0 b}{\nu} = 0.5014\text{Ra}^{0.3148} \left(\frac{b}{H}\right)^{0.418} \quad (2.2)$$

Sohn [2] carried out an extensive numerical study of turbulent natural convection in asymmetrically heated vertical parallel plate channels for the UHF heating mode. He used a LRN k - ϵ turbulence model, and gave emphasis to surface radiation and ambient temperature stratification. His results compared well with the existing experimental data. Sohn [2] has performed a parametric study and presented equations correlating the heat transfer and fluid flow inside the channel to several parameters.

2.4 Turbulence Models for Natural Convection

The prediction of turbulent heat transfer and fluid flow processes by computational methods has been a major task of fluid dynamicists for many decades. Since direct

numerical solution of time dependent governing equations require very large computer memory and speed in order to capture the smallest scale of turbulence, attention has been focused on solving the time averaged equations with the modelled turbulent fluxes (Reynolds stresses or turbulent fluxes of scalars such as $\overline{u'T'}$) resulting from the time averaging. Many turbulence models for natural convection have been developed and successfully applied in recent decades. The zero equation models based on the mixing length hypothesis have been found to be incapable of capturing the transition from laminar to turbulent flow. That is because the zero equation models do not properly account for the dynamics of turbulence. The one or higher equation models have successfully predicted the transition. Since this study employs two-equation models, namely, the standard k- ϵ turbulence model and different LRN k- ϵ turbulence models, a brief survey of the application of these models to turbulent natural convection is given below.

The standard k- ϵ turbulence model was developed using an isotropic turbulence assumption and employed empirical wall functions close to the solid boundaries. Thus it does not properly predict the flow close to the solid boundaries where anisotropy becomes important. The need to extend the model right up to the solid boundaries has resulted in the development of several LRN k- ϵ turbulence models. The first of the LRN k- ϵ turbulence models was developed by Jones and Launder [47]. Plumb and Kennedy [48], and Lin and Churchill [49] successfully applied this model to the prediction of turbulent natural convection on vertical flat plates. The model of Jones and Launder [47] was later improved by Launder and Sharma [50], and more recently by Ince and Launder [51] to account for the buoyancy effects. To and Humphrey [52] formulated a LRN k- ϵ turbulence model and an algebraic stress model for natural convection with variable fluid properties. They have compared the results of the two models with experimental data and this showed fairly good agreement for the mean flow and heat transfer. More recently, Davidson [53, 54] developed a LRN k- ϵ turbulence model and a hybrid model. Patel et al. [55] evaluated several LRN k- ϵ turbulence models developed for forced convection. Their test cases included Low

Reynolds Number boundary layers, High Reynolds Number boundary layers, and equilibrium boundary layers in adverse pressure gradients. Based on the results of the tests, the models of Launder and Sharma [50], Lam and Bremhorst [56], and Chien [57] were shown to produce accurate results. Heiss et al. [58] explored how well forced convection based k - ϵ turbulence models can predict a simple vertical natural convection flow without adjusting the model constants, wall functions or closure hypothesis of the model. Regarding the computer cost and quality of the results they concluded that the model by Lam and Bremhorst [56] was the best tool. Sohn [2] examined four different LRN k - ϵ turbulence models (Jones and Launder [47], Launder and Sharma [50], To and Humphrey [52], Lam and Bremhorst [56] for natural convection channel flow with the UHF heating mode. Comparing the calculated results with the data of Miyamoto et al. [44], he concluded that the model of To and Humphrey [52] produced best results. Henkes and Hoogendoorn [59] tested different k - ϵ turbulence models for the natural convection boundary layer on a vertical flat plate. Their results showed that the models of Jones and Launder [47], Lam and Bremhorst [56], and Chien [57] produced the best results. The standard k - ϵ turbulence model produced high heat transfer rates and high turbulent viscosity despite predicting the mean flow velocity profiles close to the experimental data. Most recently, Peeters and Henkes [60] investigated numerically the natural convection boundary layer on a single flat plate using an algebraic and differential stress model. They also tested some LRN k - ϵ turbulence models. The study indicated the supremacy of differential stress model in the prediction of turbulence structure over the LRN k - ϵ turbulence models and algebraic stress model.

The most recent study on the subject is due to Fedorov and Viskanta [76]. They analysed turbulent natural convection in a channel similar to that of the present study using a LRN k - ϵ turbulence model. Fedorov and Viskanta [76] presented correlations for average heat transfer and produced scaling relations for induced mass flow rates and average heat transfer.

CHAPTER 3. PROBLEM FORMULATION AND FLOW EQUATIONS

3.1 Description of the Physical Models

3.1.1 Laminar Flow Channel

The physical model employed for the numerical analysis of the laminar flow case is shown schematically in Figure 3.1. The model closely resembles the experimental flow channel described in Chapter 5. The extent of the calculation domain is shown by dashed lines on the figure. The channel is formed by a central wall and two outer walls. Either constant uniform heat fluxes or variable wall temperatures are applied at the walls. The heat flux at the central wall, $q_{w,h}(\mathbf{x})$, is higher than that at the outer walls, $q_{w,c}(\mathbf{x})$. The central wall is referred to as the hot wall, and the outer wall as the cold wall or front wall.

The central plate has a thickness t and is placed midway between and parallel to the outer plates. The height of the heated plate is H and that of the outer plates is L . The ratio L/H is constant at $2/3$. The channel aspect ratio, b/H , is variable. The channel is assumed infinitely large in the direction perpendicular to the plane of paper, and is situated in an infinitely large quiescent ambient. The ambient conditions are constant and uniform. An axis of symmetry is assumed at the centre of the heated plate and as such the two symmetric channels do not interact. There is no externally imposed pressure at the channel inlet. The flow through the channel is induced entirely by buoyancy. The fluid at the inlet is drawn into the channel at the ambient conditions of P_∞ , T_∞ , ρ_∞ , and the heated fluid is released into the ambient at the outlet. No thermal mixing of inlet and outlet takes place. The Bernoulli pressure defect boundary condition is applied at the inlet, and a zero pressure boundary condition is employed at the outlet..

The other physical assumptions made are:

- All transfer processes take place at steady state.
- All transfer processes are two dimensional in x - y plane.

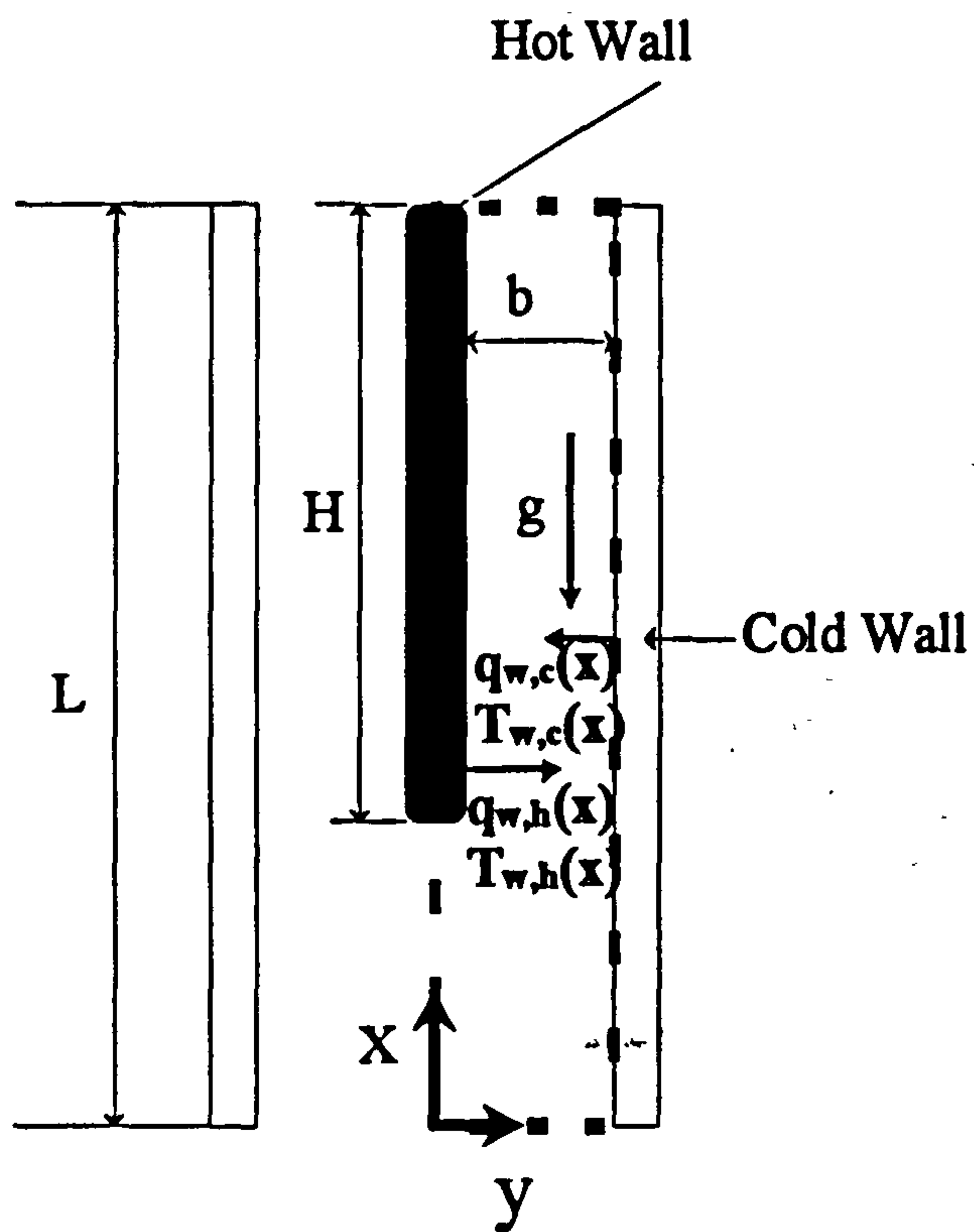


Figure 3.1 Laminar flow channel model for numerical analysis

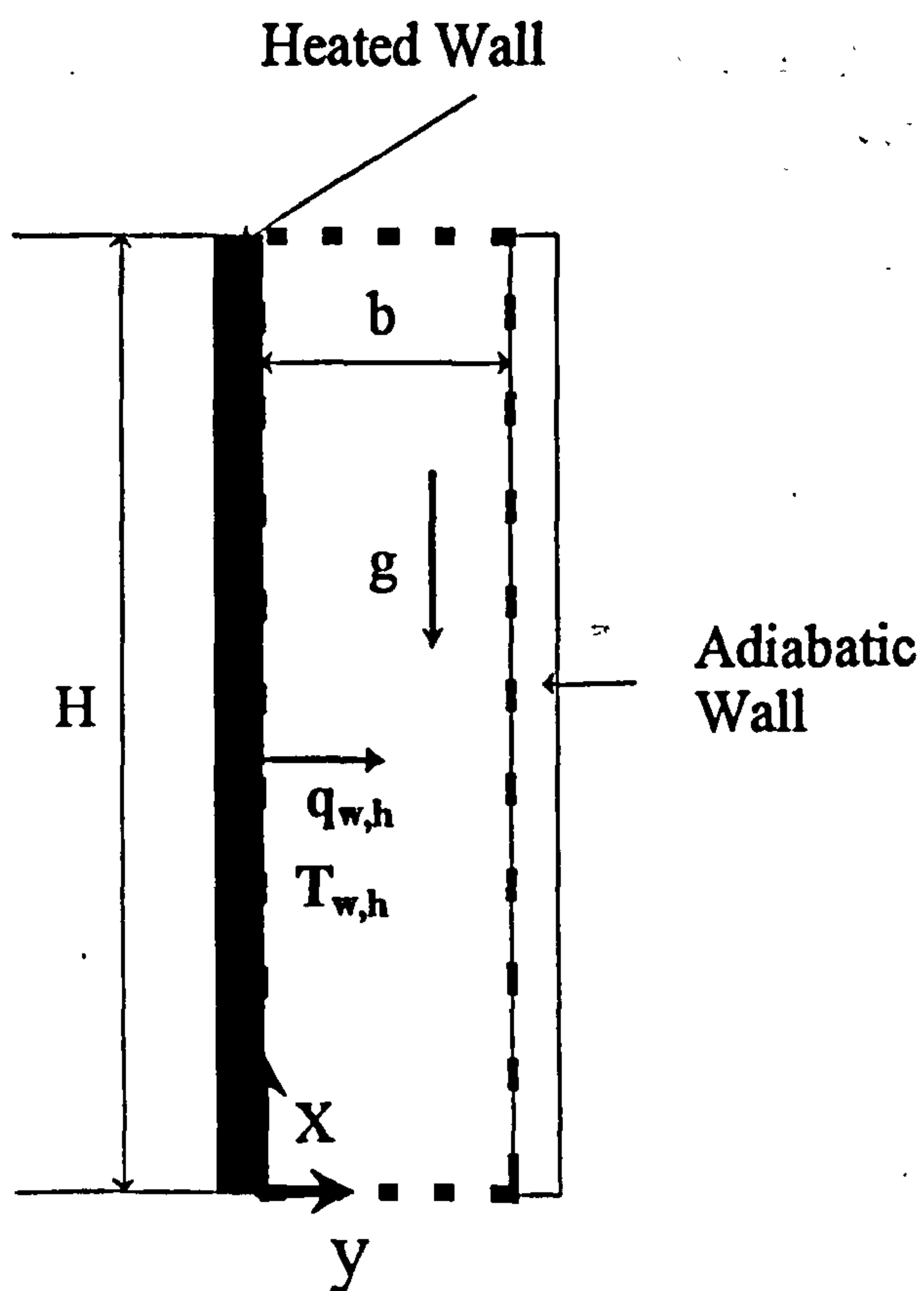


Figure 3.2 Turbulent flow channel model for numerical analysis

- The fluid is a continuum, Newtonian, and uniform in composition.
- The working fluid is air with constant Prandtl number. $Pr=0.7$.
- The properties of air other than the density are constant.
- The density of air changes only with temperature and obeys the ideal gas law.
- The conduction effect in the heated wall is neglected.
- Viscous dissipation and pressure work terms in the energy balance are negligible.
- No thermal radiation takes place
- Compressibility effects in the stress terms are negligible.
- No boundary layer simplifications applied.

3.1.2 Turbulent Flow Channel

The physical model used in the numerical analysis of turbulent natural convection channel flow is depicted in Figure 3.2. The channel consists of a heated wall and an opposing adiabatic wall. The plates are parallel to each other, and are of the same height. The channel width is b , and the height H . The heating modes employed are either UHF or UWT at the heated wall with wall heat flux of $q_{w,h}$ or wall temperature of $T_{w,h}$. The model assumptions stated in the previous subsection apply with the exception that the transport processes are turbulent throughout the channel. It is expected that the flow will start as laminar in the inlet region of the channel undergoing transition and becoming fully turbulent downstream depending upon the thermal and geometric parameters. The turbulent flow assumption, however, appears sensible due to the lack of transition criteria. The measurements made during this project has suggested that there is some level of turbulence at the channel inlet.

3.2 Mathematical Formulation

The conservation equations of mass, momentum and energy governing the natural convection flows in cartesian coordinates are given and explained in detail in Appendices A.1 and A.2 for laminar and turbulent flow respectively. Since they are

available in most textbooks [for example 43,61,62] on the subject, no attempt has been made to derive them again in this study.

3.2.1 Laminar Flow Equations

The physical model employed in this study for the numerical analysis of laminar natural convection channel flow has been described in subsection (3.1.1). The governing equations are given and explained in Appendix A.1. After making the necessary simplification to equations (A.17) to (A.20) for the model, the governing equations for the laminar natural convection channel flow are as follows.

$$\frac{\partial(\rho u)}{\partial x} + \frac{\partial(\rho v)}{\partial y} = 0 \quad (3.1)$$

$$\rho u \frac{\partial u}{\partial x} + \rho v \frac{\partial u}{\partial y} = -\frac{\partial p_m}{\partial x} + (\rho_\infty - \rho)g + \frac{\partial}{\partial x} \left[\mu \left(\frac{\partial u}{\partial x} \right) \right] + \frac{\partial}{\partial y} \left[\mu \left(\frac{\partial u}{\partial y} \right) \right] \quad (3.2)$$

$$\rho u \frac{\partial v}{\partial x} + \rho v \frac{\partial v}{\partial y} = -\frac{\partial p_m}{\partial y} + \frac{\partial}{\partial x} \left[\mu \left(\frac{\partial v}{\partial x} \right) \right] + \frac{\partial}{\partial y} \left[\mu \left(\frac{\partial v}{\partial y} \right) \right] \quad (3.3)$$

$$c_p \rho u \frac{\partial T}{\partial x} + c_p \rho v \frac{\partial T}{\partial y} = \lambda \left(\frac{\partial^2 T}{\partial x^2} + \frac{\partial^2 T}{\partial y^2} \right) \quad (3.4)$$

Boundary conditions:

In natural convection flows there is no information regarding the velocity and temperature fields before the start of calculations. Since governing equations are invariably coupled, the temperature field causes the velocity field to develop and in turn the velocity field affects the temperature field with the promotion of convective heat transfer.

$$\mathbf{x} = 0 : p = 0 = p_h + p_m, T = T_0 \quad (3.5.1)$$

$$\mathbf{x} = L : p = p_h = p_m = 0 \quad (3.5.2)$$

for $0 < \mathbf{x} \leq (L - H)$;

$$y = 0 : \frac{\partial u}{\partial y} = \frac{\partial v}{\partial y} = 0, -\lambda \frac{\partial T}{\partial y} = 0 \quad (3.5.3)$$

$$y = b : u = v = 0, -\lambda \frac{\partial T}{\partial y} = 0 \quad (3.5.4)$$

for $(L - H) \leq \mathbf{x} \leq L$;

$$y = 0 : u = v = 0, -\lambda \frac{\partial T}{\partial y} = q_{w,h}(\mathbf{x}) \text{ or } T = T_{w,h}(\mathbf{x}) \quad (3.5.5)$$

$$y = b : u = v = 0, -\lambda \frac{\partial T}{\partial y} = q_{w,c}(\mathbf{x}) \text{ or } T = T_{w,c}(\mathbf{x}) \quad (3.5.6)$$

3.2.2 Turbulent Flow Equations and k - ϵ Turbulence Models

Although equations (A.13) to (A.15) govern turbulent flows as well as laminar flows, the time dependent solution of these equations for fluid flow and heat transfer processes of practical engineering scale is almost out of the reach of today's computers. Thus the practice is to time average the transport equations and model the resultant extra terms such as $\overline{\rho u'_i u'_j}$, the Reynolds Stresses, and $\overline{\rho u'_i T'}$, the scalar turbulent fluxes. Derivation of turbulent flow equations from the time dependent equations governing the natural convection fluid flow and heat transfer processes of a Newtonian variable property fluid is given briefly in Appendix A.2. Modelling equations are also given for the Reynolds Stresses and turbulent scalar fluxes using an eddy viscosity approach. After neglecting the compressibility effects in the momentum equations and the terms involving density fluctuations such as $\overline{\rho' u'_i}$, $\overline{\rho' T'}$ in the

conservation equations since they are not important in the heating ranges considered in this study, and assuming no heat generation, no work done by pressure, no viscous dissipation including the dissipation of turbulent kinetic energy in the energy equation, the governing equations of variable property natural convection, equations (A.39) to (A.41), become;

$$\frac{\partial(\bar{\rho}\bar{u}_j)}{\partial x_j} = 0 \quad (3.6)$$

$$(\bar{\rho}\bar{u}_j) \frac{\partial \bar{u}_i}{\partial x_j} = -\frac{\partial \bar{p}_m}{\partial x_i} + (\bar{\rho} - \rho_\infty)g_i + \frac{\partial}{\partial x_j} \left[\mu \frac{\partial \bar{u}_i}{\partial x_j} + \mu_t \left(\frac{\partial \bar{u}_i}{\partial x_j} + \frac{\partial \bar{u}_j}{\partial x_i} \right) \right] \quad (3.7)$$

$$c_p (\bar{\rho}\bar{u}_j) \frac{\partial \bar{T}}{\partial x_j} = \frac{\partial}{\partial x_j} \left[\left(\lambda + \frac{c_p \mu_t}{\sigma_t} \right) \frac{\partial \bar{T}}{\partial x_j} \right] \quad (3.8)$$

where,

$$\mu_t = \bar{\rho} C_\mu f_\mu \frac{k^2}{\varepsilon} \quad (3.9)$$

k and ε are defined by equations (A.30) and (A.34) and are obtained from the solution of their differential equations. The general form of these differential equations for the LRN $k - \varepsilon$ turbulence models are given below in cartesian tensor form. Any term resulting from density-velocity correlations such as $(\overline{\rho' u_i' \dots})$ is neglected in the differential equations of k & ε .

$$\frac{\partial}{\partial x_j} [(\bar{\rho}\bar{u}_j)k] = \frac{\partial}{\partial x_j} \left[\left(\mu + \frac{\mu_t}{\sigma_k} \right) \frac{\partial k}{\partial x_j} \right] + (P + G - \varepsilon) + D \quad (3.10)$$

$$\frac{\partial}{\partial x_j} [(\bar{\rho}\bar{u}_j)\varepsilon] = \frac{\partial}{\partial x_j} \left[\left(\mu + \frac{\mu_t}{\sigma_\varepsilon} \right) \frac{\partial \varepsilon}{\partial x_j} \right] + \frac{\varepsilon}{k} (C_{\varepsilon 1} f_1 P + C_{\varepsilon 1} G - C_{\varepsilon 2} f_2 \varepsilon) + E \quad (3.11)$$

where,

$$P = -\overline{\rho u_i' u_j'} \frac{\partial \bar{u}_i}{\partial x_j} = \left[-\mu_t \left(\frac{\partial \bar{u}_i}{\partial x_j} + \frac{\partial \bar{u}_j}{\partial x_i} \right) + \frac{2}{3} k \delta_{ij} \right] \frac{\partial \bar{u}_i}{\partial x_j} \quad (3.12)$$

$$\mathbf{G} = -\bar{\rho}\beta\overline{u_i' T' g_i} = \beta \frac{\mu_t}{\sigma_t} \frac{\partial \bar{T}}{\partial x_i} g_i \quad (3.13)$$

and $i,j=1,\dots,3$.

In the above equations the terms \mathbf{P} and \mathbf{G} are the production of turbulent kinetic energy due to shearing and buoyancy respectively. C_μ , $C_{\varepsilon 1}$, and $C_{\varepsilon 2}$, are model constants. The values of the model constants for all models considered are $C_\mu=0.09$, $C_{\varepsilon 1}=1.44$, $C_{\varepsilon 2}=1.44$, $\sigma_t=0.9$, $\sigma_k=1.0$, $\sigma_\varepsilon=1.3$. f_μ , f_1 , f_2 , \mathbf{D} , and \mathbf{E} are the Low Reynolds Number model functions to account for the wall damping. The definitions of the model functions depend on the model employed and are given in Table 3.1 along with the wall boundary conditions of ε for the models considered in this study.

After expanding equations (3.6), (3.7), (3.8), (3.10), and (3.11) for the physical model described in sub-section (3.1.2), the governing equations for turbulent natural convection channel flow are as follows.

The continuity equation:

$$\frac{\partial(\bar{\rho}\bar{u})}{\partial x} + \frac{\partial(\bar{\rho}\bar{v})}{\partial y} = 0 \quad (3.14)$$

X component of momentum equation:

$$(\bar{\rho}\bar{u}) \frac{\partial \bar{u}}{\partial x} + (\bar{\rho}\bar{v}) \frac{\partial \bar{u}}{\partial y} = -\frac{\partial \bar{p}_m}{\partial x} + (\rho_\infty - \bar{\rho})g + \frac{\partial}{\partial x} [(\mu + \mu_t) \frac{\partial \bar{u}}{\partial x}] + \frac{\partial}{\partial y} [(\mu + \mu_t) \frac{\partial \bar{u}}{\partial y}] \quad (3.15)$$

Y component of momentum equation:

$$(\bar{\rho}\bar{u}) \frac{\partial \bar{v}}{\partial x} + (\bar{\rho}\bar{v}) \frac{\partial \bar{v}}{\partial y} = -\frac{\partial \bar{p}_m}{\partial y} + \frac{\partial}{\partial x} [(\mu + \mu_t) \frac{\partial \bar{v}}{\partial x}] + \frac{\partial}{\partial y} [(\mu + \mu_t) \frac{\partial \bar{v}}{\partial y}] \quad (3.16)$$

Energy equation:

$$c_p (\bar{\rho}\bar{u}) \frac{\partial \bar{T}}{\partial x} + c_p (\bar{\rho}\bar{v}) \frac{\partial \bar{T}}{\partial y} = \frac{\partial}{\partial x} \left[\left(\lambda + \frac{c_p \mu_t}{\sigma_t} \right) \frac{\partial \bar{T}}{\partial x} \right] + \frac{\partial}{\partial y} \left[\left(\lambda + \frac{c_p \mu_t}{\sigma_t} \right) \frac{\partial \bar{T}}{\partial y} \right] \quad (3.17)$$

LRN k-ε turbulence model equations:

$$(\bar{\rho}\bar{u})\frac{\partial k}{\partial x} + (\bar{\rho}\bar{v})\frac{\partial k}{\partial y} = \frac{\partial}{\partial x}\left[\left(\mu + \frac{\mu_t}{\sigma_k}\right)\frac{\partial k}{\partial x}\right] + \frac{\partial}{\partial y}\left[\left(\mu + \frac{\mu_t}{\sigma_k}\right)\frac{\partial k}{\partial y}\right] + (P + G - \varepsilon) + D \quad (3.18)$$

$$\begin{aligned} (\bar{\rho}\bar{u})\frac{\partial \varepsilon}{\partial x} + (\bar{\rho}\bar{v})\frac{\partial \varepsilon}{\partial y} = \frac{\partial}{\partial x}\left[\left(\mu + \frac{\mu_t}{\sigma_k}\right)\frac{\partial \varepsilon}{\partial x}\right] + \frac{\partial}{\partial y}\left[\left(\mu + \frac{\mu_t}{\sigma_k}\right)\frac{\partial \varepsilon}{\partial y}\right] \\ + \frac{\varepsilon}{k}(C_{\varepsilon 1}f_1P + C_{\varepsilon 1}G - C_{\varepsilon 2}f_2\varepsilon) + E \end{aligned} \quad (3.19)$$

where;

$$P = \mu_t \left\{ 2\left[\left(\frac{\partial \bar{u}}{\partial x}\right)^2 + \left(\frac{\partial \bar{v}}{\partial y}\right)^2\right] + \left(\frac{\partial \bar{u}}{\partial y} + \frac{\partial \bar{v}}{\partial x}\right)^2 \right\} \quad (3.20)$$

$$G = \beta \frac{\mu_t}{\sigma_t} \frac{\partial \bar{T}}{\partial x} g \quad (3.21)$$

The boundary conditions:

The argument mentioned under the boundary conditions subheading of subsection (3.2.1) applies for turbulent natural convection as well.

$$x = 0 : \bar{p} = \bar{p}_h + \bar{p}_m = 0, \bar{T} = T_0, k = k_0, \varepsilon = \varepsilon_0, \text{ (Equation (3.31.1 - 2))} \quad (3.22.1)$$

$$x = H : \bar{p} = \bar{p}_h = \bar{p}_m = 0 \quad (3.22.2)$$

$$y = 0 : \bar{u} = \bar{v} = 0, -\lambda \frac{\partial \bar{T}}{\partial y} = q_{w,h}, \text{ or } \bar{T} = T_{w,h}, k = 0, \varepsilon = \text{ as in Table 3.1} \quad (3.22.3)$$

$$y = b : \bar{u} = \bar{v} = 0, -\lambda \frac{\partial \bar{T}}{\partial y} = 0, k = 0, \varepsilon = \text{ as in Table 3.1} \quad (3.22.4)$$

The k-ε models employed in this study are The Standard k-ε Model (ST), Launder and Sharma LRN k-ε Model (LS) [50], To and Humphrey LRN k-ε Model (TH) [52],

Davidson LRN k-ε Model (DA) [53,54], and Lam and Bremhorst LRN k-ε Model (LB) [56]. The model functions and wall boundary conditions of ε are presented in Table 3.1. The turbulent Reynolds numbers appearing in Table 3.1 are defined as follows.

$$Re_t = \frac{k^2}{\nu \varepsilon} \quad (3.23)$$

$$Re_y = \frac{y\sqrt{k}}{\nu} \quad (3.24)$$

Table 3.1 The functions of the Low Reynolds Number k-ε turbulence models.

Model	f_μ	f_1	f_2	ε_w	D	E
ST	1.0	1.0	1.0	Law of the Wall	0.0	0.0
LS	$\text{Exp}\left[\frac{-34}{(1+0.02Re_t)^2}\right]$	1.0	$1-0.3\text{Exp}[-Re_t^2]$	0.0	$-2\mu\left(\frac{\partial k^{0.5}}{\partial y}\right)^2$	$2\mu\mu_t\left(\frac{\partial^2 \bar{u}}{\partial y^2}\right)^2$
TH	$\text{Exp}\left[\frac{-25}{1+0.02Re_t}\right]$	1.0	$1-0.3\text{Exp}[-Re_t^2]$ $(1-\text{Exp}[-Re_t^2])$	$2\nu\left(\frac{\partial k^{0.5}}{\partial y}\right)^2$	0.0	0.0
DA	$\text{Exp}\left[\frac{-34}{(1+0.02Re_t)^2}\right]$	$1+\left(\frac{0.14}{f_\mu}\right)^3$	$1-0.27\text{Exp}[-Re_t^2]$ $(1-\text{Exp}[-Re_y])$	$\frac{\partial \varepsilon}{\partial y} = 0$	0.0	0.0
LB	$(1-\text{Exp}[-0.0165Re_y])^2$ $(1.0 + \frac{20.5}{Re_t})$	$1.0 + \left(\frac{0.05}{f_\mu}\right)^3$	$(1-\text{Exp}[-Re_t^2])$	$\frac{\partial \varepsilon}{\partial y} = 0$	0.0	0.0

3.2.3 Dimensional and Dimensionless Parameters

The governing equations for both laminar and turbulent natural convection are solved in dimensional form in this project. In order to present the numerical and experimental results the following dimensional and dimensionless parameters are defined similar to those used in the literature on natural convection channel flows.

Prandtl Number:

$$\text{Pr} = \frac{\nu}{\alpha} ; \quad \alpha = \frac{\lambda}{\rho c_p} \quad (3.25)$$

Reynolds Number:

$$\text{Re} = \frac{u_{0,\text{ave}} b}{\nu} \quad \text{or} \quad \text{Re} = \frac{\bar{u}_{0,\text{ave}} b}{\nu} \quad (3.26)$$

Grashof Number:

$$\text{Gr} = \frac{g\beta q_c b^4}{\nu^2 \lambda} \quad (\text{UHF}) \quad \text{or} \quad \text{Gr} = \frac{g\beta(T_{w,h} - T_0)b^3}{\nu^2} \quad (\text{UWT}) \quad (3.27)$$

Rayleigh Number:

$$\text{Ra} = \text{Gr Pr} \quad (3.28)$$

Nusselt Number:

$$\text{Nu} = \frac{q_c b}{(T_{w,h,1/2} - T_0)\lambda} \quad (\text{UHF}), \quad \text{Nu} = \frac{q_c b}{(T_{w,h} - T_0)\lambda} \quad (\text{UWT}) \quad (3.29)$$

Turbulence Intensity:

$$\text{Tu} = \left(\frac{u'^2 + v'^2 + w'^2}{3} \right)^{1/2} / (\bar{u}^2 + \bar{v}^2 + \bar{w}^2)^{1/2} \quad (3.30.1)$$

$$\text{Tu}_0 = \left(\frac{u'^2 + v'^2 + w'^2}{3} \right)^{1/2} / (\bar{u}_{0,\text{ave}}) \quad (3.30.2)$$

Values of k & ε at the Inlet:

$$k_0 = \frac{3}{2} (\text{Tu}_0)^2 (\bar{u}_{0,\text{ave}})^2 \quad (3.31.1)$$

$$\varepsilon = \varepsilon_0 = C_\mu^{3/4} \frac{k_0^{3/2}}{\kappa b} \quad (3.31.2)$$

where, $\kappa=0.41$ (Karman coefficient).

CHAPTER 4. NUMERICAL SOLUTION METHOD

4.1 Introduction

Predictive methods are one of the most indispensable tools of engineering analysis. Although the most reliable information about a physical process is obtained through experiments, the predictive tools such as CFD can play a valuable role if the process under consideration can be realistically modelled into soluble mathematical relations. The mass, momentum, and energy conservation equations in the form of equations (A.1 - A.3) are exact representation of mass and energy transfer. However, there is no analytical solution for them as they stand because of the non-linearity of the equations, and in the case of natural convection, the coupling of the equations. Several numerical methods have been developed to numerically solve the conservation equations. The method followed in CFD is to discretise the governing partial differential equations into a set of linear algebraic equations that can be solved using iterative numerical techniques. The finite-difference and finite-volume are frequently used discretisation methods. The commercial CFD code PHOENICS used in this study employs a finite-volume discretisation which is explained in one of the following sub-sections. The modelling and solution of fluid flow and heat transfer by PHOENICS is explained in the following section.

4.2 PHOENICS CFD Code

PHOENICS is an acronym standing for **Parabolic, Hyperbolic Or Elliptic Numerical-Integration Code Series**. PHOENICS is a finite-volume based general purpose CFD program for the solution of one or two phase, steady or unsteady fluid flow and heat transfer problems either reacting or non-reacting flows in one, two or three dimensional geometries of cartesian, polar or body-fitted coordinates.

4.2.1 The Overall Structure of PHOENICS

PHOENICS has three main components. These are the preprocessor called **SATELLITE**, the main processor called **EARTH**, and the post processor called **PHOTON**. PHOENICS has three stand-alone components called **GUIDE**, **AUTOPLOT**, and **PINTO**.

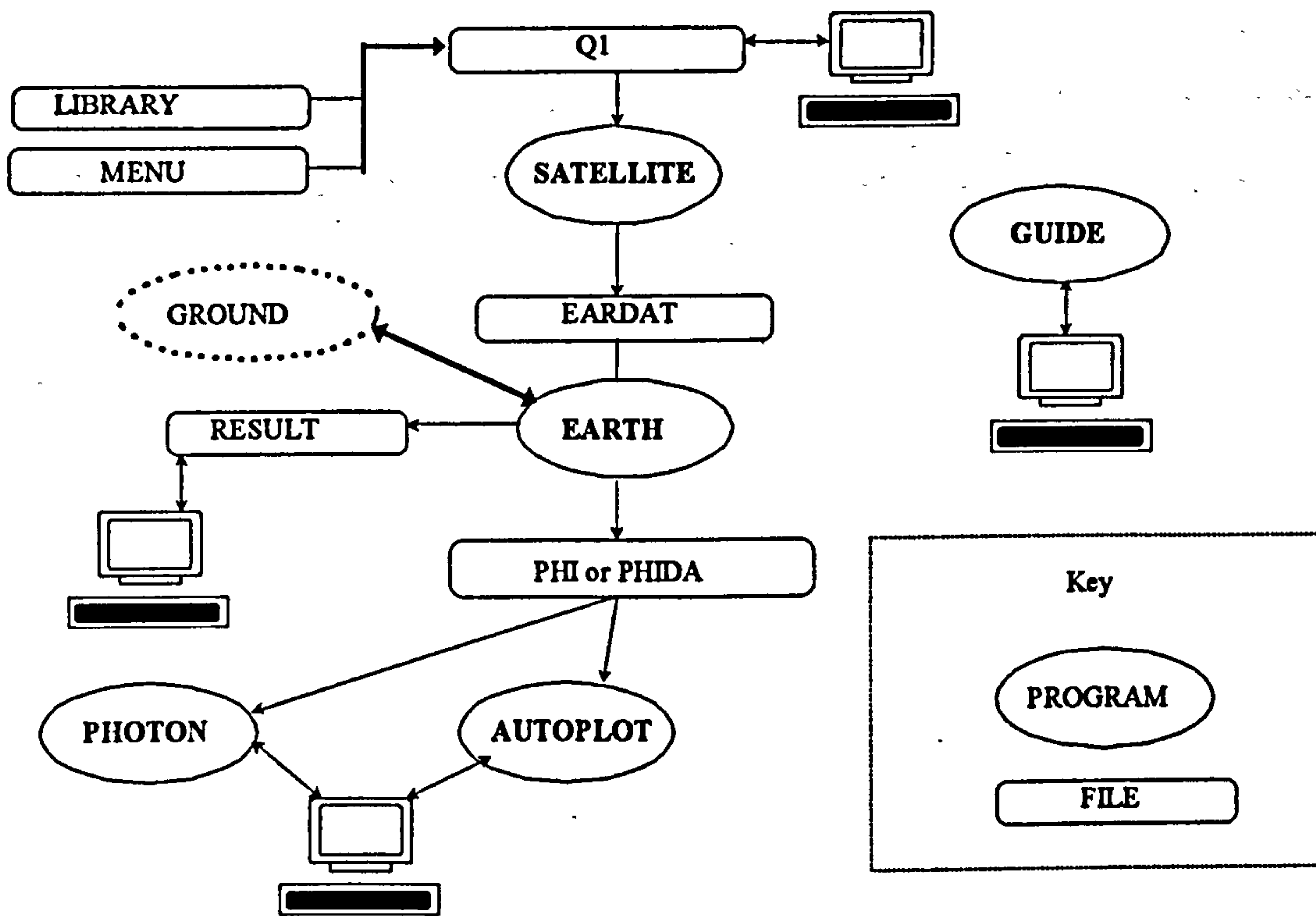


Figure 4.1 The layout of PHOENICS code.

SATELLITE receives instructions from the user either via the input file called **Q1** or, during an interactive session, through the input device, and creates a data file called **EARDAT** that **EARTH** can understand and execute. The main processor, **EARTH**, contains the main flow simulation code. It processes the instruction supplied by the satellite via **EARDAT** and produces two files, namely **RESULT** and either **PHIDA** or **PHI**. The **RESULT** is a text file with crude graphics for the inspection by the user. **PHIDA** or **PHI** are binary and ASCII files respectively, and are the input files containing the results and geometry information of the calculation domain for the post processing. The post-processor, **PHOTON**, visualises the solution data provided by

either of the **PHI** or **PHIDA**. The stand-alone component **GUIDE** provides information about **PHOENICS**, how to run it and about **CFD** in general. **AUTOPLOT** facilitates the plotting of graphs either from **PHOENICS** data or of other origin. **PINTO** is the code that lets the transfer of **PHOENICS** data from one grid to another of different fineness. A schematic diagram of the components of **PHOENICS** and their relationship is given in Figure 4-1.

Both **EARTH** and **SATELLITE** provide option for additional **FORTTRAN** coding as required by the user. This allows the user to build in extra modelling and property equations that are not provided as standard by the **PHOENICS**. These coding frameworks are called **GROUND** and **SATLIT** for earth and satellite respectively.

4.2.2 The General Transport Equation Solved by **PHOENICS**

The general transport equation solved by **PHOENICS**, in cartesian tensor notation has the following form.

$$\frac{\partial}{\partial t}(\rho\phi) + \frac{\partial}{\partial x_j}(\rho u_j \phi) = \frac{\partial}{\partial x_j}(\Gamma_\phi \frac{\partial \phi}{\partial x_j}) + S_\phi \quad (4.1)$$

This equation represents transport of mass when ϕ is replaced by **1**, and conservation of the variable what ever variable ϕ is replaced with. The terms of this differential equations are known as **transient**, **convective**, **diffusive**, and **source** terms from left to right respectively. Γ_ϕ is the exchange coefficient of variable ϕ .

4.2.3 Modelling of Fluid Flow and Heat Transfer within **PHOENICS**

Any analytic solution of the general transport equation, equation (4.1), would contain continuous information about the variable ϕ in space and time within the calculation domain. Since analytical solution is impossible, numerical solutions are sought. The practice in the numerical solution of differential equations is to replace the continuous information that would be contained in the exact solution with discrete values. That is

achieved by transforming the differential equations into algebraic equations involving the unknown values of the variable ϕ at discrete points in the calculation domain. Thus the distribution of variable ϕ within the calculation domain is discretised. If the number of discrete points in space and time within the calculation domain are infinitely large the numerical solution will be the same as the exact solution. There are different methods of discretisation. The method used in PHOENICS is the finite volume discretisation which is explained in detail in the following subsection.

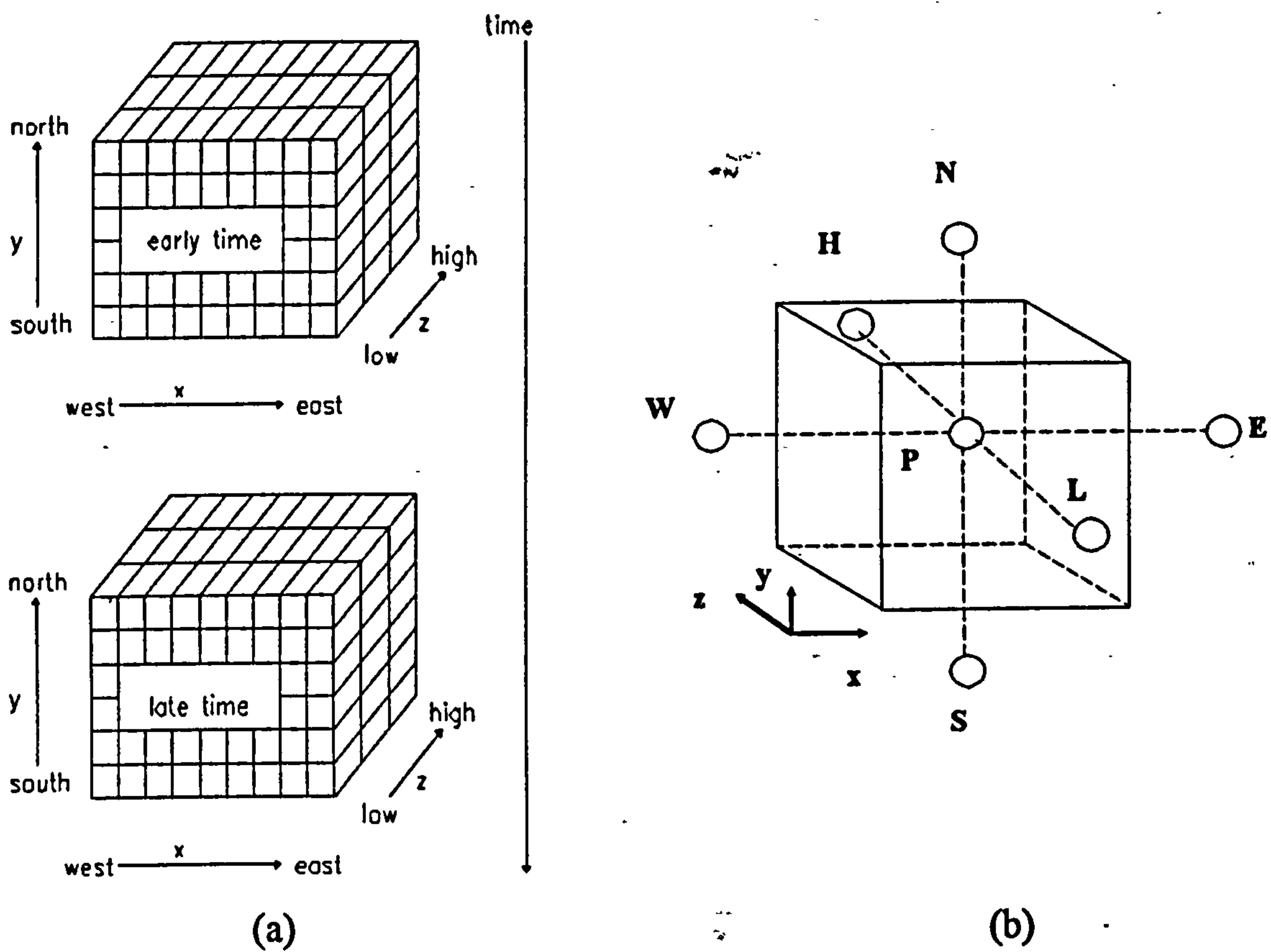


Figure 4.2 Space-time domain and a computational cell in PHOENICS.

4.2.3.1 Derivation of the Finite Volume Discretisation Equations

The principle of finite volume discretisation is to subdivide the calculation domain into a number of volumes or cells and integrate the general transport equation over each volume with profile assumptions for the variable ϕ within the volume. Figure 4.2

depicts the space time domain (a) and a computational cell (b) of PHOENICS in cartesian coordinates. Each computational cell has six faces with six neighbouring cells and a grid point P at the centre. E, W, N, S, H and L stand for east, west, north, south, high and low respectively. The derivation of the finite volume equations will be explained for the one dimensional cell cluster shown in Figure 4.3. P, W and E denote the grid points, e and w denote the east and west interfaces of the centre cell with the respective neighbouring cell.

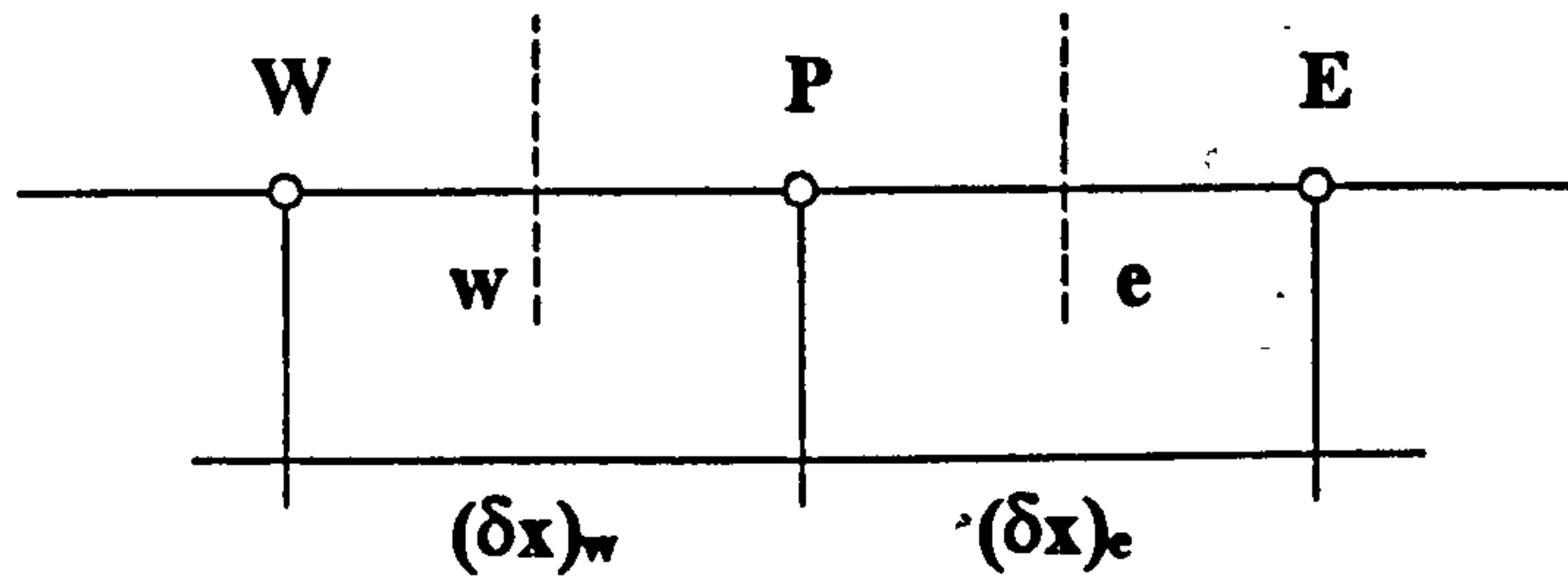


Figure 4.3 One dimensional cell cluster

The general steady transport equation for the cell cluster of Figure 4.3 can be written as:

$$\frac{d}{dx}(\rho u \phi) = \frac{d}{dx} \left[\Gamma_{\phi} \frac{d\phi}{dx} \right] + S_{\phi} \quad (4.2)$$

integrating over the cell P gives,

$$\int_w^e \frac{d}{dx}(\rho u \phi) dx = \int_w^e \frac{d}{dx} \left[\Gamma_{\phi} \frac{d\phi}{dx} \right] dx + \int_w^e S_{\phi} dx \quad (4.3)$$

and assuming a step-wise profile for the source term then

$$(\rho u \phi)_e - (\rho u \phi)_w = \left[\Gamma_{\phi} \frac{d\phi}{dx} \right]_e - \left[\Gamma_{\phi} \frac{d\phi}{dx} \right]_w + S_{\phi,P} \frac{1}{2} [(\delta x)_e + (\delta x)_w] \quad (4.4)$$

With a piece-wise linear profile assumption for the diffusive term the equation becomes

$$(\rho u \phi)_e - (\rho u \phi)_w = \frac{\Gamma_{\phi,e} (\phi_E - \phi_P)}{(\delta x)_e} - \frac{\Gamma_{\phi,w} (\phi_P - \phi_W)}{(\delta x)_w} + S_{\phi,P} \frac{1}{2} [(\delta x)_e + (\delta x)_w] \quad (4.5)$$

For the sake of brevity we define $\Gamma_{\phi,e} / (\delta x)_e = D_e$, $\Gamma_{\phi,w} / (\delta x)_w = D_w$, $(\rho u)_e = F_e$, $(\rho u)_w = F_w$, and $S = S_{\phi,P} \frac{1}{2} [(\delta x)_e + (\delta x)_w]$. Therefore equation (4.5) becomes:

$$F_e \phi_e - F_w \phi_w = D_e (\phi_E - \phi_P) - D_w (\phi_P - \phi_W) + S \quad (4.6)$$

Diffusive and source terms have already been discretised in relation to the grid points. The convective term, however, does not contain any information regarding the level of contribution by the neighbouring cells. There are several different discretisation schemes for the convective terms such as central difference, upwind, hybrid and power-law [63]. The default in PHOENICS is the hybrid scheme which combines the benefits of central difference and upwind schemes [63]. The discretisation equation for the grid point P can be written as:

$$a_P \phi_P = a_E \phi_E + a_W \phi_W + S \quad (4.7)$$

where, a 's are the coefficients and S is the source term contribution to ϕ_P . a_E and a_W contain information on the contribution of east and west cells by convection and diffusion. For the hybrid scheme a_E and a_W are defined as:

$$a_E = \left[-\text{Pe}, 1, -\frac{\text{Pe}}{2} \right] \quad (4.8)$$

$$a_W = \left[\text{Pe}, 1, +\frac{\text{Pe}}{2} \right] \quad (4.9)$$

where $[]$ stands for the largest of the quantities contained within, Pe is the Peclet number and is defined as $\text{Pe} = F_e / D_e$. It can be seen from equations (4.8) and (4.9) that for $-2 \leq \text{Pe} \leq 2$ where convection and diffusion have similar magnitude, the hybrid scheme will reduce to the central difference scheme. Out of this range, where convection is dominant, it will take the form of the upwind scheme.

4.2.3.2 Finite Volume Equation Solved by PHOENICS

Finite volume discretisation equations for a steady one dimensional process have been derived in the previous subsection. The general form of finite volume discretisation equations employed in PHOENICS for cartesian and polar coordinates can be written as:

$$a_P \phi_P = a_E \phi_E + a_W \phi_W + a_N \phi_N + a_S \phi_S + a_H \phi_H + a_L \phi_L + a_T \phi_T + S \quad (4.10)$$

where a 's are coefficients, S stands for the source term, subscript T indicates transient effects and the other subscripts denote the computational cell and the neighbouring cells as depicted in Figure 4.2'(a). The definitions of coefficients depends on the discretisation scheme as explained in the previous subsection. PHOENICS allows different discretisation schemes for the convective term and the fully implicit scheme for the transient term. Patankar [63] gives a detailed account of finite volume discretisation methods and their implications.

4.2.3.3 Staggered Grid Approach

Equation (4.10) implies that the $\phi_p, \phi_p, ..$ refer to the value of the dependent variable at the grid point in the centre of the computational cell. When dependent variable ϕ refers to the velocity, however, there are numerical problems associated with central differencing schemes [63, 64]. To avoid this problem PHOENICS employs a staggered grid for the solution of the momentum equations as shown in Figure 4.4. PHOENICS solves the equations for the scalar variables such as pressure and temperature for their values at the centre of the cells in the grid cell structure introduced by the user. The velocity components are calculated at the centre of the cell interfaces.

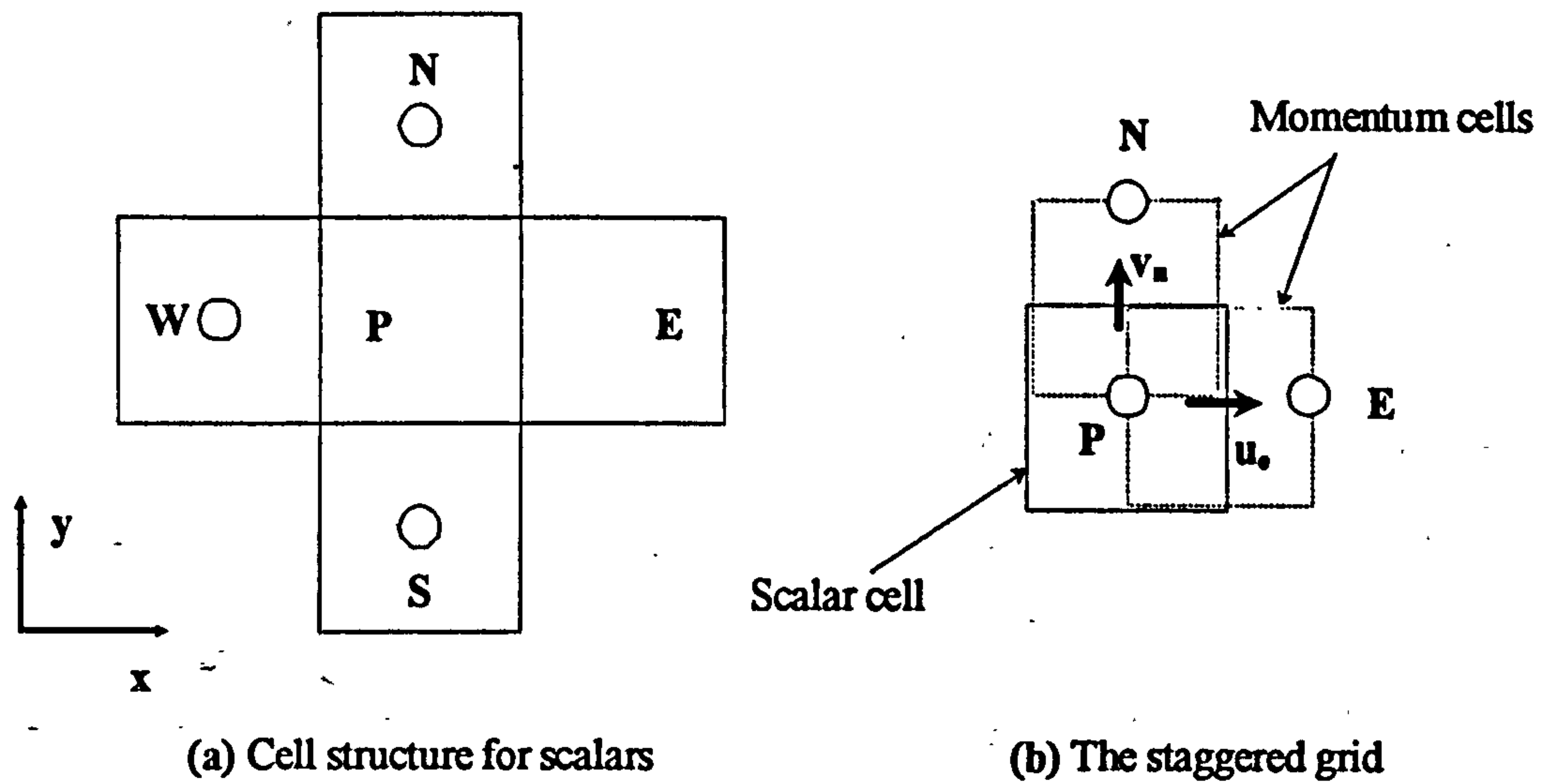


Figure 4.4 The cell structure of PHOENICS for scalars and velocity

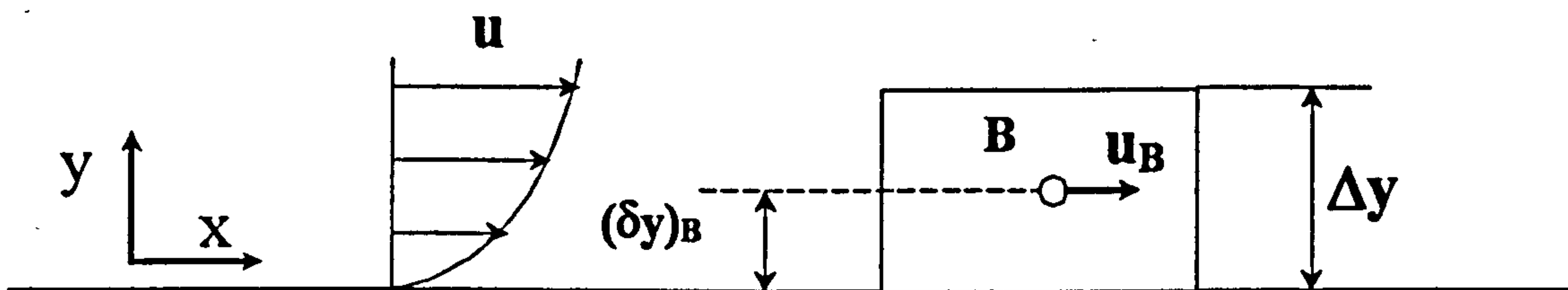


Figure 4.5 Laminar flow boundary cell in PHOENICS

4.2.3.4 Boundary Conditions and Source Terms

By default all fluxes of variable ϕ at the cell boundaries are zero in PHOENICS. Any boundary condition or source / sink term must be introduced by the user. Boundary conditions are implemented in PHOENICS as additional source or sink terms in the finite volume equations of the boundary cells of the calculation domain. The source terms in PHOENICS are introduced with the combination of the **PATCH** and **COVAL** commands [65,66]. The **PATCH** command defines in which cells of calculation domain and where in the cell the sources are to be applied. The **COVAL** command determines the magnitude of the source. The following relationship is employed for the source terms;

$$S_{\phi} = f * CO * (VAL - \phi) \quad (4.11)$$

where ϕ is the dependent variable for which the boundary condition is being introduced, f is multiplication factor depending on the PATCH type, CO is the coefficient of the source and VAL is the required value of the variable at the boundary of the cell or all over the cell if the boundary condition is going to be applied in the cell. Equation (4.11) is a linear relationship so that it will be compatible with the linear algebraic finite volume equations. Any non-linear source must be rearranged into the form of equation (4.11) and **GROUND** coding must be written for the CO 's and VAL 's, as explained in subsection 4.3, that might be the functions of the dependent variables themselves. The no-slip boundary condition at the wall for the x-direction momentum equation is explained below as an example of the implementation of linear sources in PHOENICS. The wall shear stress in Figure 4.5 is $\tau_x = -\mu(\partial u / \partial y)$ exactly. For the boundary cell in Figure 4.5, the velocity gradient can be approximated as $(\partial u / \partial y) = u_b / (\delta y)_b$ as the velocity at the wall is zero for the no-slip condition. The shear force acting on the boundary cell is:

$$\tau_x \Delta x \Delta z = \Delta x \Delta z \frac{\mu}{(\Delta y / 2)} (0 - u_b) = f CO (VAL - u_b) \quad (4.12)$$

The multiplication factor f is $\Delta x \Delta z \frac{\mu}{(\Delta y / 2)}$ in PHOENICS for wall type boundaries.

Equation (4.12) indicates that $CO = 1$ and $VAL = 0$ are needed to set no-slip boundary conditions for the momentum equations in laminar flow. This produces a sink of momentum in the finite volume equation at the boundary cell.

4.2.3.5 Solution of Finite-Volume Equations

The general transport equation solved by PHOENICS might be non-linear. The convective term in the momentum equation is non-linear. As for natural convection all equations are non-linear and coupled. After discretisation the coefficients of finite volume equations will be functions of the dependent variables such as velocity and

temperature. PHOENICS employs an iterative solution of the finite volume equations, regularly updating their coefficients and the auxiliary variables as the solution progresses.

The unknown pressure field poses a difficulty in the solution of the momentum equations to produce velocity components. There is no equation for the pressure, unlike the velocity, energy, etc., that it can be calculated from. It is possible that the pressure field can be indirectly determined by the continuity equation. If the correct pressure field is substituted into the momentum equations, the consequent velocity field satisfies the continuity equation. With a guess and correct procedure for the pressure field, the momentum equations are solved with the guessed pressure field and the pressure field is corrected until the continuity equation is satisfied. The pressure correction process along with the solution procedure is known as the SIMPLE (SEMI-IMPLICIT METHOD for PRESSURE LINKED EQUATIONS) algorithm [63]. Patankar [63] explains a revised version of it, the SIMPLER algorithm. However, PHOENICS uses another variant called SIMPLEST [67].

4.3 Modelling of Natural Convection Channel Flows by PHOENICS

The modelling and solution of fluid flow and heat transfer by PHOENICS has been explained in the previous section. It is equally applicable to both natural and forced flows. The user is required to supply the geometry, source, and boundary condition information for the calculation domain by way of the Q1 file. This is well documented in references [65, 66] and on-line in PHOENICS, and will not be explained here. This section explains how to implement the models formulated in Chapter 3 by PHOENICS and additional modelling and related FORTRAN coding .

4.3.1 Laminar Natural Convection Channel Flow

The laminar natural convection channel flow problem formulated in Chapter 3 can be solved with the standard features of PHOENICS without additional modelling.

4.3.2 Turbulent Natural Convection Channel Flow

4.3.2.1 PHOENICS Implementation of Turbulent Transport

PHOENICS has the Standard k - ϵ turbulence model and some other Eddy Viscosity models for turbulent fluid flow and heat transfer and the Reynolds Stress model for isothermal flows built in by default. For the LRN k - ϵ turbulence models, however, additional Fortran coding must be provided by way of the **GROUND** file. The general transport equation solved by PHOENICS was given in subsection 4.2.2 and its discretised form in subsection 4.2.3.2. The same finite volume equations of continuity, momentum and energy are used in PHOENICS for the solution of laminar and eddy viscosity modelled turbulent transport with the difference between the two being the exchange coefficient Γ_ϕ in the diffusive term and any additional sources resulting from the modelling. In addition to the continuity, momentum and energy equation, finite volume discretised differential equations of k and ϵ are solved for the k - ϵ modelled turbulent transport. The exchange coefficient Γ_ϕ of equation (4.1) for the variable solved in laminar flows is the molecular exchange coefficient, $\Gamma_{\phi,l}$. In the turbulent flows, PHOENICS uses an effective exchange coefficient which is the sum of the molecular exchange coefficient, $\Gamma_{\phi,l}$, and turbulent exchange coefficient, $\Gamma_{\phi,t}$. PHOENICS works out the exchange coefficient from the Prandtl number as given below.

$$\text{Pr}_\phi = \frac{\mu}{\Gamma_\phi} \quad (4.13)$$

The user is required to input the laminar and turbulent Prandtl numbers of the variable solved, in the Q1 file.

4.3.2.2 The LRN k - ϵ Turbulence Modelling of Natural Convection by PHOENICS

The LRN k - ϵ Models considered in this study are Launder and Sharma (LS) [50], To and Humphrey (TH) [52], Davidson (DA) [53,54], and Lam and Bremhorst (LB)

[56]. In order to solve the turbulent natural convection problem formulated in subsection 3.2.2 using PHOENICS, Fortran coding is required to be inserted by way of **GROUND** to calculate the additional sources in the governing equations, the LRN k - ϵ model functions, the wall boundary condition of ϵ for one of the models considered and the inlet boundary condition of ϵ . The **GROUND** file written to implement the LRN k - ϵ models of this study is given in Appendix B.1. The sources, functions and variables for which **GROUND** coding is provided are explained below.

The governing equations for the turbulent natural convection considered in this study have been obtained in Chapter 3 and are given below.

The continuity equation:

$$\frac{\partial(\bar{\rho}\bar{u})}{\partial x} + \frac{\partial(\bar{\rho}\bar{v})}{\partial y} = 0 \quad (4.14)$$

X component of momentum equation:

$$(\bar{\rho}\bar{u}) \frac{\partial\bar{u}}{\partial x} + (\bar{\rho}\bar{v}) \frac{\partial\bar{u}}{\partial y} = -\frac{\partial\bar{p}_m}{\partial x} + (\rho_\infty - \bar{\rho})g + \frac{\partial}{\partial x} [(\mu + \mu_t) \frac{\partial\bar{u}}{\partial x}] + \frac{\partial}{\partial y} [(\mu + \mu_t) \frac{\partial\bar{u}}{\partial y}] \quad (4.15)$$

Y component of momentum equation:

$$(\bar{\rho}\bar{u}) \frac{\partial\bar{v}}{\partial x} + (\bar{\rho}\bar{v}) \frac{\partial\bar{v}}{\partial y} = -\frac{\partial\bar{p}_m}{\partial y} + \frac{\partial}{\partial x} [(\mu + \mu_t) \frac{\partial\bar{v}}{\partial x}] + \frac{\partial}{\partial y} [(\mu + \mu_t) \frac{\partial\bar{v}}{\partial y}] \quad (4.16)$$

Energy equation:

$$c_p(\bar{\rho}\bar{u}) \frac{\partial\bar{T}}{\partial x} + c_p(\bar{\rho}\bar{v}) \frac{\partial\bar{T}}{\partial y} = \frac{\partial}{\partial x} [(\lambda + \frac{c_p\mu_t}{\sigma_t}) \frac{\partial\bar{T}}{\partial x}] + \frac{\partial}{\partial y} [(\lambda + \frac{c_p\mu_t}{\sigma_t}) \frac{\partial\bar{T}}{\partial y}] \quad (4.17)$$

LRN k - ϵ turbulence model (k and ϵ) equations:

$$(\bar{\rho}\bar{u}) \frac{\partial k}{\partial x} + (\bar{\rho}\bar{v}) \frac{\partial k}{\partial y} = \frac{\partial}{\partial x} [(\mu + \frac{\mu_t}{\sigma_k}) \frac{\partial k}{\partial x}] + \frac{\partial}{\partial y} [(\mu + \frac{\mu_t}{\sigma_k}) \frac{\partial k}{\partial y}] + (P + G - \epsilon) + D \quad (4.18)$$

$$\begin{aligned}
(\overline{\rho u}) \frac{\partial \varepsilon}{\partial x} + (\overline{\rho v}) \frac{\partial \varepsilon}{\partial y} &= \frac{\partial}{\partial x} \left[\left(\mu + \frac{\mu_t}{\sigma_k} \right) \frac{\partial \varepsilon}{\partial x} \right] + \frac{\partial}{\partial y} \left[\left(\mu + \frac{\mu_t}{\sigma_k} \right) \frac{\partial \varepsilon}{\partial y} \right] \\
&+ \frac{\varepsilon}{k} (C_{\varepsilon 1} f_1 P + C_{\varepsilon 1} G - C_{\varepsilon 2} f_2 \varepsilon) + E
\end{aligned} \tag{4.19}$$

where;

$$\mu_t = \bar{\rho} C_\mu f_\mu \frac{k^2}{\varepsilon} \quad \text{or} \quad \nu_t = C_\mu f_\mu \frac{k^2}{\varepsilon} \tag{4.20}$$

$$P = \mu_t \left\{ 2 \left[\left(\frac{\partial \bar{u}}{\partial x} \right)^2 + \left(\frac{\partial \bar{v}}{\partial y} \right)^2 \right] + \left(\frac{\partial \bar{u}}{\partial y} + \frac{\partial \bar{v}}{\partial x} \right)^2 \right\} \tag{4.21}$$

$$G = \beta \frac{\mu_t}{\sigma_t} \frac{\partial \bar{T}}{\partial x} g \tag{4.22}$$

When equations (4.14) to (4.19) are compared with the general transport equation solved by PHOENICS, equation (4.1), there are some terms that are to be considered as the source term of equation (4.1). PHOENICS makes provision for the pressure term and the buoyancy term in the momentum equation such that they can be switched on. Thus we are left with the provision of the code to calculate the turbulent kinematic (or dynamic) viscosity and the sources of k and ε in the linear form described in sub-section 4.2.3.5. Instead of altering the subroutines available in PHOENICS for the standard $k - \varepsilon$ model, all subroutines to calculate the turbulent kinematic viscosity and sources of k and ε are written from scratch in this study.

Turbulent kinematic viscosity and the f functions:

Turbulent kinematic viscosity as described by equation (4.20) changes in the calculation domain from point to point. It must be calculated at each cell in the calculation domain while the computation progresses. The definition of the multiplying function f_μ is given in Table 3.1 along with the other f functions for the models considered. The subroutine TYLRVT of the GROUND (Appendix B.1)

calculates turbulent kinematic viscosity, and TYLRFN, which is called from TYLRVT calculates the f functions.

The source terms of k and ε equations:

When equations (4.18) and (4.19) are arranged in the form of equation (4.1), the source terms of k and ε becomes:

$$S_k = (P + G - \varepsilon) + D \quad (4.23)$$

$$S_\varepsilon = \frac{\varepsilon}{k} (C_{\varepsilon 1} f_1 P + C_{\varepsilon 1} G - C_{\varepsilon 2} f_2 \varepsilon) + E \quad (4.24)$$

These terms should be rearranged in the form:

$$S_\phi = f * CO * (VAL - \phi) \quad (4.25)$$

so that the sources are linearised.

Defining :

$$\Sigma = \{2[(\frac{\partial \bar{u}}{\partial x})^2 + (\frac{\partial \bar{v}}{\partial y})^2] + (\frac{\partial \bar{u}}{\partial y} + \frac{\partial \bar{v}}{\partial x})^2\} \quad (4.26)$$

$$\Sigma \Sigma = \frac{\partial \bar{T}}{\partial x} \quad (4.27)$$

and rearranging equations (4.23) and (4.24) and taking the multiplying factor f as the mass of the computational cell the sources become:

$$S_k = v_t \Sigma + \frac{v_t \Sigma \Sigma \beta g}{\sigma_t} + D - \varepsilon \quad (4.28)$$

$$S_\varepsilon = \frac{\varepsilon}{k} (C_{\varepsilon 1} f_1 v_t \Sigma + \frac{C_{\varepsilon 1} v_t \Sigma \Sigma \beta g}{\sigma_t} + \frac{Ek}{\varepsilon} - C_{\varepsilon 2} f_2 \varepsilon) \quad (4.29)$$

The functions D and E appear only in the LS model. Making the necessary substitutions and rearranging, the CO and VAL parts of the sources for the TH, LB and DA models are obtained as:

$$\text{CO}_k = \frac{C_\mu f_\mu k}{v_t} \quad (4.30)$$

$$\text{VAL}_k = \frac{v_t^2 \Sigma}{C_\mu f_\mu k} + \frac{v_t^2 \Sigma \Sigma \beta g}{C_\mu f_\mu k \sigma_t} \quad (4.31)$$

$$\text{CO}_\epsilon = \frac{C_{\epsilon 2} f_2 k C_\mu f_\mu}{v_t} \quad (4.32)$$

$$\text{VAL}_\epsilon = \frac{C_{\epsilon 1} f_1 v_t \Sigma}{C_{\epsilon 2} f_2} + \frac{C_{\epsilon 1} v_t \Sigma \Sigma \beta g}{C_{\epsilon 2} f_2 \sigma_t} \quad (4.33)$$

For the LS model the CO's are the same as the above. The VAL's, however, become:

$$\text{VAL}_k = \frac{v_t^2 \Sigma}{C_\mu f_\mu k} + \frac{v_t^2 \Sigma \Sigma \beta g}{C_\mu f_\mu k \sigma_t} - \frac{2\nu v_t \left(\frac{\partial \sqrt{k}}{\partial y}\right)}{C_\mu f_\mu k} \quad (4.34)$$

$$\text{VAL}_\epsilon = \frac{C_{\epsilon 1} f_1 v_t \Sigma}{C_{\epsilon 2} f_2} + \frac{C_{\epsilon 1} v_t \Sigma \Sigma \beta g}{C_{\epsilon 2} f_2 \sigma_t} + \frac{2\nu v_t k \left(\frac{\partial^2 u}{\partial y^2}\right)^2}{C_{\epsilon 2} f_2 \epsilon} \quad (4.35)$$

The subroutine TYLRSO of the GROUND (Appendix B.1) calculates the sources given above.

Wall boundary condition of ϵ for the TH model:

The value of ϵ at the wall for the TH model is defined as:

$$\epsilon_{y=0} = 2\nu \left(\frac{\partial \sqrt{k}}{\partial y}\right)^2 \quad (4.36)$$

which is dependent on the calculated variable k . Thus it should be introduced as a source of ϵ at the wall cells. When linearised the CO and VAL parts of this source are obtained as:

$$CO = \frac{1}{\sigma_\epsilon} \quad (4.37)$$

$$VAL = 2\nu\left(\frac{\partial\sqrt{k}}{\partial y}\right)^2 \quad (4.38)$$

fixing the value of ϵ at the wall to that of equation (4.36). Since CO is not dependent on any calculated variable, there is no need for ground coding. The VAL however is calculated by the TYLRWL subroutine of the GROUND (Appendix B.1).

4.3.2.3 The Q1 File for the LRN k - ϵ Turbulence Models

The Q1 file of PHOENICS to implement the LRN k - ϵ Turbulence Models of this study is given in Appendix B.2. The setting in the Q1 file to activate the models are explained below.

GROUP 7. Variables stored, solved & named

SOLVE(P1,U1,V1,H1,KE,EP);SOLUTN(P1,Y,Y,Y,P,P,P)
STORE(ENUT,ENUL,RHO1)

The above settings are needed to solve k and ϵ and to provide storage for v_t , ν , and ρ .

GROUP 9. Properties of the medium (or media)

ENUT=GRND;

This activates the calculation of v_t from its GROUND code.

GROUP 11. Initialization of variable or porosity fields

KEIN=..... Value of k at the inlet

EPIN=(0.09** 0.75*KEIN**1.5)/(0.41*YVLAST)

The value of k at the inlet is entered and the value of ϵ at the inlet is calculated from equation (3.31.b).

GROUP 13. Boundary conditions and special sources

PATCH(LRSOURCE,PHASEM,1,NX,1,NY,1,1,1,1)

COVAL(LRSOURCE,KE,GRND,GRND)

COVAL(LRSOURCE,EP,GRND,GRND)

PATCH(INLET,EAST,1,1,1,NY,1,1,1,1)

COVAL.....

COVAL(INLET,KE,ONLYMS,KEIN)

COVAL(INLET,EP,ONLYMS,EPIN)

These settings activate the calculation of the sources of k and ϵ in the domain and set the values of k and ϵ at the channel inlet.

PATCH(HOTWALL,SWALL,1,NX,1,1,1,1,1,1)

COVAL.....

COVAL(HOTWALL,KE,1.0,0.0)

COVAL(HOTWALL,EP,1.0/PRT(EP),GRND)) (Only for TH model)

PATCH(COLDWALL,NWALL,1,NX,NY,NY,1,1,1,1)

COVAL.....

COVAL(COLDWALL,KE,1.0,0.0)

COVAL(COLDWALL,EP,1.0/PRT(EP),GRND) (Only for the TH model)

The values of k and ϵ at the heated and adiabatic walls are set. The value of ϵ at the wall is needed only for the TH model. Since the derivative of ϵ at the wall is zero for all other models and PHOENICS assumes no flux at the cell interfaces, no boundary condition is required for zero gradient.

GROUP 19. Data communicated by satellite to GROUND

ISG1=1

The value of ISG1 determines which model is used. It is 1 for LS, 2 for TH, 3 for LB and 4 for DA model.

Further details of boundary conditions are given in Chapter 7.

CHAPTER 5. EXPERIMENTAL SETUP AND MEASUREMENT METHODS

5.1 Introduction

One of the main objectives of this study was to obtain velocity and temperature information from experimental channels closely resembling the numerical model so that the numerical predictions could be evaluated. Three different channels have been used in order to conduct the experimental part of this study, one for laminar flow and two for the turbulent flows. In the case of laminar flow the channel was constructed to give a constant uniform wall heat flux. For the turbulent flows, however, an existing experimental channel giving a UWT heating mode was altered slightly, and a new channel was constructed to enable measurements for the UHF heating mode.

Two different LDA systems were used for velocity measurements. A temperature data acquisition system was developed to be used for the turbulent flow cases such that mean and turbulent temperature data could be recorded.

The experimental channels, instrumentation, and experimental procedures are detailed in the following two sections for the laminar and turbulent flow regimes respectively.

5.2 Laminar Flow

5.2.1 The Flow Channel

A schematic diagram of the flow channel is shown in Figure 5.1 and a photograph of it in Figure 5.2. Two symmetric channels were formed by an aluminium central heated wall, two parallel perspex front walls, and perspex side walls. The heater wall was fabricated by sandwiching a flat uniformly dissipating resistance film heating element powered by a manually controlled AC voltage regulator, between two aluminium plates. The heater wall was 6 mm thick, 150 mm wide, and 320 mm high. The leading

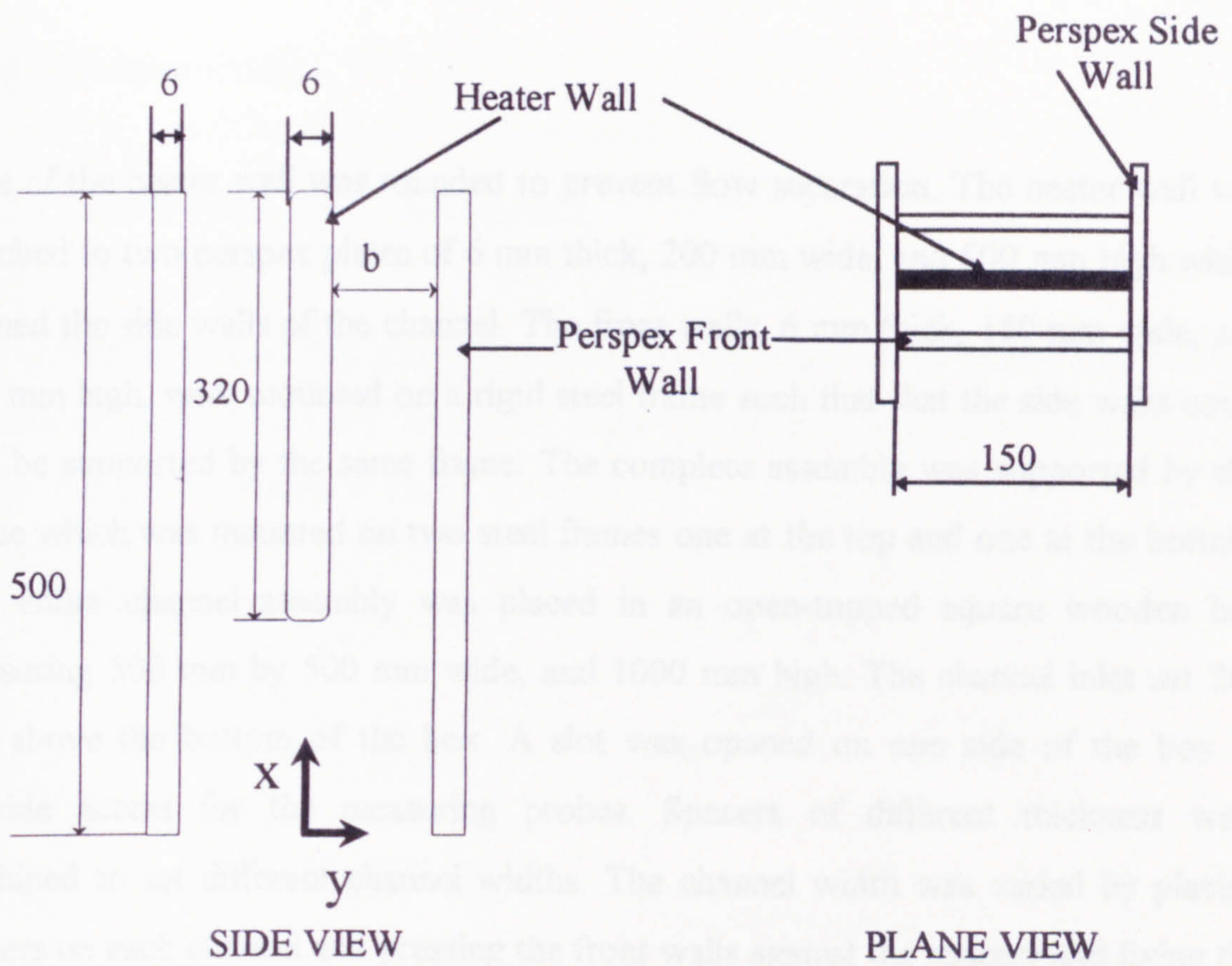


Figure 5.1 Schematic diagram of the laminar flow channel

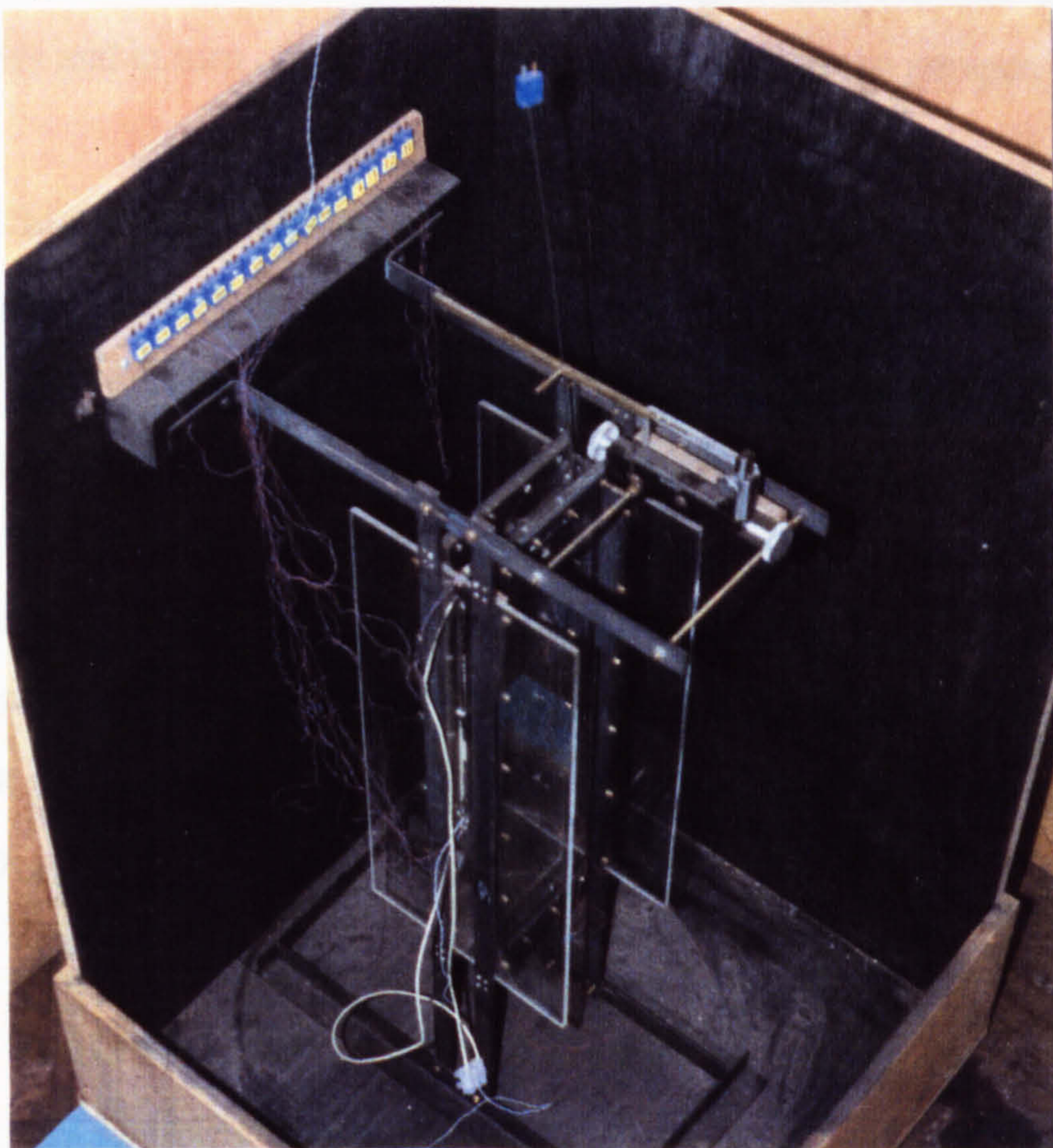


Figure 5.2 Photograph of the laminar flow channel

edge of the heater wall was rounded to prevent flow separation. The heater wall was attached to two perspex plates of 6 mm thick, 200 mm wide, and 500 mm high which formed the side walls of the channel. The front walls, 6 mm thick, 150 mm wide, and 500 mm high, were mounted on a rigid steel frame such that the side walls could also be supported by the same frame. The complete assembly was supported by this frame which was mounted on two steel frames one at the top and one at the bottom. The entire channel assembly was placed in an open-topped square wooden box measuring 500 mm by 500 mm wide, and 1000 mm high. The channel inlet sat 200 mm above the bottom of the box. A slot was opened on one side of the box to provide access for the measuring probes. Spacers of different thickness were machined to set different channel widths. The channel width was varied by placing spacers on each channel and pressing the front walls against the spacers and fixing the wall support frame at the bottom and top to the support frames. The heater plate was painted matt black to reduce the reflection of laser light. This resulted in increased surface emissivity and in turn considerable thermal radiation to the perspex walls.

70 μm thick Teflon coated Cu-Const. thermocouples were fixed at the centre on both sides of the heater wall at four heights ($x=200$ mm, $x=300$ mm, $x=400$ mm, $x=480$ mm) and also at the corresponding positions of one of the perspex front walls. Thermocouples were also fitted at two different vertical positions ($x=300$ and $x=400$ mm) halfway between the centreline and the side wall to monitor symmetry. Thermocouples were located at the channel inlet and outlet levels to measure the ambient temperature. The experimental rig was inside a large room. The room measuring 3 m by 5 m, and 4 m high, has also housed the LDA system and other instrumentations.

5.2.2 Instrumentation

5.2.2.1 He-Ne Fibre Flow LDA System

A DANTEC fibre flow one component LDA system was used to measure the velocity distribution inside the channel. The layout of the LDA system together with the traversing mechanism and the channel is shown in Figure 5.3.

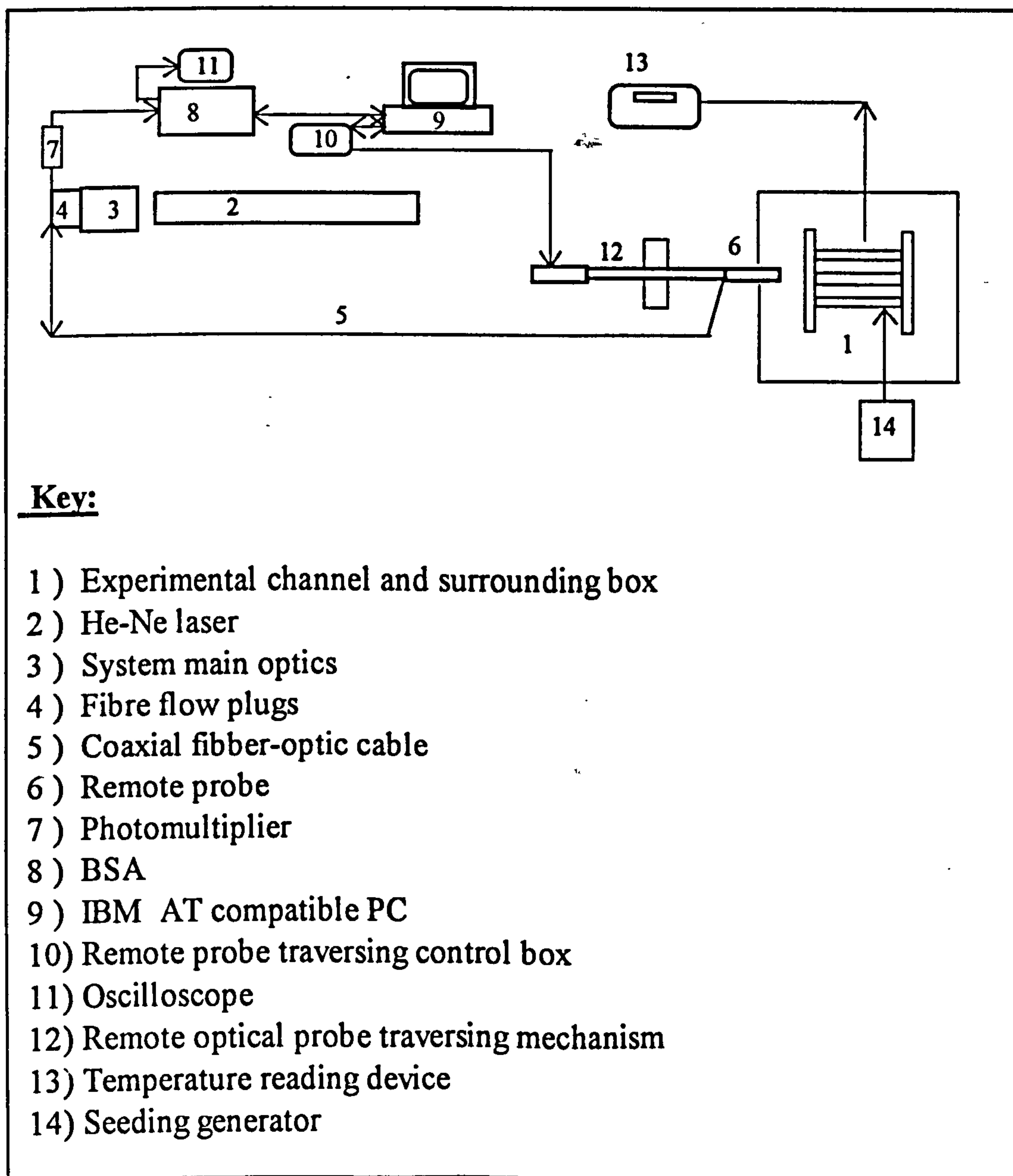


Figure 5.3 Layout of the He-Ne LDA system and the experimental channel

The system consists of a 25 mW, 632.8 nm He-Ne laser source, main system optics, a DANTEC 60X13 remote optical probe head, a DANTEC 57 N 10 Burst Spectrum Analyser (BSA), a DANTEC 57G15 traversing mechanism, a photo-multiplier with pre-amplification, a launch and collect coaxial fibre-optic cable, and an IBM AT host computer together with BSA or Burstware software. The system operates in backscatter mode. The light from the laser source is split and one of the beams is shifted in the main system optics before being launched into the fibre-optic cable. The light scattered from the seeding particles are collected at the remote probe head and transmitted through the fibre-optic cable back to the photo-multiplier from which an electrical signal is generated and fed into the BSA. The approximate dimensions of the optical probe volume are 2 mm by 0.2 mm. The focal length of the remote probe is 50 mm and the beam separation is 8 mm. The fibre-optic cable is formed by three separate cables one for each beam and one for the backscattered light. The remote probe is mounted on a DANTEC 57G15 traversing mechanism which is described later. After conditioning the signal from the photo-multiplier, the BSA performs a Discrete Fourier Transform (DFT) on the Doppler signal to extract the frequency and hence the velocity. It allows the Arrival Time, Transit Time and the velocity to be recorded and makes provision for the Doppler signal to be monitored on an oscilloscope. The BSA is connected to an AT computer via an IEEE 488 bus and the system is fully computer controlled by the BSA or Burstware software. The operation principles of the BSA, the operation modes, and other technical specifications are given in the BSA manual [68].

5.2.2.2 Flow Seeding Arrangement

It is well known, the velocities measured using LDA are those of the seeding particles moving within the fluid. It is therefore important that the flow must be seeded with particles that can follow the flow with negligible slip velocity between the fluid and the particles. The substance used for flow seeding must not pose any health hazard. Water, corn oil, tobacco smoke, and silicon oil are widely used substances for seeding. In this study, silicon oil was preferred as the seeding substance. Calculations were performed with assumed slip velocities. The results have indicated that, for a slip velocity of 5 mm/s, the

particle sizes could be around 10 μm . A seeding generator producing an aerosol of silicon oil with an average particle size of 5 μm was used. A photograph of the seeding generator is given in Figure 5.4. The slip velocities resulting for this particle size were calculated to be less than 2 mm/s which was negligible for the flow under consideration. The silicone oil aerosol from the seeding generator was introduced into a flat box filled with metal wool placed under the channel.

5.2.2.3 Temperature Measurements

70 μm diameter Cu-Const. thermocouples were used to measure surface temperatures on the heater wall, on the perspex front walls and the air temperature distribution across the channel. A probe was manufactured by sliding a thermocouple wire inside a 0.5 mm diameter 350 mm long steel tube and fixing the wires at the measuring end to the tube with epoxy resin. The thermocouple wire legs were kept long enough so that the temperature support tube would not affect the readings. The thermocouples were connected to a manual multiplexer and the output was connected to CIL TA 880 multipurpose measuring device. The air temperature thermocouple was connected directly to one channel of the device. The CIL TA 880 multipurpose measuring device has 10 channels for temperature measurements using different thermocouple types with 0.1 C precision. Specifications of CIL TA 880 device are given in Appendix D. Thermocouples were calibrated with respect to the ice point and the boiling point of water. The ice point and boiling point sources were achieved using distilled water. Calibrations were performed by connecting the thermocouples to the measuring device via the manual multiplexer and reading the temperatures from the device directly, thus including the effects of complete system. Best fit calibration curves for each thermocouples were obtained as actual temperature vs. read temperature. The calibration characteristics of all thermocouples are presented in Appendix C.

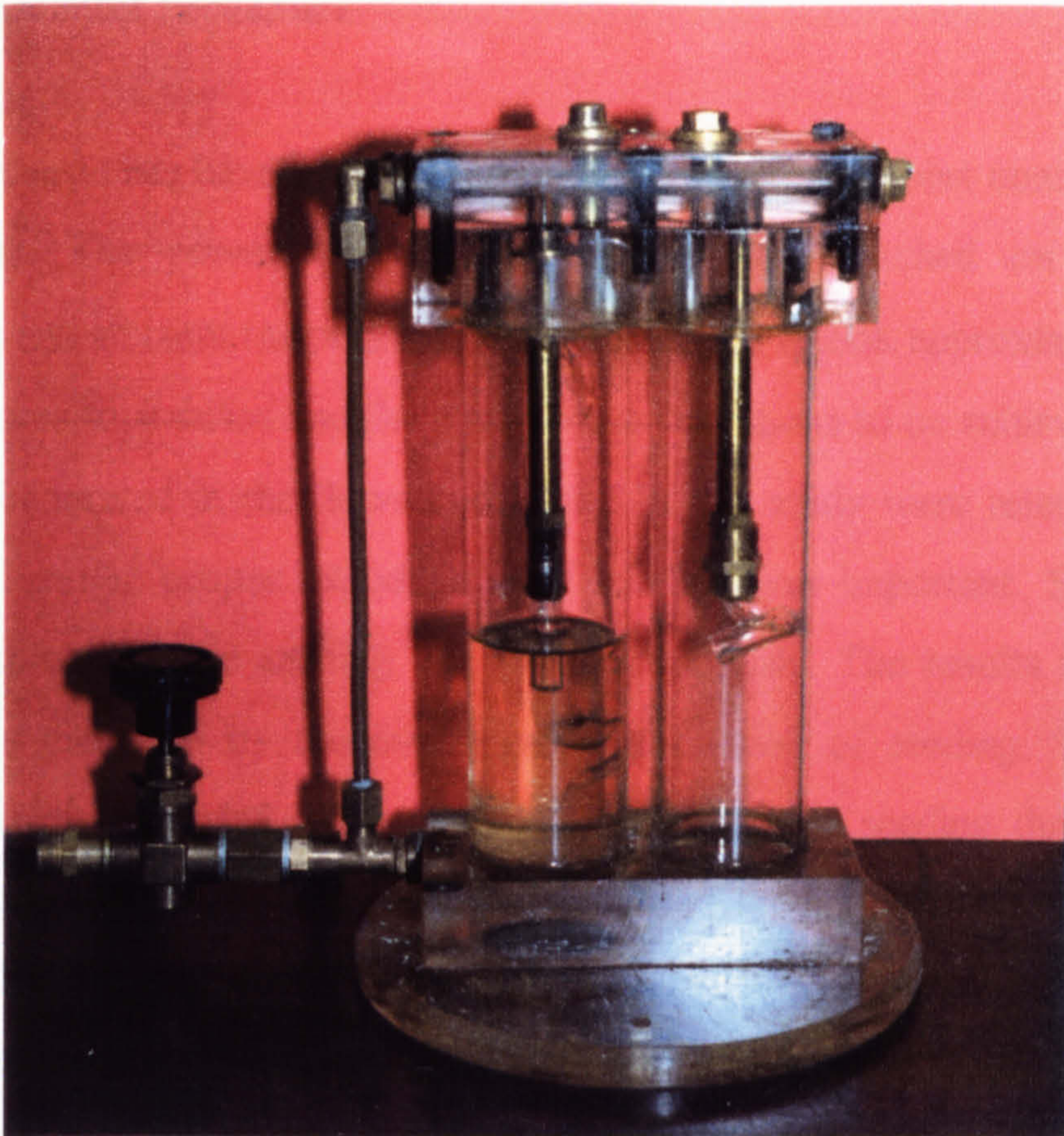


Figure 5.4 Photograph of seeding generator

5.2.2.4 Traversing Mechanisms

A DANTEC 57 G 15 traversing mechanism was used for traversing the optical probe. The 57G15 had manual traversing in one direction, motorised traversing perpendicular to the manual traversing direction and motorised rotation around the motorised traversing direction. The motorised traversing and rotation could be controlled from the host computer via an IEEE 488 bus interface. Repeatability (excluding backlash) and minimum movement values were $\pm 0.3^\circ$ and $\pm 0.4 \mu\text{m}$ for rotation and traverse respectively. The manual traversing direction had a movement precision of $10 \mu\text{m}$. In this study the manual traversing was used due to the orientation of the system to traverse the optical probe across the channel. A small manual traversing mechanism mounted on top of the channel was used to traverse the temperature probe. The mechanism allowed traversing across the channel and movement in the vertical direction. The mechanism had a movement resolution of 0.1 mm .

5.2.3 Experimental Procedure

Some preliminary tests have been carried out to determine the best conditions for the measurements. The power to the heater plate was switched on and surface temperatures and ambient temperature were monitored. It took approximately 2 hours for temperatures to stabilise and the steady state conditions to be achieved. Since the velocities encountered in the flows considered in this study were relatively low, 10 mm/s to 400 mm/s, proper introduction of seeding was important. Some velocity measurements were made seeding the flow continuously. The results indicated that the flow was disturbed by the continuous introduction of seeding. Thus a batch seeding approach was used. This involved introducing the seeding through a metal wool filled box under the channel until a cloud of seeding particles filled the box surrounding the channel. Velocity measurements indicated that the disturbances due to seeding died away within 2 to 10 minutes after the seeding supply was switched off, depending upon the heating rate, and thus the average time scale of the flow in the channel. The batch seeding approach also helped to improve the measurement accuracy by reducing the velocity bias since large particles tended to fall out of the flow before the measurements started. One batch of seeding allowed more than 10 minutes of measurements before the flow needed to be re-seeded. The data rate achieved in this way was over 20 bursts per second. The power supplied to the heater wall was measured and compared with the calculated power assuming ohmic dissipation. The difference between the measured and calculated power was found to be negligible suggesting negligible capacitance and inductance of the heater wall. Due to the limitation of the focal length of the remote LDA probe, measurements could only be taken at 40 mm from the inner surface of the side walls.

One difficulty observed was to determine the position of the measuring probe with respect to wall. The laser beams could not be set exactly parallel to the surface. Thus, the probe was tilted by approximately 5 degrees and corrections were made by the software to account for the inaccuracy due to tilt angle. In order to set the traversing position the probe was traversed to the wall, (heated or front wall), far enough to

eliminate backlash and then moved away from the wall while observing the signal on the oscilloscope. When the centre of the optical probe volume is at the surface of the wall, the signal on the oscilloscope is that of the optical noise due to reflection from the wall. The probe was traversed very slowly away from the wall toward the centre of the channel monitoring the signal on the oscilloscope. When the amplitude of the signal (noise) was a maximum, the position was assumed to be zero (i.e., at the wall surface). From that position the probe was moved to the first measurement location. The procedure was repeated for both walls.

The temperature probe was located 1 mm above the optical measuring volume. To set the position, the thermocouple bead was submerged into the optical probe volume which gave a sudden rise of temperature due to heating by the laser beam. When this condition was obtained the temperature probe was raised back 1 mm above the optical probe before any reading was taken. In the setting of the position of measuring probes, visual observation was also used together with the procedures explained above.

A typical experimental procedure followed for the measurement of velocity and temperature profile across the channel is outlined below.

- Set the required power level by the voltage regulator and turn on the power 4 hours before the start of measurements.
- Set the positions of optical and temperature probes for the first measurement point.
- Record ambient pressure and temperature and the surface temperatures of the channel
- Start measurements and continue until no traversing could be done due to the front wall.
- Set reference position from the front wall and continue measurements until all the channel width is spanned by traversing from each side of the channel gap.
- Monitor and record surface and ambient temperatures at regular intervals during the experiment.

- Repeat above for different vertical locations for the specified heating rate and channel width.

Controlling the ambient conditions was impossible, therefore, measurements were carried out for a specified set of parameters, (channel width and heating rate), under as closely as possible the same ambient conditions.

5.3 Turbulent Flow

5.3.1 The Flow Channels

5.3.1.1 The Flow Channel Used for the UWT Heating Mode

A schematic diagram of the experimental channel used for the UWT heating mode turbulent channel flow is shown in Figure 5.5. The channel is formed by an aluminium heater wall, an opposing glass wall (front wall) and side walls which were either wood or perspex. The aluminium heater wall comprised two pieces of 6.35 mm thick by 1 m wide carefully polished plates, the first 2 m long and the second 1 m long, which were joined together to make a total channel height of 3 m. Nine serpentine shaped graphite heating elements were located on the back surface of the aluminium plates and the heating elements were backed with 25 mm thick sheets of insulation material (TRITON KAOWOOL ceramic fibre) which were in turn supported by 19 mm thick plywood boards. A thin sheet of the same insulating material was used to electrically insulate the heating elements from the aluminium plates. Three 1.01 m wide, 4 mm thick sheets of plate window glass were held in a metal frame to form the front wall. One transparent side wall was formed by 8 mm thick by 3 m long perspex and the opposite side wall by 10 mm thick by 3 m long wooden board. Different widths of side walls were fabricated for use with each channel width. The heating elements, each covering area of 0.98 m by 0.3 m were powered via four manual voltage regulators.

70 μm diameter Teflon coated Cu-Const. thermocouples were embedded in the aluminium plate to monitor temperature. Thermocouples were located at 0.3 m intervals at the centreline of the plate and at 1 and 2 m heights 4 thermocouples were positioned halfway between the centreline and the side walls . Three 200 μm diameter Teflon coated Cu-Const. thermocouples were fitted on to the inner surface of the glass wall at $x=0.8\text{m}$, 1.8m and 2.4 m to measure surface temperatures. The channel was mounted on a steel frame which was supported by a frame of scaffolding structure holding the channel inlet 0.5 m above the floor. The channel assembly was positioned next to one wall of a large laboratory and was surrounded by a 4 m high open-topped hardboard enclosure leaving a 1 m gap around the channel. A door on one side of the enclosure provided access. The purpose of enclosure was to reduce the effects of external draughts and to comply with the laser safety regulations. The channel, which was used in a previous study is described in detail by Al- Azzawi [1].

5.3.1.2 The Flow Channel Used for the UHF Heating Mode

A pair of symmetric channels were formed by an aluminium heater wall in the middle, two glass front walls and wooden or perspex side walls. The channel was built on the support structure of the experimental channel described in the previous subsection. Figure 5.6 depicts the channel schematically. The heater plate, measuring 1 m wide and 3 m high, was formed by sandwiching 8 film heating elements, dissipating uniformly, of 0.35 m by 0.8 m between two 0.5 mm thick aluminium plates. The plates were mounted together along the edges and the edges were sealed by a silicone adhesive. A vacuum connection was fitted close to the bottom edge of one plate so that any trapped air could be evacuated. The heater plate was suspended in the support frame by steel springs attached to the suspending elements riveted to the edges of the plate. The springs could be tightened or loosened by a screw arrangement on the support frame so that any buckling of the plate could be eliminated.

One side of the channel was formed by utilising the front and side wall arrangement of the previously disassembled channel, the other side by fitting wooden boards to the support frame and screwing aluminium bars to the boards to form the side walls with a frame to hold the glass plates. Since the heating elements were only 0.8 m wide and suspending elements were fitted at the edges, 0.1 m wide at both sides were blocked by polystyrene leaving a symmetric channel 0.8 m deep, 3 m high with variable width.

The heaters were powered via four manual voltage regulators each supplying two heating elements connected in parallel. Cu-Const. thermocouples of 0.2 mm diameter were fixed on the inside surface of the plates at 150 mm intervals along the centreline so that the flow is not disturbed by thermocouple wires. Readings from the thermocouples during initial preliminary experiments were unrealistic indicating that the thermocouples had become detached from the inside surface of the plate. Therefore, a total of eighteen 70 μm diameter Cu-Const. thermocouples were fixed on the outer surface of the heater plate on the front channel side. The positioning of thermocouples were such that the first 13 of them were placed at 150 mm intervals from the leading edge downstream and the last 5 of them at 200 mm intervals. Thermocouples were also fixed at the half distance between the centreline and channel edge at three different vertical locations ($x=0.8, 1.6$ and 2.4 m) to monitor symmetry of heating.

5.3.2 Instrumentation

5.3.2.1 Ar-Ion Fibre Flow LDA System

A two component fibre flow DANTEC LDA system was used for the turbulent flow velocity measurements. The system comprised an Ar-Ion laser source (water cooled),

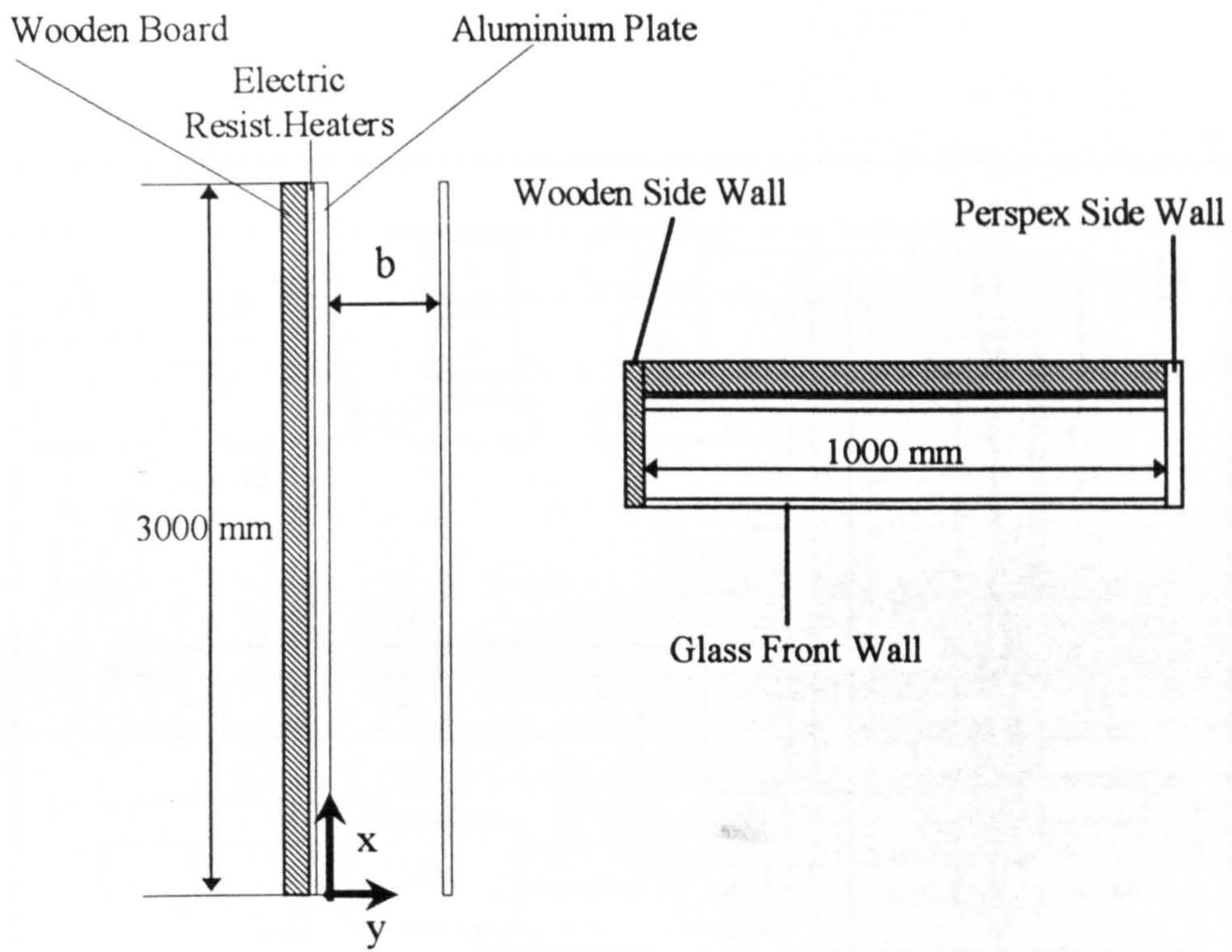


Figure 5.5 Schematic diagram of the UWT turbulent flow channel

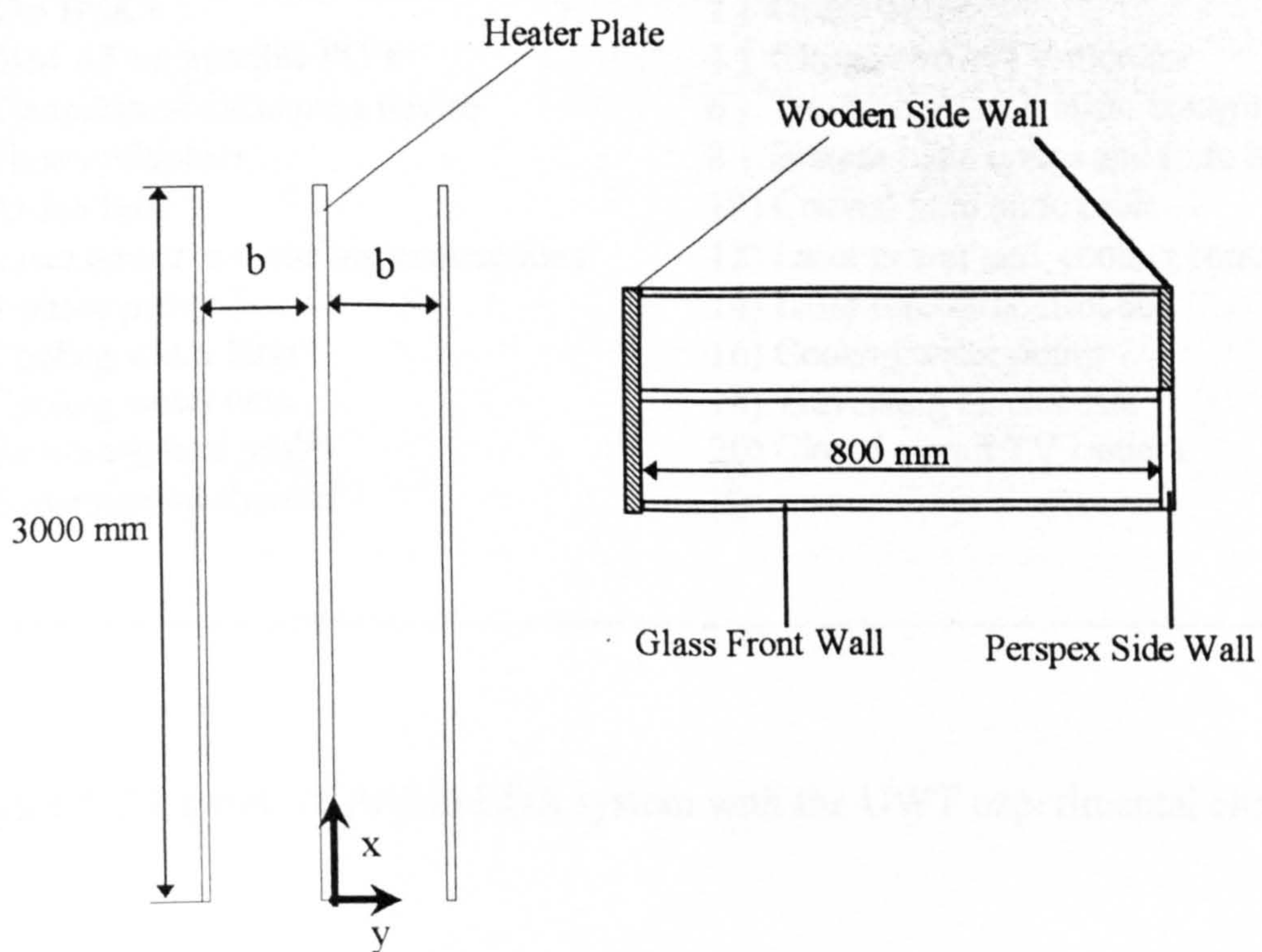
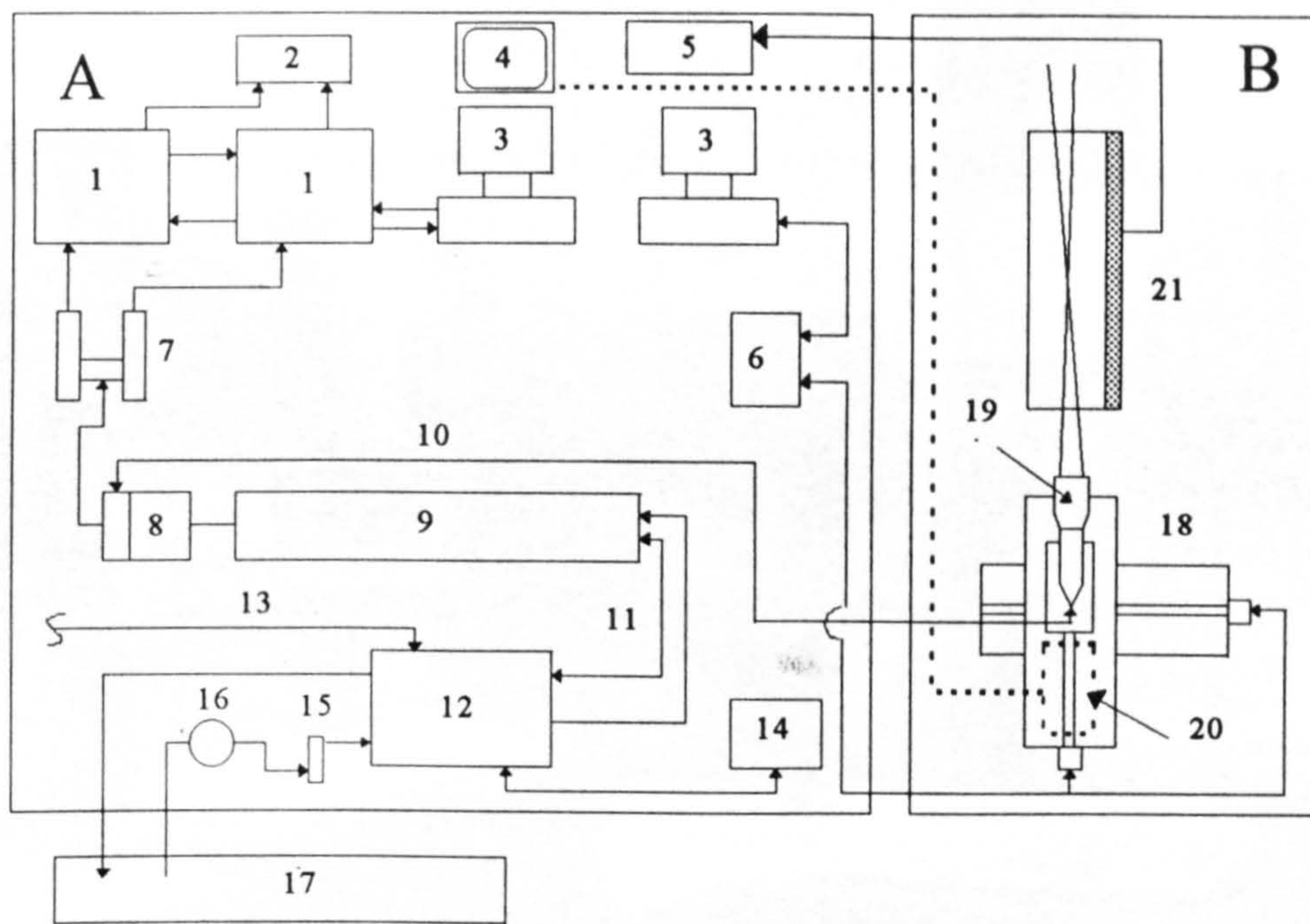


Figure 5.6 Schematic diagram of the UHF turbulent flow channel



Key:

A) Control room

1) The BSA's

3) IBM AT compatible PC's

5) Temperature measuring device

7) Photomultipliers

9) Ar-Ion laser

11) Laser power and cooling connections

13) 3-phase power line

15) Cooling water filter

17) Cooling water tank

19) Remote optical probe

21) Experimental channel

B) Experimental room

2) Oscilloscope

4) Closed circuit TV monitor

6) Traversing mechanism control box

8) System main optics and fibre launch

10) Coaxial fibre optic cable

12) Laser power and cooling control box

14) Laser remote control box

16) Cooling water pump

18) Traversing mechanism

20) Closed circuit TV camera

Figure 5.7 Layout of Ar-Ion LDA system with the UWT experimental channel

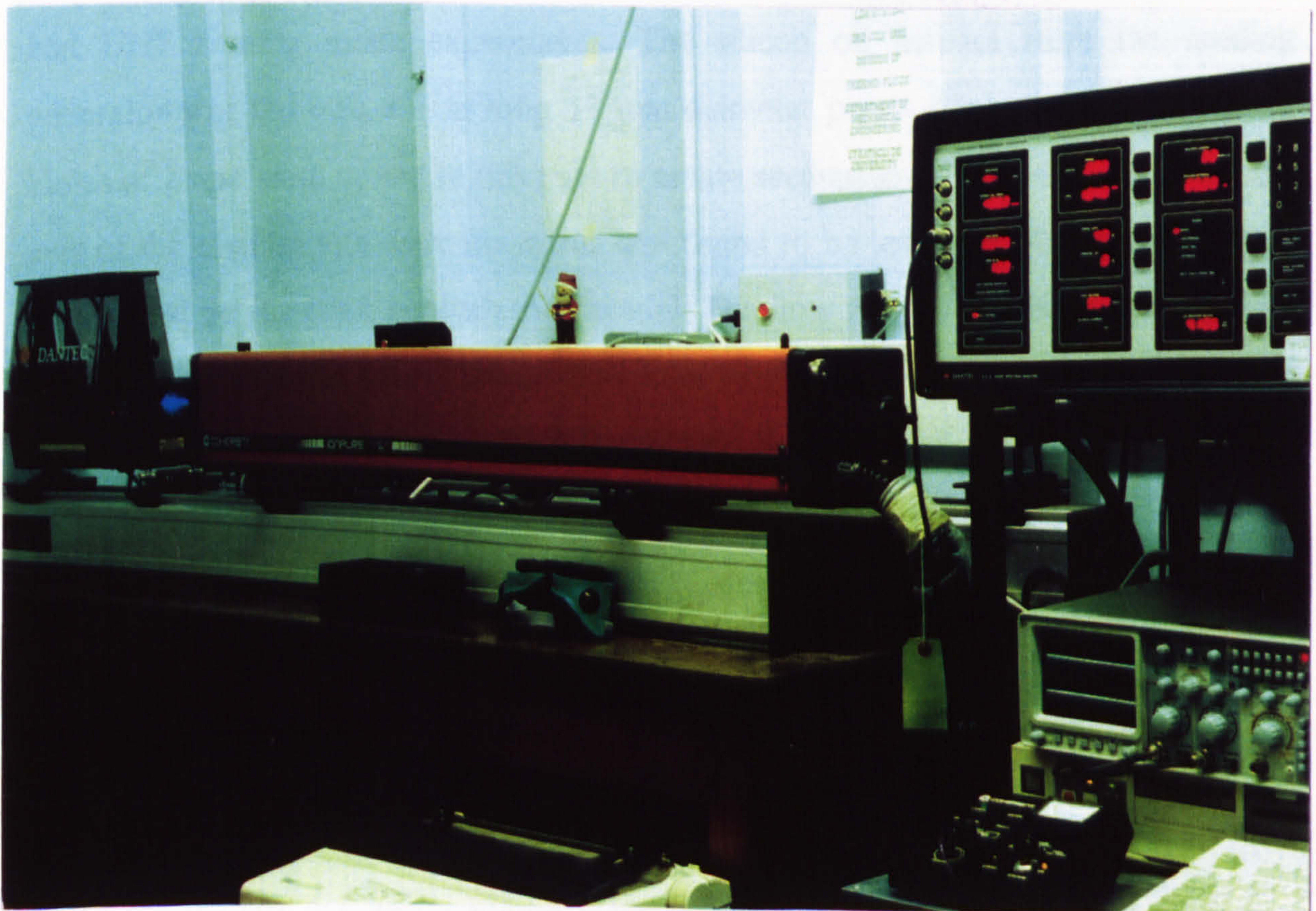


Figure 5.8 Partial photograph of the Ar-Ion LDA system

a DANTEC 60X-40 transmission optics (main system optics), a DANTEC 60X-10 remote probe, 20 m long fibre-optic cable, two DANTEC 57 N 10 BSA's, two photomultipliers with pre-amplification, the power supply and control box and an AT host computer running Burstware software. The operation principle of the system is the same as that of He-Ne system described in subsection 5.2.2.1, except the system enables simultaneous measurement of velocities in two directions. The BSA's were linked to each other and to the host computer via an IEEE 488 bus. They were also linked via the BSA synchroniser bus. The system exploited the blue (488 nm) and green (514.5 nm) wavelengths of the Ar-Ion laser. The system was fully computer controlled by Burstware software enabling all parameters to be software set. The remote probe had a focal length of 160 mm which could be increased with expansion optics to 600 mm. A schematic diagram of the Ar-Ion LDA system is given in Figure 5.7 and a photograph of the part of the system in Figure 5.8.

5.3.2.2 Flow Seeding Arrangement

The flow seeding generator described in subsection 5.2.2.2 was used in both UWT and UHF heating mode experiments. The silicon oil aerosol from the seeding generator was fed into a 1 m long 30 mm diameter perspex tube with closed ends. Holes of 2 mm were drilled in this tube to create seeding jets. The velocities along the axis of the seeding jets were measured and found to be less than 50 mm/s. The tube was placed on the floor beneath the channel. The flow was continuously seeded since the seeding jets 0.5m below the channel inlet were judged not to influence the mean flow compared with any unavoidable draughts in the enclosure.

5.3.2.3 Temperature Measurements

5.3.2.3.1 Surface Temperature Measurements

Surface temperature measurements on both the UHT and UWT channels were carried out using the CIL TA 880 multipurpose measuring device. Calibration and connection

of the thermocouples to the measuring device were performed as described in subsection 5.2.2.3.

5.3.2.3.2 Air Temperature Measuring System

A temperature data acquisition system was designed, manufactured and used for the measurement of mean and turbulent temperature data simultaneous with the velocity inside the channel. The system consisted of a temperature probe, an Amplicon PC-39 Analogue Multifunction Board, a signal conditioning unit and a Philips P AT computer.

The temperature probe was fabricated by sliding a pair of 25 μm diameter Cr-Al thermocouple wires into a 300 mm long 0.5 mm diameter steel tube. The wires were butt jointed on one end to form the bead and connected to a K type plug fixed on the other end of the tube. The exposed length of thermocouple wire was 5 mm long and epoxy resin was used to fix the wires at the end of the tube. A photograph of the temperature probe is given in Figure 5.9. Smith [37], has performed some calculations and experiments for a thermocouple bead of 25 μm diameter and found that the response would be over 200 Hz. Since the frequencies of turbulent fluctuations in natural convection rarely exceed 100 Hz [37], a temperature probe made from 25 μm diameter Cr-Al thermocouple wires was deemed to be satisfactory for the purpose of this study.

A signal conditioning unit for the thermocouple signal was manufactured. The signal was linearised and pre-amplified by an AD 595 K type thermocouple amplifier with cold junction compensation. The signal was then fed into the second amplification circuitry which allowed the signal to be amplified to the input range of the data acquisition board. Before the temperature signal was connected to the data acquisition board, it was first low-pass filtered by a fifth order Chebishev filter of 100 Hz cut-off frequency and then the 50 Hz component was removed by a notch filter (band stop) to eliminate the noise from the mains electrical supply. The temperature probe was

connected to the signal conditioning unit by a 5 m long twist-pair thick thermocouple wire of the same type as used for the probe.

The Amplicon PC-39 Analog Multifunction Board is a 12 bit analogue to digital, digital to analogue (AD/DA) conversion card for IBM PC AT/Compatibles with digital Input / Output (I/O) and Direct Memory Access (DMA) capabilities. The card had a facility to initiate sampling by an external triggering signal so that sampling could be synchronised with an external measurement device. The card had onboard programmable timers to control sampling frequency. The maximum sampling rate under Turbo Pascal software was 6 kHz which is much higher than the requirements of the current study. The board was used in monopolar mode so that the highest resolution could be exploited. The specification of the data acquisition board is given in Appendix E.

A Turbo Pascal software was developed for data acquisition. The listing of the data acquisition software is given in Appendix F.1. Preliminary tests of the card indicated that neither the external trigger nor the internal timer initiated sampling features were functioning properly. This meant that software polling needed to be used for sampling. The temperature data acquisition was achieved by software polling of the card to create a 100 Hz sampling rate. The synchronisation of temperature and velocity measurements was achieved by a connection between the clock reset line of the BSA synchronisation bus and one of the analogue input channels of the card. This assured a common time reference for the BSA's and the temperature data acquisition system. The procedure to achieve synchronisation was first to run the temperature data acquisition software on its computer and start reading the channel to which the synchronisation signal from the BSA's was connected. The parameters were then set and Burstware software was started to record velocity data. When the clock reset signal from the BSA's was detected on the synchronisation channel of the temperature data acquisition card, temperature reading was started by the data acquisition software. The delay between the synchronisation signal detection and first temperature reading was approximately 10 ms.

The temperature probe was calibrated with respect to the ice point and the boiling point of water. The calibration procedure and calibration characteristics of the probe are given in Appendix C.

5.3.2.4 Traversing Mechanisms

Separate traversing mechanisms were used to traverse the velocity (remote optical probe) and temperature probes. These are described below.

5.3.2.4.1 LDA Probe Traversing Mechanism

A two-dimensional computer controlled traversing mechanism was used to traverse the optical probe across the channel. The traversing mechanism was located on a platform. To position the optical probe in vertical measurement locations the platform was mounted on a 4 m high pillar structure of scaffolding tubes incorporating sliding supports such that it could be moved vertically. The platform could thus be located and firmly clamped at the desired vertical location. The cross channel traversing was controlled from the data acquisition card used for the temperature probe. A Turbo Pascal software was developed to control the traversing mechanism and it is listed in Appendix F.2. The traversing mechanism had a minimum movement of 10 μm . A photograph of the traversing mechanism with the optical probe mounted is shown in Figure 5.10.

5.3.2.4.2 Temperature Probe Traverse Mechanism

The DANTEC 57G15 traversing mechanism was used for temperature probe traversing. The mechanism was mounted on top of the channel support structure in such a way that computer controlled vertical movement and rotation around vertical axis could be utilised.

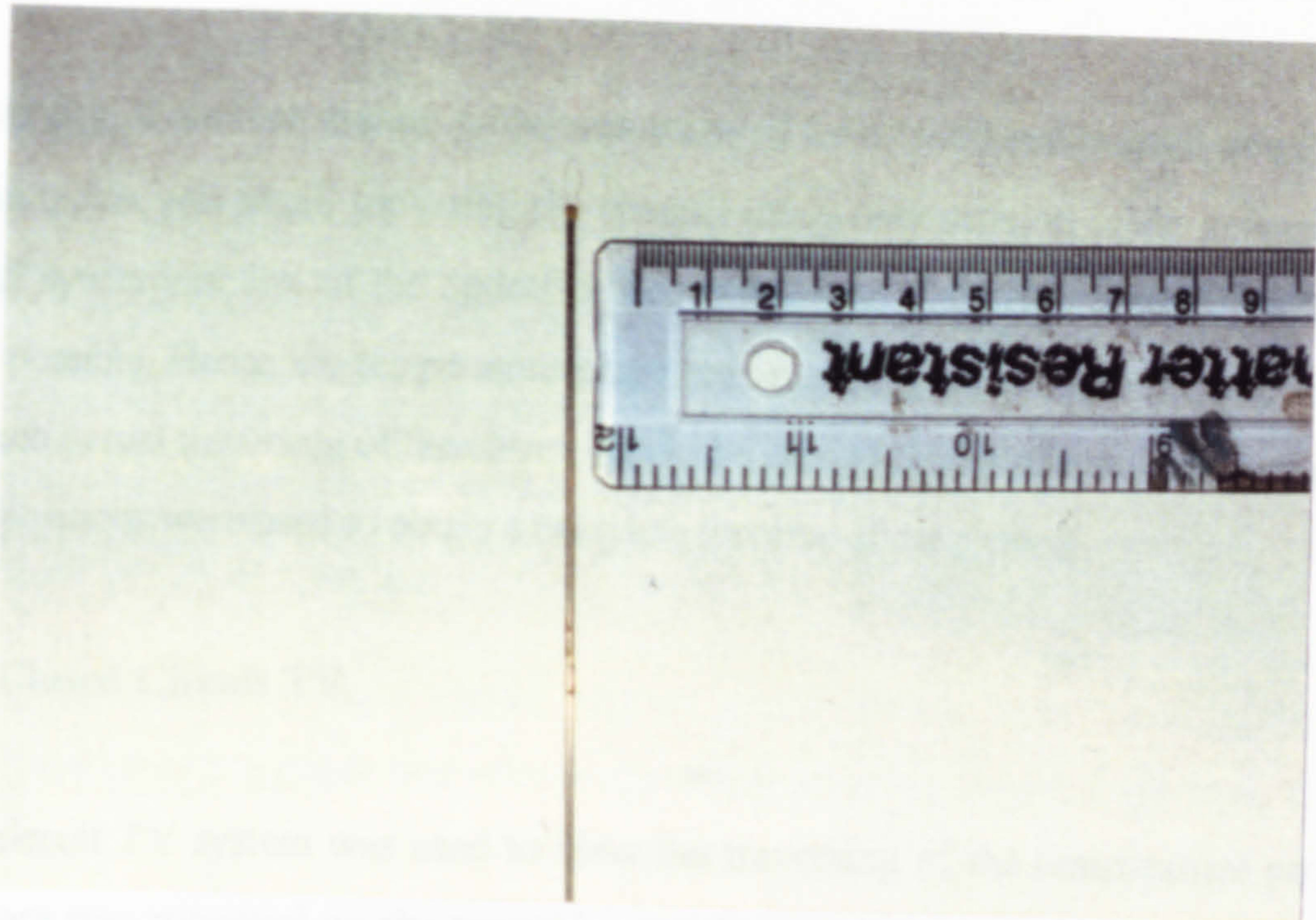


Figure 5.9 Photograph of the air temperature probe

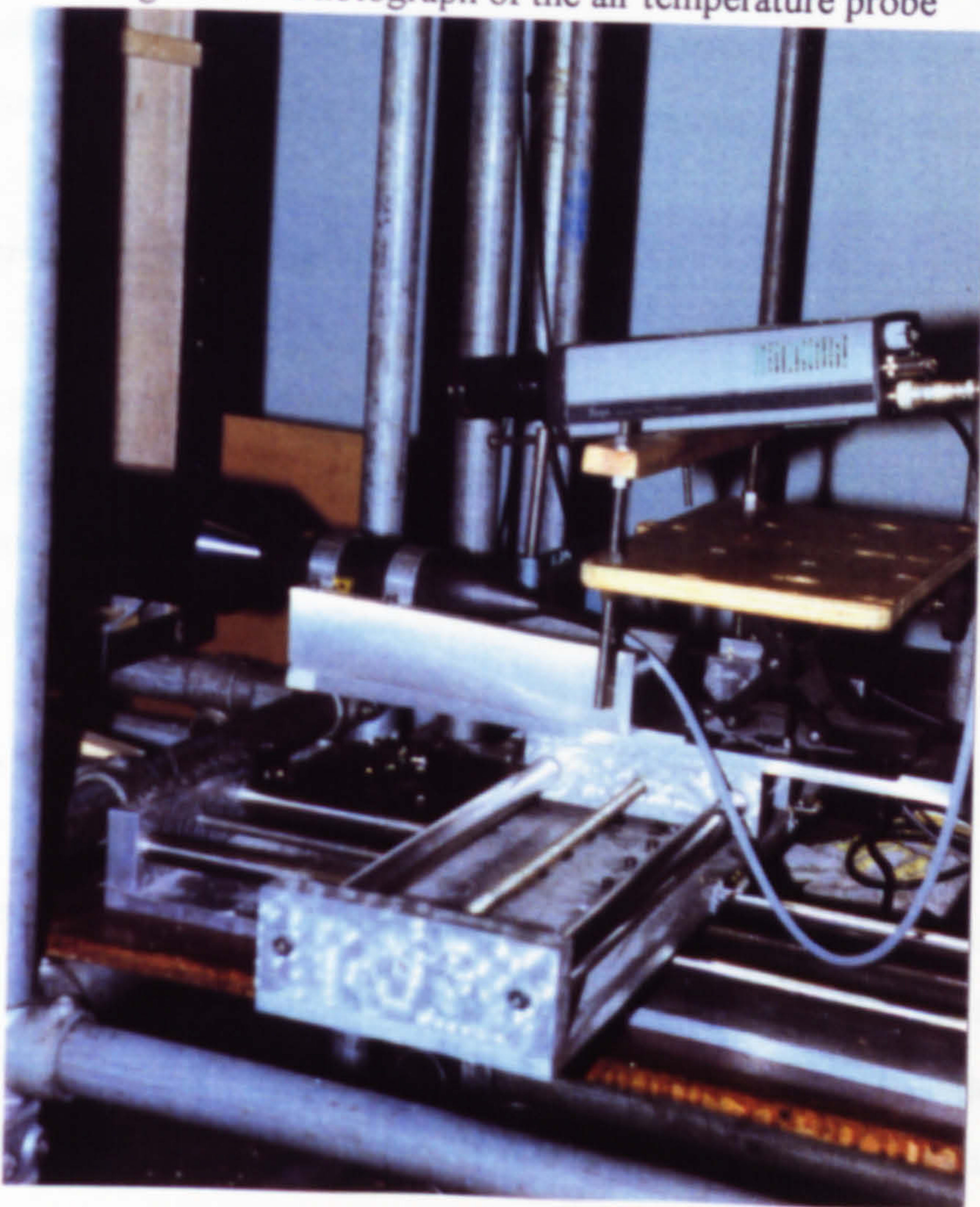


Figure 5.10 Photograph of the optical probe and traversing mechanism

An extension arm was designed and the probe was bent and fixed to the arm which could rotate around vertical axis. The radius from the axis to the thermocouple bead was 0.3 m.

The traversing of the temperature probe was achieved by rotation and manual traversing. Since the radius was small, traversing the channel using only rotation while maintaining positional synchronisation of the optical probe volume and the temperature probe bead was not possible. Hence the temperature probe was manually traversed to a set position from which partial traversing of the channel could be carried out by rotation. A number of such set positions were used to obtain a complete traverse of the channel.

5.3.2.5 Closed Circuit TV

A close circuit TV system was used to view the traversing of the temperature probe. The camera was mounted on the traversing mechanism inline with the laser beam so that the position of probes could be viewed while traversing the probes. The monitor was in the room where the LDA system and computers were accommodated.

5.3.3 Experiments and Experimental Procedure

Preliminary tests were carried out to determine the best conditions for both the UWT and the UHF heating mode experiments. At every point, a minimum of 10,000 samples were recorded for the velocity. Due to the limitations of Turbo Pascal, temperature measurements were limited to 10,000 samples per measurement.

5.3.3.1 The UWT Heating Mode

The heater plate power supply was switched on and the surface temperatures, ambient temperature were monitored. It took approximately 2 to 3 hours for the temperatures to stabilise and steady state conditions to be achieved. Approximate voltage levels for each heater group were determined for different wall temperatures by trial and error.

Over the surface of the heated wall, the prescribed uniform temperature could be maintained within $\pm 2^\circ\text{C}$.

Beam separation size of the optical probe prevented measurements being made at the centreline of the channel. Measurements were made 100 mm away from the centreline. The probe required to be tilted by approximately 6 to 8 degrees with respect to the wall. Correction to the y direction velocity readings were made through software to account for the effect of tilt angle. Position setting for velocity measurement traversing was made as explained in subsection (5.2.3).

The temperature probe position was set by submerging the bead into the optical probe volume. This gave a sudden rise of temperature due to heating from the laser beam and also produced strong noise on the optical signal. When these condition were obtained, the temperature probe was raised back 1 mm above the optical probe before any reading was taken. When setting the position of measuring probes visual observation was also made by means of the closed circuit TV. Measurement of velocity and temperature profiles were carried out in two stages, starting from each wall and traversing towards the centre. Making a profile reading across the channel took 4 to 6 hours. Surface temperatures were monitored throughout the experiments and small adjustments were made in order to maintain the prescribed surface temperature.

A typical experimental procedure followed for the measurement of velocity and temperature profiles across the channel is outlined below.

- Set the required power level using the voltage regulator and turn on the power 4 hours before the start of measurements.
- Set the positions of optical and temperature probes for the first measurement point.
- Monitor and record ambient pressure and temperature and the surface temperatures.

- Start measurements and continue until no traversing could be done due to the blockage of the beams by the opposing wall.
- Set reference position from the second wall and continue measurements until the complete channel width is spanned.
- Monitor and record surface temperatures at regular intervals during the experiment and make any necessary adjustment of the power supply.
- Repeat the above for different vertical locations.

As stated previously controlling the ambient conditions was impossible, therefore measurements were carried out for a specified set of parameters under as closely as possible the same ambient conditions.

5.3.3.2 The UHF Heating Mode

Experiments and the experimental procedure for the UHF heating mode were similar to that of the UVT except for the generation of the thermal boundary condition. In the UHF mode the time for steady state conditions to be reached was around 1 hour. The voltage of the mains supply was monitored during the experiments and was found to be essentially constant. The power supplied to the heaters was measured using a calibrated powermeter and compared with calculations assuming ohmic dissipation only. The difference between the measured and calculated powers were negligible. In other words, the heated wall had negligible capacitance and inductance.

CHAPTER 6. PRESENTATION AND DISCUSSION OF EXPERIMENTAL RESULTS

6.1 Introduction

The main objective of the experimental part of the present study was to obtain velocity and temperature information from the experimental channels for comparison with numerical models so that the predictive capability of the model could be asserted. Experimental data were processed using the commercial spreadsheet software Excel which can produce polynomial (up to the 6th degree) power law curve fits. The velocity and temperature profiles for laminar flow could be represented with sufficient accuracy using polynomial expressions of differing degree. For the turbulent flow cases 6th degree polynomials were fitted to the velocity profiles. Mean temperature profiles of turbulent flow near the channel exit exhibited a power law character. However, power law expressions could not represent the data across the channel with sufficient accuracy and hence polynomial curves were fitted to the mean temperature data. Heat and mass flow rates for the channels were obtained by integration of the curve fit expressions using Excel with a strip integration technique. Calculation method for the heat and mass flow rates is detailed in Section 4 of Appendix C.

In the following subsections the experimental results are presented in the form of Tables and graphs. The mean velocity profiles were non-dimensionalised using the highest recorded value of the velocity measured within the channel for a particular test condition. The temperature profiles were non-dimensionalised according to equation (6.1). An origin shift method of plotting was adopted for the velocity and temperature profiles in order to present the profiles clearly.

$$\frac{T - T_0}{T_{w,m} - T_0} \quad \text{or} \quad \frac{\bar{T} - T_0}{T_{w,m} - T_0} \quad (6.1)$$

6.2 Laminar Flow Experiments

The experimental channel, measurement techniques and a typical experimental procedure for laminar flow experiments have been detailed in section 2 of Chapter 5. Experiments were conducted for seven cases by changing the channel width and the heat flux and the cases are listed in Table 6.1. The experiments covered three channel widths, b , of 10, 20 and 50 mm which gave corresponding aspect ratios, b/H of 1/32, 1/16, 5/32 respectively. The average heat fluxes applied by the heater were 165, 210 and 265 W/m^2 . Velocity profiles inside the channel at five different heights and temperature profiles at the highest measurement positions were recorded for all cases. The vertical velocity profile measurement positions (x direction coordinates, see Figure 5.1) were 190 mm, 300 mm, 350 mm, 400 mm and 490 mm giving the dimensionless distance from the channel inlet, $X=0.38, 0.6, 0.7, 0.8, 0.98$, respectively. For the channel width of 20 mm, however, temperature profiles in the channel were also recorded at the same positions as for the velocity.

Heat convected (absorbed) by the air from the channel was calculated for every case from the temperature and velocity data for the highest measurement position (i.e. $X=0.98$) and the values are listed in the Table 6.1 as a heat flux q_c , i.e., the convected heat for a channel 1m long, 1m deep and wide as listed. The density used for the calculation of mass flow rates was calculated using the bulk temperature at $X=0.98$. Calculation method for the heat and mass flow rates is detailed in Section 4 of Appendix C.

Surface temperatures on the heated and unheated walls of the channel at four vertical positions, $X=0.4, X=0.6, X=0.8, X=0.96$ were monitored and recorded. The ratio of the temperature of the cold wall to that of hot wall, r_T , using temperature $^{\circ}C$, are listed in Table 6.2 for all the cases. The measured wall temperatures for all the cases are given in Appendix G.

Table 6.1 List of laminar flow experiments.

Case No	b [mm]	q [w/m ²]	q _c [w/m ²]	m [g/s]	Measured Vel. (u)	Profiles Temp.(T)
1	10	165	128.6	1.89	√	at X=0.98 only
2	10	265	206.6	2.36	√	at X=0.98 only
3	20	165	139.2	3.88	√	√
4	20	210	172.5	4.35	√	√
5	20	265	215.4	4.52	√	√
6	50	165	126.48	3.63	√	at X=0.98 only
7	50	265	195.51	4.82	√	at X=0.98 only

Table 6.2 List of the ratio of surface temperatures for the laminar flow channels.

Case No:	1	2	3	4	5	6	7
X	r _T						
0.96	0.705	0.654	0.641	0.616	0.584	0.579	0.540
0.8	0.712	0.662	0.649	0.623	0.584	0.585	0.543
0.6	0.670	0.613	0.533	0.606	0.572	0.574	0.534
0.4	0.562	0.499	0.568	0.536	0.491	0.508	0.462

Examination of Tables 6.1 and 6.2 indicates that thermal radiation played an important role in the heat transfer process, causing the perspex front walls to be passively heated to quite high temperatures. The highest values of surface temperature ratios, r_T, occurred with the smallest channel width. For a given channel width, higher wall temperatures occurred on the front walls at lower heat fluxes, suggesting that at high heat fluxes the greater induced flow rates increased convective heat transfer and reduced the effect of radiation. The amount of heat absorbed by the air was the highest for the intermediate channel width (Case 1, 2 and 3) for all the wall

heat fluxes and it was the lowest for the widest channel. This can be attributed to the effect of radiation. In cases 1 and 2, higher front wall temperatures should have resulted in higher heat losses at the back of the front walls. In cases 6 and 7, however, the large channel increases the view factors of the walls to the region outwith the channel resulting in high heat losses to the ambient by thermal radiation to the ambient through inlet and outlet of the channel. The highest wall temperatures for all cases on both heated wall and front walls occurred just above the half height of the heated portion of the channel and the wall temperature was almost constant throughout the upper third of the channel.

6.2.1 Velocity Profiles

The velocity profiles across the channel for the seven cases were measured at five elevations. The number of samples taken for every point were always over 1000. The dead time measurement mode of the BSA was used in order to reduce the effect of velocity bias. The dead time mode allowed the recording of data to be carried out for a determined period of time and no recording for the next period. The dead time period used was 100 ms. Near the wall for all cases and in the core region of the channel for Cases 6 and 7, there was difficulty with the seeding particles due to the low velocities. This meant measurement times up to 10 minutes were required for a single point. The maximum velocity encountered for all the cases considered was under 400 mm/s.

The velocity profiles for the seven cases are presented below in Figures 6.1 to 6.7. In the Figures an origin shift has been used for the velocity so that profiles for all vertical positions could be plotted on the same diagram and the flow development could easily be seen.

Figures 6.1 to 6.7 shows that the flow along the channel has the characteristics of a developing flow with asymmetric heating. The maximum velocity for all the cases occurs at the highest elevation. For the lowest aspect ratio, Cases 1 and 2 (Figures 6.1 and 6.2), the asymmetry is not very pronounced. The velocity profile is skewed

towards the heated wall, as it develops upward the skewness reduces and the velocity maximum is shifted to $y/b=0.4$. The reason for the skewed velocity profile at the first elevation is thought to be the entrainment towards the heated wall since the temperature of the lower part of the front wall is quite low. The non-dimensional velocity profiles for Cases 1 and 2 are almost the same. The velocity profiles for the intermediate aspect ratio, Cases 3, 4 and 5 (Figures 6.3, 6.4 and 6.5), indicates stronger asymmetry. The velocity maximum for different elevations falls into the range of $y/b=0.2$ to 0.25 . For these cases however, skewness is the least at the first elevation as opposed to the lowest aspect ratio cases. Again, the non-dimensional velocity profiles for Cases 3 to 5 are almost the same. The velocity profiles of the highest aspect ratio, Cases 6 and 7

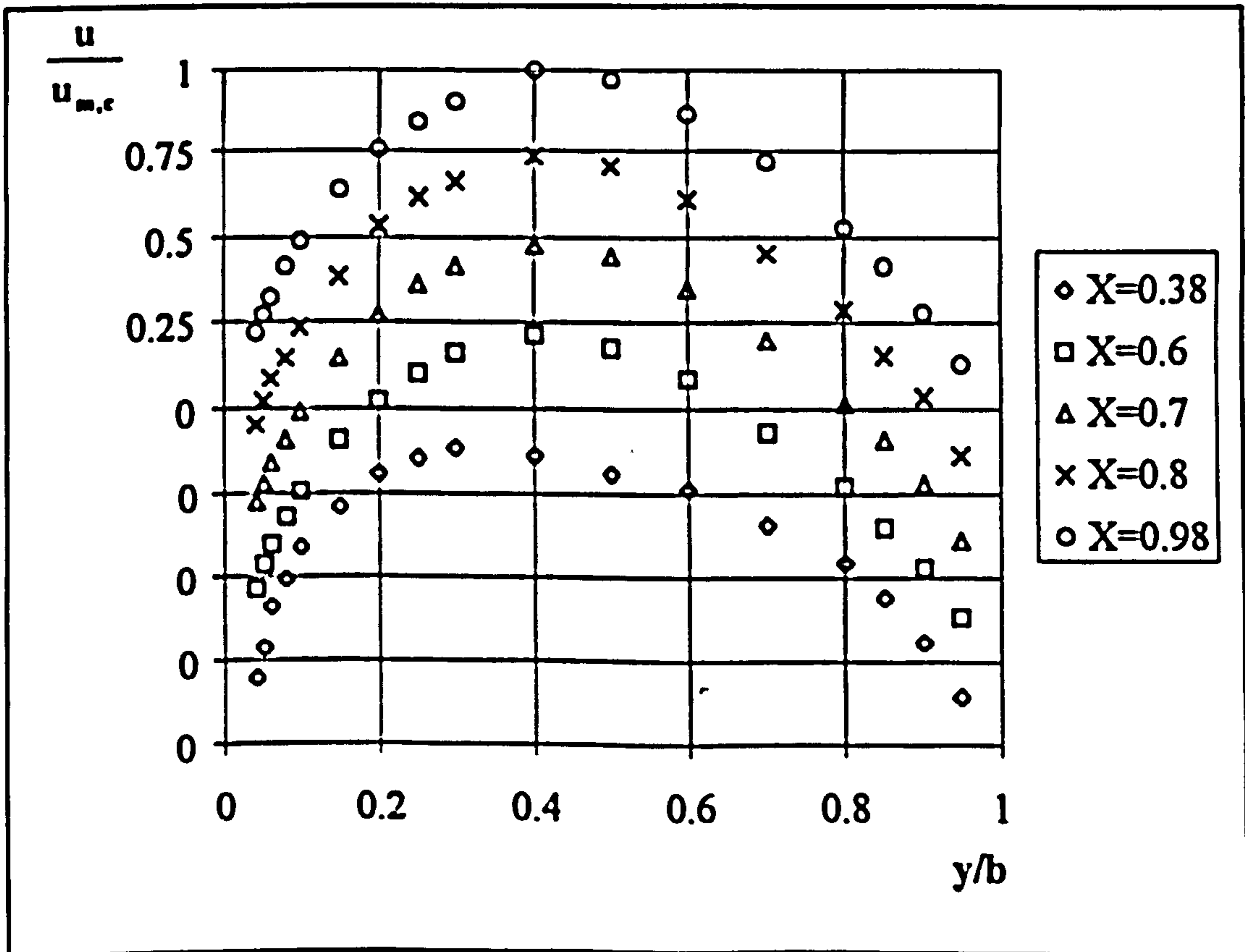


Figure 6.1 Laminar flow velocity profiles, Case 1, $b/H=1/32$

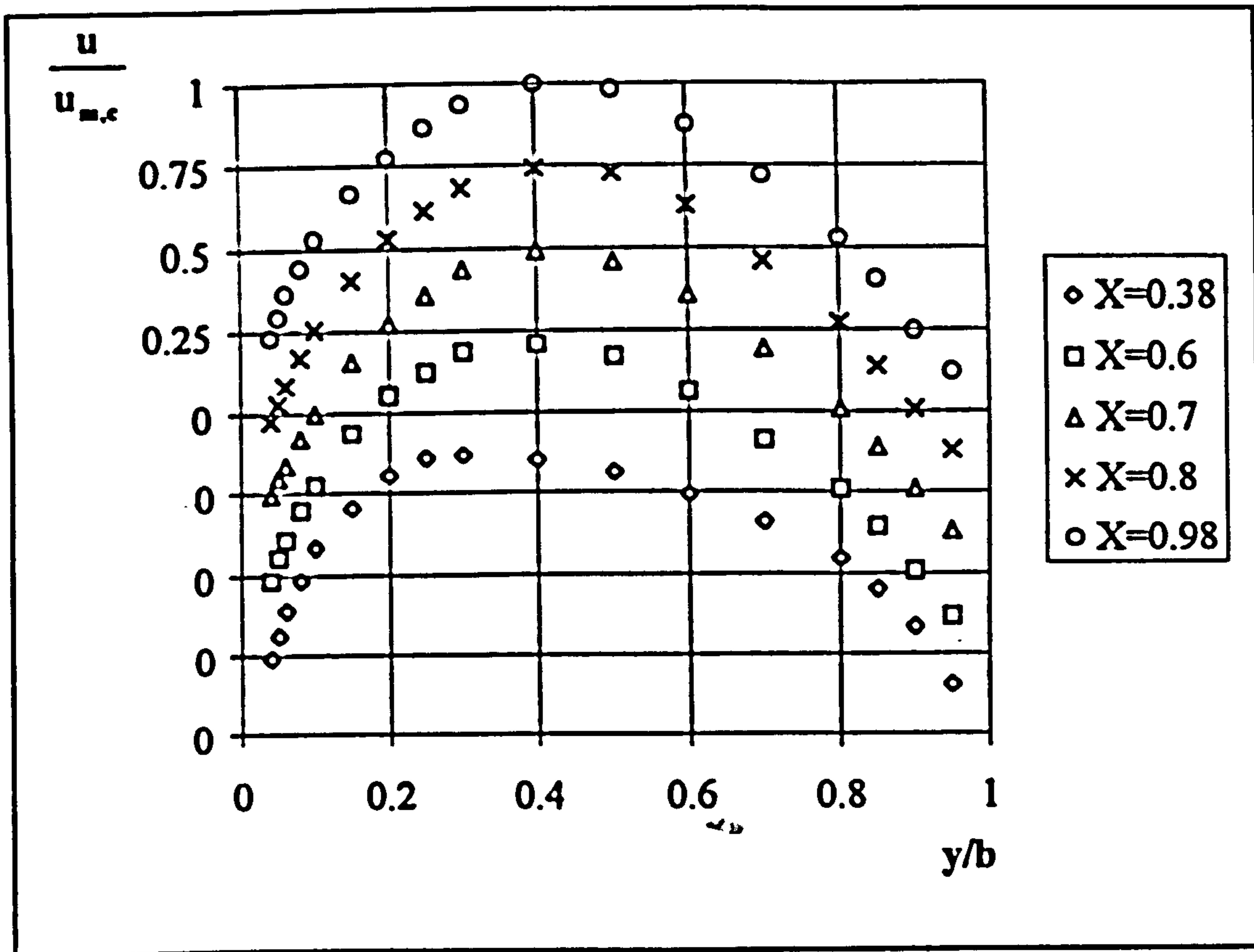


Figure 6.2 Laminar flow velocity profiles, Case 2, $b/H=1/32$

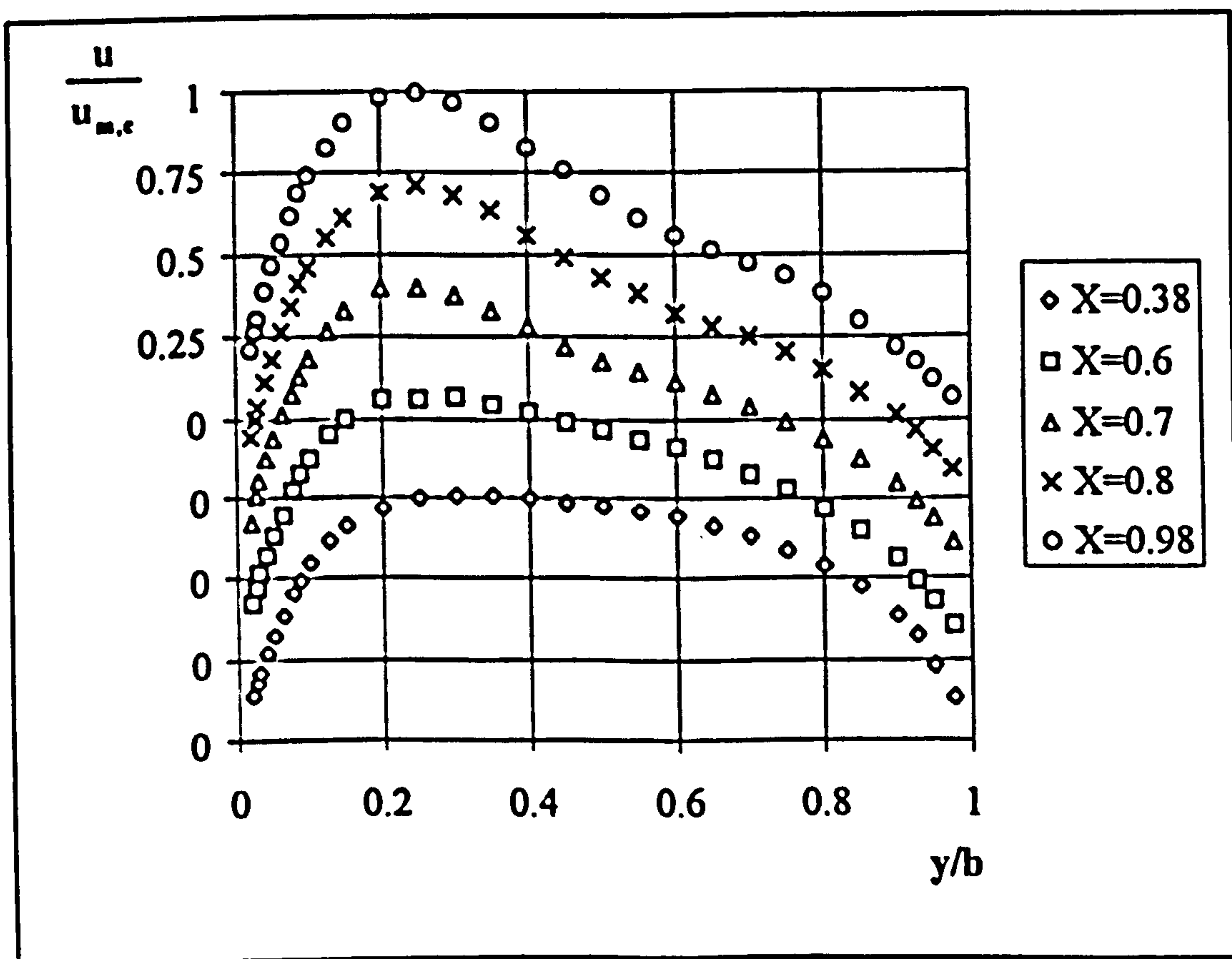


Figure 6.3 Laminar flow velocity profiles, Case 3, $b/H=1/16$

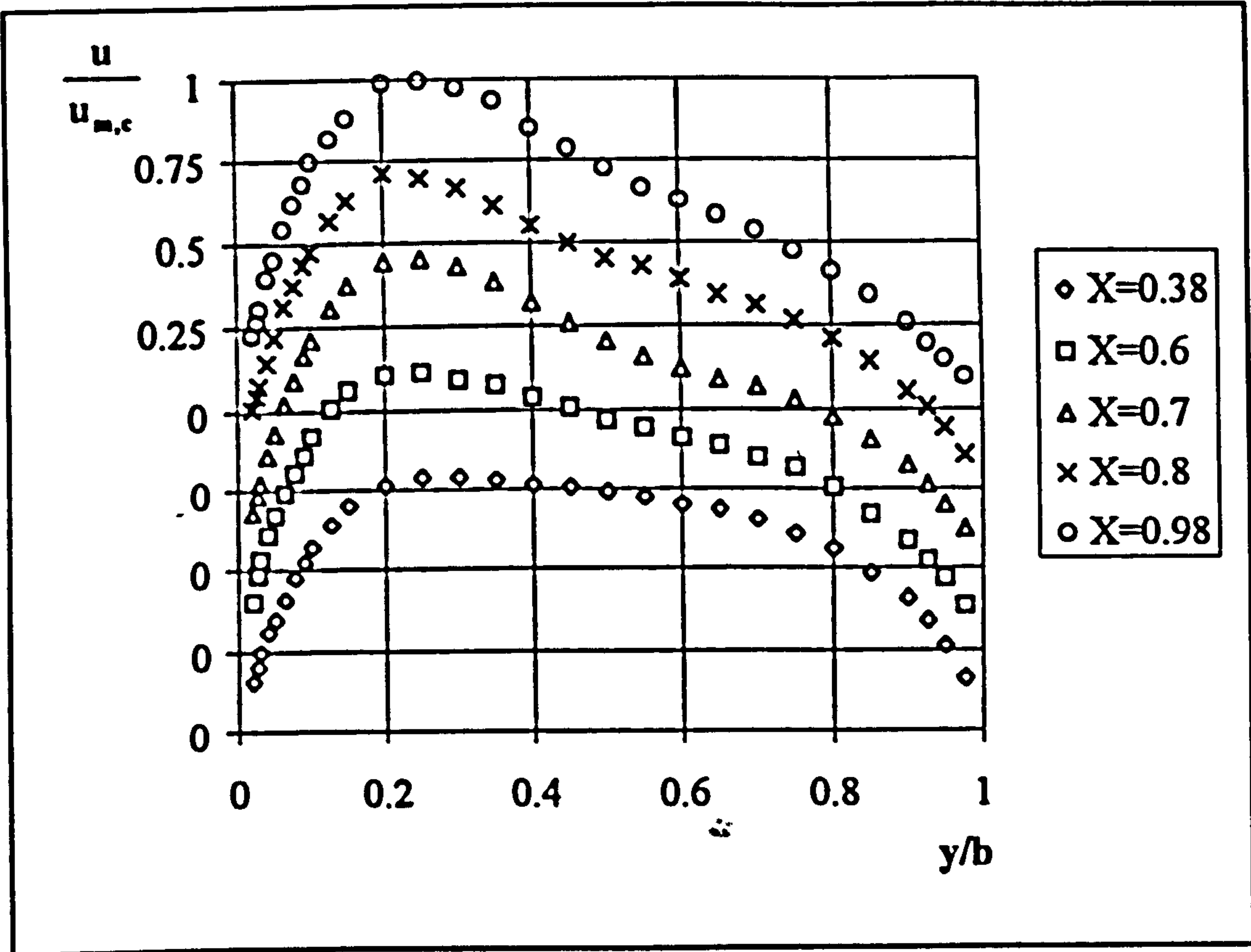


Figure 6.4 Laminar flow velocity profiles, Case 4, $b/H=1/16$

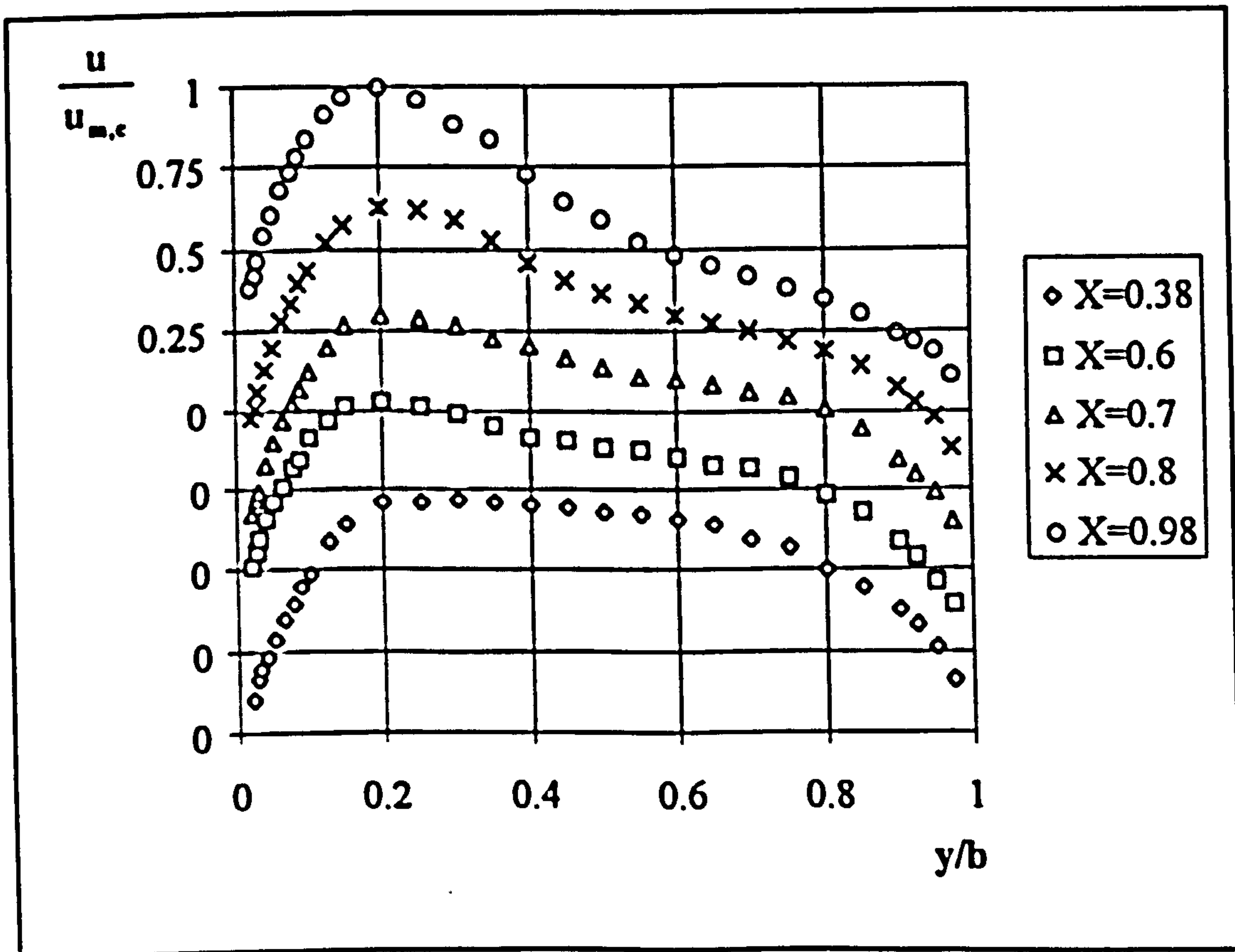


Figure 6.5 Laminar flow velocity profiles, Case 5, $b/H=1/16$

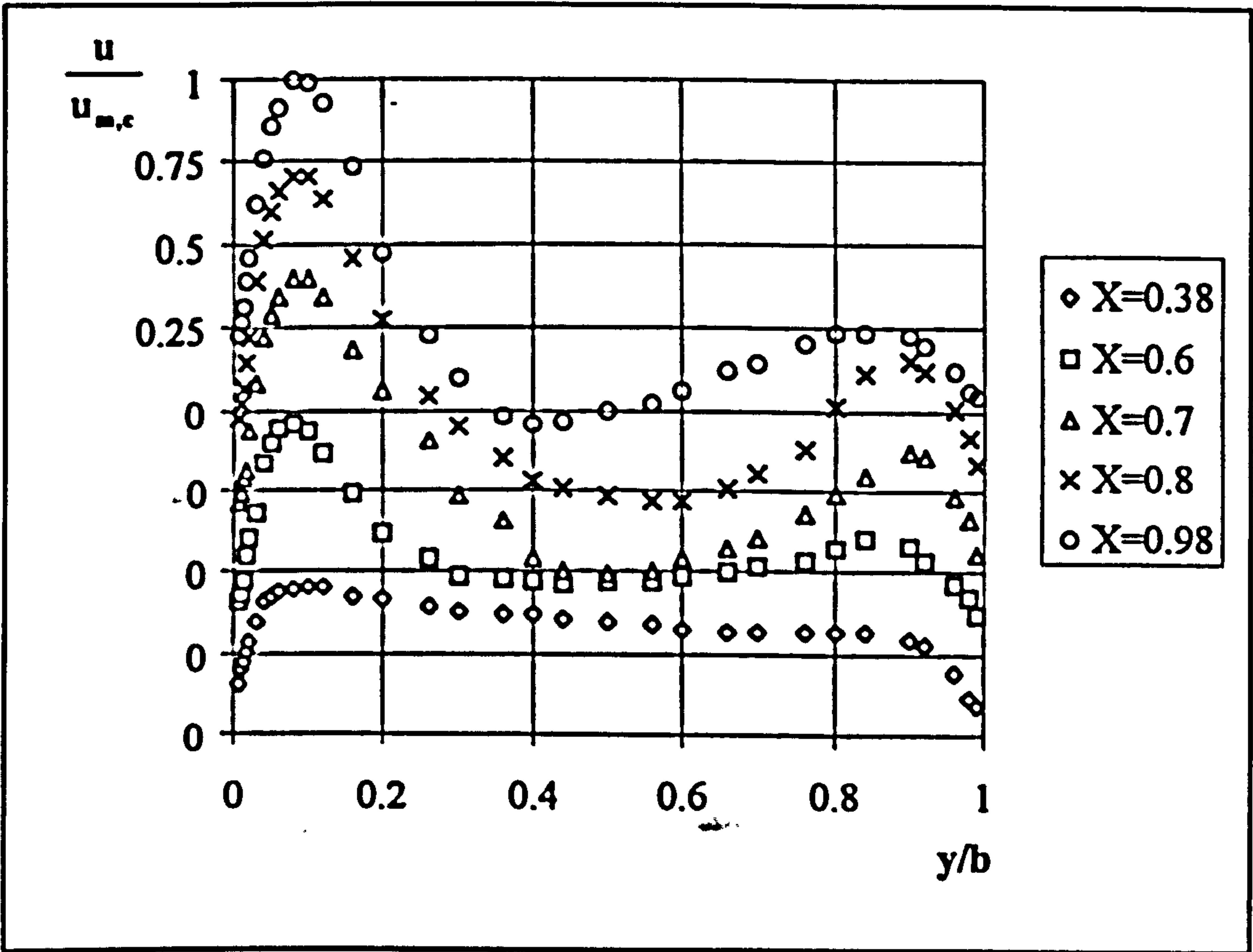


Figure 6.6 Laminar flow velocity profiles, Case 6, $b/H=5/32$

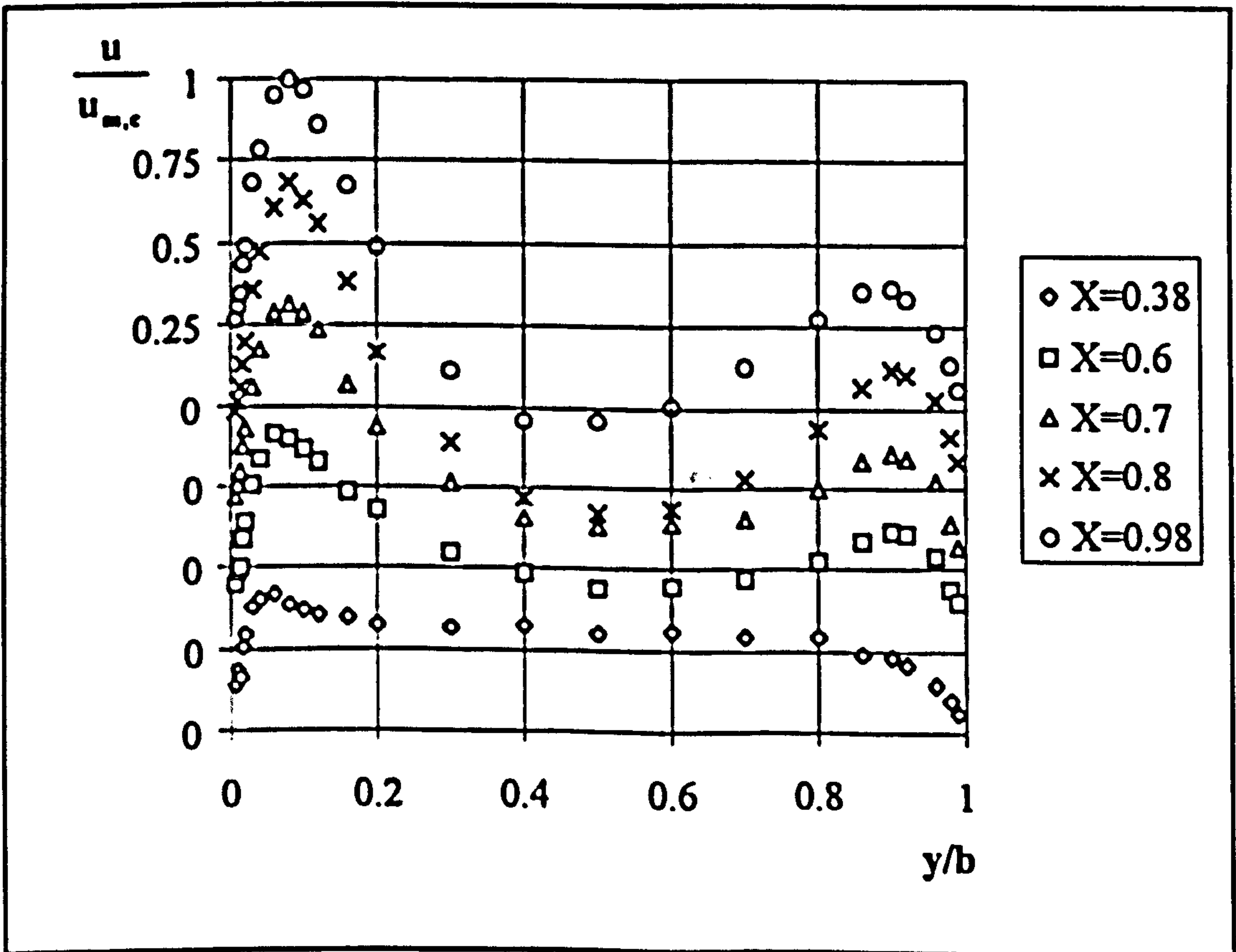


Figure 6.7 Laminar flow velocity profiles, Case 7, $b/H=5/32$

(Figures 6.6 and 6.7), are typical of developing boundary layers on both walls. The velocity profiles at the lowest elevation are almost uniform with a slight peak near the heated wall which is sharper for the higher heat flux (Case 7). At the higher elevations two separate boundary layers develop on the walls with two velocity peaks. Flow reversals are observed in the upper portion of the channel penetrating as deep as half the length of the heated part of the channel. The reversal penetration is deepest for the lowest heat flux.

6.2.2 Temperature Profiles

Temperature profiles along the channel, at the same elevations as for the velocity

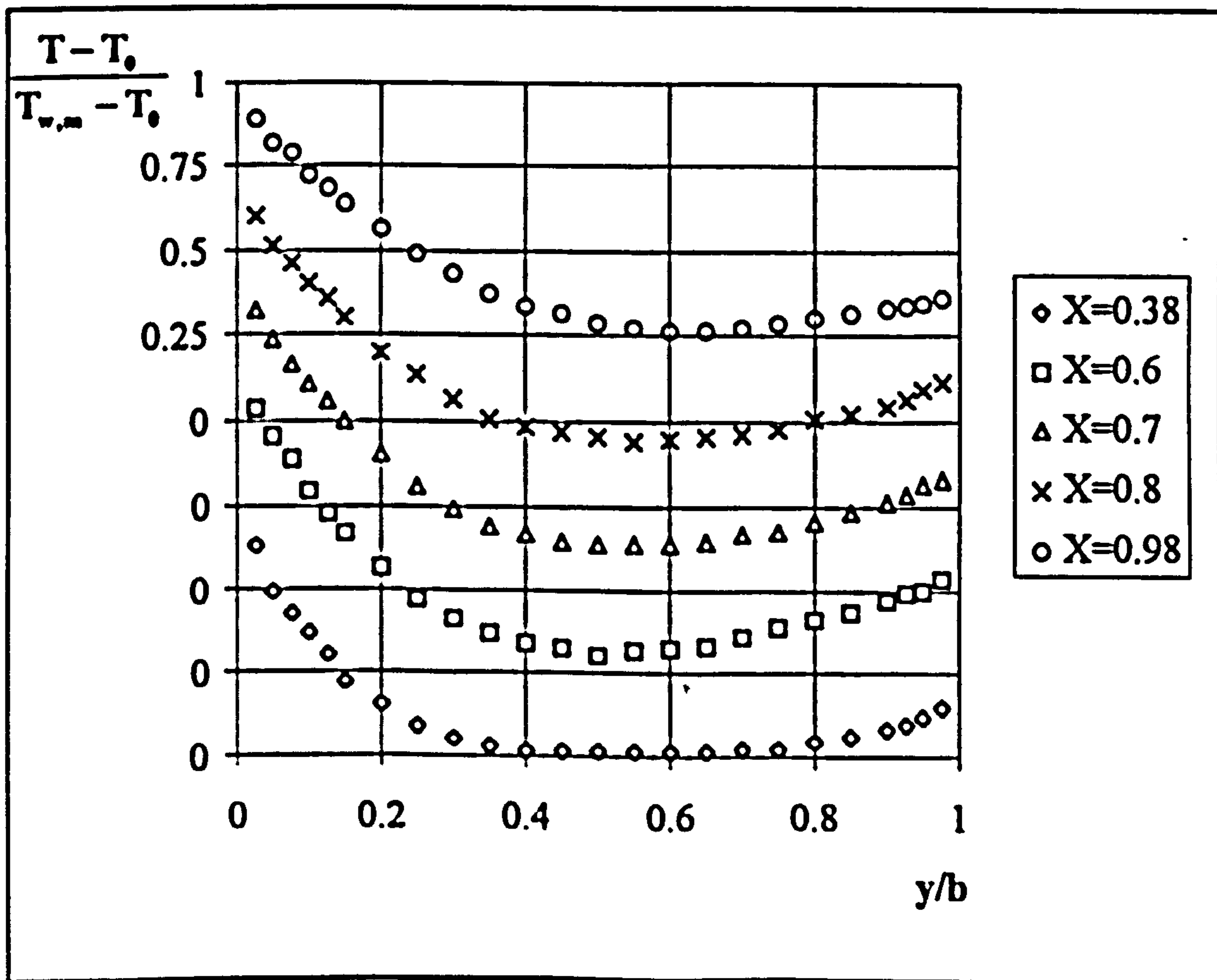


Figure 6.8 Laminar flow temperature profiles, Case 3, $b/H=1/16$

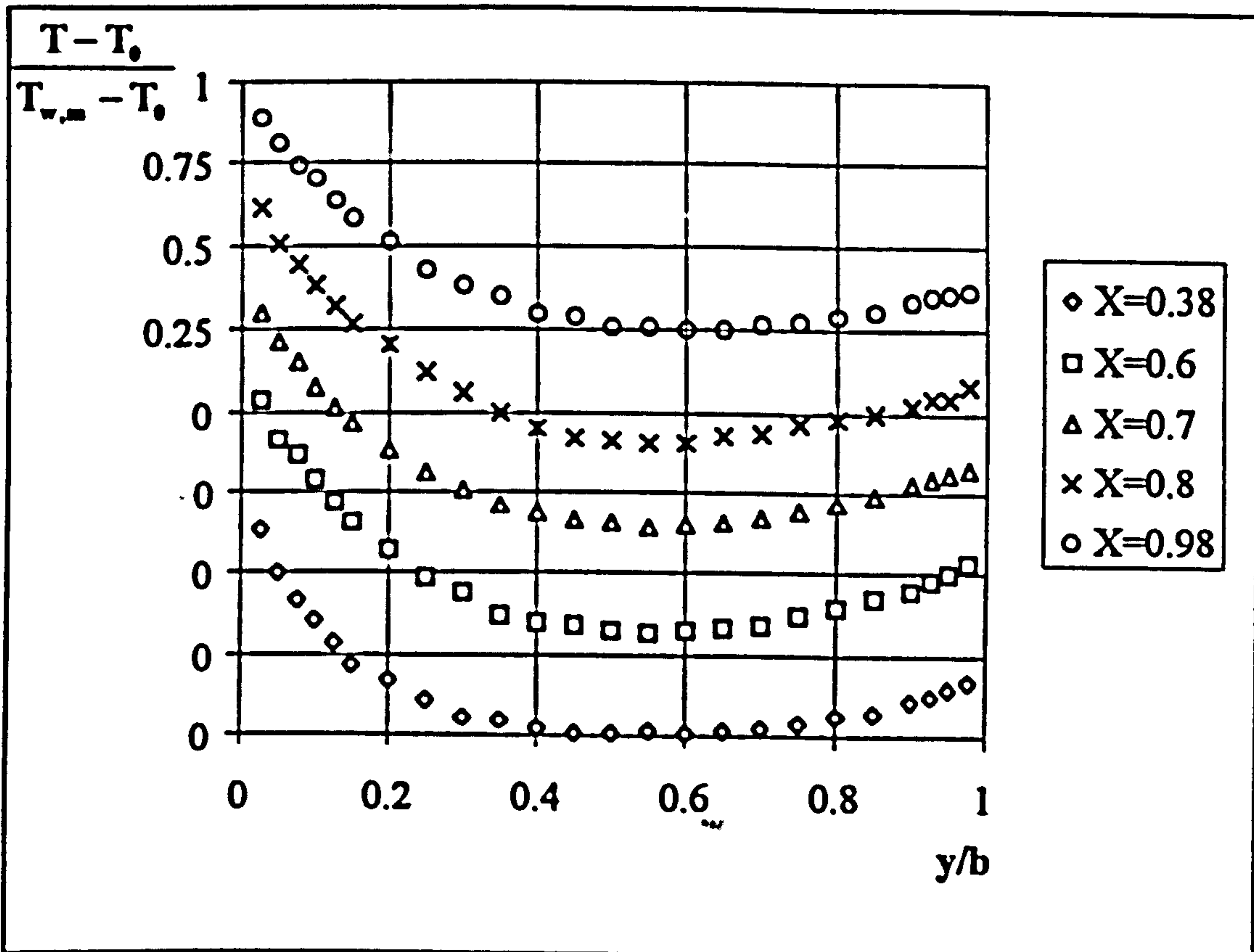


Figure 6.9 Laminar flow temperature profiles, Case 4, $b/H=1/16$

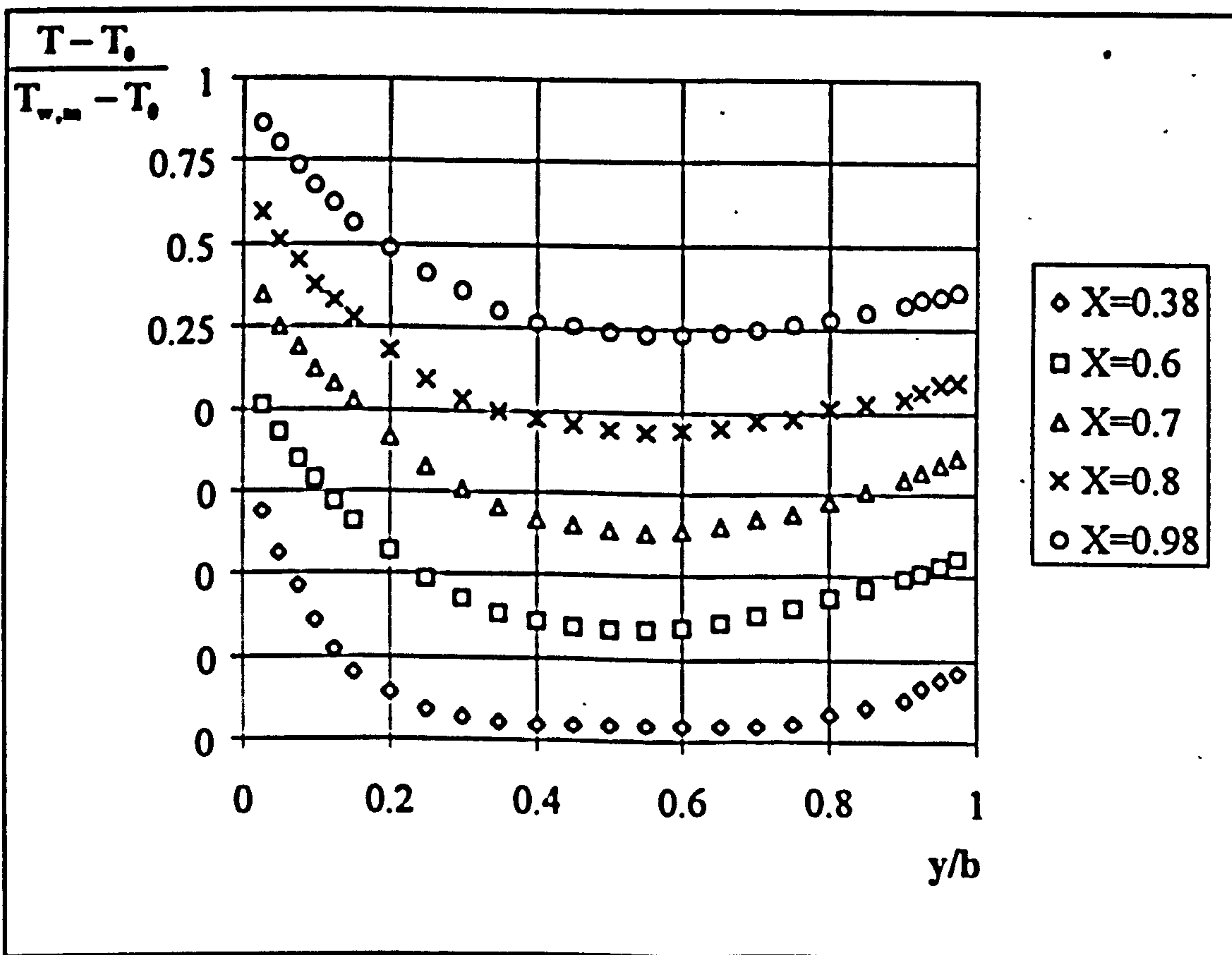


Figure 6.10 Laminar flow temperature profiles, Case 5, $b/H=1/16$

profiles, were measured only for the intermediate aspect ratio cases and are presented in Figures 6.8 to 6.10. Temperature was non-dimensionalised using equation (6.1) and again an axis shift was used in the figures for charting. The profiles have steep gradients at the lower elevations and the gradients become less steep higher up the channel. The steepest temperature gradient at the first elevations occurs for the highest wall heat flux (Case 5). In section 6.2 it was mentioned that wall temperatures in the upper third of the channel were almost constant. This can be seen to be the case by looking at the first data points of the two uppermost profiles of each case.

6.2.3 Time Histories of Velocity

Velocity time histories at the centre of the channel at three different elevations for three aspect ratios (Cases 2, 5 and 7) are presented in Figures 6.11 to 6.13. Figure 6.11 (Case 2) shows that the velocity time series for all elevations have the characteristics of a laminar flow. For Case 5, however, the velocities have a low frequency fluctuation. The amplitude of the fluctuations are quite large, particularly for locations A and C. The amplitude of the fluctuations for location C is almost 0.2 of the mean velocity. For Case 7 (figure 6.13), the velocity fluctuations have multiple frequencies.

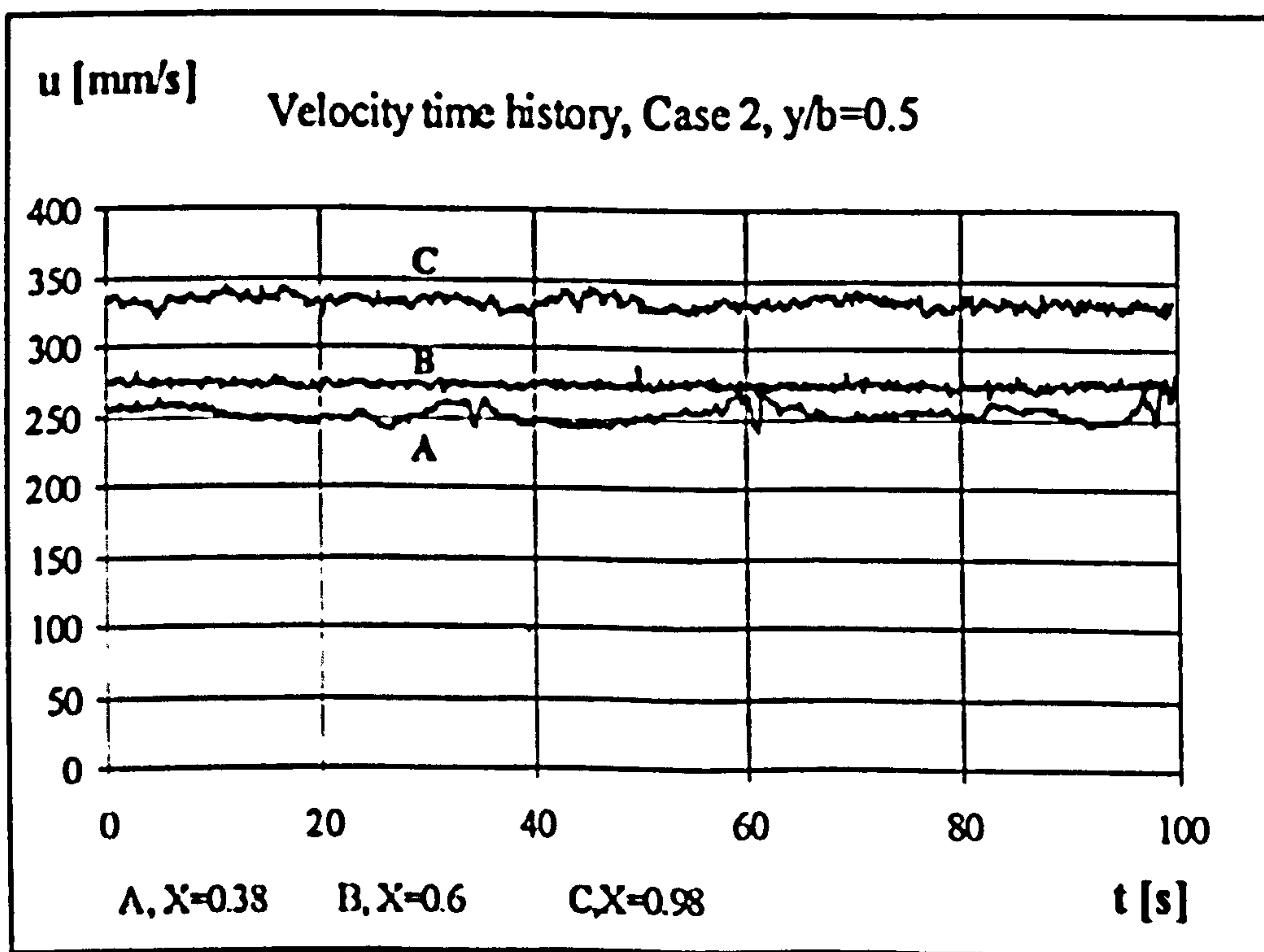


Figure 6.11 Laminar flow velocity time history, Case 2, b/H=1/32

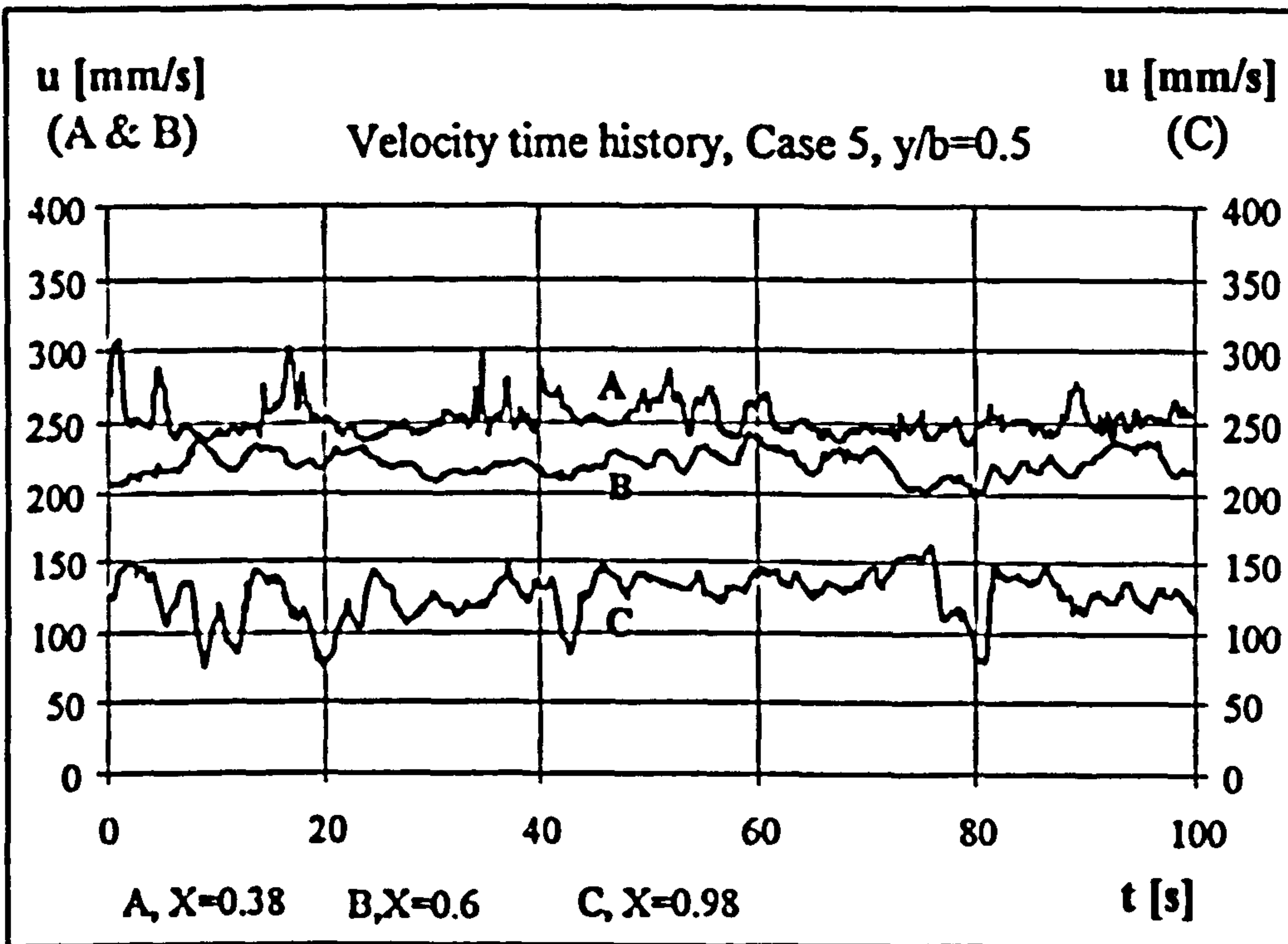


Figure 6.12 Laminar flow velocity time history, Case 5, $b/H=1/16$

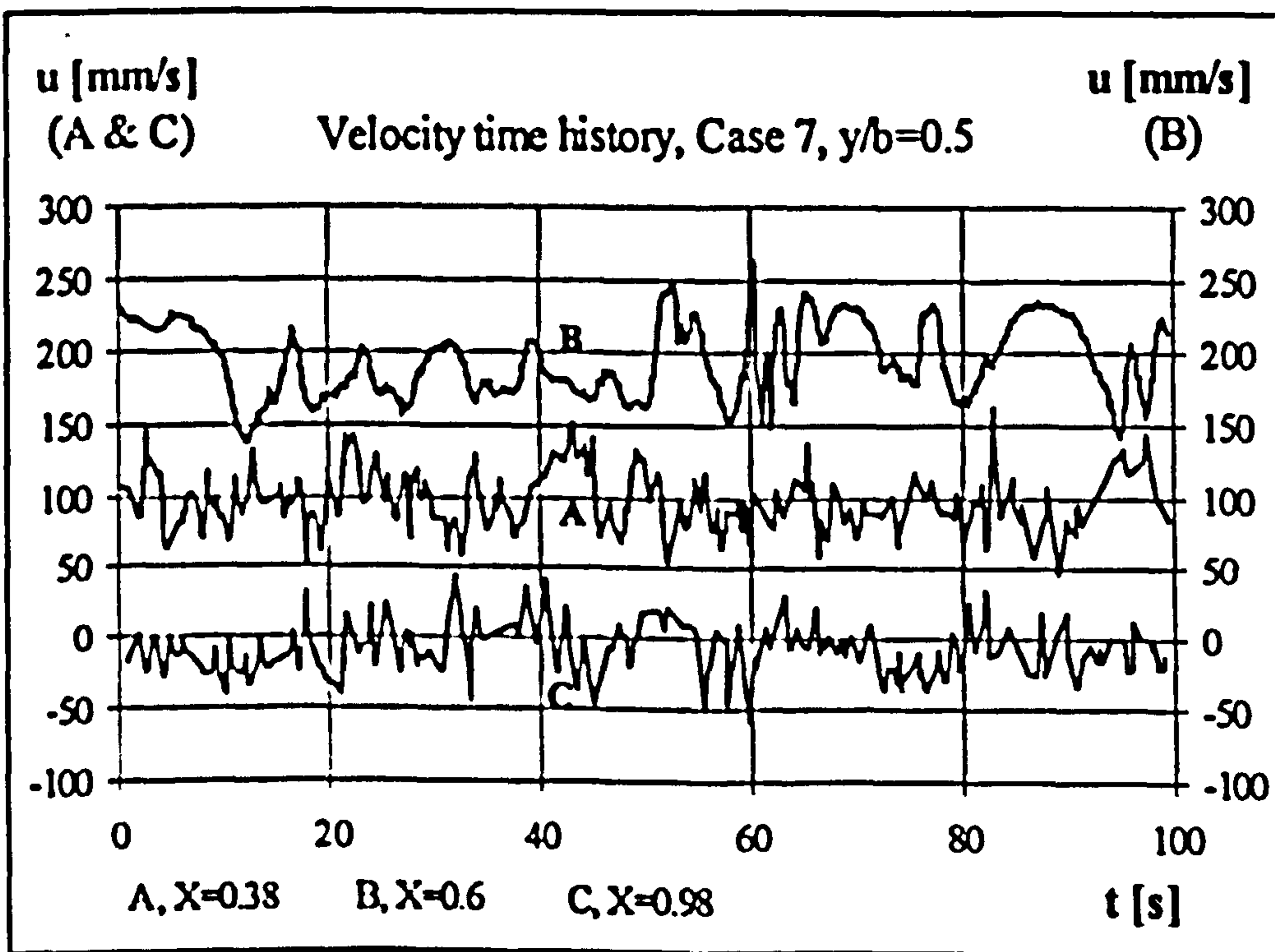


Figure 6.13 Laminar flow velocity time history, Case 7, $b/H=5/32$

As the channel aspect ratio increased it was found that the amplitude and frequency of the fluctuations increased. The fluctuations recorded for Cases 5 and 7 appear to

suggest an instable laminar flow. The time series presented here do not possess the high frequency fluctuations which characterise turbulent flows.

6.2.4 Summary and Conclusions

The laminar flow experiments indicated that if the wall emissivities are high, thermal radiation plays an important role in the heat transfer processes. For the three aspect ratios considered, the highest heat loss to the ambient, the difference between q and q_c , Table 6.1, occurred for the highest aspect ratio cases. The front walls, which are passively heated from the heated wall had the highest temperatures at the lowest aspect ratio cases. For all the cases considered the wall temperatures on the upper third of the heated section of the channel was almost constant. The velocity time histories possess the characteristics of laminar flow, although for the high aspect ratio cases the flow appeared to experience some instability.

6.3 Turbulent Flow Experiments

The experimental channel, measurement techniques and experimental procedures for the turbulent flow experiments have been detailed in Chapter 5. Experiments were conducted for five cases with the UWT heating mode and for three cases with the UHF heating mode. Only one channel aspect ratio was used for each of the UWT and UHF heating modes, $b/H=1/30$ for UWT and $b/H \approx 1/20$ for UHF. However, for $b/H \approx 1/20$ in the UWT heating mode, velocity profiles at $X=0.033$ and 0.983 were measured at wall temperature of 130°C . The conducted experimental cases are listed in Table 6.3 and 6.4 for UWT and UHF heating modes respectively.

UWT experiments were performed for five wall temperatures of 60, 75, 90, 100, 130°C . Mean velocity profiles across the channel were measured at five elevations of $X=0.033, 0.2, 0.5, 0.63, 0.983$. Simultaneous measurements of vertical and cross components of velocity were performed only for Cases 4 and 5. Temperature profiles were recorded only at the highest elevation of $X=0.983$ simultaneously with velocity for all the five cases. Heat convected (absorbed) by the air passing through the

channel was calculated for every case from the temperature and velocity data for the highest measurement position ($X=0.983$) and listed in the Table 6.3 as an average heat flux q_c , i.e. the convected heat per unit heated wall area of the channel. The density used for the calculation of mass flow rates was calculated using average bulk temperature at $X=0.983$. Calculation method is detailed in Section 4 of Appendix C.

Surface temperatures on the front wall of the channel at three vertical positions, $X=0.17, 0.5, 0.83$ were monitored. Comparison of these temperatures with that of ambient at the same elevation indicated that the front wall could be assumed adiabatic. This was proved by the mean temperature profiles at the highest elevation showing zero gradient at the front wall.

Table 6.3 List of turbulent flow experiments, UWT

Case No	b [mm]	T_w [°C]	q_c [w/m ²]	\dot{m} [g/s]	Ra(b/H)
1	100	60	139.43	60.16	95096
2	100	75	212.44	67.78	120027
3	100	90	294.17	79.74	138725
4	100	100	350.00	85.56	149105
5	100	130	540.67	106.23	169125

UHF experiments were carried out for three different wall heat fluxes, $q_w = 260, 375, 450$ w/m². In these experiments, simultaneous velocity and temperature profiles were recorded at five elevations, $X=0.033, 0.27, 0.5, 0.8, 0.983$ for Cases 2 and 3, and $X=0.033$ and 0.983 for Case 1. Heated wall temperatures were monitored and recorded by eighteen thermocouples and the results are shown plotted in Figure 6.14. The front wall temperatures were monitored at the same positions as in the UWT experiments. Examinations of these temperatures together with the mean temperature profiles, indicate that the front wall is essentially an adiabatic wall. Heat absorbed by the air passing through the channel was calculated for every case from the temperature and velocity data for the highest measurement position (i.e. $X=0.983$) and is listed in the Table 6.4 as a heat flux q_c . Mass flow rates and heat absorbed by the were calculated as in the UWT experiments. Examination of Figure 6.14 shows

that the maximum heated wall temperature occurs at around $X=0.4$ in all cases. From the 4th degree polynomials fit to the wall temperature data, the maximum is found to occur at $X=0.38, 0.39, 0.40$ for Cases 1, 2 and 3 respectively. In analogy with the single plate case [44], the peak could be assumed as being located at the end of transition from laminar to turbulent flow. The reason for the somewhat sharp fall of the temperature at the last measurement position is due to the unheated section at the end of the wall and also to the radiative heat losses to the ambient. From the results it can be concluded that higher wall heat flux delays transition to turbulent flow for the same channel aspect ratio, although very slightly. More experimental data are needed for a more definite conclusion to be drawn.

Table 6.4 List of turbulent flow experiments, UHF

Case No	b [mm]	q_w [w/m ²]	q_c [w/m ²]	\dot{m} [g/s]	$Ra(b/H)$ equation (3.28)
1	155	260	190.8	64.1	3.3 E7
2	155	375	280.4	73.83	4.8 E7
3	155	450	322.3	82.97	5.6 E7

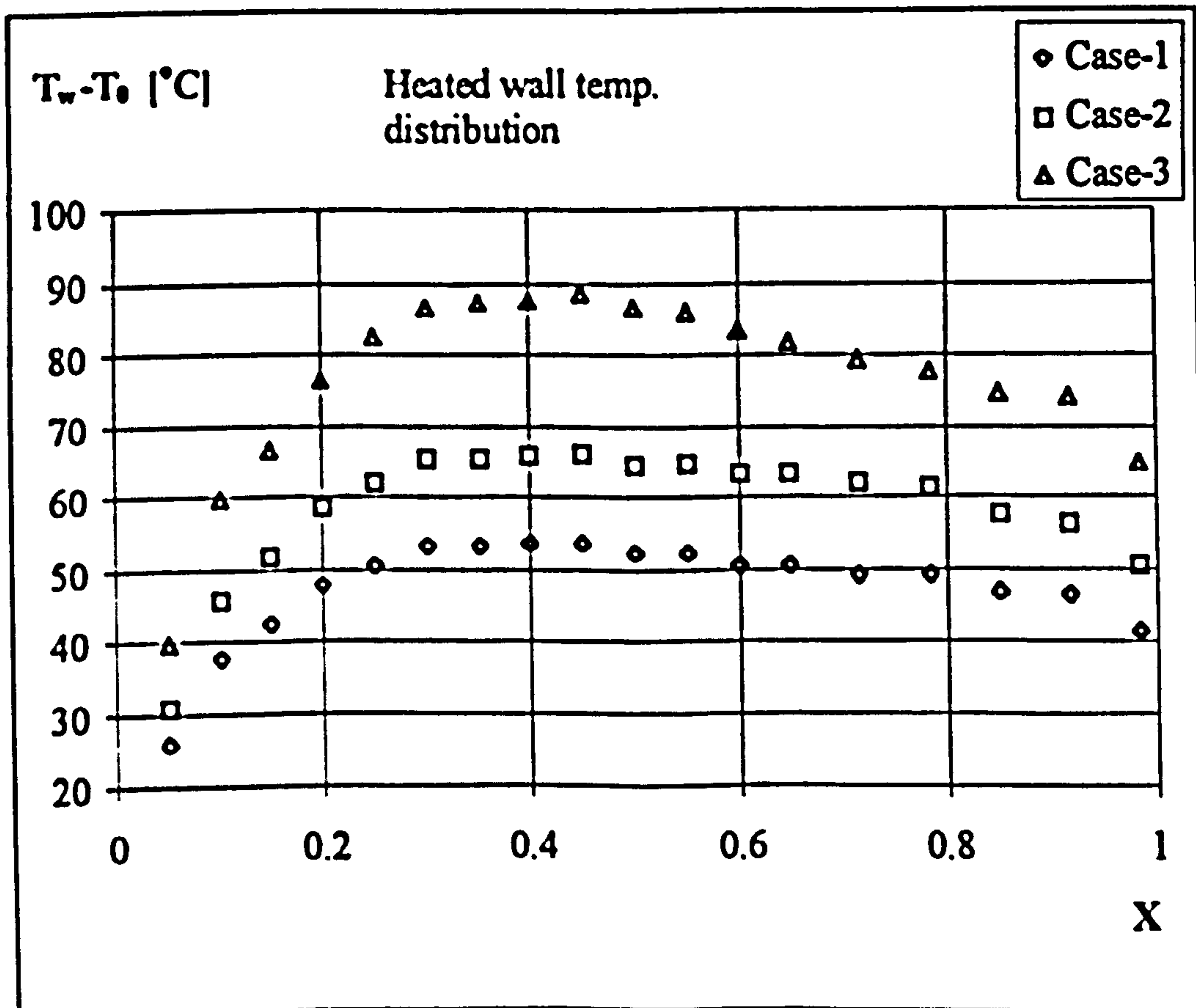


Figure 6.14 UHF turbulent flow heated wall temperature distributions.

6.3.1 Mean Velocity Profiles

The mean velocity profiles across the channel for both UWT and UHF turbulent flows are presented in Figures 6.15 to 6.22. The number of samples taken for the measurement of velocity at every point were kept over 10000. The velocity profiles are non-dimensionalised using the maximum velocity reading of the respective case. Again an axis shift was adopted when plotting the results order to clearly present all of the profiles on the same diagram.

The UWT mean velocity profiles presented in Figures 6.15 to 6.19 indicates that the flow starts as an almost uniform flows near the channel inlet with only a slight distortion towards the heated wall, the distortion being the highest in Case 1. Upwards through the channel a clear velocity peak develops near the heated wall. The peak is most obvious at $X=0.5$ (half height of channel). Near the channel exit the velocity peak weakens and the profile becomes smoother which indicates diffusion of momentum across the channel towards the adiabatic wall. All of the five cases are qualitatively similar although the velocity peaks become sharper as the wall temperatures become higher. The maximum velocity occurs at the uppermost elevation for all the cases considered. The mean velocity profiles possess some noticeable variations. This is attributed to the velocity bias effect. Although the number of samples for every point were over 10000, the time history of velocity for some points where variations are observed indicated that the time taken for the measurements was sometime less than a period of the lowest observed frequency of the velocity variations.

The UHF mean velocity profiles are presented in Figures 6.20 to 6.22. These figures show that the velocity starts as nearly uniform across the channel inlet with slight distortion towards the heated wall. The flow develops downstream such that a velocity peak develops near the heated wall.

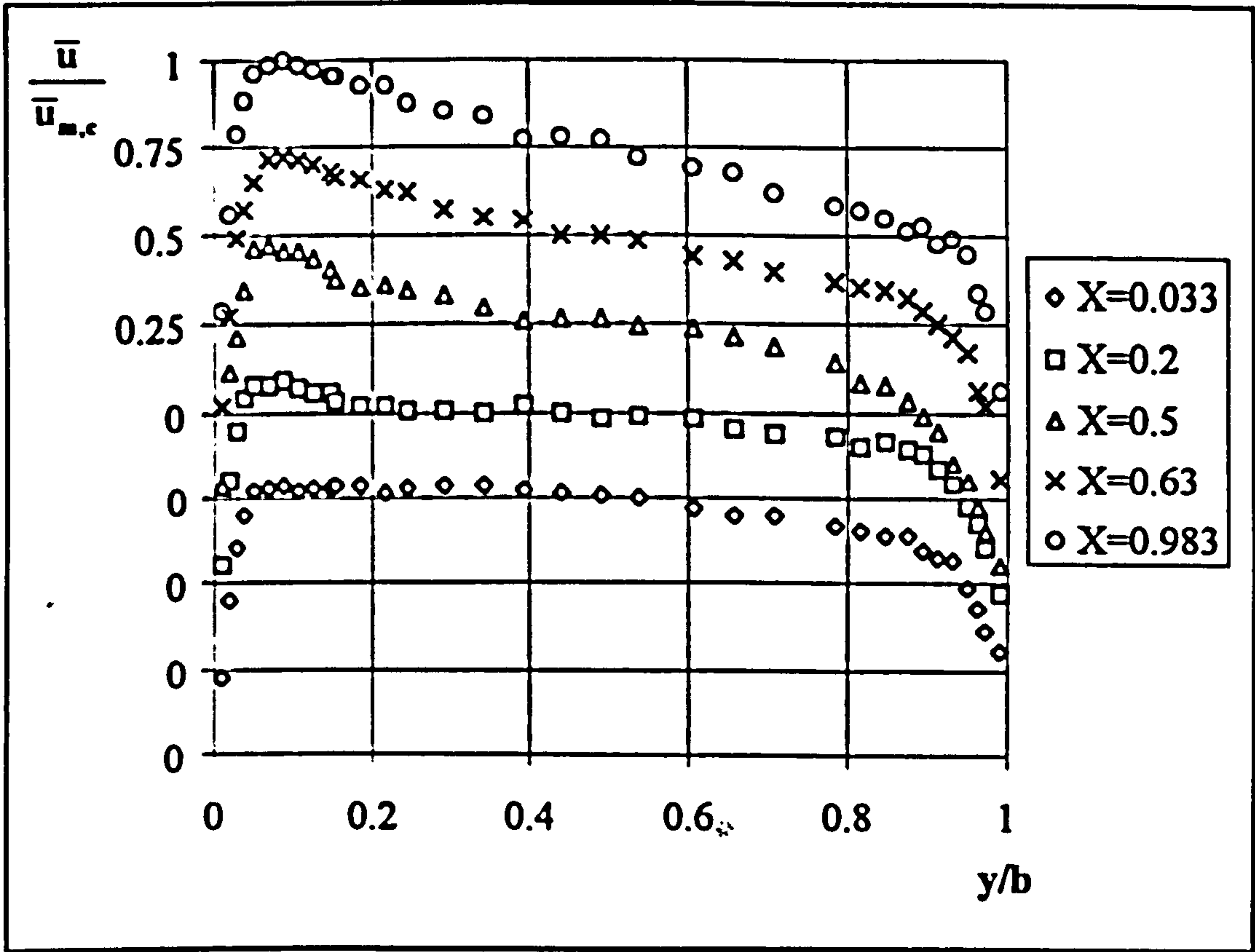


Figure 6.15 UWT turbulent flow mean velocity profiles, Case 1 $T_w = 60$ C.

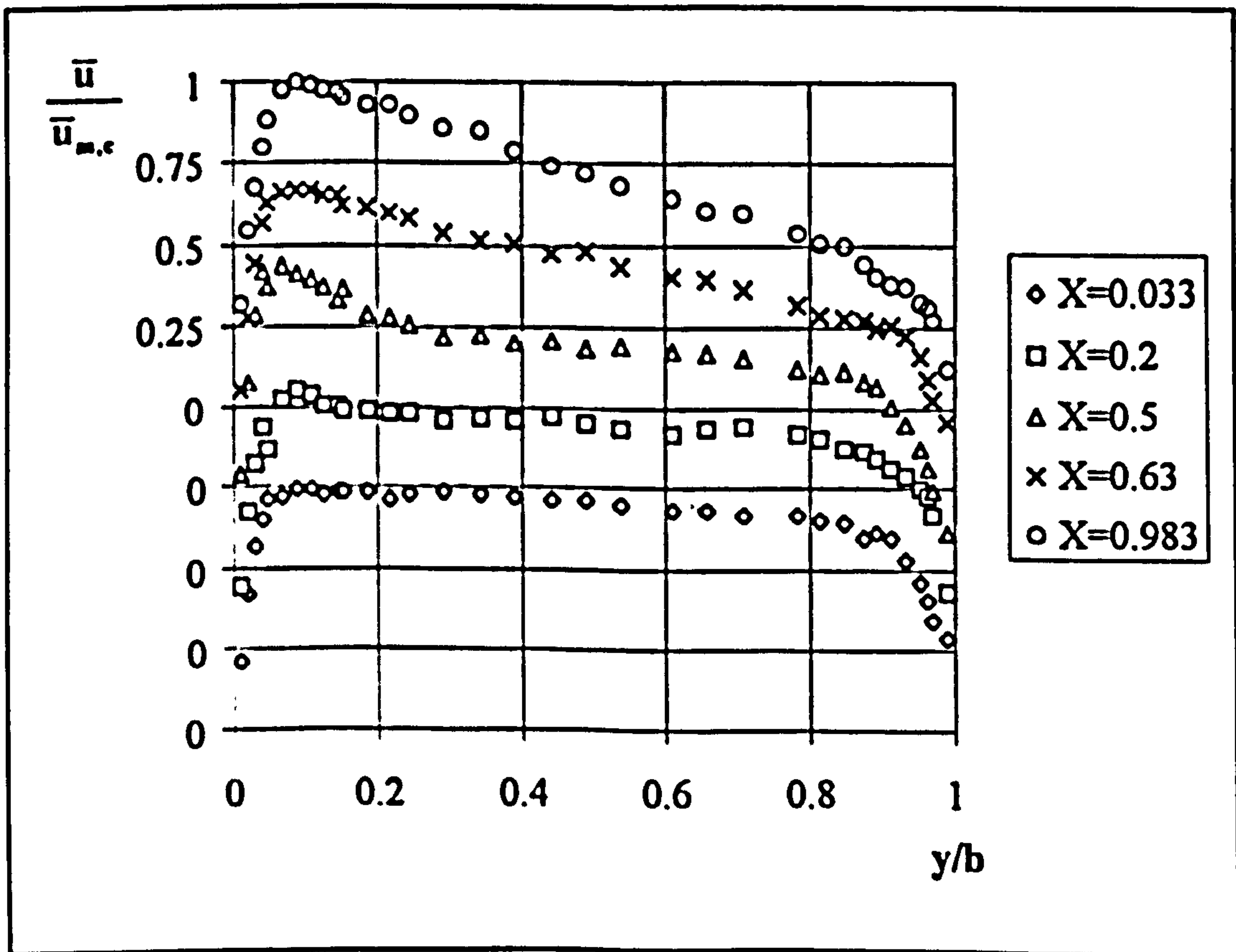


Figure 6.16 UWT turbulent flow mean velocity profiles, Case 2 $T_w = 75$ C.

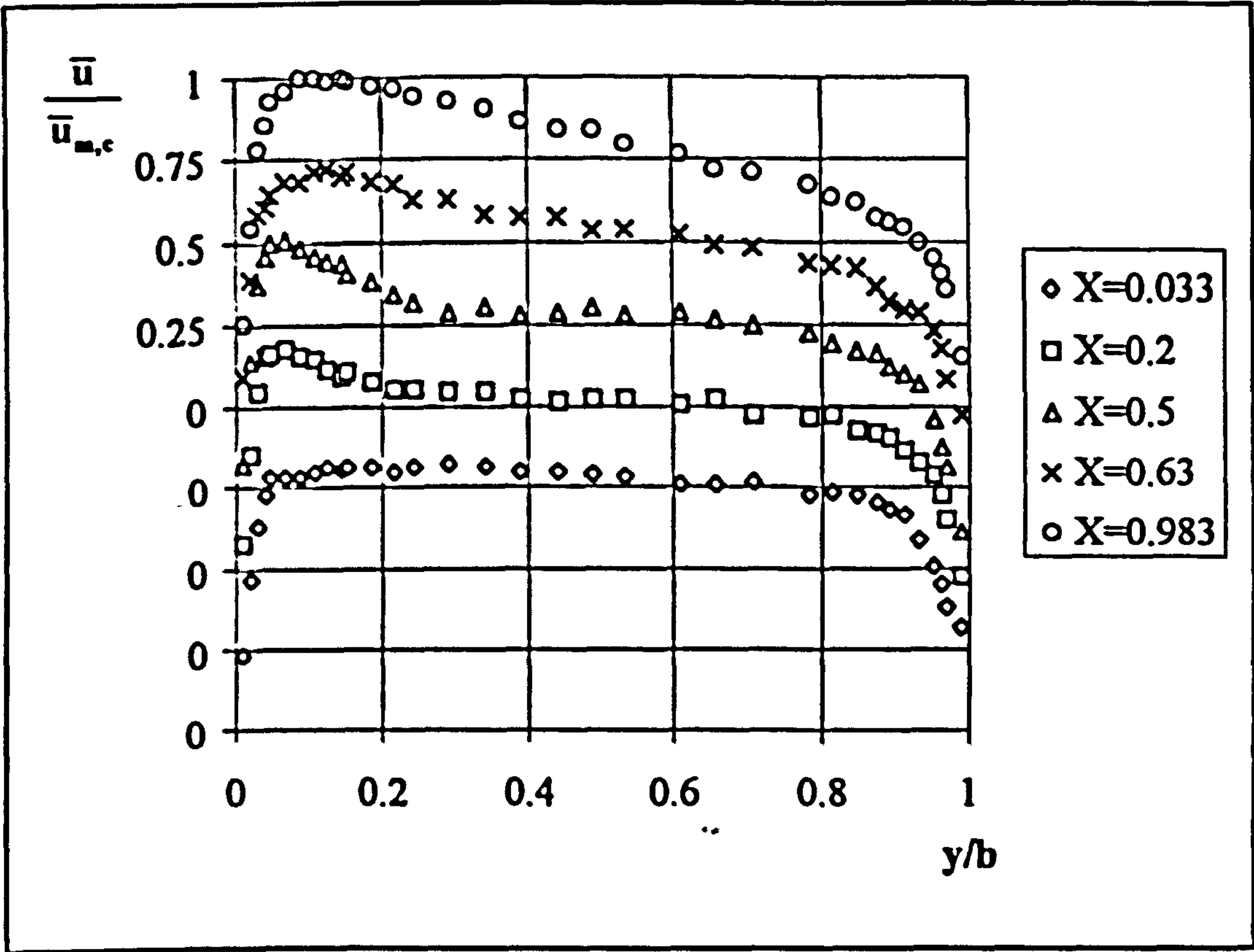


Figure 6.17 UWT turbulent flow mean velocity profiles, Case 3 $T_w = 90$ C.

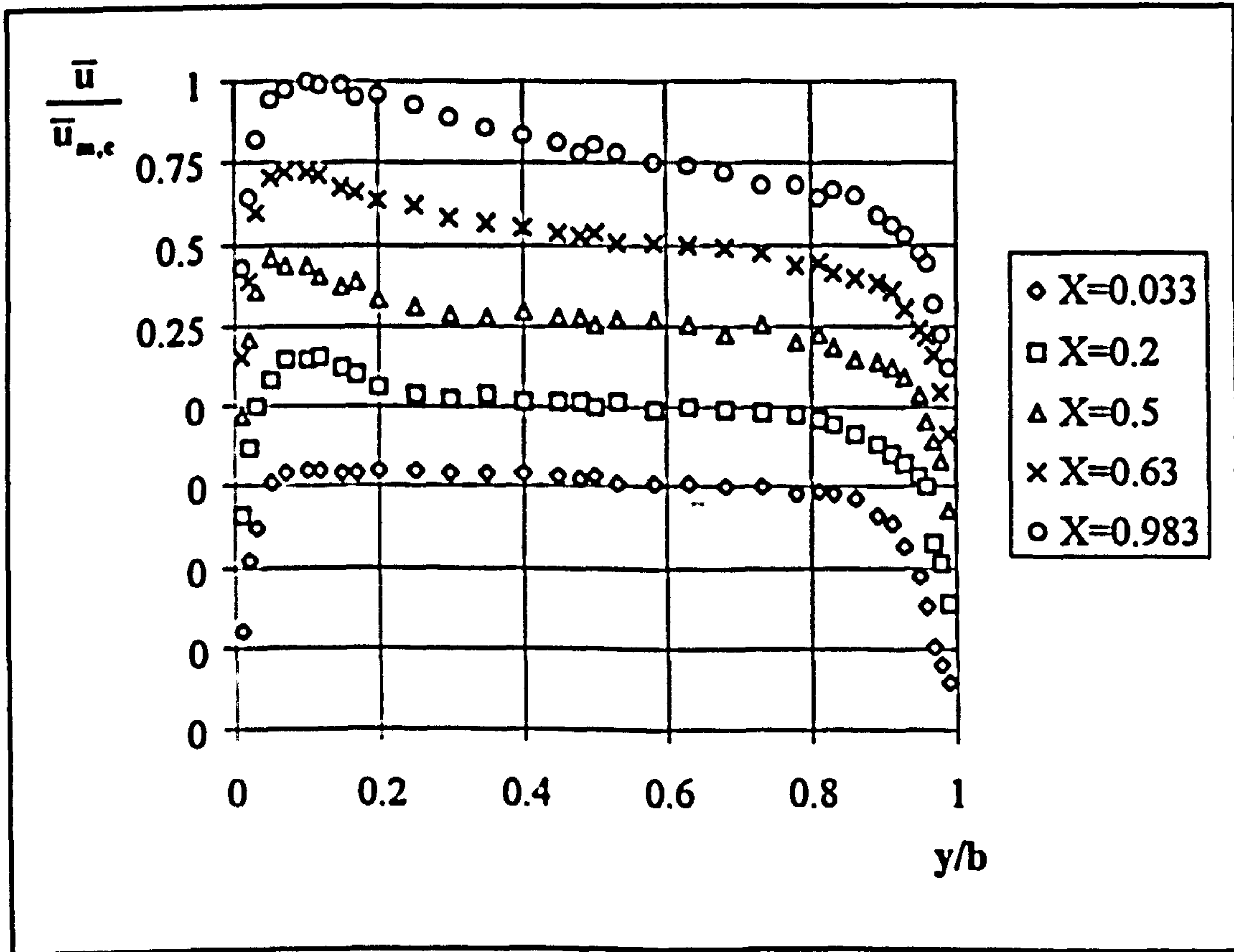


Figure 6.18 UWT turbulent flow mean velocity profiles, Case 4 $T_w = 100$ C.

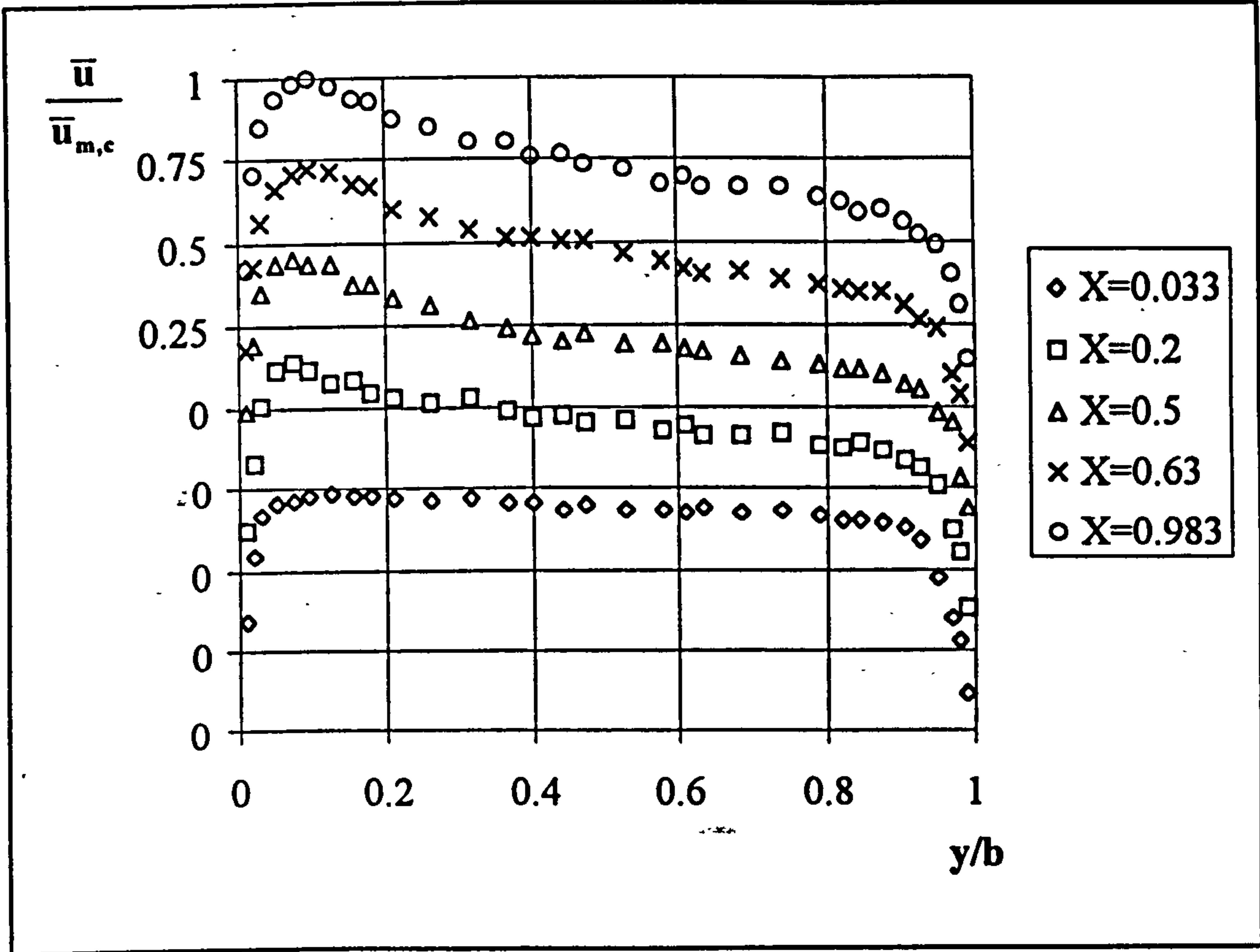


Figure 6.19 UWT turbulent flow mean velocity profiles, Case 5 $T_w = 130$ C.

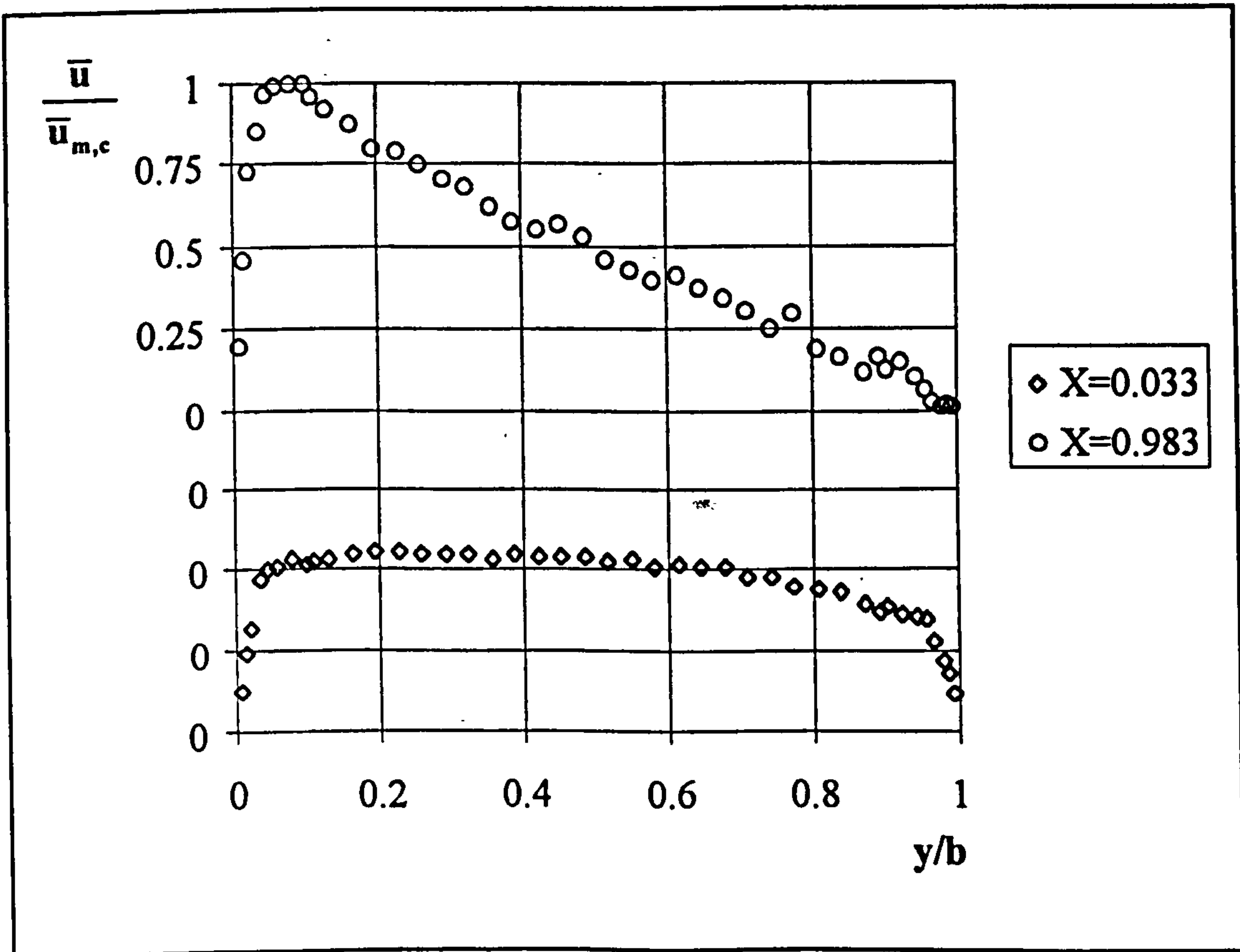


Figure 6.20 UHF turbulent flow mean velocity profiles, Case 1, $q_w = 260$ [w/m²].

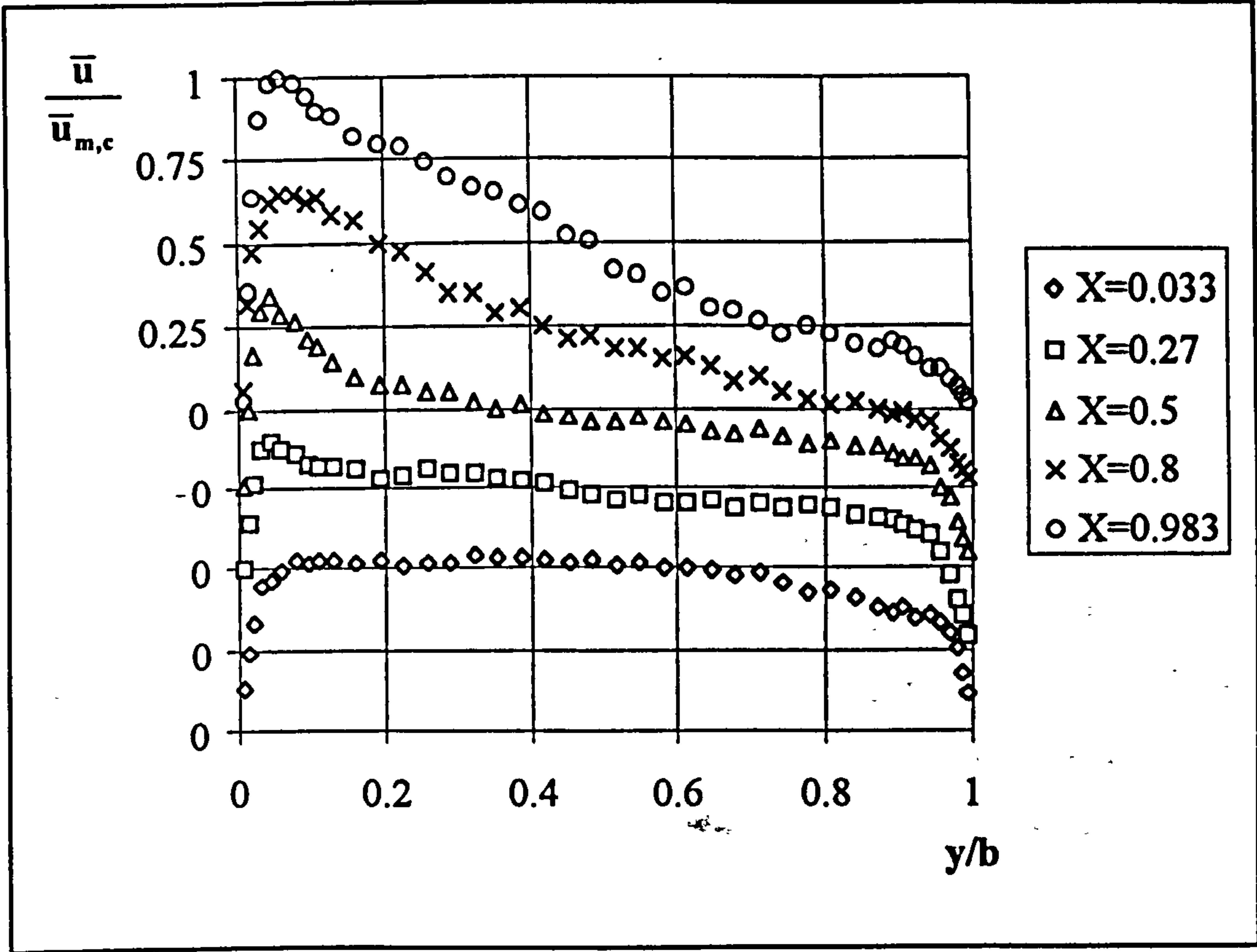


Figure 6.21 UHF turbulent flow mean velocity profiles, Case 2, $q_w = 375 \text{ [w/m}^2\text{]}$.

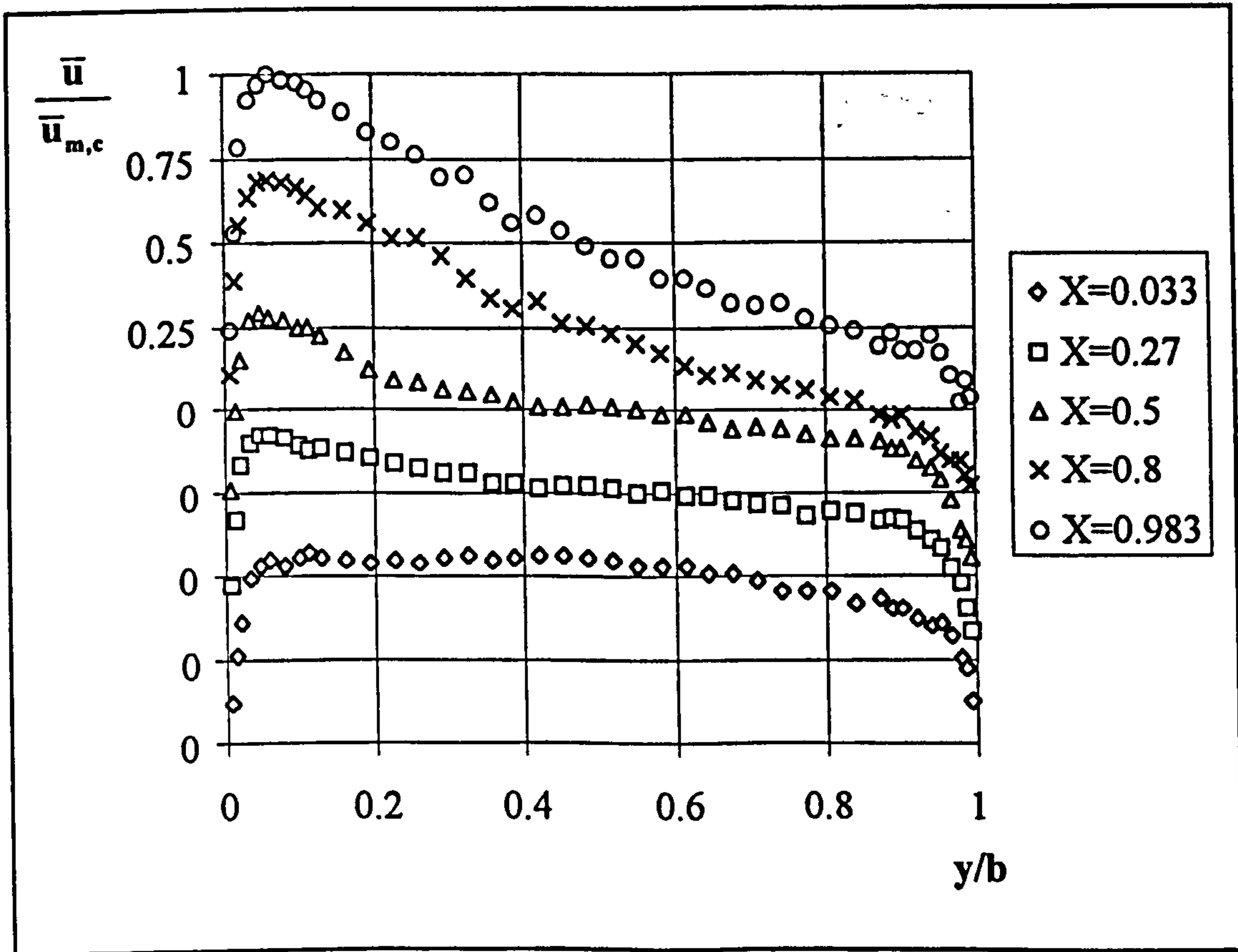


Figure 6.22 UHF turbulent flow mean velocity profiles, Case 3, $q_w = 450 \text{ [w/m}^2\text{]}$.

The variations of the mean velocity profiles are much larger for the UHF cases than for the UWT cases. The argument for these variations is as mentioned previously for the UWT cases.

6.3.2 Mean Temperature Profiles

Temperature profiles near the channel exit ($X=0.983$) for the five cases of the UWT heating mode are presented in Figure 6.23 and those for the UHF heating mode mean temperature profiles in Figures 6.24 to 6.26. Temperatures were non-dimensionalised using equation (6.1) and an axis shift was used when plotting data. The temperature profiles for the UWT indicated that the highest dimensionless temperature for all the cases was 0.75 or less. The profiles also indicate that the front wall is adiabatic. The steepest gradient occurred for Case 1 ($T_w = 60\text{ C}$) and the gradient decreased as the wall temperature increased..

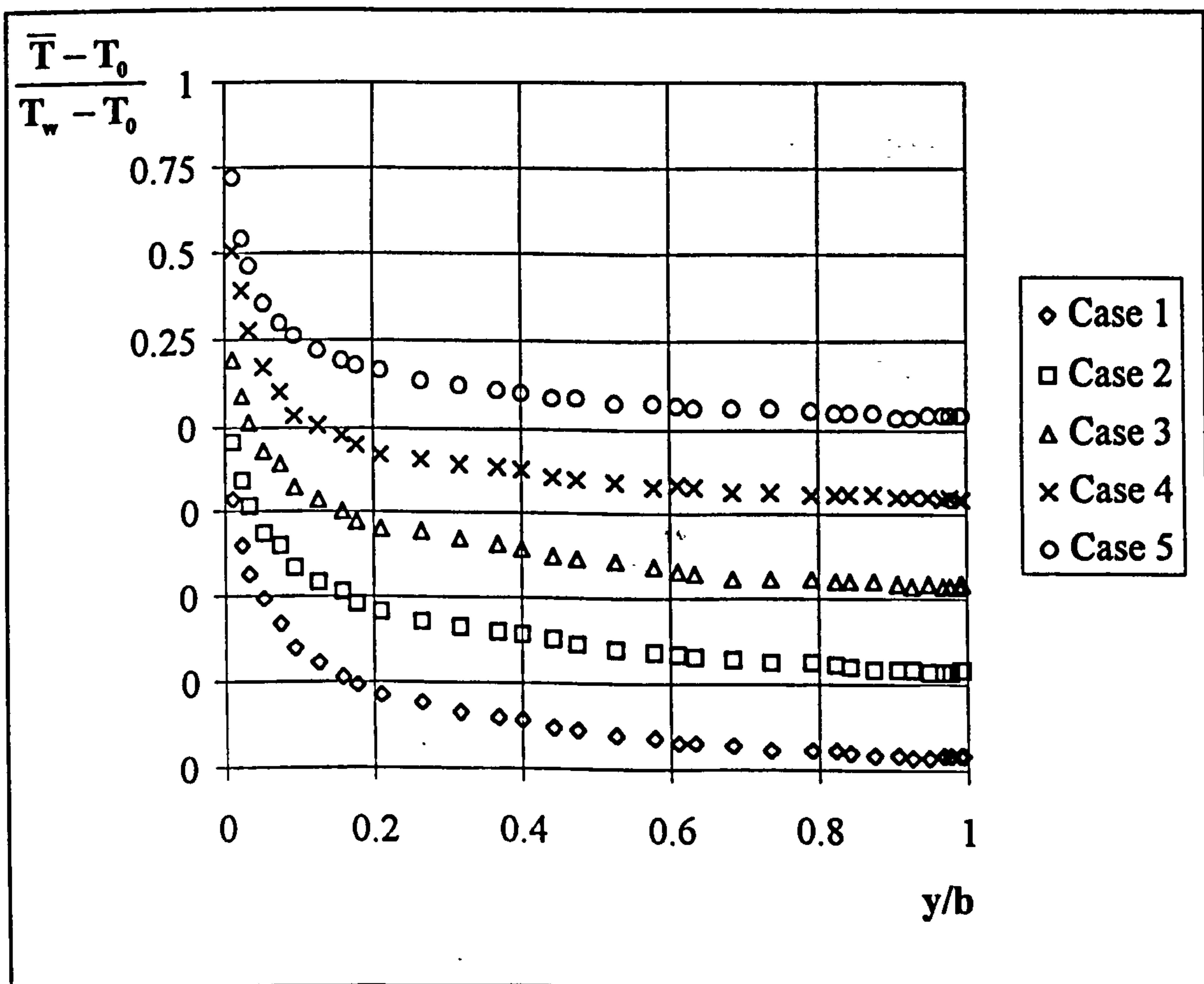


Figure 6.23 UWT turbulent flow mean temperature profiles, at the channel exit.

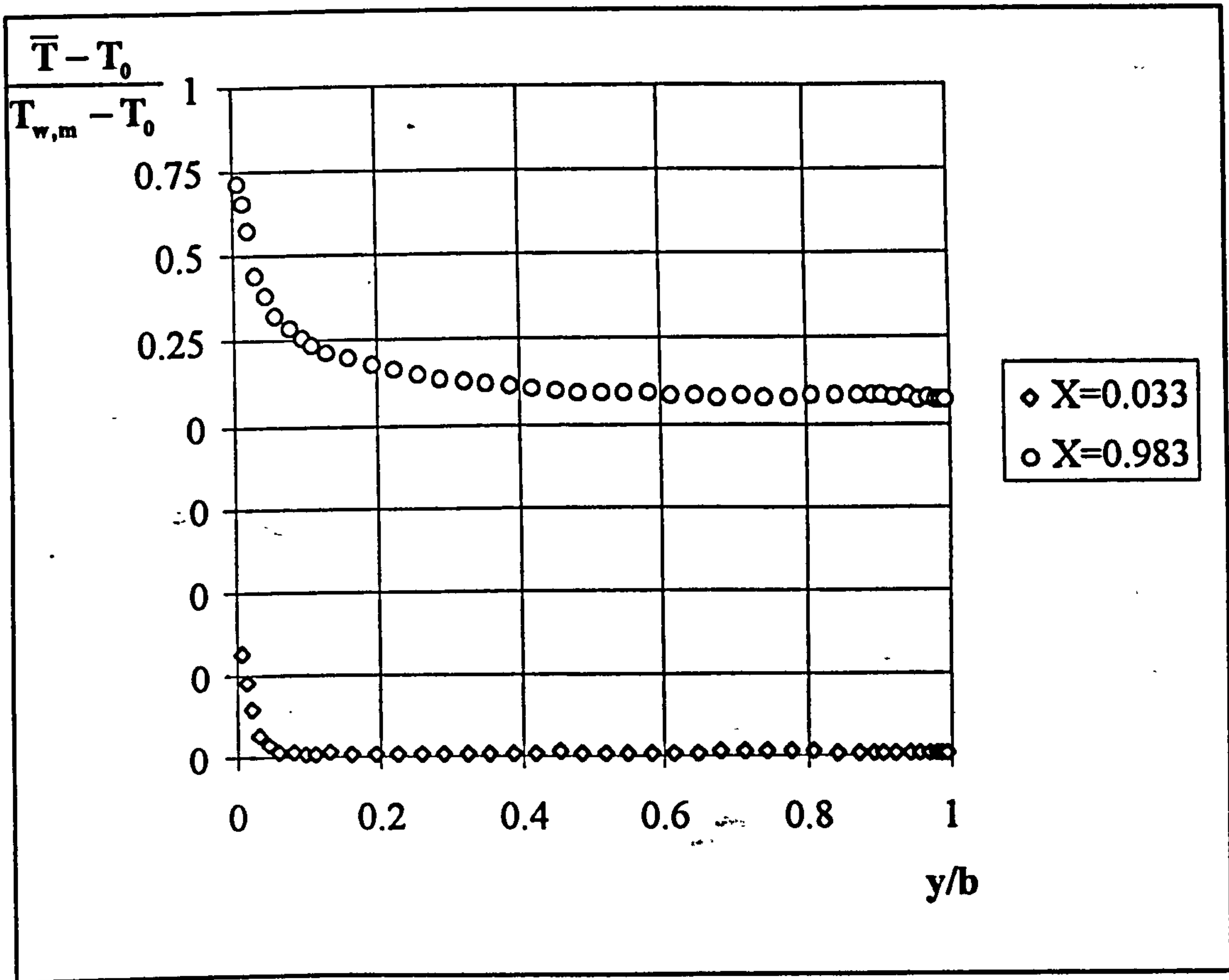


Figure 6.24 UHF turbulent flow mean temperature profiles, Case 1, $q_w = 260$ [w/m^2].

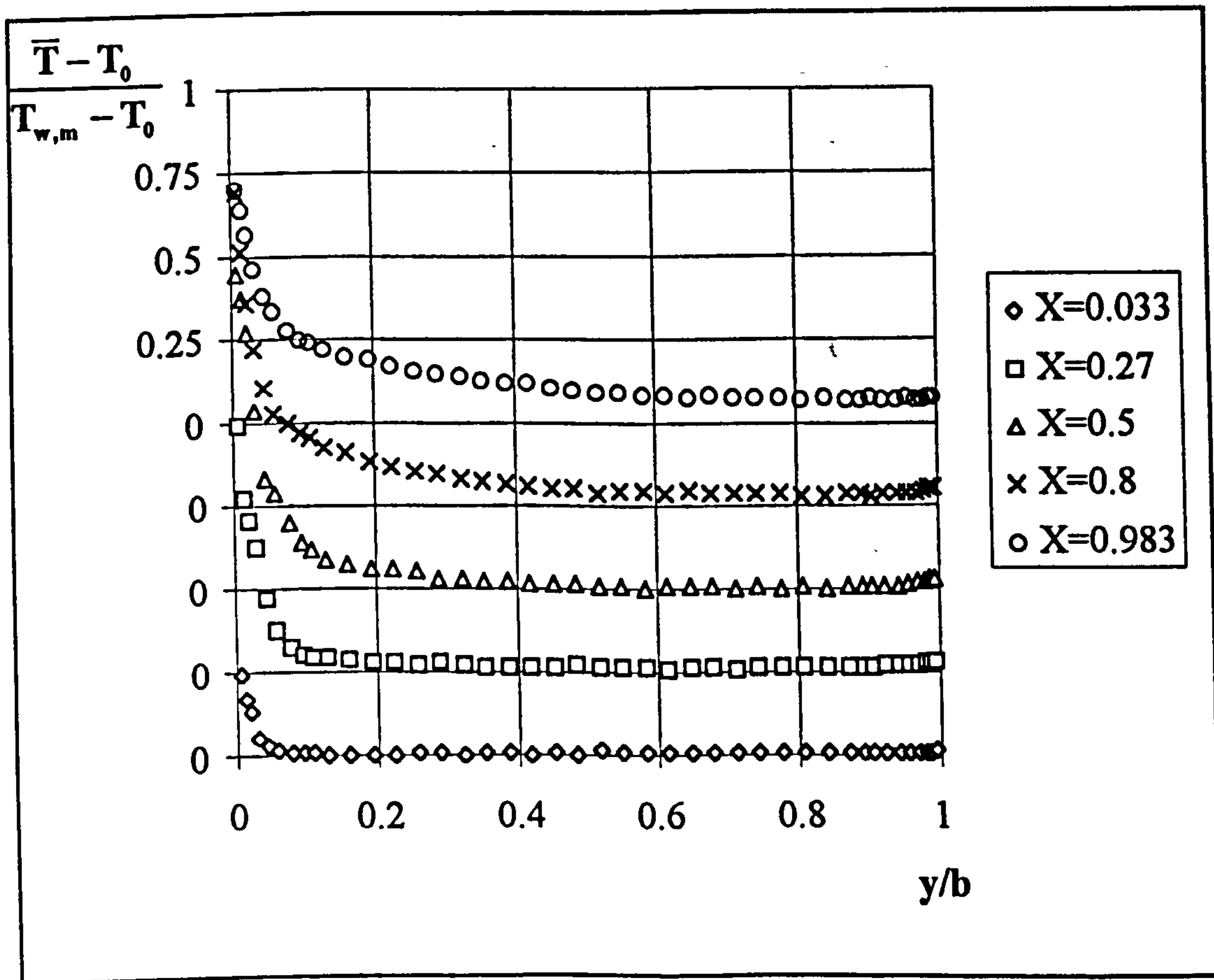


Figure 6.25 UHF turbulent flow mean temperature profiles, Case 2, $q_w = 375$ [w/m^2].

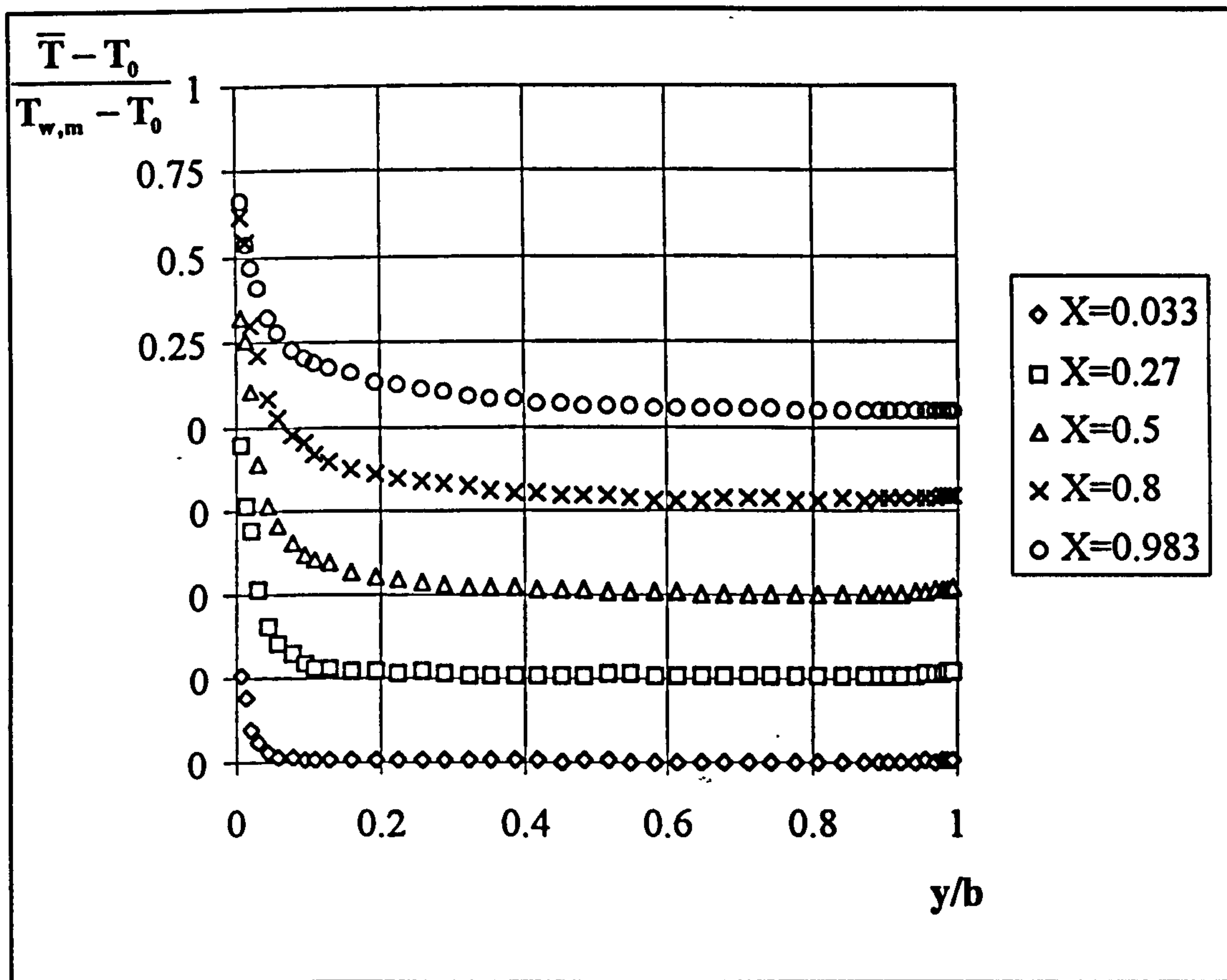


Figure 6.26 UHF turbulent flow mean temperature profiles, Case 3, $q_w = 450$ [w/m^2].

This suggests an increase in turbulent mixing as the wall temperature increases.

The mean velocity profiles for the UHF cases are similar for all the three cases. The thermal boundary layer development along the channel in the flow direction can clearly be seen from the figure. In agreement with the wall temperatures presented in Figure 6.14, the highest temperature occurs on profiles at $X=0.5$ and the second largest on that at $X=0.8$. All of the UHF temperature profiles indicate an essentially adiabatic front wall

6.3.3 Turbulent Kinetic energy and Reynolds Stress Profiles

In order to obtain an insight into the structure of the flow through the channel, turbulent kinetic energy profiles for Case 4 ($T_w = 100$ C) of the UWT heating mode and for Case 3 of the UHF heating mode, together with the normal components of the

Reynolds Stress are presented in Figures 6.27 to 6.35. The cross components of the Reynolds Stress, $(\overline{u'v'})$, for UHF Cases 1, 2 and 3 are given in Figures 6.33 to 6.35. Turbulent kinetic energy profiles and the cross components of Reynolds Stress, $(\overline{u'v'})$, are presented in dimensional form while the normal component of Reynolds Stress are non-dimensionalised using the average of the vertical component of local velocity.

Examination of Figure 6.27, UWT case 4 ($T_w = 100^\circ\text{C}$), shows that the turbulent kinetic energy (k) profile is skewed towards the front wall at the lowest elevation. As the flow develops downstream, some of the k is destroyed. At the third elevation, mid-height of the channel, the k profile possesses two peaks close to the walls but skewed towards the heated wall. At the two uppermost elevations, the k profile becomes almost uniform as the turbulent kinetic energy is distributed across the channel. The profiles of the normal components of Reynolds Stresses, $\sqrt{u'^2}$ and $\sqrt{v'^2}$, for UWT Case 4 are given in Figures 6.28 and 6.29. The figures indicate that $\sqrt{u'^2}$ profiles have a similar character to that of k profiles. The $\sqrt{v'^2}$ profiles are all similar and almost symmetric except for the first elevation which is skewed towards the front (adiabatic) wall. It is also clear from the figures that the highest values of $\sqrt{u'^2}$ and $\sqrt{v'^2}$ are just above 20 and 10 percent respectively of the average of the vertical component of velocity.

The k profiles for UHF Case 3 given in Figure 6.30 look similar to that of the UWT Case 4. However the scatter of the data is larger, especially at the two uppermost elevations, and the peaks are much sharper. The highest values of k measured are slightly larger those for UWT Case 4. The similarity of $\sqrt{u'^2}$ profiles to k profiles can also be observed for UHF cases. As for the $\sqrt{v'^2}$ profiles for UHF Case 3, the profile at the first elevation is skewed towards the front wall, at the second elevation it is almost uniform, at the following two elevations they become skewed towards the heated wall and finally at the uppermost elevation it becomes symmetric. The highest

values of $\sqrt{u'^2}$ and $\sqrt{v'^2}$ for UHF case 3 are as high as 40 and 25 per cent respectively of the vertical component of velocity.

The cross component of Reynolds Stresses ($\overline{u'v'}$), which is the most reliable indicator of turbulence, is recorded for the three cases with the UHF heating mode and presented in Figures 6.33 to 6.35. For Case 1, measurements were performed at two elevations only. As can be seen clearly from the figures there is turbulence near the channel inlet next to the front wall. The depth of the turbulent region is as great as half of the channel width depending upon the wall heat flux. The higher the wall heat flux the greater the depth. Downstream from the channel inlet, some of the turbulence is destroyed and the profile becomes uniform. Further downstream, the level of turbulence starts to increase and the profile becomes skewed towards the heated wall. At the uppermost elevation the level of turbulence reaches its peak and the profile is nearly symmetric with a slight skew towards the heated wall.

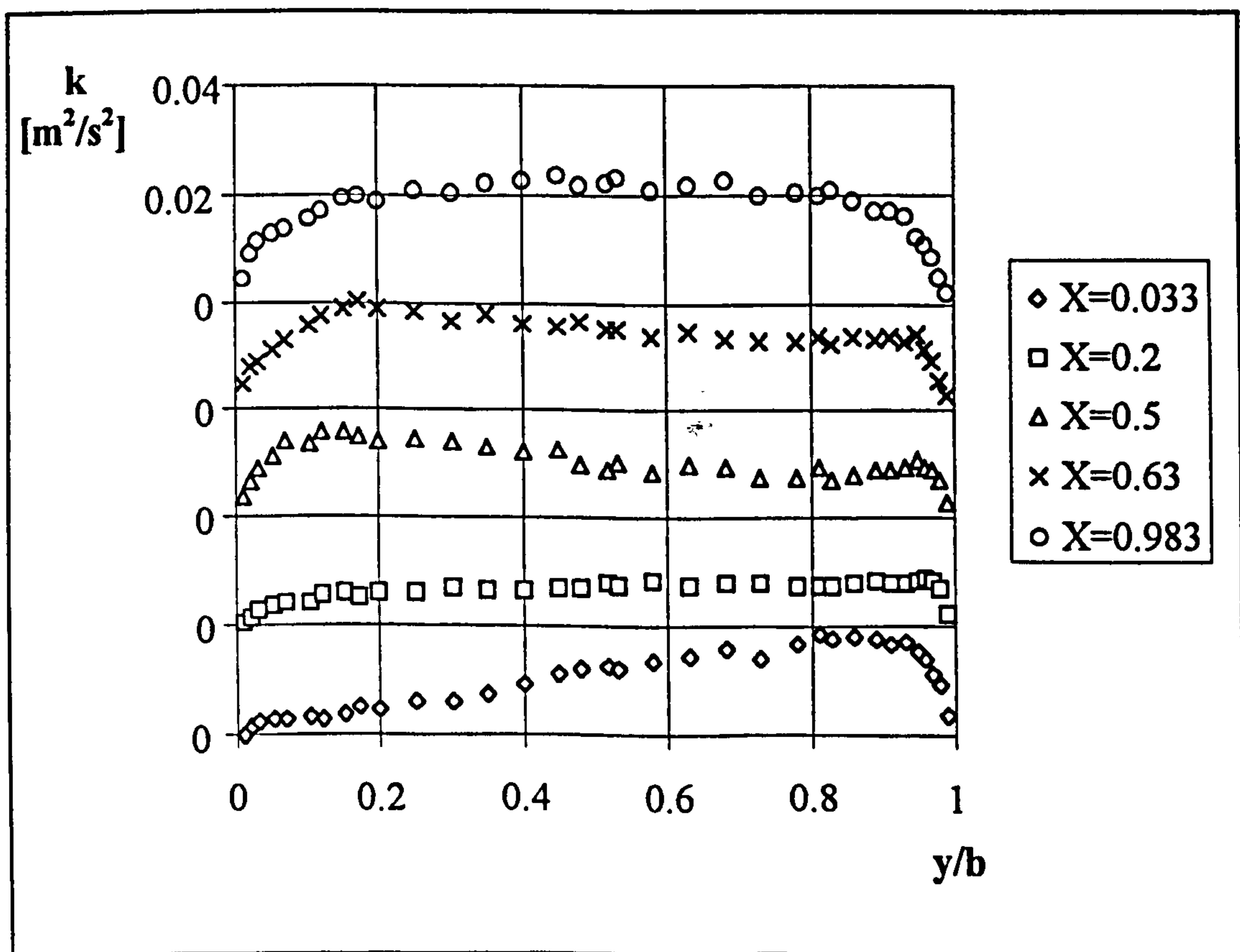


Figure 6.27 UWT turbulent flow turbulent kinetic energy profiles, Case 4.

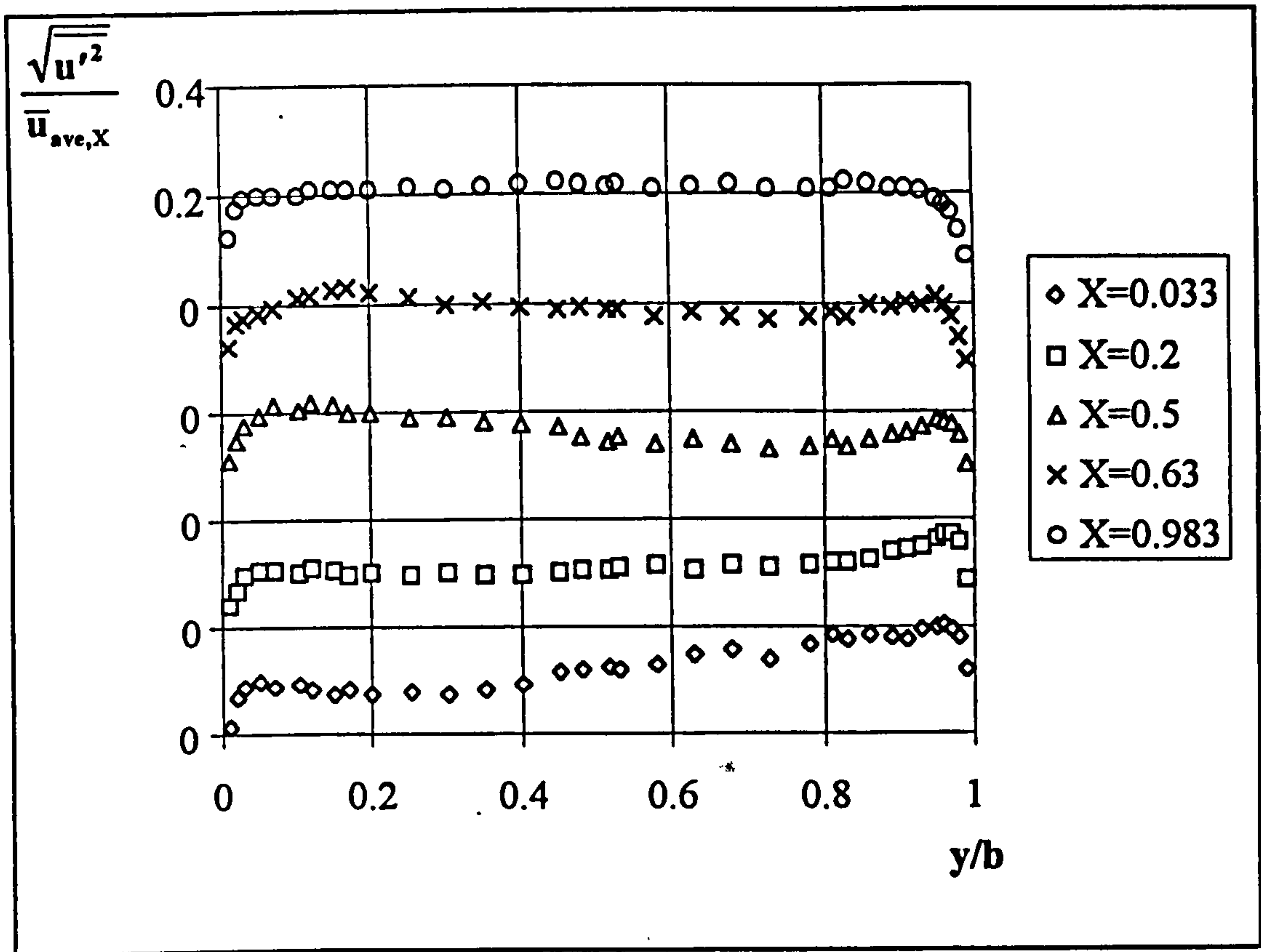


Figure 6.28 UWT turbulent flow x-comp. normal Reynolds stress profiles, Case 4.

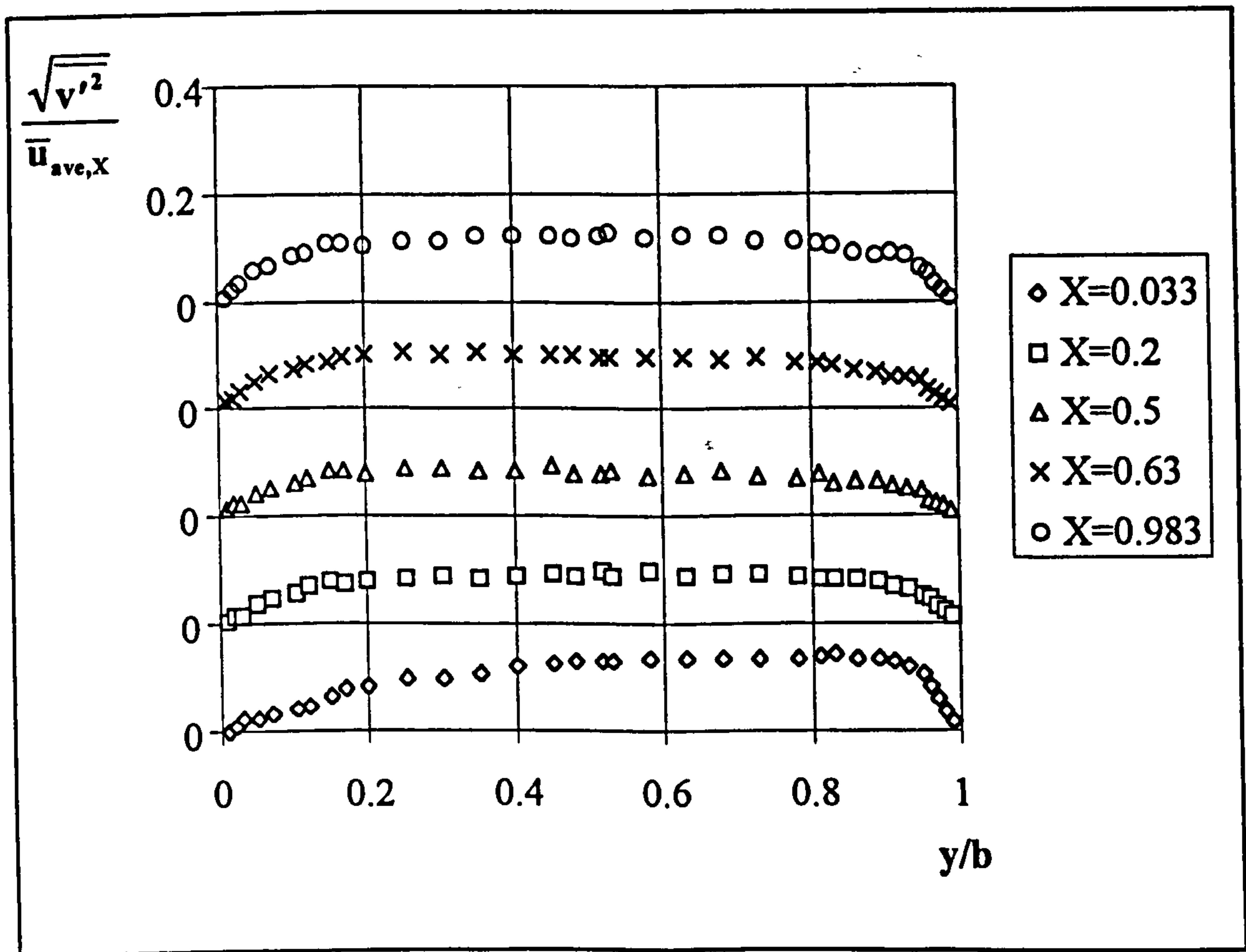


Figure 6.29 UWT turbulent flow y-comp. normal Reynolds stress profiles, Case 4.

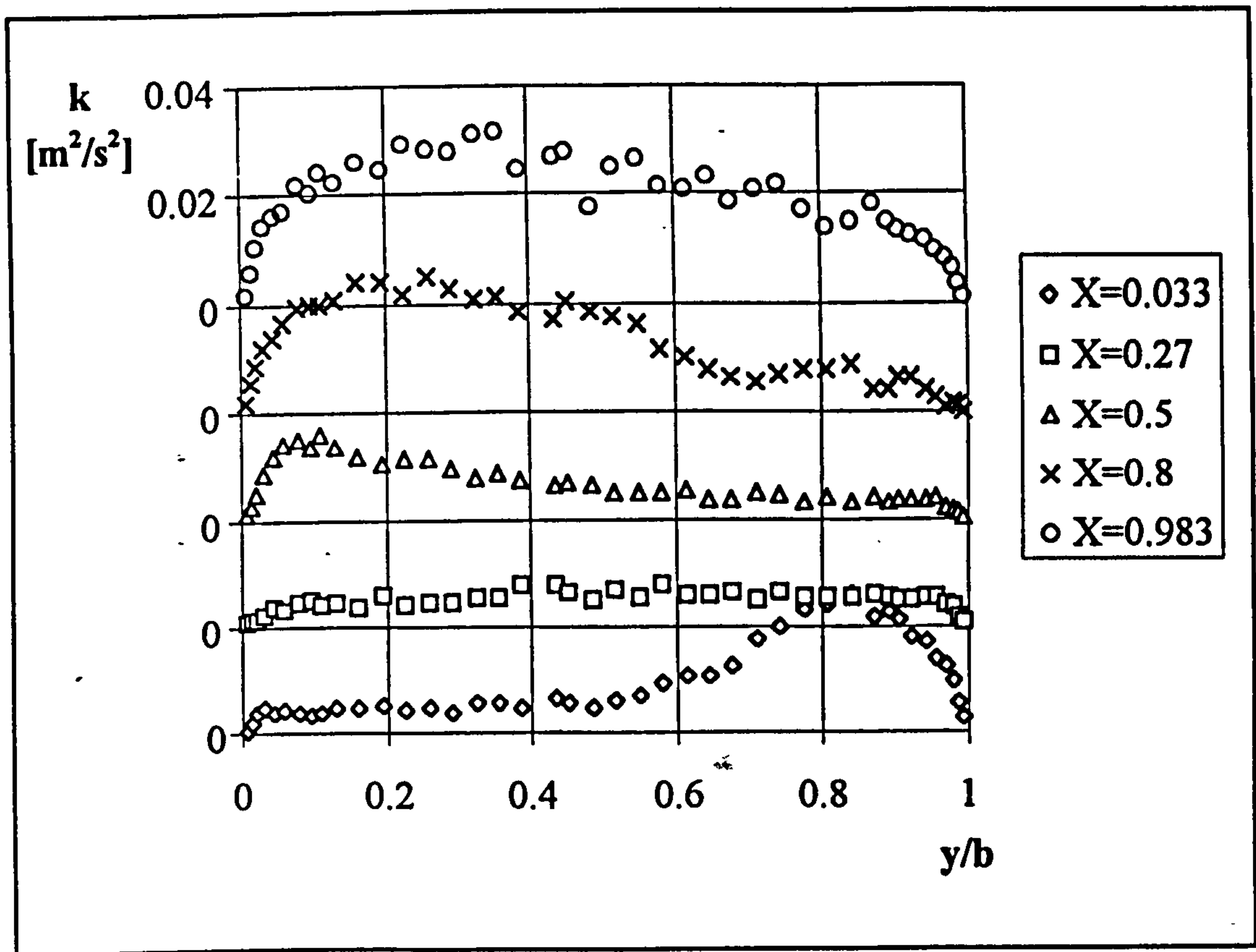


Figure 6.30 UHF turbulent flow turbulent kinetic energy profiles, Case 3.

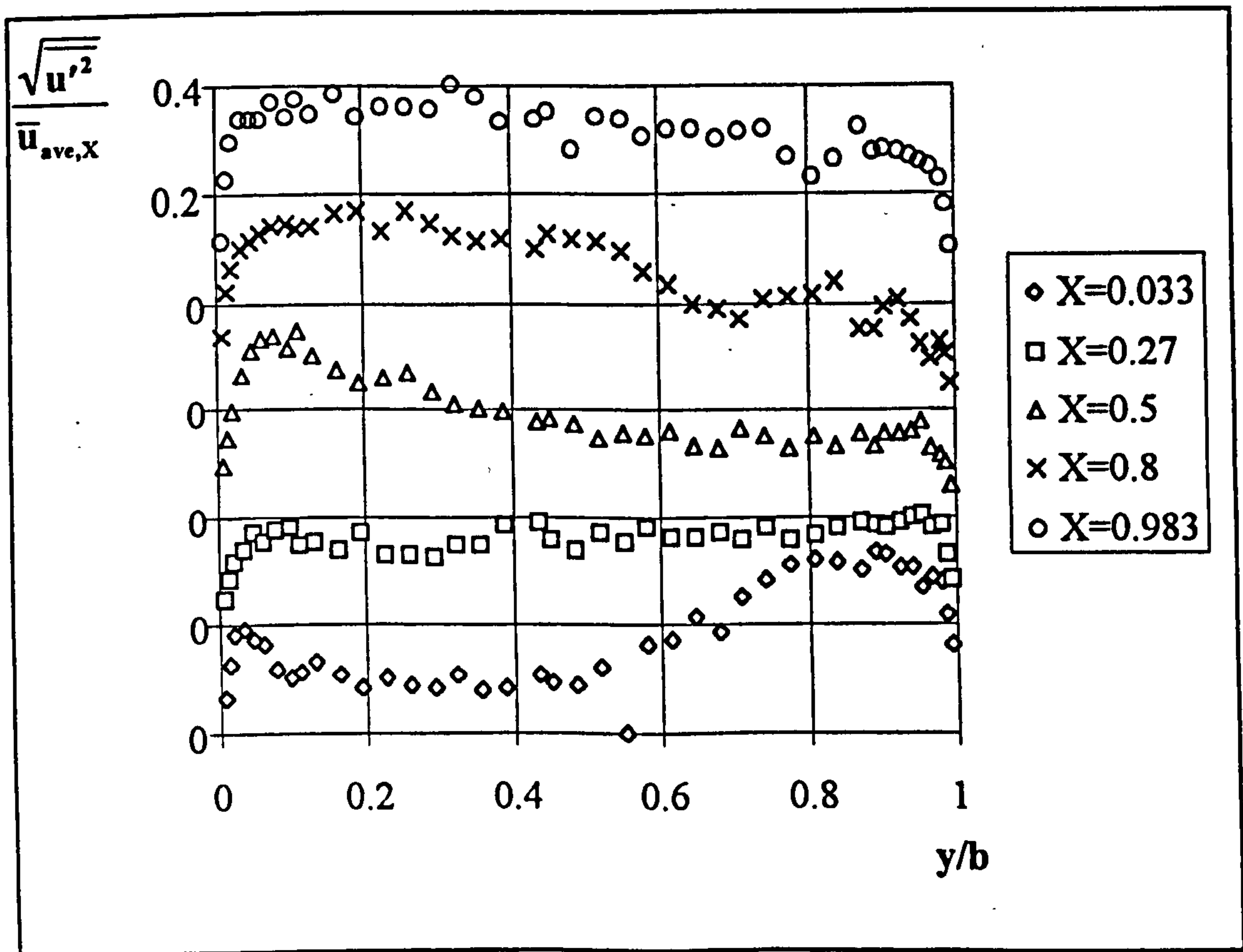


Figure 6.31 UHF turbulent flow x-comp. normal Reynolds stress profiles, Case 3.

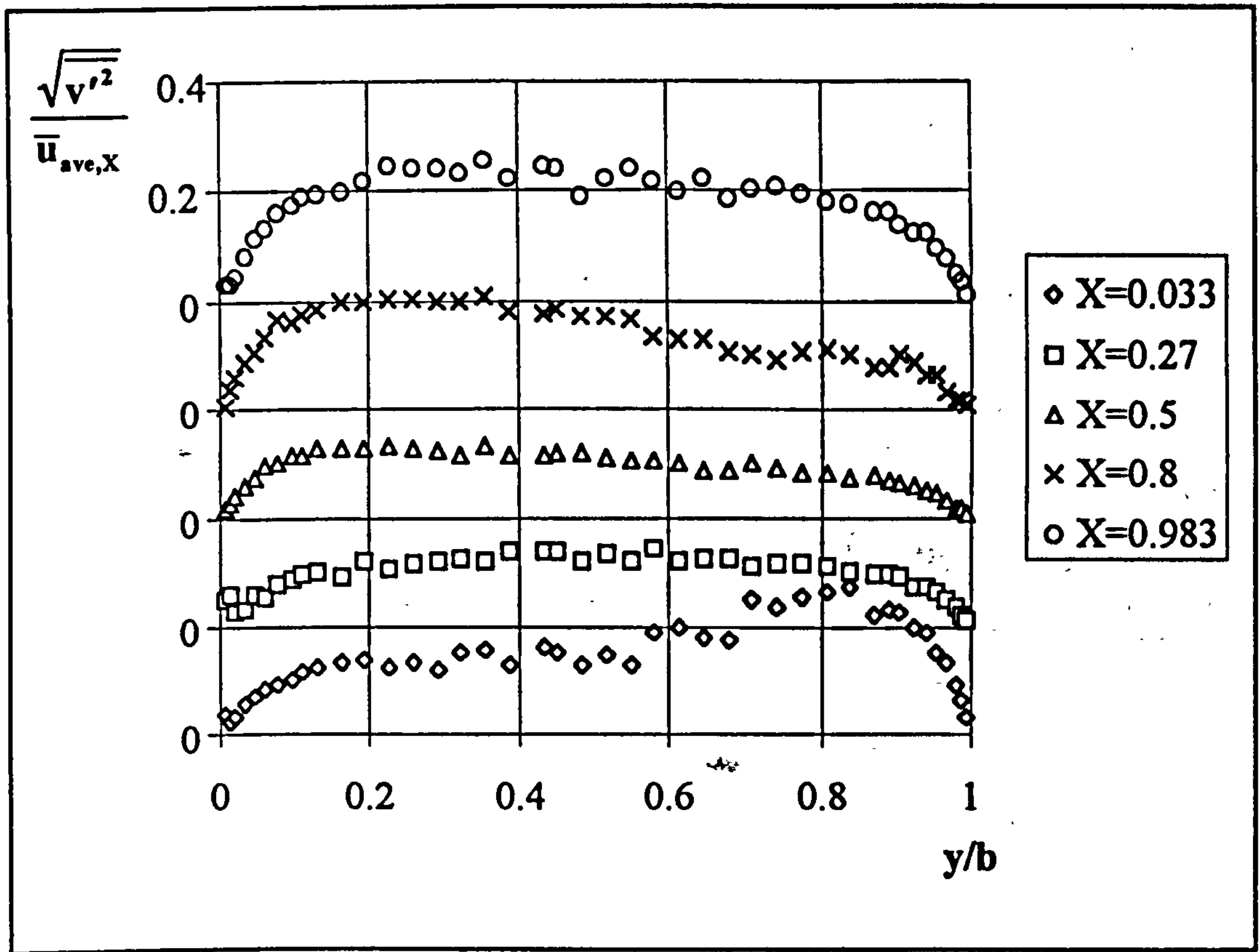


Figure 6.32 UHF turbulent flow y-comp. normal Reynolds stress profiles, Case 3.

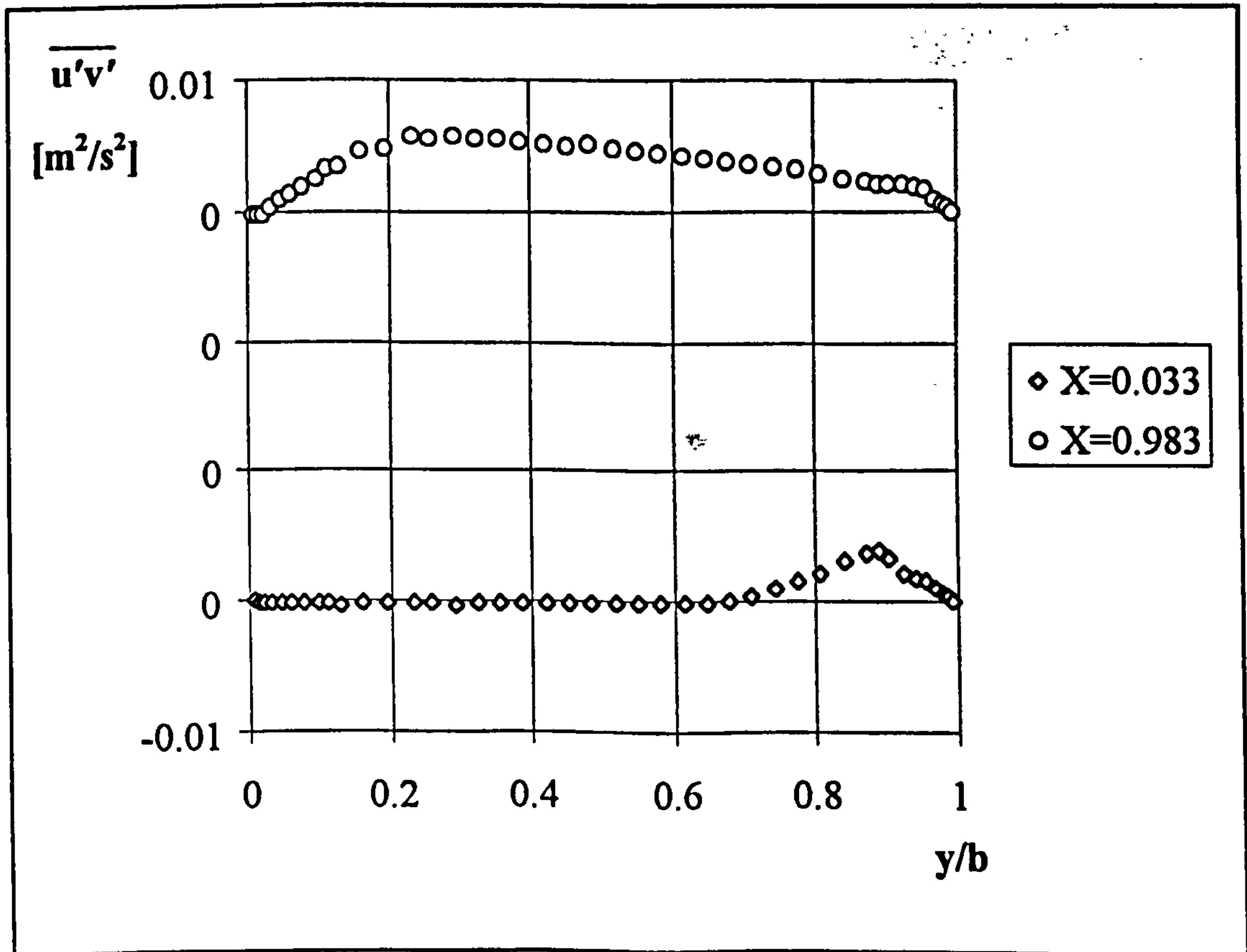


Figure 6.33 UHF turbulent flow Reynolds stress ($\overline{u'v'}$) profiles, Case 1.

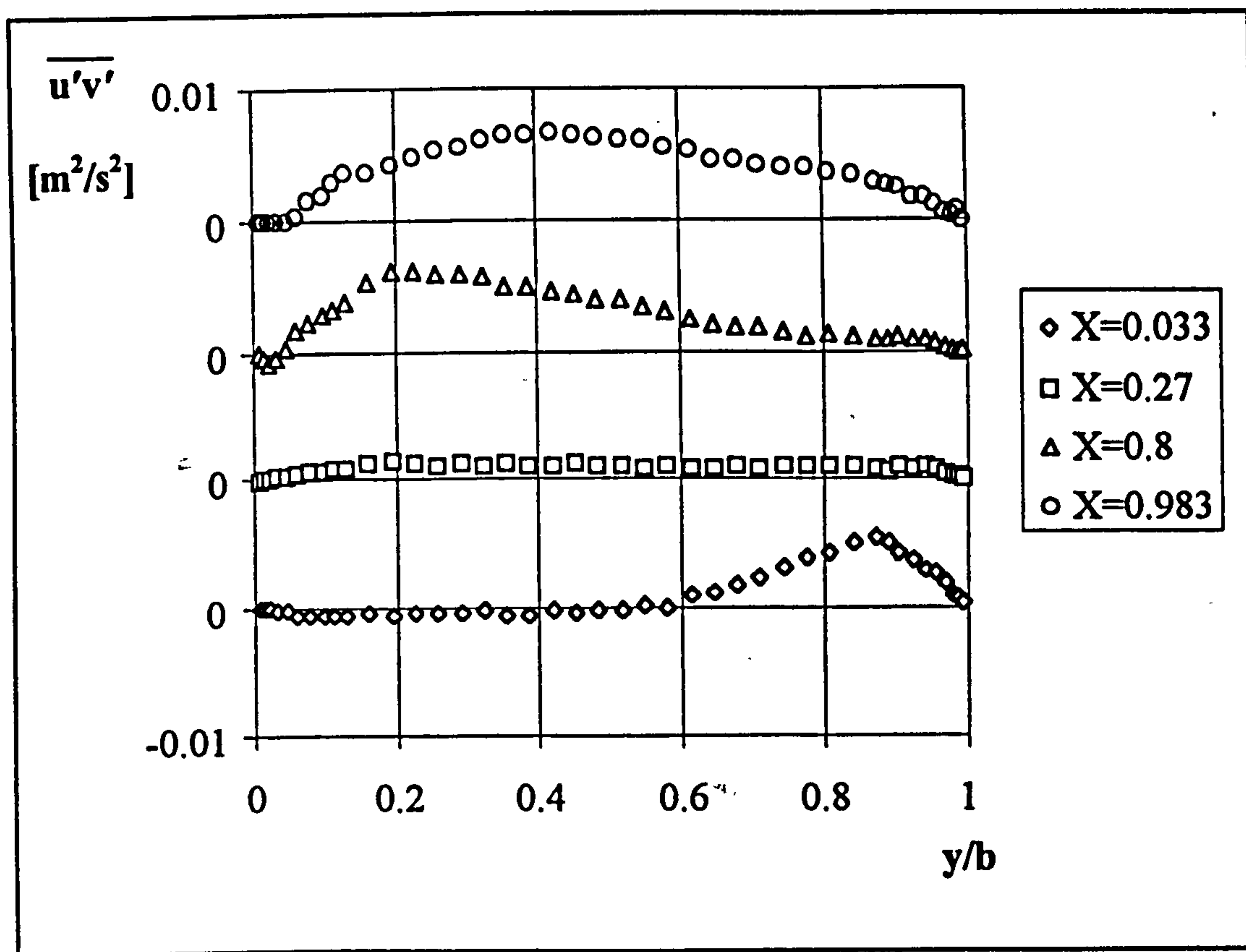


Figure 6.34 UHF turbulent flow Reynolds stress ($\overline{u'v'}$) profiles, Case 2.

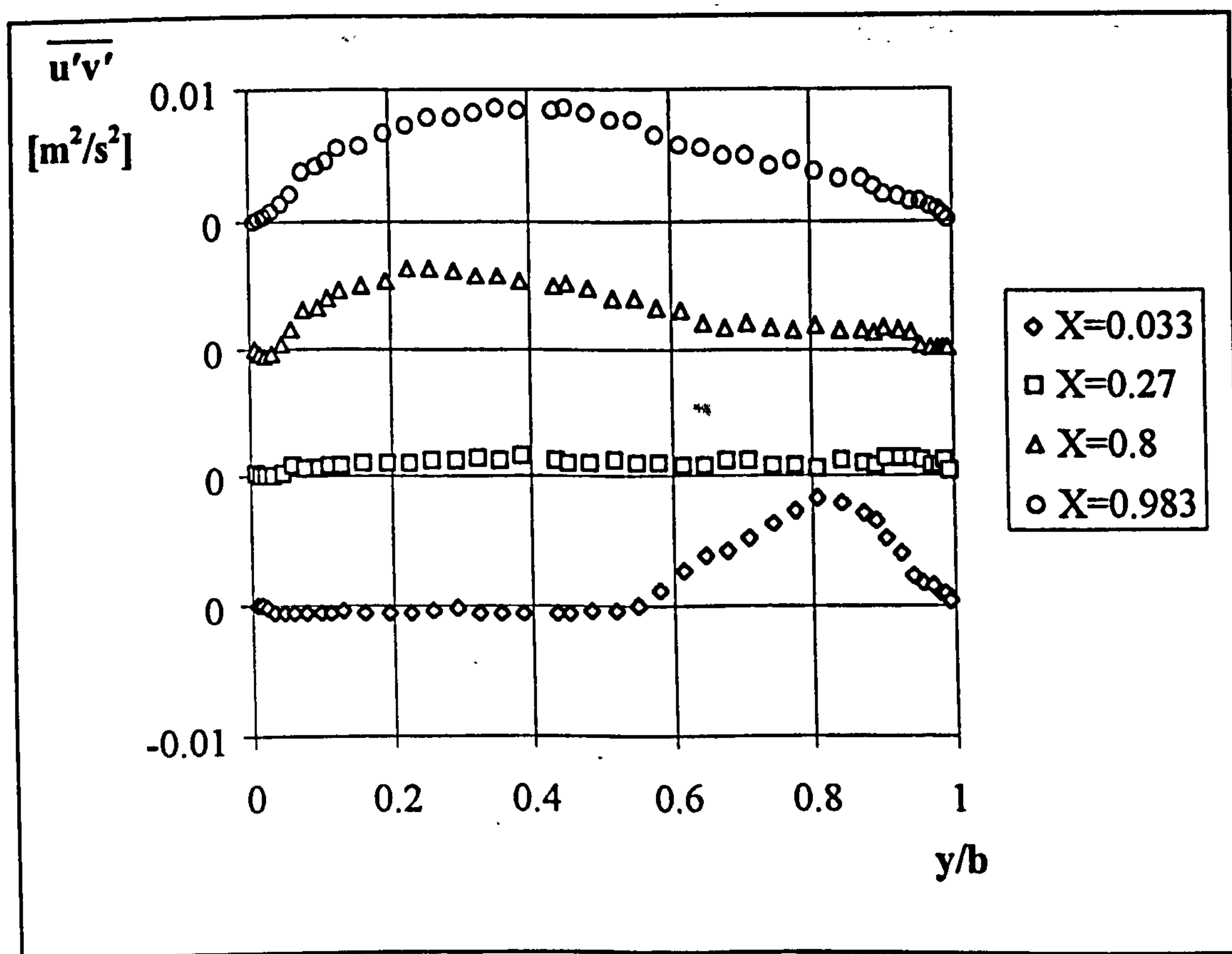


Figure 6.35 UHF turbulent flow Reynolds stress ($\overline{u'v'}$) profiles, Case 3.

Near the heated wall, especially at the two uppermost elevations, the profiles contain some negative and zero values. The negative value can be explained by the entrainment towards the heated wall. However, especially for case 2, there could be some uncertainty in the measurements since it was difficult to achieve seeding close to the wall to make coincident measurements of the two components of velocity.

6.3.4 Time Histories of Velocity and Temperature

Time histories of velocity and temperature have been recorded at all measurement points inside the channel for the UHF cases. Time histories at four points across the channel at the first and the uppermost elevations for Case 1 are presented in Figures 6.36 to 6.53. The points selected for presentation are $y/b=0.097, 0.26, 0.48$ and 0.74 . Velocity and temperature are given in dimensional form and the same scale is used on the graphs for the two elevations considered.

Examination of Figures 6.36 to 6.39 indicates that the velocity at the three points, $y/b=0.097, 0.26, 0.48$, possess the characteristics of laminar flow with a relatively low frequency fluctuation of the mean values. At the fourth point, $y/b=0.74$ (Figure 6.37), multiple frequency fluctuations occur and the vertical and cross components are quite well correlated. This is in agreement with the Reynolds Stress profile given in Figure 6.33. One interesting point is that at $y/b=0.26$ intermittency exists, suggesting intermittently turbulent flow at the channel inlet. This might either be because of some external disturbance or some disturbance arising from the flow itself. Temperature time histories, Figure 6.40 to 6.43, at all points for this elevation do not have any high amplitude fluctuation. They do however contain some bursts of very small amplitude about the mean. This is as expected since none of the points lie in the developing thermal boundary layer.

At the uppermost elevation, the velocity time histories at all points across the channel, Figures 6.44 to 6.47, exhibit the characteristics of a turbulent flow with multiple high

frequency high amplitude fluctuations, as high as 50 % of the mean for u . The correlation

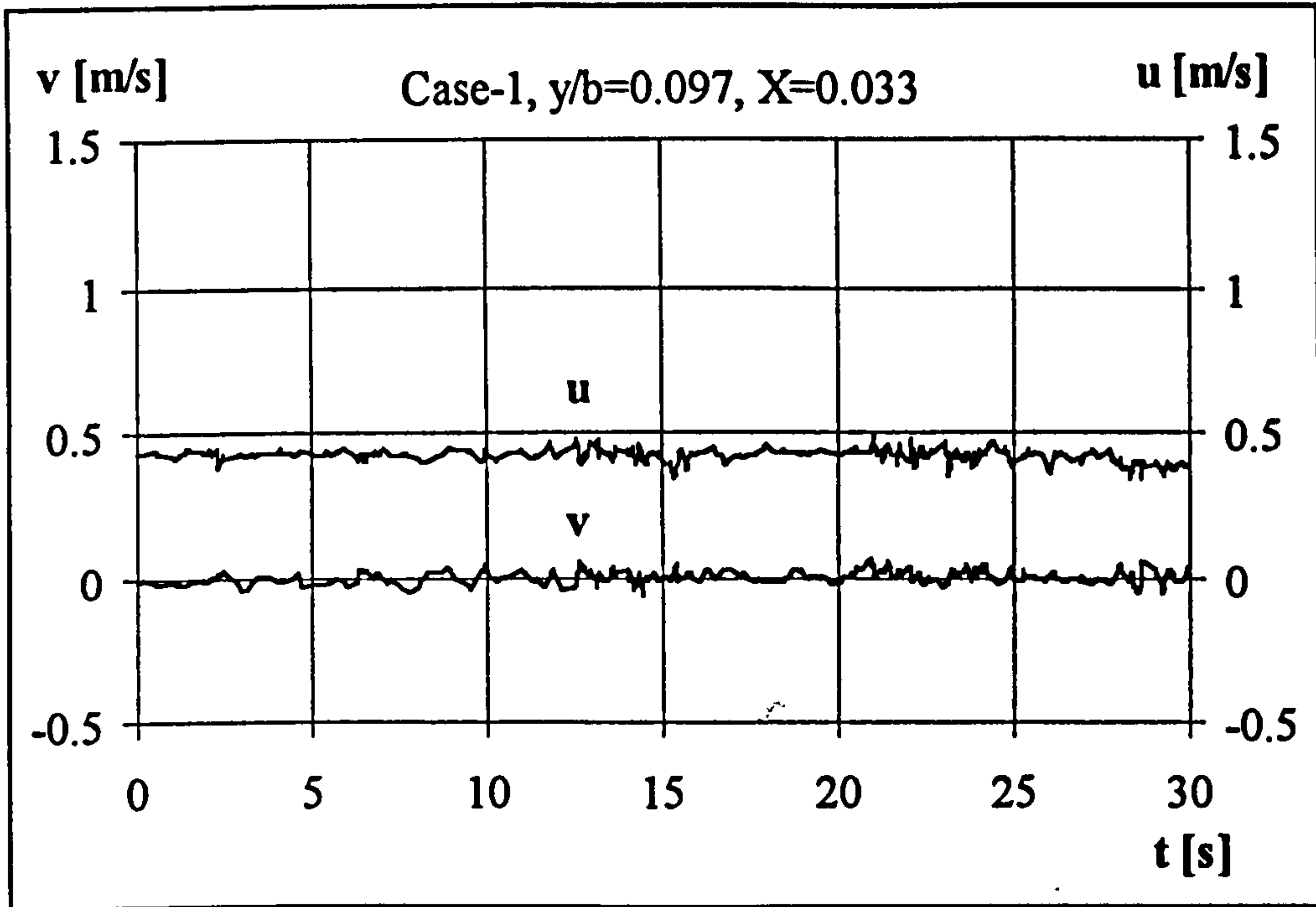


Figure 6.36 Time history of velocity, Case 1, $X=0.033$.

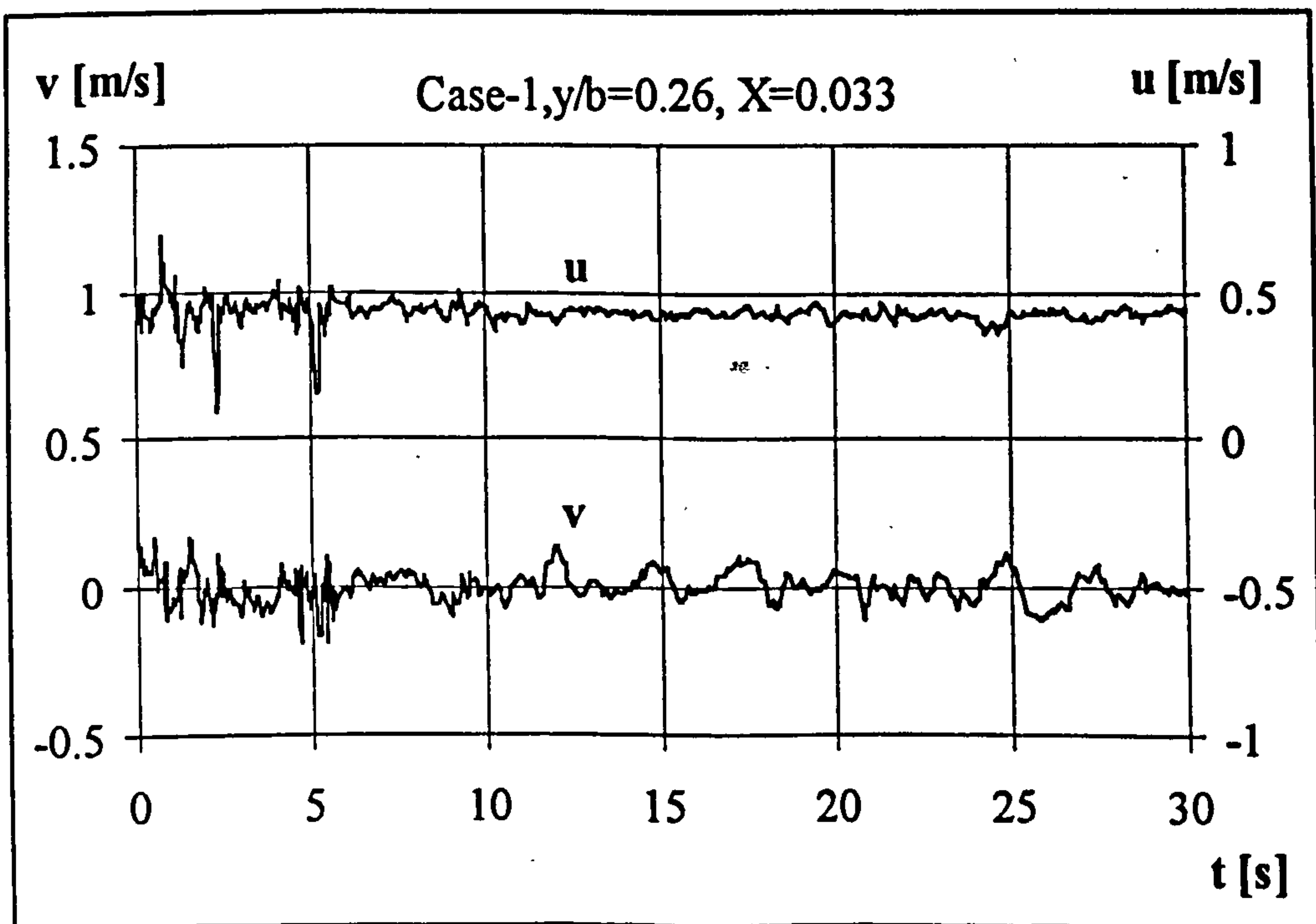


Figure 6.37 Time history of velocity, Case 1, $X=0.033$.

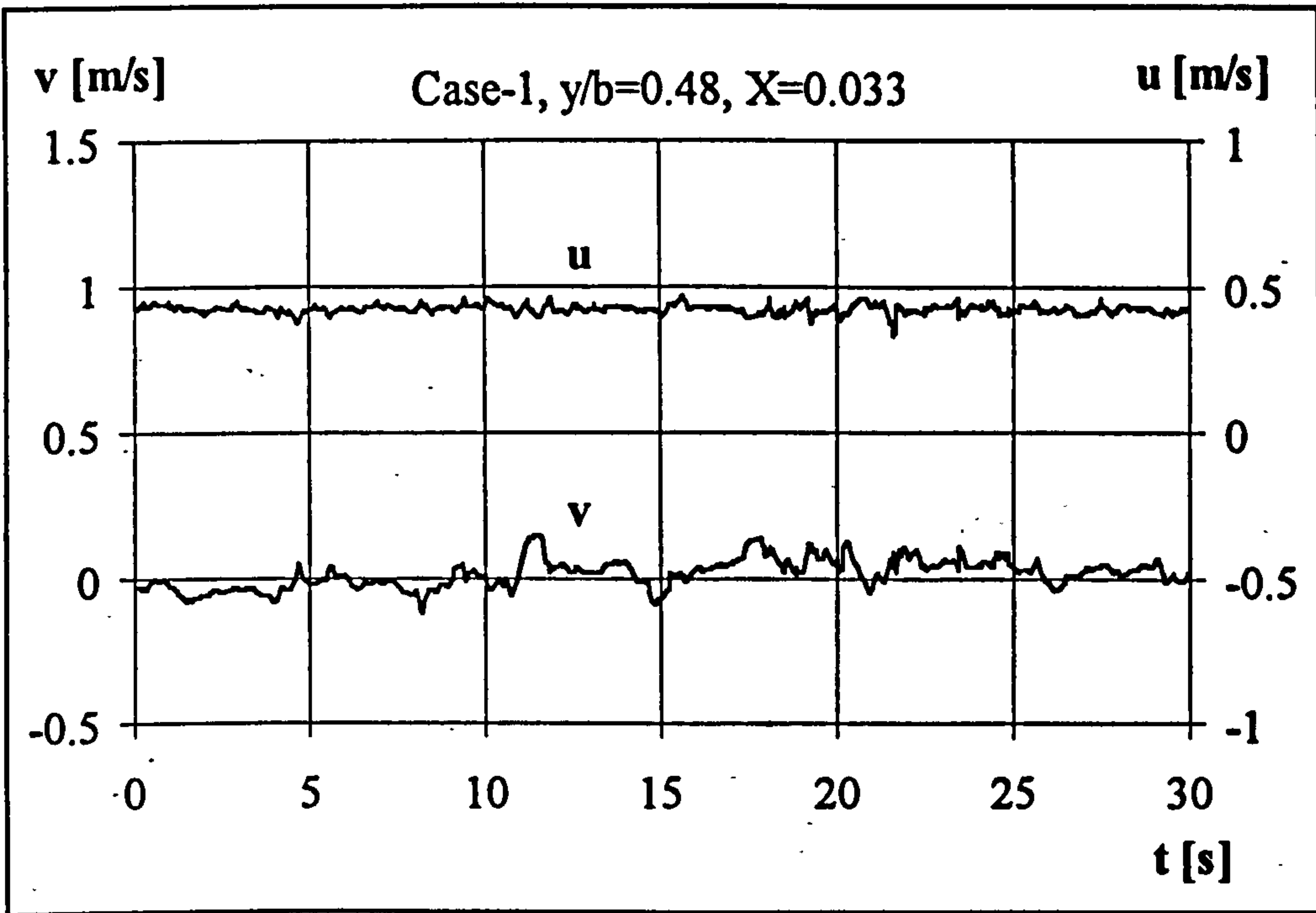


Figure 6.38 Time history of velocity, Case 1, $X=0.033$.

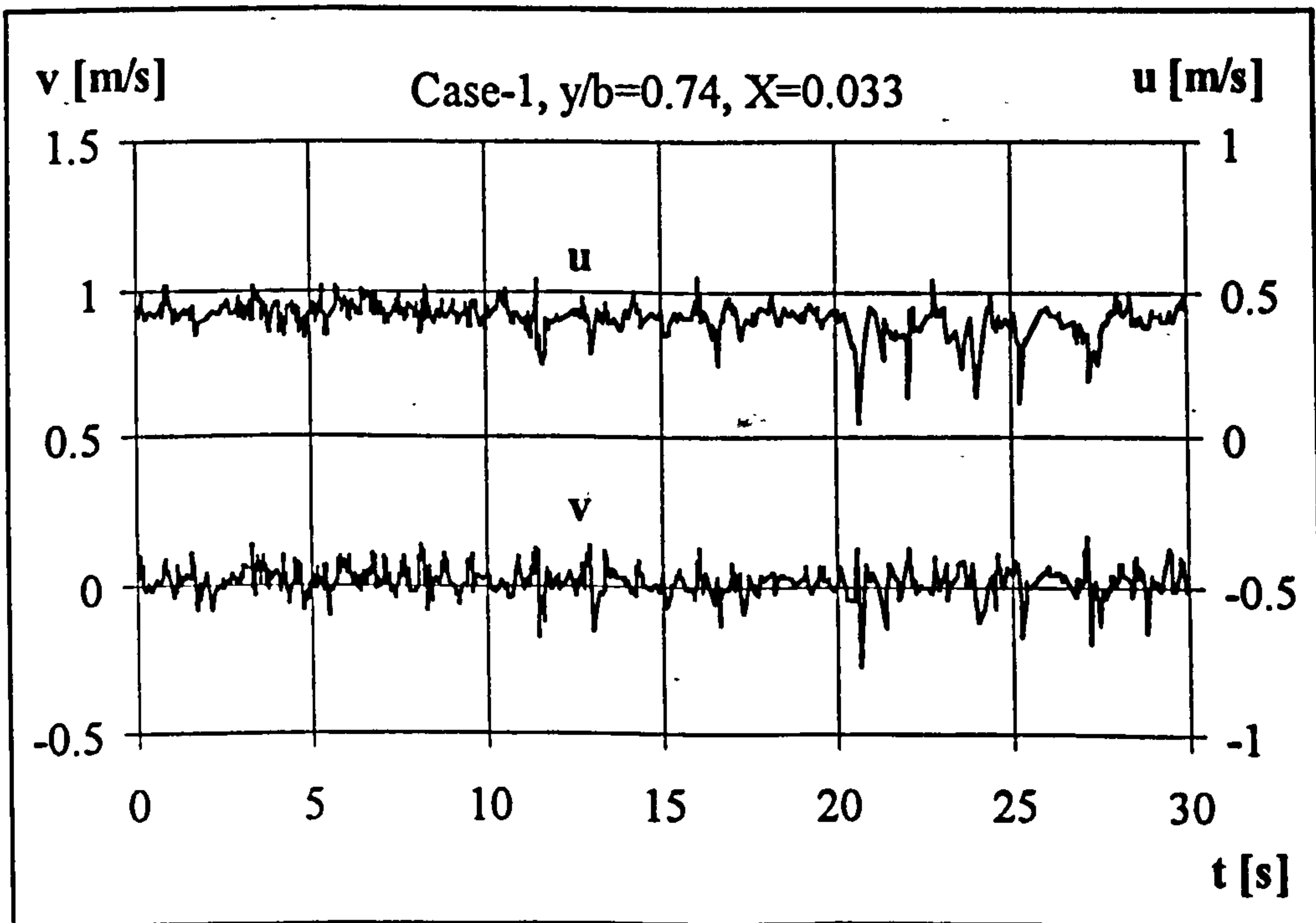


Figure 6.39 Time history of velocity, Case 1, $X=0.033$.

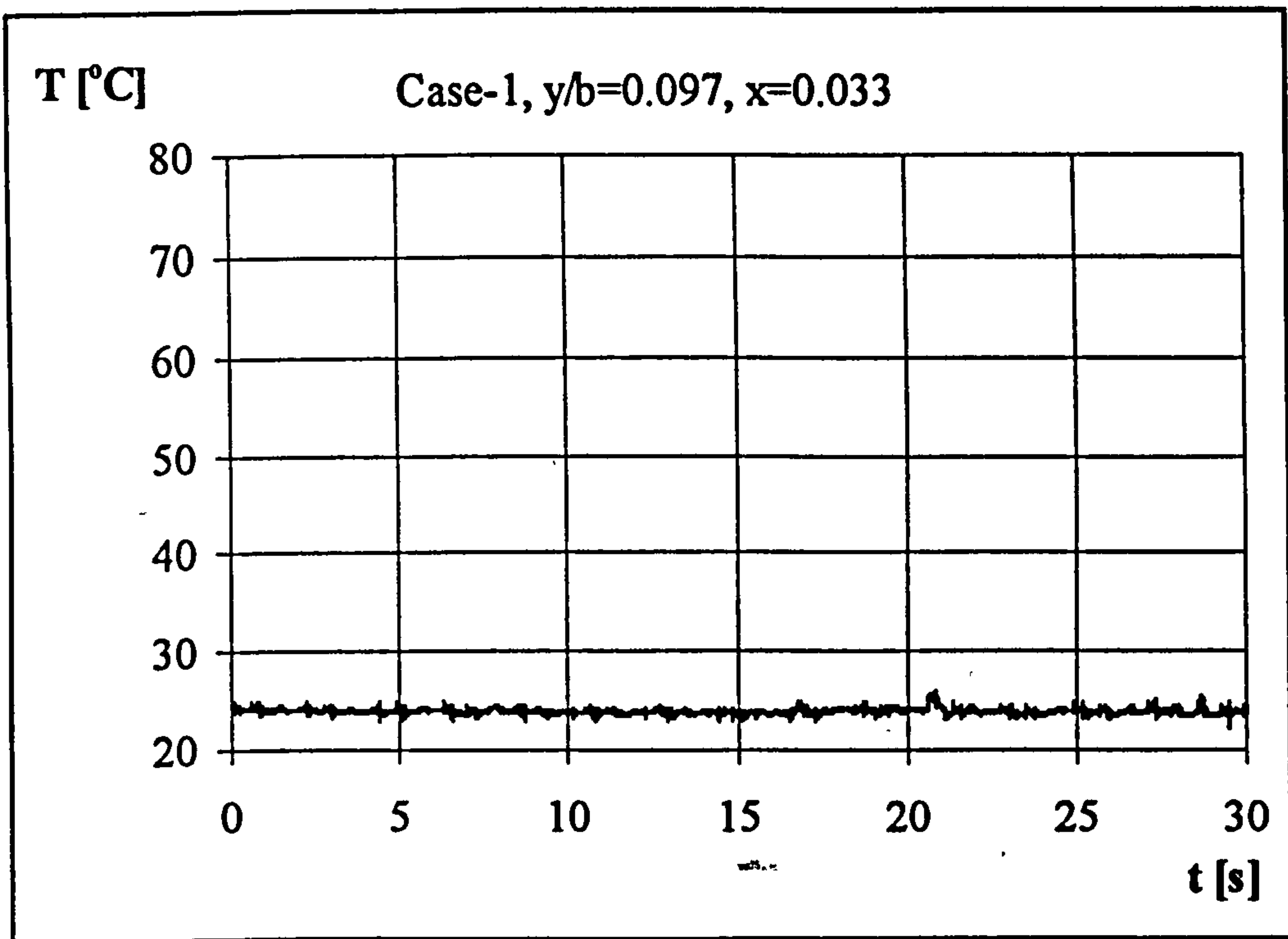


Figure 6.40 Time history of temperature, Case 1, $X=0.033$.

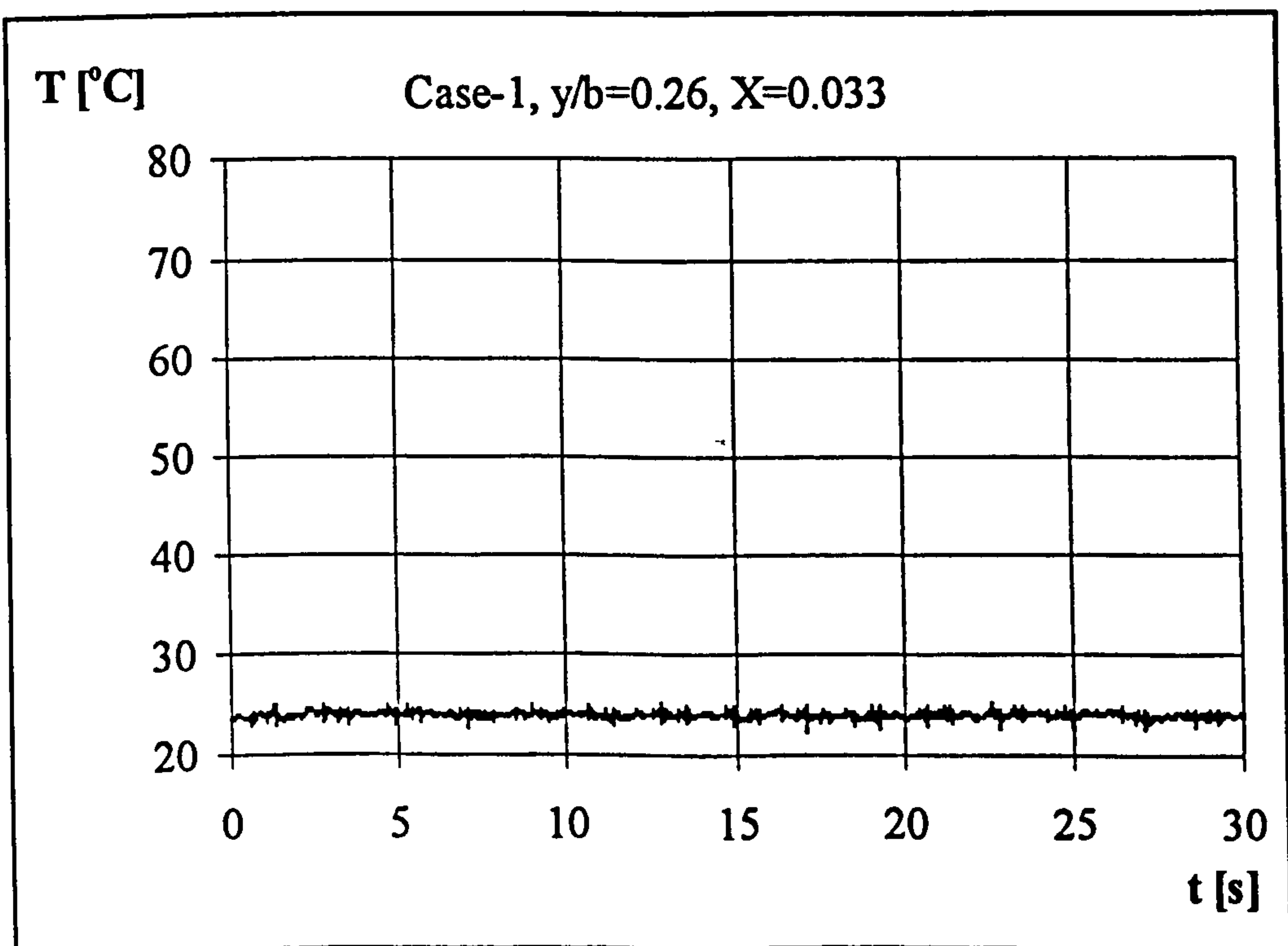


Figure 6.41 Time history of temperature, Case 1, $X=0.033$.

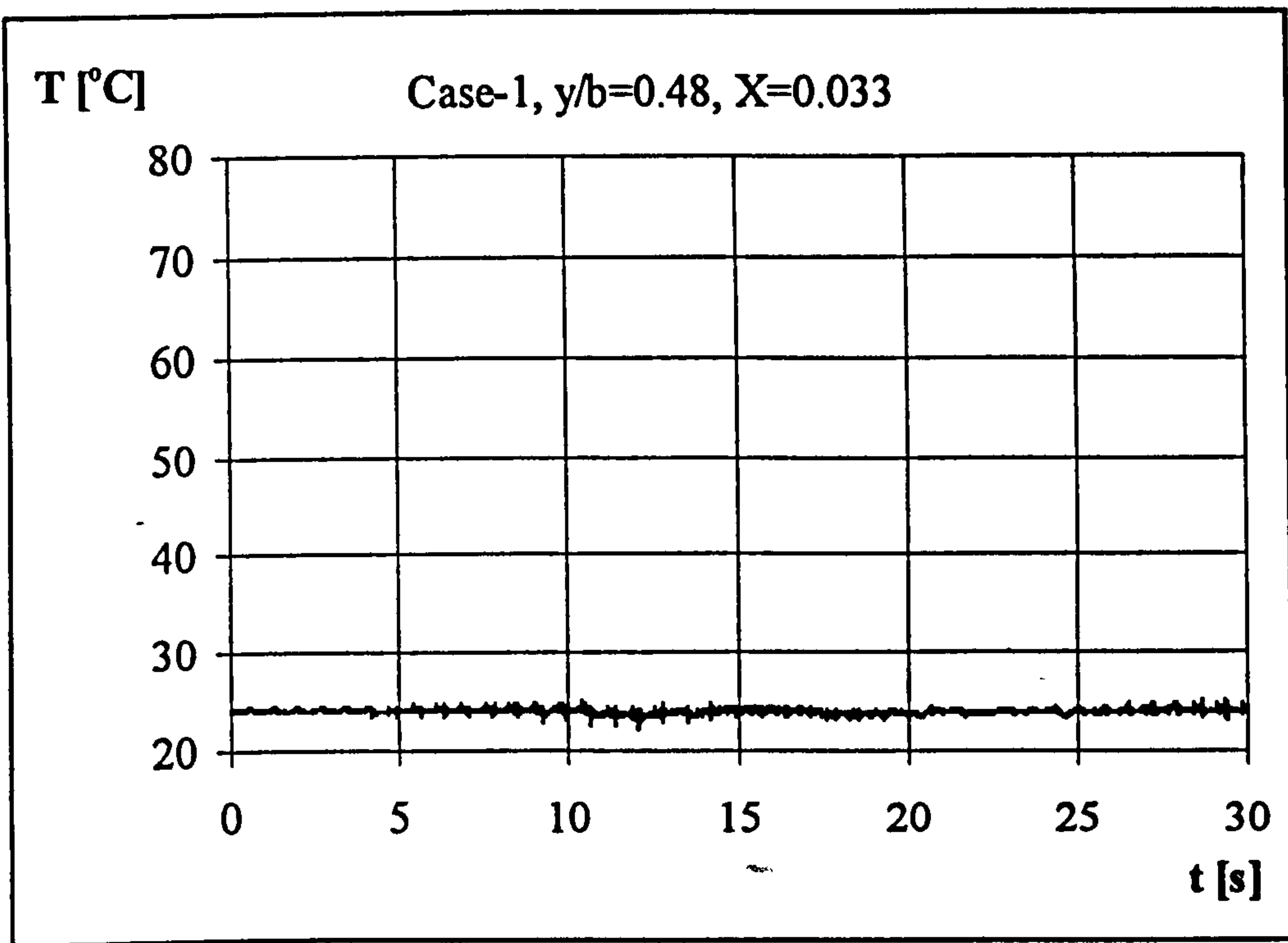


Figure 6.42 Time history of temperature, Case 1, $X=0.033$.

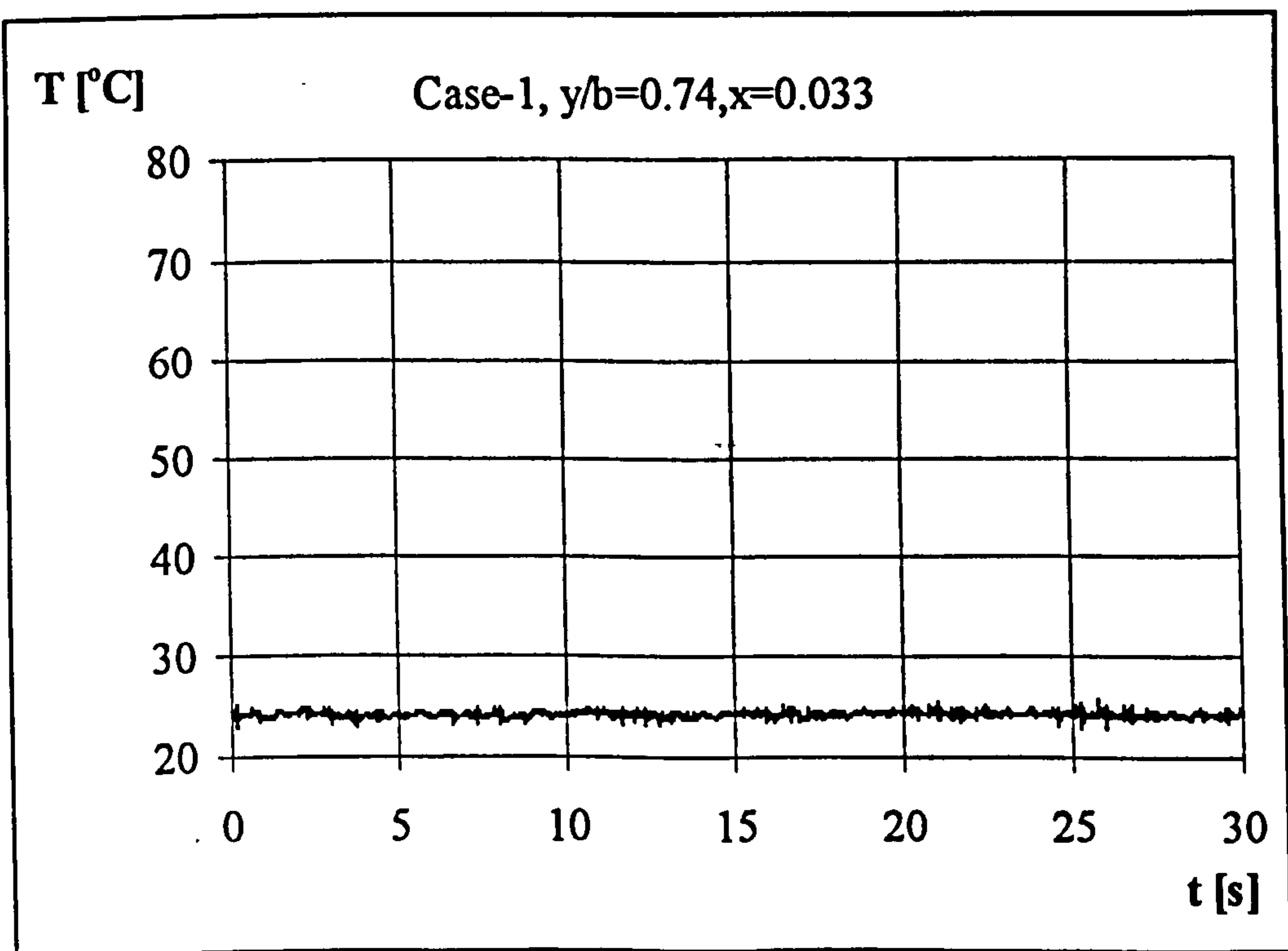


Figure 6.43 Time history of temperature, Case 1, $X=0.033$.

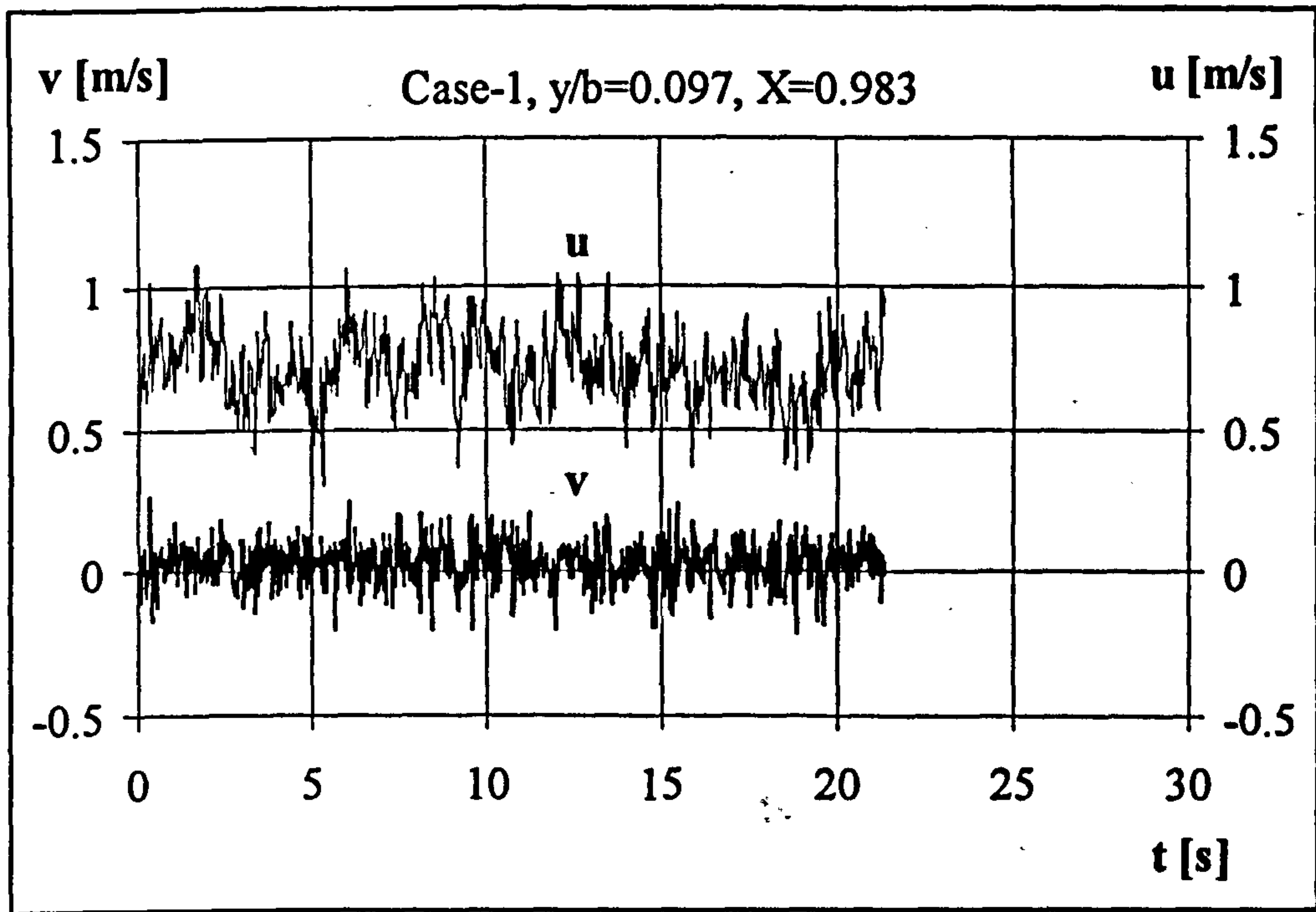


Figure 6.44 Time history of velocity, Case 1, $X=0.983$.

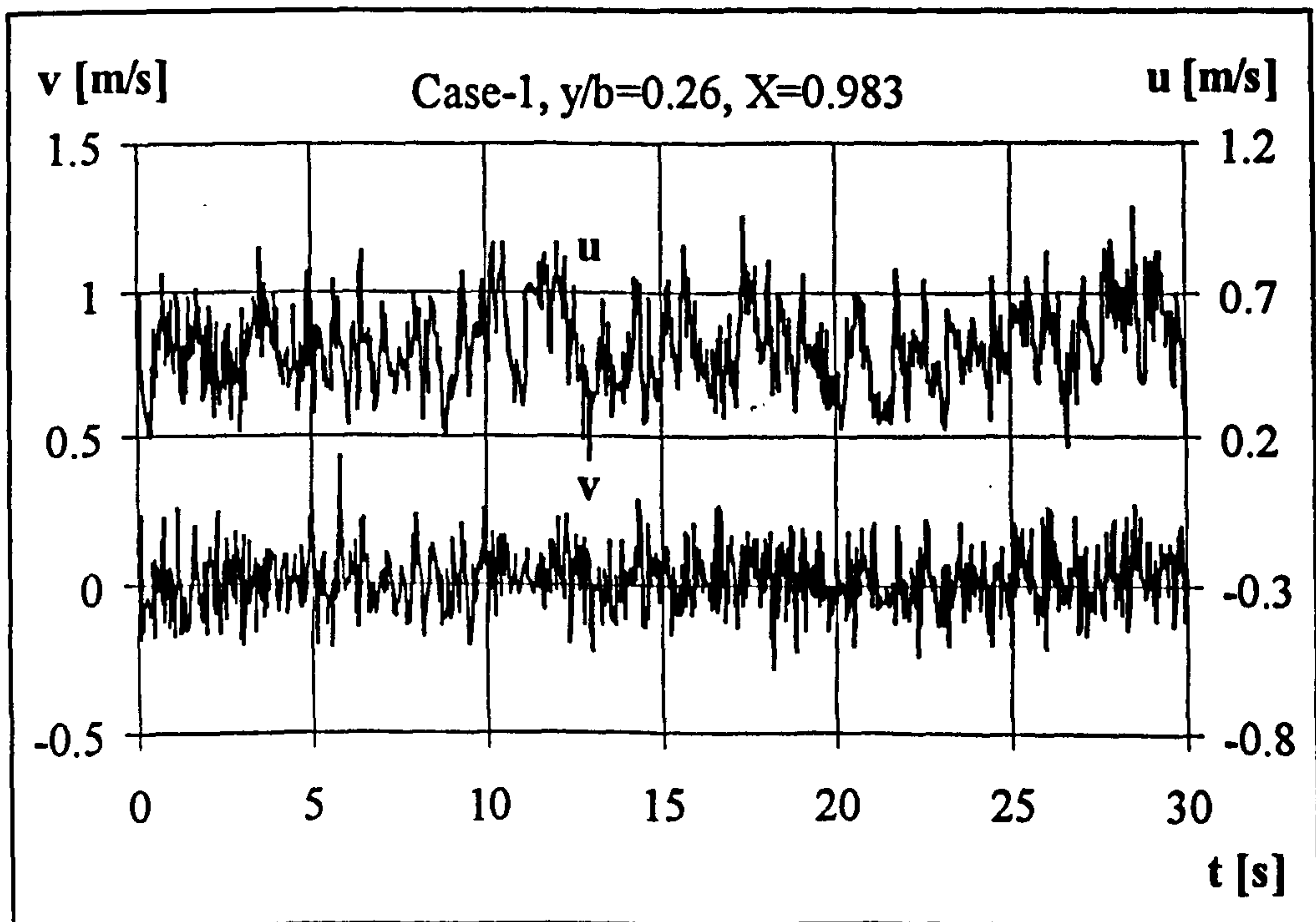


Figure 6.45 Time history of velocity, Case 1, $X=0.983$.

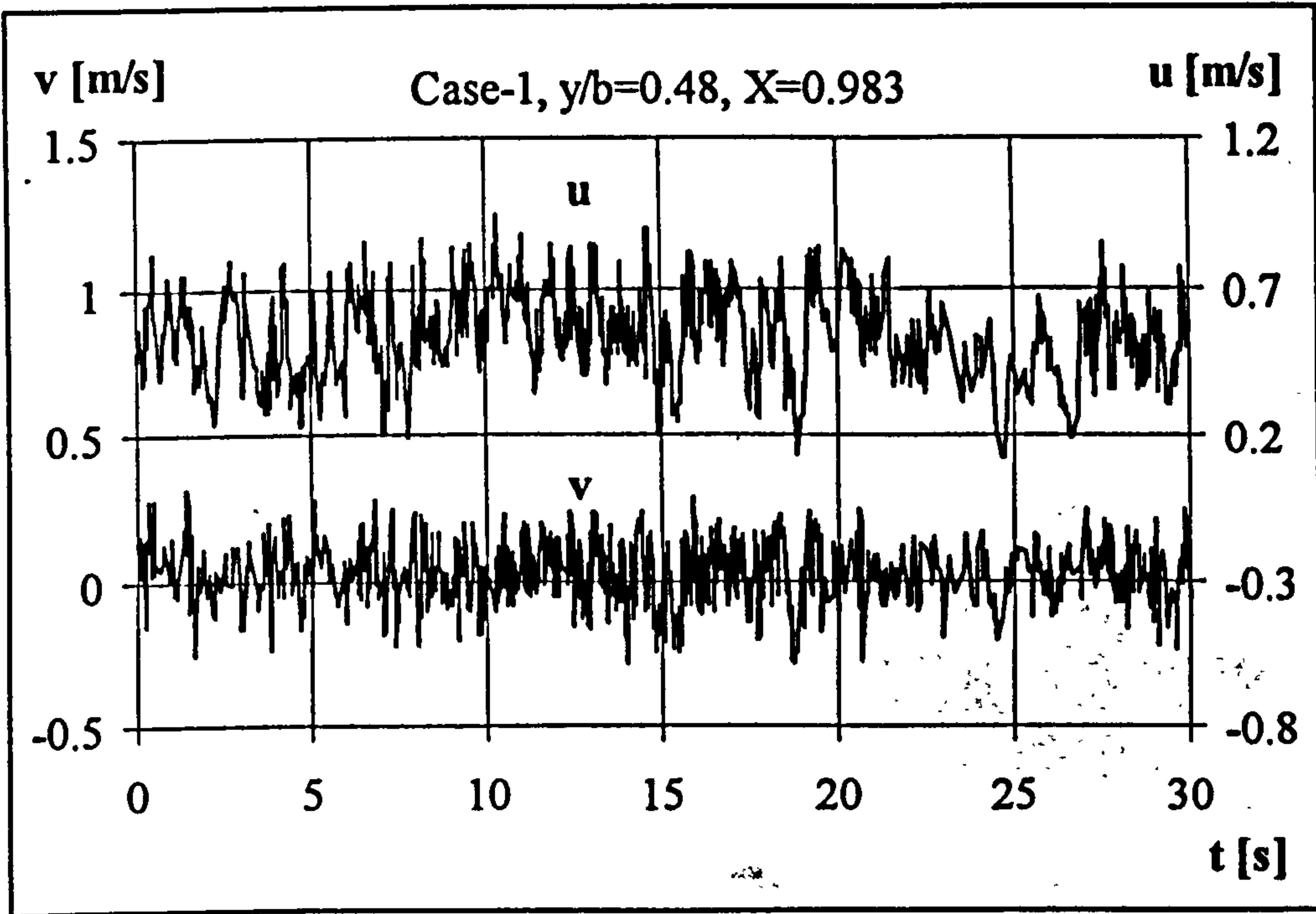


Figure 6.46 Time history of velocity, Case 1, $X=0.983$.

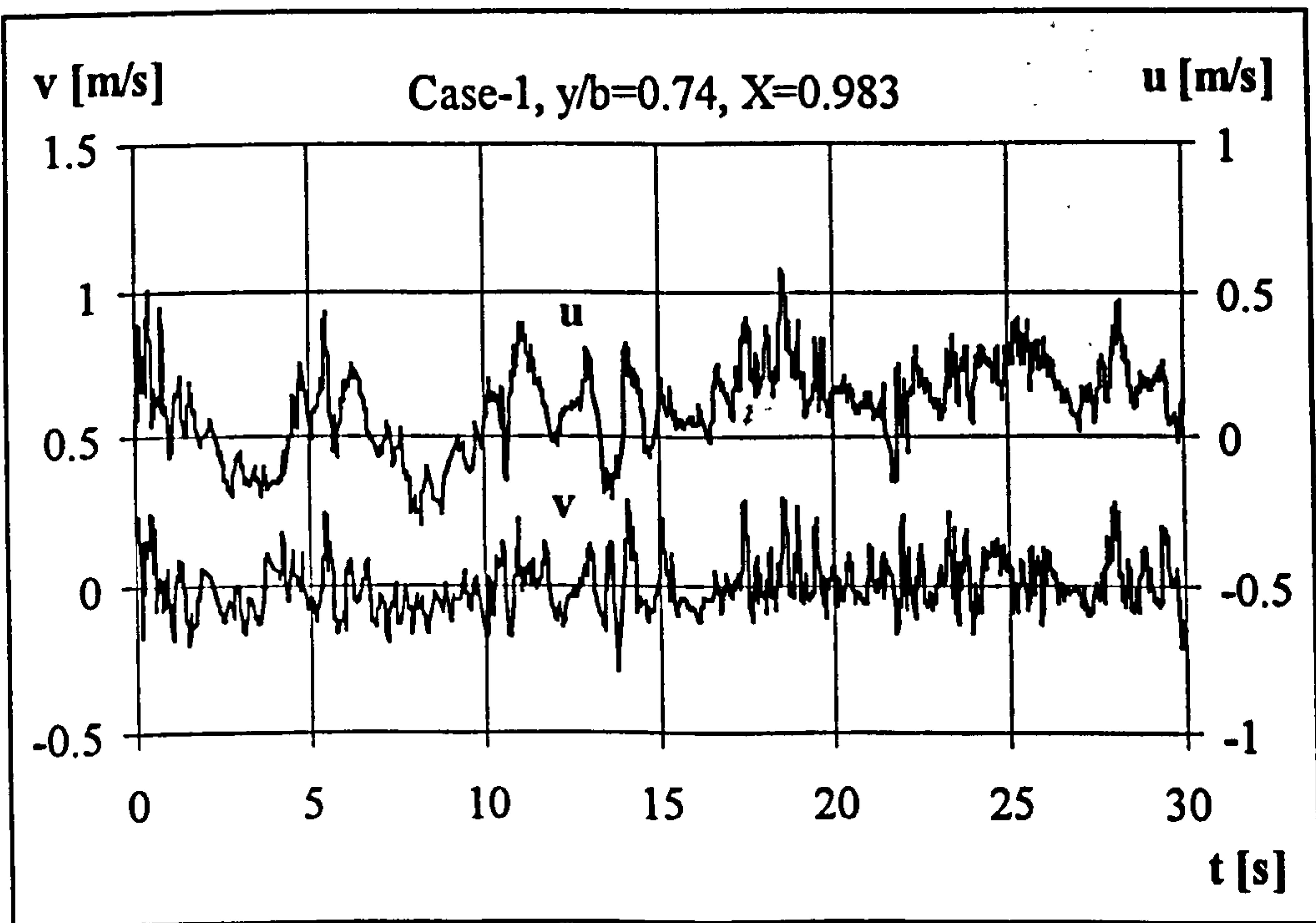


Figure 6.47 Time history of velocity, Case 1, $X=0.983$.

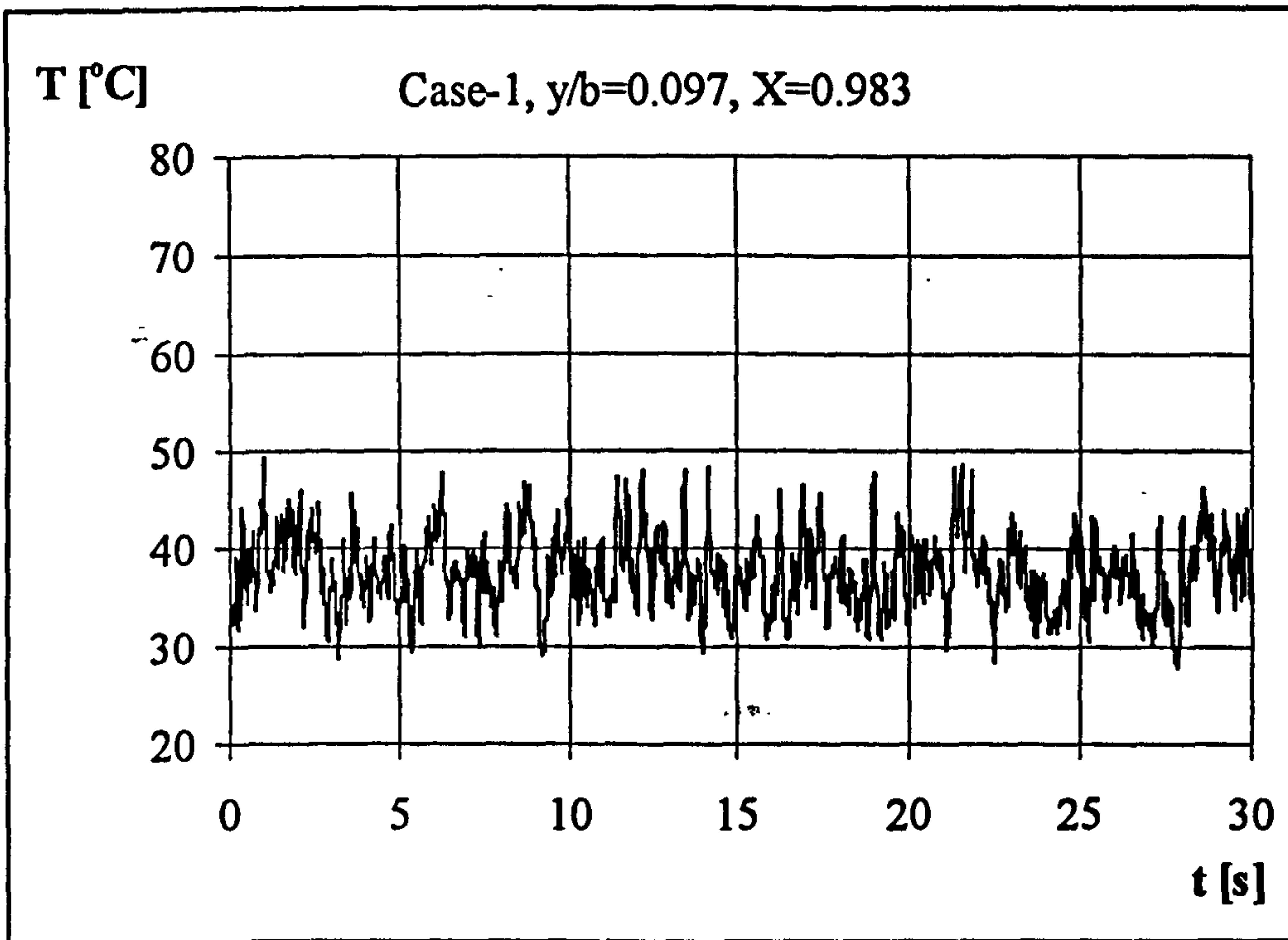


Figure 6.48 Time history of temperature, Case 1, $X=0.983$.

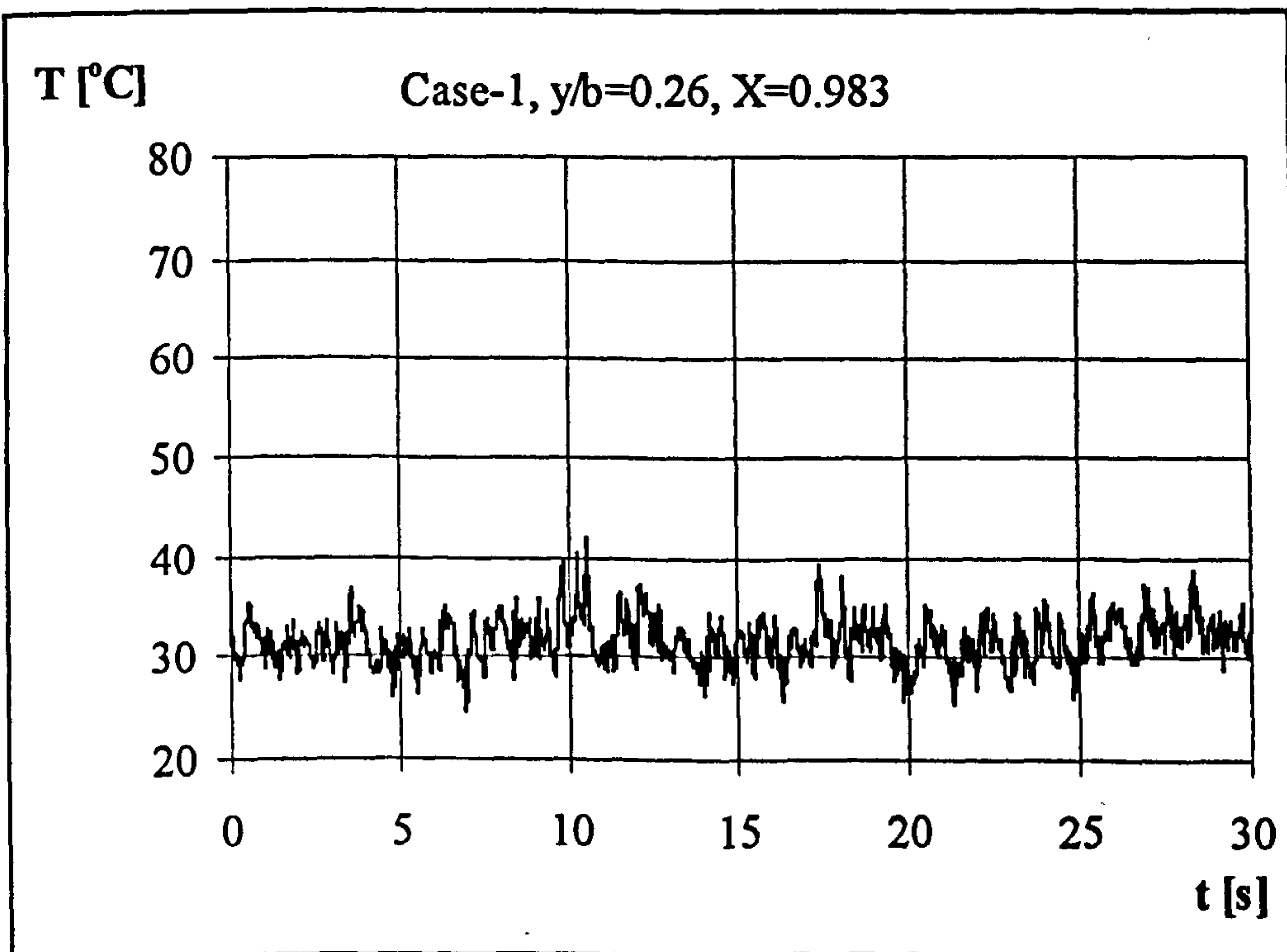


Figure 6.49 Time history of temperature, Case 1, $X=0.983$.

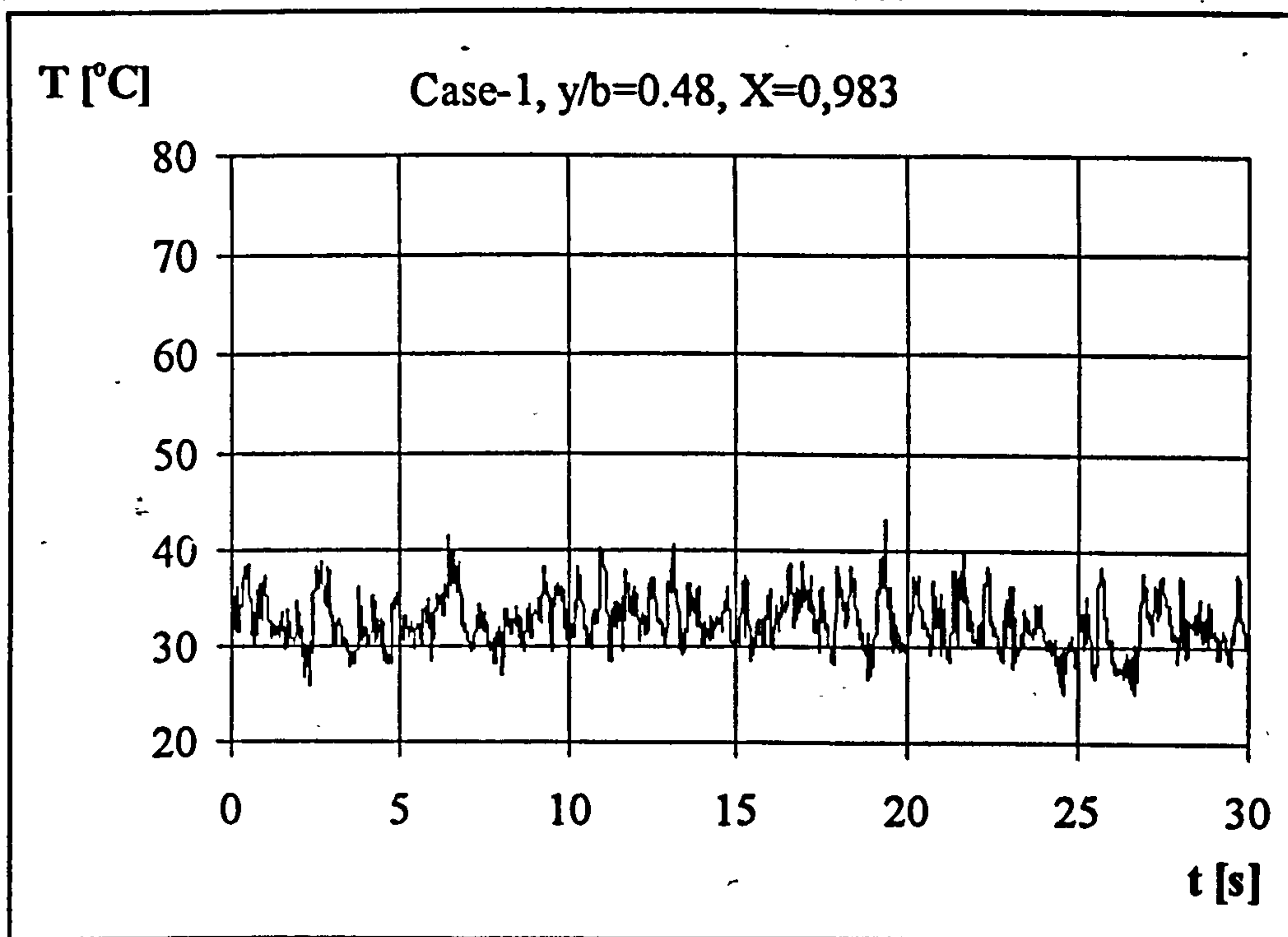


Figure 6.50 Time history of temperature, Case 1, $X=0.983$.

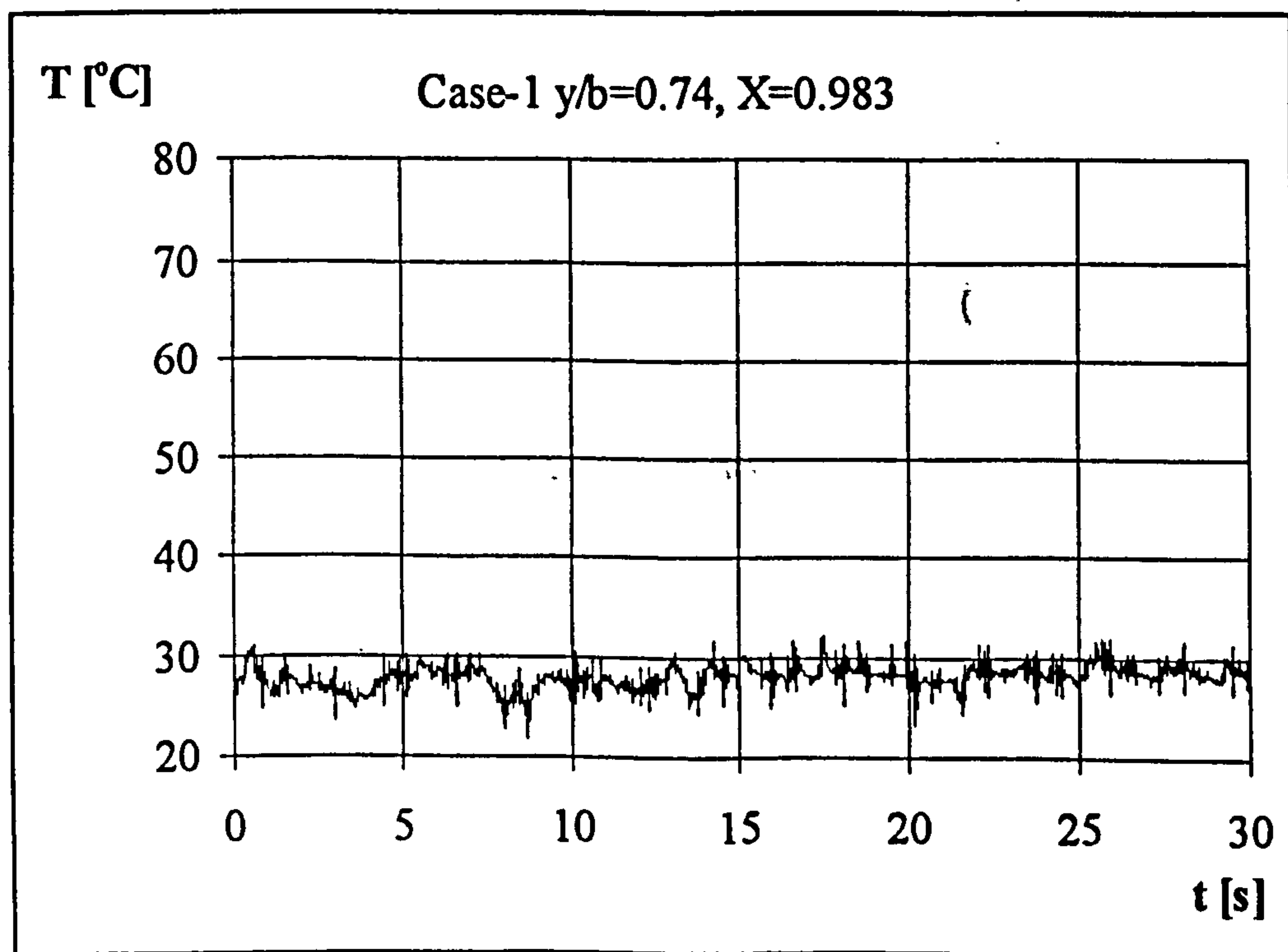


Figure 6.51 Time history of temperature, Case 1, $X=0.983$.

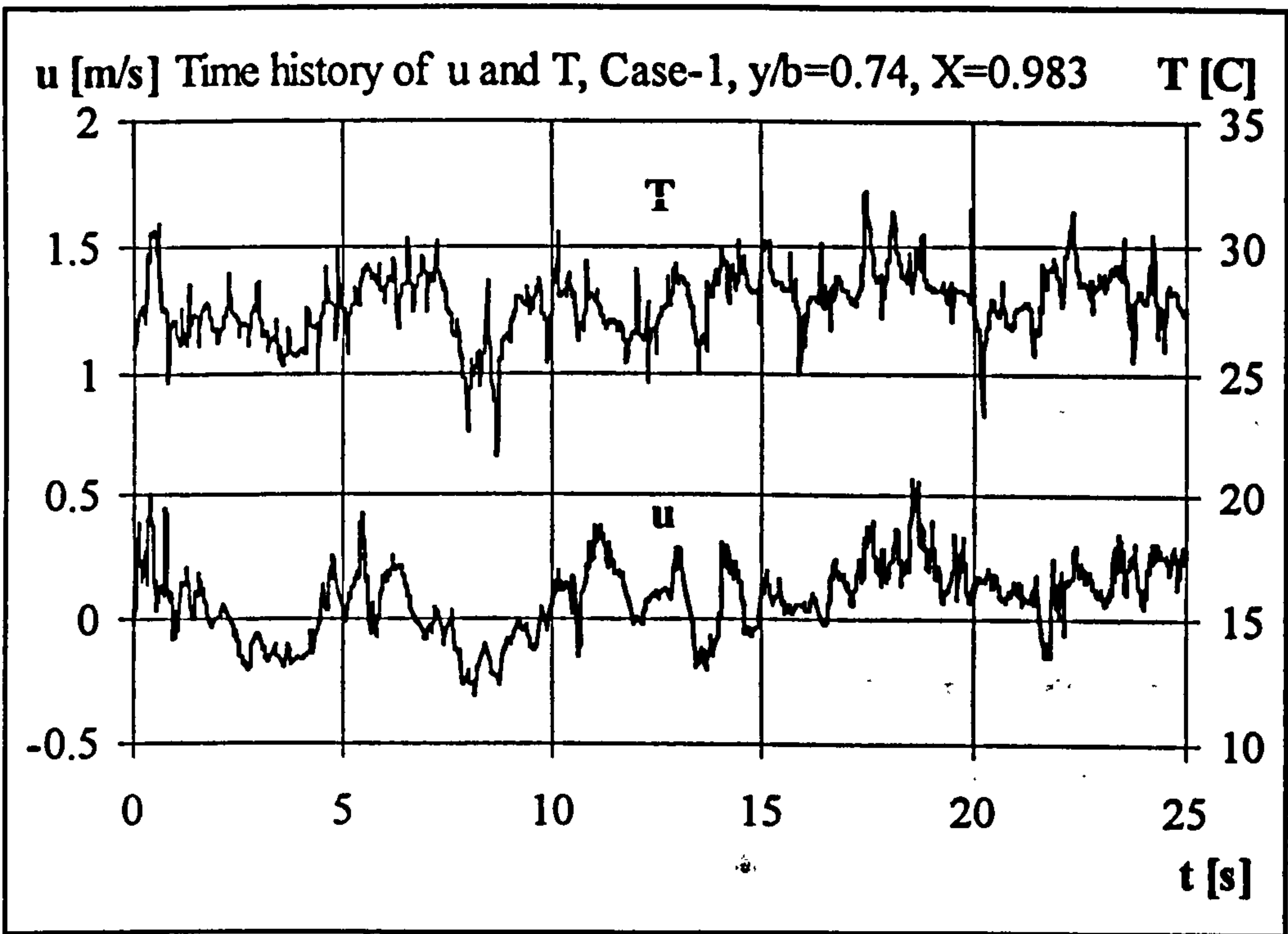


Figure 6.52 Time history of velocity and temperature, Case 1, X=0.983.

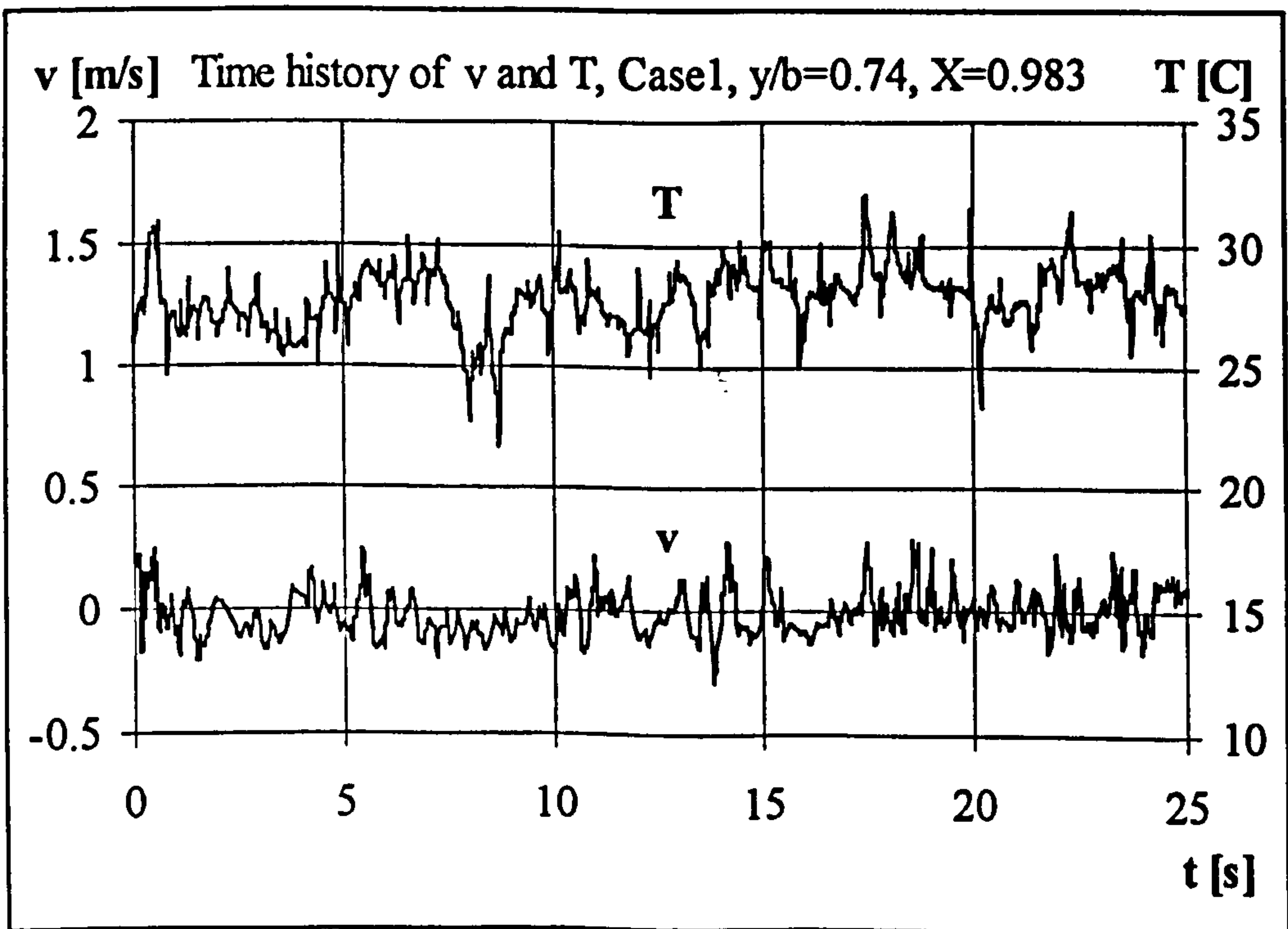


Figure 6.53 Time history of velocity and temperature, Case 1, X=0.983.

of the two components of velocity can be clearly seen, especially for the last three points. Temperature time histories given in Figures 6.48 to 6.51 possess similar characteristics to that of velocity suggesting turbulent mixing across the channel width. The amplitude of the fluctuations are as high as 40 % of the mean. Closer to the front wall, the number of frequencies reduces, with high frequency fluctuations superimposed on a low frequency mean temperature. That is also the case for velocity.

Time histories of the temperature and of the two velocity components at $y/b=.74$ and $X=0.983$ for Case 1 are shown together in Figures 6.52 and 6.53. As can be seen from these figures the temperature and velocity are well correlated. Temperature follows the velocity very nicely, especially the main low frequencies of temperature and u component velocities are exactly the same.

No data was recorded concerning temperature time history across the channel for the UWT cases. However the velocity time histories, which are not presented here, had similar characteristics to those for the UHF heating mode. The similarity of the turbulent kinetic energy profiles for both UWT and the UHF heating modes suggest similar flow structures within the channels.

6.3.5 Summary and Conclusions

The results presented above indicate that the flow at the channel inlet starts as laminar with some slight turbulence confined to the half of the channel next to the front wall side. Downstream and along the channel some of the above mentioned turbulence is suppressed. At nearly the half-height of the channel transition to turbulence is completed and at the exit of the channel fully developed turbulence is reached. In the cases considered thermal radiation did not play an important role in the heat transfer

process within the channel, the front wall being essentially adiabatic for all the cases considered.

6.4 Uncertainty of Experimental Data

Uncertainty of the measured and calculated values of experimental data was analysed in detail and presented in Appendix C.

CHAPTER 7. NUMERICAL ANALYSIS AND COMPARISON OF NUMERICAL AND EXPERIMENTAL RESULTS

7.1 Introduction

Numerical analyses and the results are presented in the following subsections. Mathematical models of laminar and turbulent natural convection or flows through vertical channels considered in this study have been presented in Chapter 3. The method of numerical solution and the numerical models together with the software code used, PHOENICS, has been detailed in Chapter 4. Numerical analysis was carried out using PC version 1.66 of PHOENICS. The code was run on an IBM 468 and a Pentium PC.

Comparisons of experimental data with numerical results have been made and correlating equations for induced flow rate and heat transfer have been obtained.

7.2 Laminar Flow

Numerical analysis of laminar natural convection inside the vertical channel described in Chapter 3 has been carried out. Case 5 of the experiments was selected as a test case for the analysis. Grid sensitivity of the numerical solutions, the effect of different boundary conditions and three dimensionality have been investigated. After selecting a convenient grid, numerical solutions of all the experimental cases have been performed. Comparisons of experimental results with numerical solutions have been made in respect of induced flow rates, heat transfer to the air through the channel and the flow fields inside the channels.

7.2.1 Boundary Conditions

The boundary conditions (BCs) of the governing equations have been given in equations (3.5). In order to evaluate the numerical predictions, measured wall

temperatures have been used directly as BCs. In order to see the effect of different BCs UWT and UHF heating mode were considered for one case (section 7.2.4.4). Second degree polynomials were fitted to the experimental wall temperature data. This gives the thermal BCs in the form $T=T(\mathbf{x})$. Standard settings within PHOENICS can not implement non-linear BCs and therefore additional FORTRAN coding was written in the GROUND to impose BCs in the form $T=T(\mathbf{x})$. The GROUND file and a typical Q1 file are given in Appendices B.3 and B.4 respectively.

7.2.2 Convergence Criteria

Convergence to a solution was determined by checking overall balances of mass and energy. When the inflow and outflow mass flow rates were equal and the overall balance of energy was satisfied, the run of that case was assumed to have converged to give the steady state solution. PHOENICS allows the observation of the total residuals of the variables throughout the calculation domain during execution. Test runs were performed to determine the number of sweeps necessary for a converged solution. This sweep number was then set for subsequent runs.

7.2.3 Selection of Grid Pattern and Grid Size

The calculation domain was selected as half of the channel given in Figure 3.1. The domain extended from inlet to exit edges in the x-direction and from the centre of the heated wall to the surface of the front wall. The dimensions of the experimental channel were used exactly for the calculation domain. The domain was divided into two regions in both x and y directions, ie. 4 regions. The first region in the x-direction (along the channel) covered the unheated section and the first region in the y-direction (across the channel) covered half the thickness of the heated wall. The result of the experiments suggested that a power-law grid should be employed for the calculation domain in both directions. PHOENICS creates power-law grids using the GRDPWR statement. The GRDPWR statement can be examined in the Q1 file given in Appendix B 4. The fourth argument of the statement is the power and determines the grid

pattern in the respective direction. The use of the GRDPWR statement and how it creates grids is explained in TR/200 [66]. The unheated section of the channel was represented with 18 cells in the x-direction with the grid starting fine from both ends with coarser grids towards the centre. The thickness of the heated wall was represented with 5 cells in the y-direction throughout the length of the domain. The grid in this region started coarse and got finer towards the wall surface.

Table 7.1 Grid dependence of numerical solutions.

Dependence on the cell number in x-direction (Case 5)			
NX x NY	$q_{c,num}/q_{c,exp}$	$\dot{m}_{num}/\dot{m}_{exp}$	Relative Comp. Time
50x35	1.092	1.098	0.6
82x35	1.079	1.075	1.0
112x35	1.076	1.064	1.4
128x35	1.074	1.06	1.8
178x35	1.074	1.055	2.2
210x35	1.069	1.053	2.5
242x35	1.069	1.049	2.9
Dependence on the cell number in y-direction (Case 5)			
NX x NY	$q_{c,num}/q_{c,exp}$	$\dot{m}_{num}/\dot{m}_{exp}$	
82x25	1.083	1.078	
82x35	1.079	1.075	
82x45	1.077	1.071	
82x55	1.076	1.069	
Dependence on gridpower in x-direction (Case 5), NXxNY (82x35)			
Gridpower (x)	$q_{c,num}/q_{c,exp}$	$\dot{m}_{num}/\dot{m}_{exp}$	
1.1	1.081	1.076	
1.2	1.079	1.075	
1.3	1.078	1.073	

The number of cells of the second region in the x and y directions were varied to analyse grid size dependence of the solutions. The grid pattern employed in the second x-direction region was such that it started fine at the beginning of the heated region, becoming coarser in the downstream direction. The y-direction grid used in that region was one of a symmetric power-law, finer near the walls and coarser towards the centre of the channel, grid power being 1.2.

For that part of the domain representing the length and half thickness of the heated wall, the cells were regarded as solid elements.

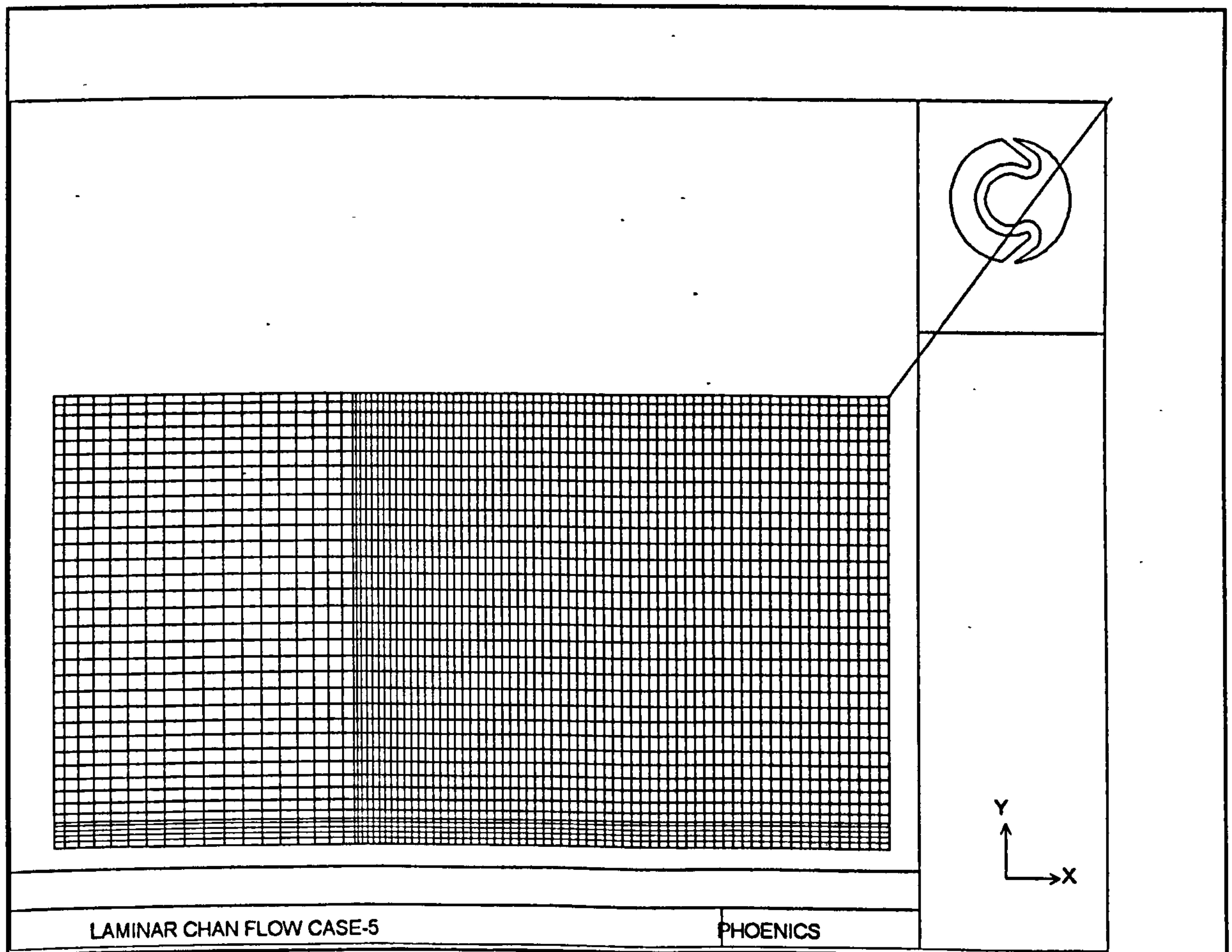


Figure 7.1 The grid used in laminar natural convection calculations.

Numerically calculated and measured heat transfer and mass flow rates are compared and listed in Table 7.1. It can be seen from the table that numerical solutions were more sensitive to the number of grids in the x-direction. The closest numerical results were obtained for the highest number of cells in the x-direction, over predicting the heat transfer and mass flow rates by 4.9 and 6.9 percent respectively. However computer time increased considerably. By using the grid size of 82x35, the computer time increased almost three times just to give 1 per cent better prediction of the heat transfer rate.

Numerical solutions were almost insensitive to the number of cells in the y-direction. Among the four different cell configurations examined the difference in the predicted heat transfer rates were under 0.2 per cent, whereas the mass flow rates differed by under 0.3 per cent. The gridpower dependence of numerical solutions were also examined for three different gridpowers in the x-direction. The results listed in Table 7.1 indicate that the solutions are insensitive to gridpower compared with the sensitivity to the number of cells in that direction.

Judging from the results listed in Table 7.1 it was decided that the grid of 82x35 with the gridpower of 1.2 in both direction and region should be sufficient for subsequent calculations. The grid used in the final calculations of laminar flow cases is depicted in Figure 7.1. It is not drawn to the scale in order to show the details in the y-direction.

7.2.4 Comparison of Numerical Solutions with Experimental Results

Calculations were performed for all the experimental cases using a 82X35 grid. The results of the numerical solutions are presented comparatively in the following subsections in respect of heat transfer, mass flow rates and the velocity and temperature fields within the channel. Unfortunately no comparison was possible with other research since no study was found in the literature which dealt with the same geometry.

7.2.4.1 Comparisons of Experimental and Numerical Heat Transfer and Mass Flow rates

Calculated heat transfer and mass flow rates for the seven experimental cases are listed in Table 7.2. The results show that heat transfer rates are predicted to within 10 per cent of the measured values for all the cases. The predicted mass flow rates remained within 8.4 percent of that of the experiments for the low and intermediate channel aspect ratios, Cases 1 to 5. For the high aspect ratio cases, however, the mass flow rates were grossly over predicted by up to 73.2 per cent of the measured values. This suggests that at high channel aspect ratios three dimensional effects may be important and should be considered in the calculations. Otherwise, the predictions are in good agreement with the experiments, considering that the thermal boundary conditions were taken from the curve fit values of the wall temperatures based on just four measurement locations along the channel.

Table 7.2 Comparison of experimental results with numerical solutions

Case Num.	b/H	$q_{c,num}/q_{c,exp}$	$\dot{m}_{num}/\dot{m}_{exp}$
1	1/32	1.021	1.067
2	1/32	1.060	1.045
3	1/16	1.053	1.084
4	1/16	1.102	1.071
5	1/16	1.079	1.075
6	5/32	0.913	1.732
7	5/32	1.010	1.578

7.2.4.2 Comparisons of Velocity and Temperature Profiles of Selected Cases with Experimental Results

Numerical and experimental velocity profiles for the high wall heat flux rate cases for the three channel aspect ratios are presented in Figures 7.2 to 7.4. Temperature

profiles for Case 5 are given in Figure 7.5. The axis shift method of plotting as used in the presentation of experimental results in Chapter 6 has again been used. The profiles were non-dimensionalised in the same way using the highest velocity as reference whether it is an experimental or a numerical value. Temperatures were non-dimensionalised according to equation (6.1). In all of the figures numerical values are graphed with a continuous line.

Examination of Figures 7.2 to 7.4 shows a good qualitative agreement between the measurements and the numerical results. However, the quantitative agreement is not good for the high channel aspect ratio case, Figure 7.4. Although the character of the velocity profiles are captured numerically the values are grossly over estimated away from the walls.

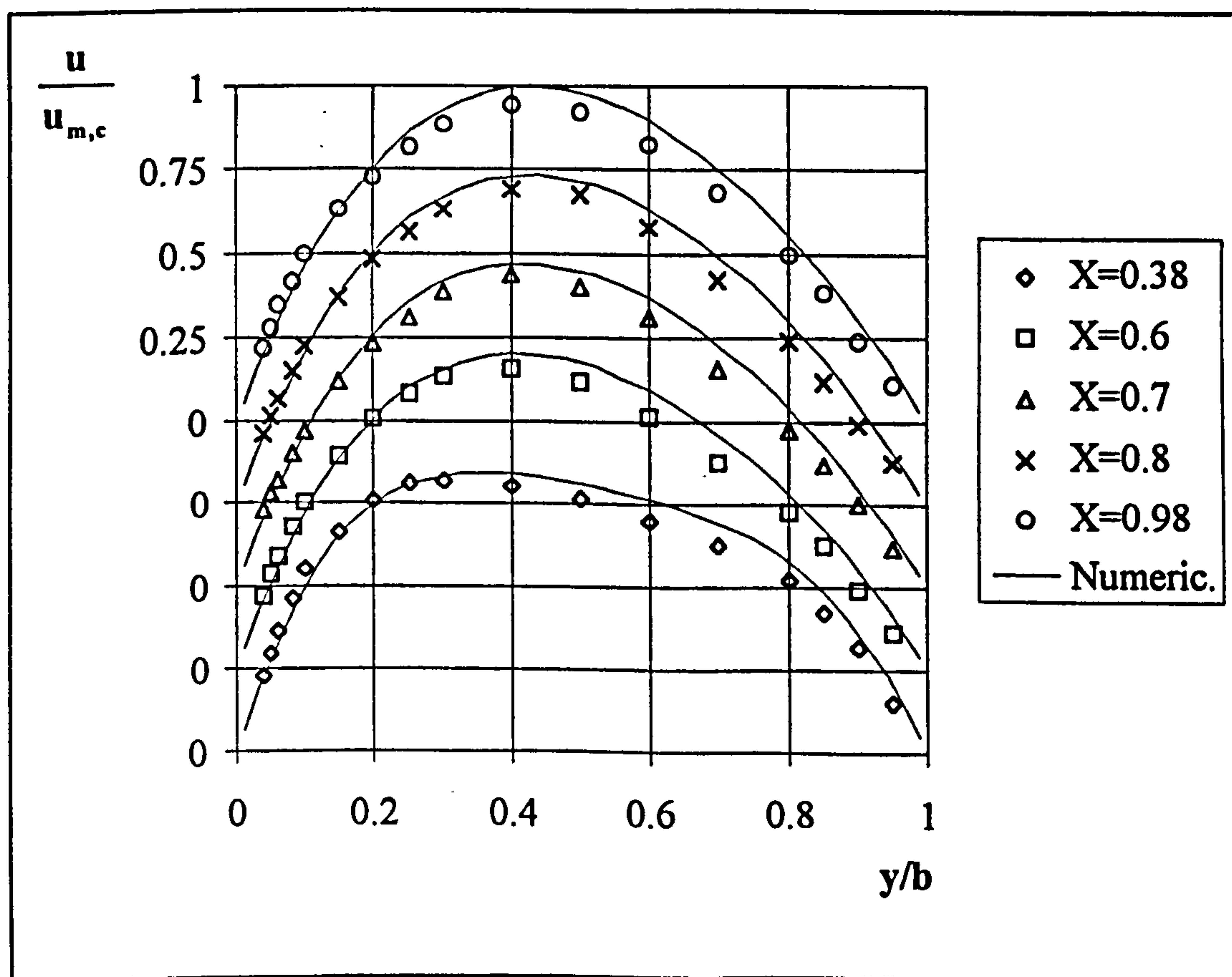


Figure 7.2 Comparison of experimental and numerical velocity profiles, Case 2.

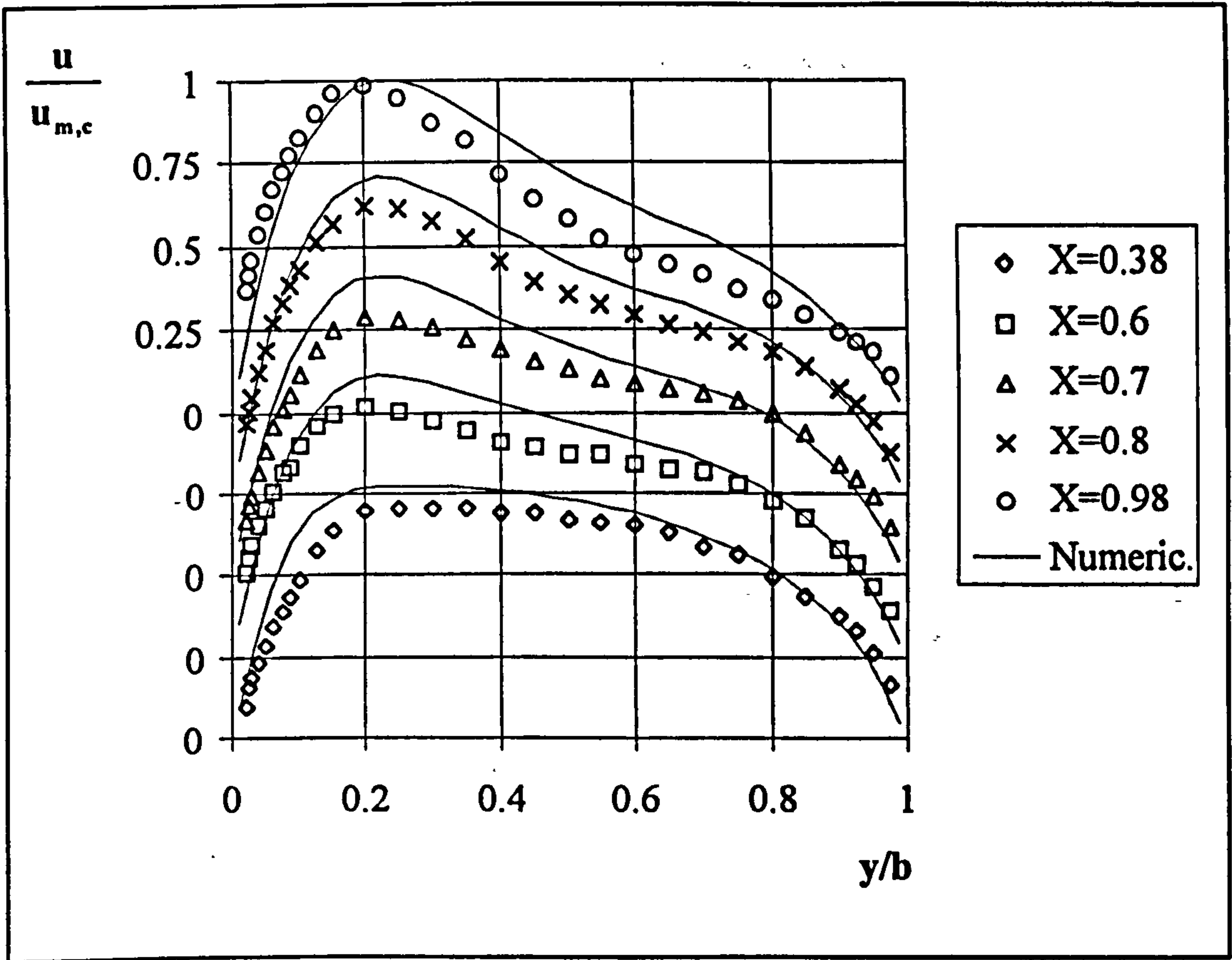


Figure 7.3 Comparison of experimental and numerical velocity profiles, Case 5.

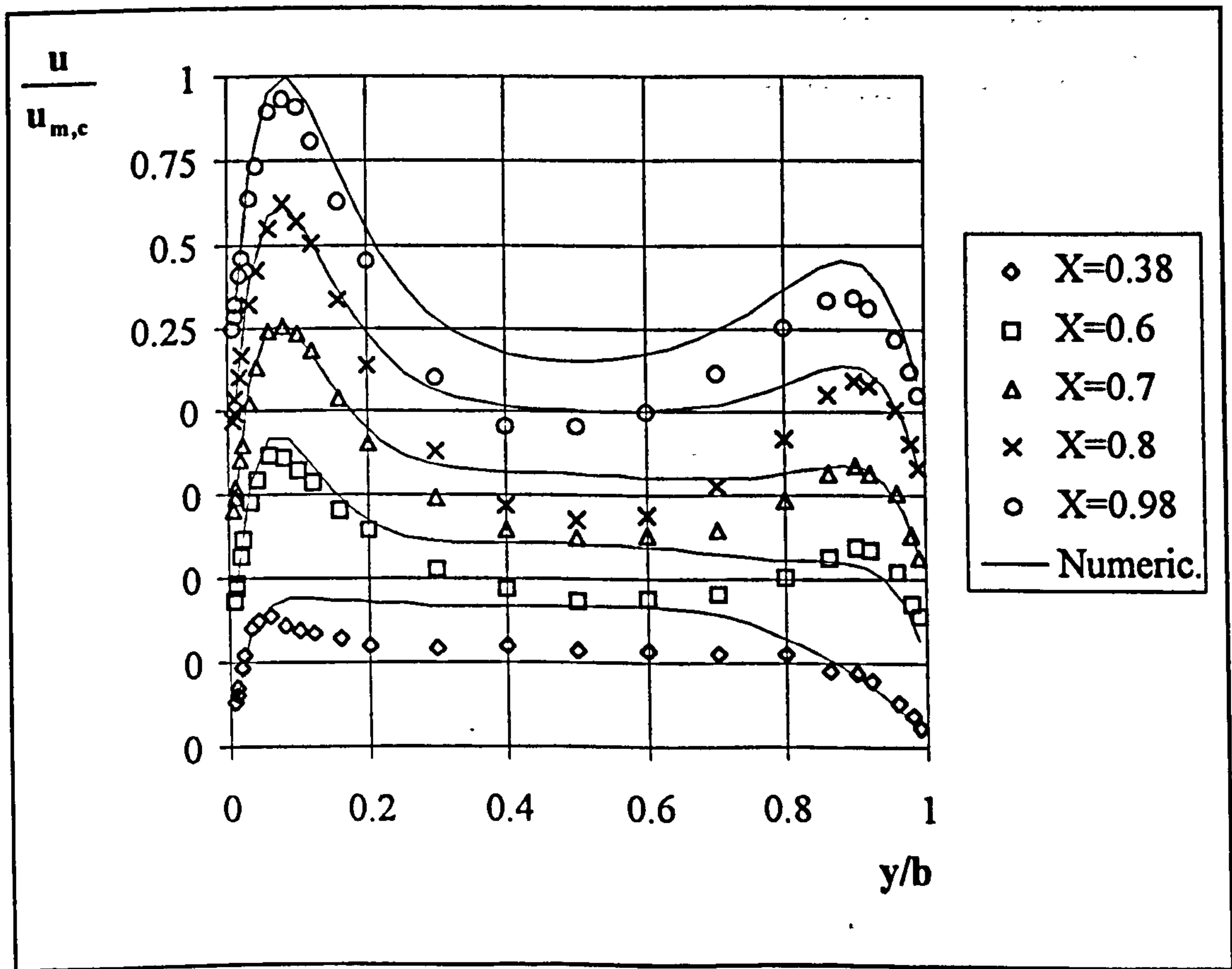


Figure 7.4 Comparison of experimental and numerical velocity profiles, Case 7.

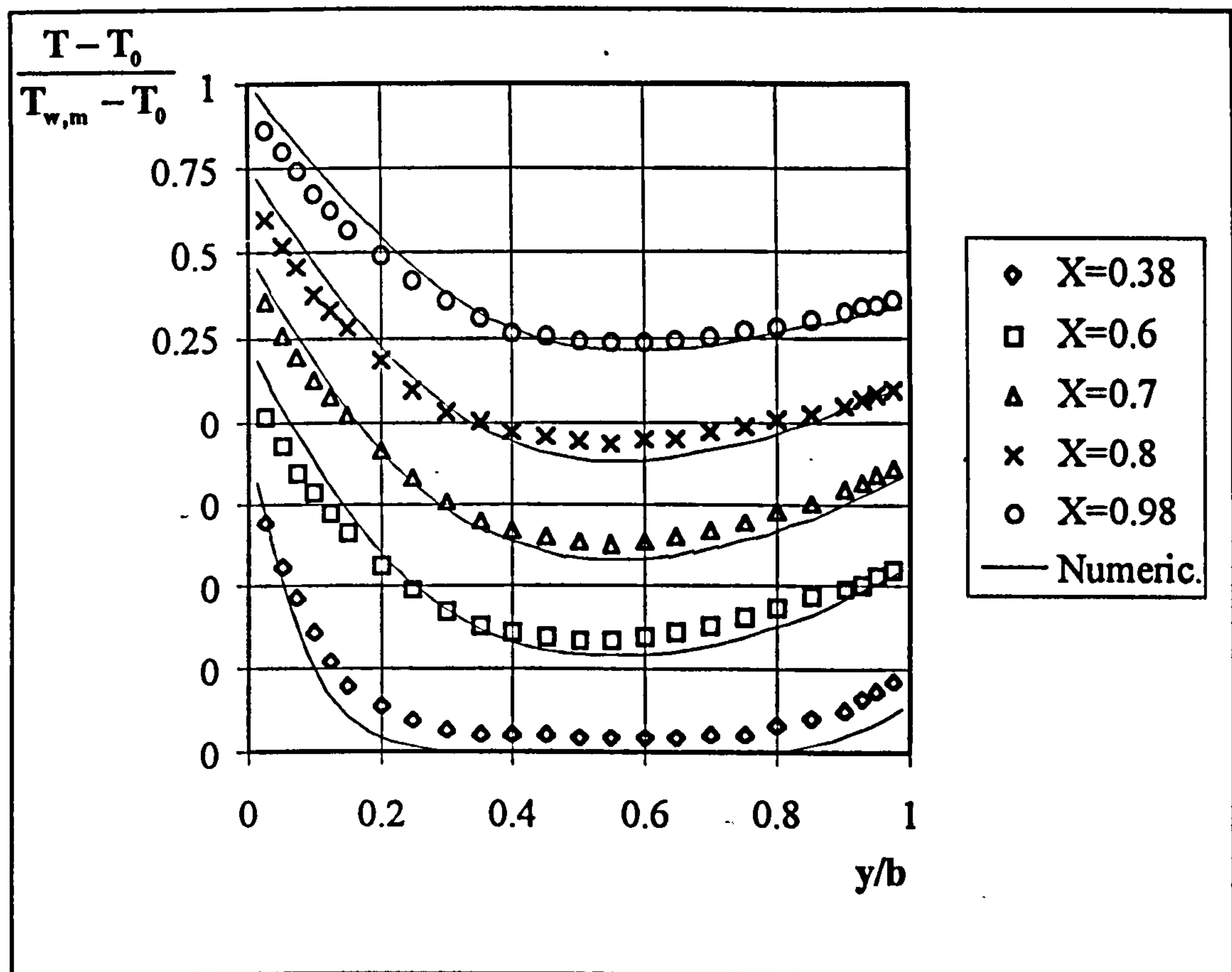


Figure 7.5 Comparison of experimental and numerical temperature profiles, Case 5.

The numerical solution has failed to capture the flow reversals encountered in the measurements for that case. The velocity in the core region of the channel has been over estimated from the channel inlet to the exit, though the predictions within the 0.2 of the channel width near the walls are in very good agreement with the measurements.

Figure 7.5 indicates good agreement of the experimental and numerical temperature profiles. Temperatures near the heated wall have been overestimated except for the first elevation. The agreement near the cold wall is almost perfect. The discrepancy between the measured and predicted values may have been the result of inexact thermal boundary conditions, since the wall temperatures were measured at only four points along the channel. The profile at the first elevation has been slightly underestimated and this may have been due to the imposed thermal boundary condition. In the calculations, the thermal boundary conditions were applied from the level of the heated wall even for the cold wall. In fact, some of the lower part of the

cold wall may have been heated above the ambient temperature due to thermal radiation from the heated wall resulting in heat transfer to the air before the start of the heated wall region, thus giving high air temperatures inside the channel.

7.2.4.3 The Effect of Three Dimensionality

Since the velocity measurements were made away from the centre of the channel depth, some three-dimensional calculations were performed in order to check whether 3-d effects extend to the measurement plane. The measurements were made at the z-direction plane of $Z=0.4$ where Z is defined as z/d and d is the channel depth. Calculations were performed for Cases 5 and 7 using adiabatic side walls. The results for both cases indicated that the three-dimensional effects did not extend to the measurement plane. In other words the velocity profiles from the measurement plane to the mid-plane in the z direction remained the same. The overall heat transfer and mass flow rates were 1 and 2 per cent respectively better predicted than the two-dimensional results for Case 5. For Case 7, however, the mass flow rate was predicted as 12 per cent lower than that for the two-dimensional solution, giving a 46 per cent over prediction of the measured value. This implies that, at the higher channel aspect ratios three dimensionality becomes important. Since no side wall temperature measurements were made along the channel it was impossible to make a proper examination of the effect of three dimensionality.

7.2.4.4 The Effect of Different Boundary Conditions

A 'what if ?' analysis was performed to investigate the effect of different boundary conditions. For this purpose three different thermal boundary conditions on the walls were considered. These are, the measured

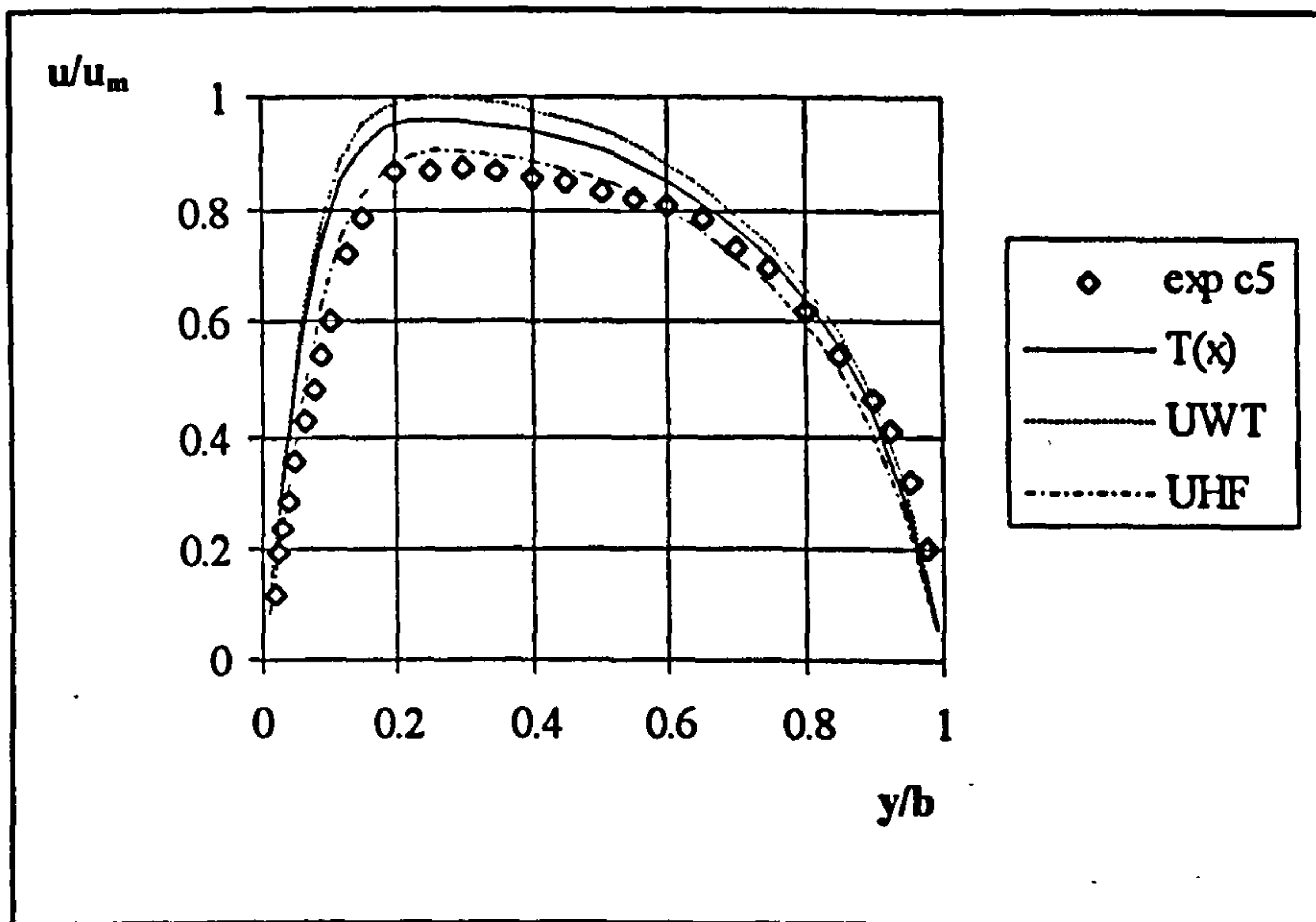


Figure 7.6 Comparison of velocity profiles for different boundary conditions, $X=0.38$, Case 5

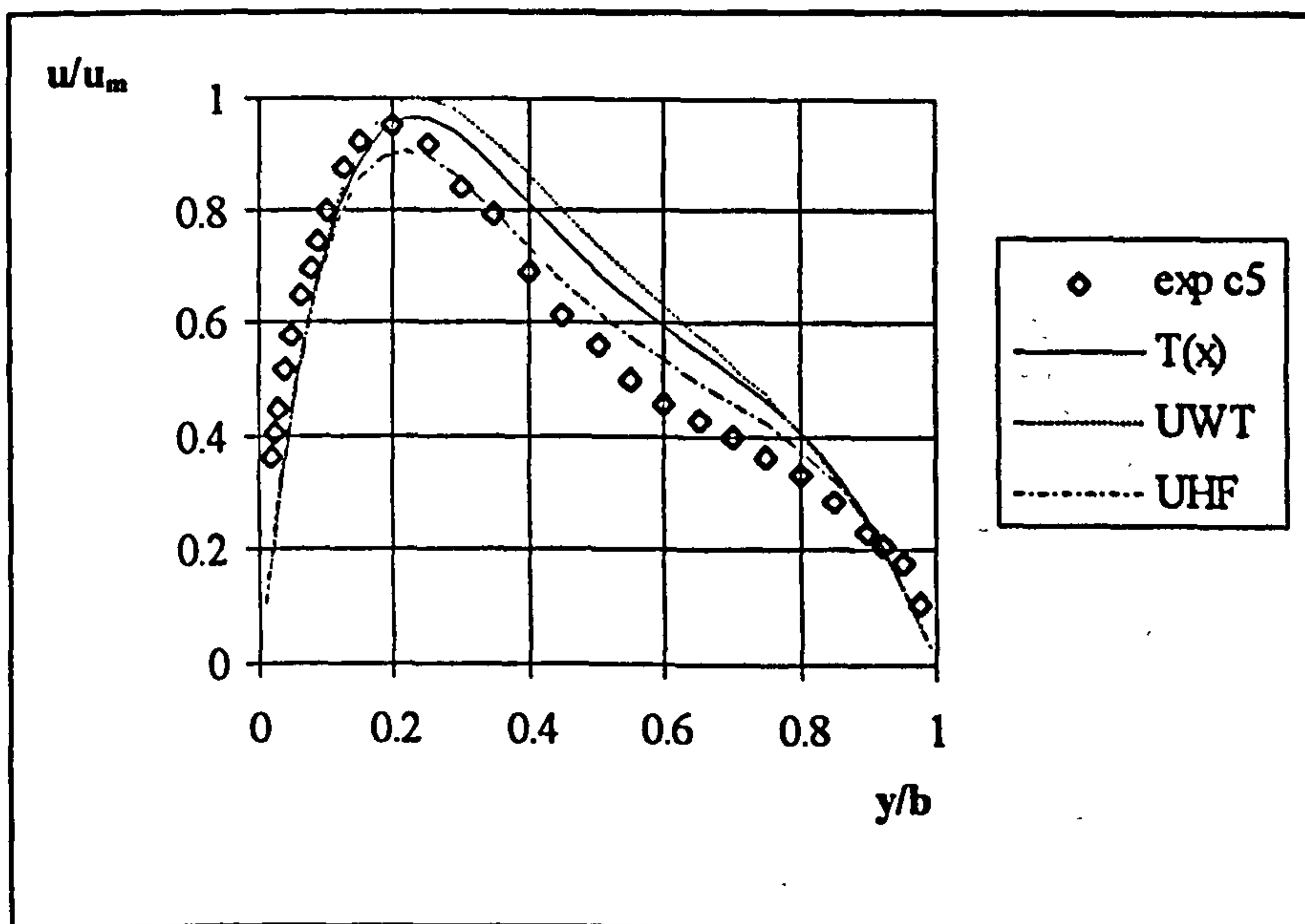


Figure 7.7 Comparison of velocity profiles for different boundary conditions, $X=0.98$, Case 5

temperatures on the walls, $T_w=T_w(x)$, a UWT boundary condition with the temperature taken as being the average of the measured wall temperatures, $T_w=T_{w,ave}$ and a UHF on the walls. For the UHF boundary condition, the measured heat flux, q_c , was applied to the walls at the ratios calculated from the $T=T(x)$ boundary condition solution. With the UHF boundary condition, the predicted air mass flow rate was

almost exactly the same as the measured one. For the $T_w=T_w(x)$ boundary condition, the results have already been given in Table 7.2. For the UWT boundary condition, the predicted mass flow rate was 12 per cent higher and the heat transfer rate was 7.3 percent higher than the measured values. The UWT case predicted the heat transfer rate as almost the same as for the $T_w=T_w(x)$ boundary condition. The velocity profiles calculated by these boundary conditions are presented in Figures 7.6 and 7.7 for $X=0.38$ and 0.98 . The figures show that the velocity profile is better estimated by UHF boundary condition near the inlet, $X=0.38$, and by $T_w=T_w(x)$ boundary condition near the exit, $X=0.98$, of the channel.

7.2.5 Summary and Conclusions

Numerical analysis of laminar natural convection cases have been carried out. Grid sensitivity of the numerical solutions, the effect of different boundary conditions and three dimensionality have also been investigated. Numerical solutions were sensitive to the number of cells in x -direction. A grid of 82×35 was decided upon for the calculations.

Comparisons of experimental results with numerical solutions have been made in respect of induced flow rates, heat transfer to the air flowing through the channel and the flow fields within the channels. The numerical solutions have predicted the heat transfer rates within 10.2 per cent, and the mass flow rates within 8.4 per cent of the measured values. For the high channel aspect ratio cases, the mass flow rates were over predicted by up to 73 per cent. The effect of three dimensionality has also been investigated and found to be important in the high channel aspect ratio cases. Examination of different imposed boundary conditions has indicated that the experimental channel wall conditions gave results between UWT and UHF boundary conditions. It can be concluded from the results that, if the thermal BCs are exactly known, the numerical method employed in this study can predict the heat transfer and mass flow rates in vertical channels within ± 10 per cent or better accuracy.

7.3 Turbulent Flow

Numerical analyses of turbulent natural convection inside the vertical channel described in Chapter 3 has been carried out. Case 4 of the UWT and Case 3 of the UHF experiments have been selected as test cases for the analysis. Grid sensitivity of the numerical solutions and the effect of different boundary conditions of turbulent kinetic energy at the inlet have been investigated. After selecting a convenient grid, numerical solution of all the experimental cases were performed. Comparison of experimental results with numerical solutions has been made in respect of induced flow rates, heat transfer to the air flow and the velocity and temperature flow fields within the channels. Preliminary calculations showed that the standard $k-\epsilon$ model (the ST model) has over estimated the mass flow rates, and that the Launder and Sharma model (the LS model) produced convergence problems especially for finer grids. Therefore, the Low Reynolds Number $k-\epsilon$ models of To and Humphrey (the TH model), Davidson (the DA model) and Lam and Bremhorst (the LB model) were employed for the numerical analysis.

7.3.1 Boundary Conditions

The boundary conditions of the governing equations have been given in Chapter 3, equations (3.22). Experiments were performed for both the UWT and UHF boundary conditions. The default settings of PHOENICS are sufficient to implement boundary conditions of pressure and velocity. This is also the case for k and ϵ for all the turbulence models except for the TH model. Additional FORTRAN coding was required in GROUND to implement the wall boundary conditions of ϵ for the TH model. The GROUND file and a typical Q1 file are given in Appendices B.1 and B.2 respectively.

7.3.2 Convergence Criteria

Convergence of solutions was decided in the same way as for the laminar natural convection analysis.

7.3.3 Selection of Grid Pattern and Size

A power-law grid was adopted for the numerical analysis of turbulent natural convection. The grid in the x-direction started as fine at the inlet, getting coarser in the downstream direction. A symmetric grid was created in the y-direction, starting fine at the walls and getting coarser towards the centre of the channel. UWT, Case 5, of the experiments was used as the test case for grid dependence analyses. The grid power in the y-direction used for the analysis was taken as 2. The lowest number of grids in the y-direction was taken 40 so that a molecular diffusion boundary condition for velocity and temperature could be applied. The average of the measured k values across the channel at the first elevation was used as the uniform inlet boundary condition for k .

Runs of the code were made to determine the dependence of solutions on the number of cells and the grid power in both directions for the three turbulence models considered. The results of the runs are listed in Table 7.3 in the form of heat transfer and mass flow rates. The entries in the table are normalised values using experimental values.

Table 7.3 Grid dependence of numerical solutions.

Dependence on the cell number in x-direction (UWT, Case 4)						
Grid Size	TH		DA		LB	
NX x NY	$\frac{q_{c,num}}{q_{c,exp}}$	$\frac{\dot{m}_{num}}{\dot{m}_{exp}}$	$\frac{q_{c,num}}{q_{c,exp}}$	$\frac{\dot{m}_{num}}{\dot{m}_{exp}}$	$\frac{q_{c,num}}{q_{c,exp}}$	$\frac{\dot{m}_{num}}{\dot{m}_{exp}}$
60x60	1.16	1.04	1.03	0.99	0.92	1.05
90x60	1.15	1.04	1.02	1.00	0.92	1.05
120x60	1.14	1.03	1.01	1.00		
200x60	1.14	1.03	1.01	1.00		
Dependence on the cell number in y-direction (UWT, Case 4)						
	TH		DA		LB	
NX x NY	$\frac{q_{c,num}}{q_{c,exp}}$	$\frac{\dot{m}_{num}}{\dot{m}_{exp}}$	$\frac{q_{c,num}}{q_{c,exp}}$	$\frac{\dot{m}_{num}}{\dot{m}_{exp}}$	$\frac{q_{c,num}}{q_{c,exp}}$	$\frac{\dot{m}_{num}}{\dot{m}_{exp}}$
60x40	1.14	1.04	1.13	0.96	0.93	1.05
60x60	1.16	1.04	1.03	0.99	0.92	1.05
60x80	1.15	1.04	1.00	1.02	0.92	1.05
Dependence on grid power in x-direction (UWT, Case 4), NXxNY (60x60)						
	TH		DA			
Grid power(x)	$\frac{q_{c,num}}{q_{c,exp}}$	$\frac{\dot{m}_{num}}{\dot{m}_{exp}}$	$\frac{q_{c,num}}{q_{c,exp}}$	$\frac{\dot{m}_{num}}{\dot{m}_{exp}}$		
1.1	1.16	1.05	1.04	0.99		
1.2	1.16	1.04	1.03	0.99		
1.3	1.15	1.03	1.02	0.99		

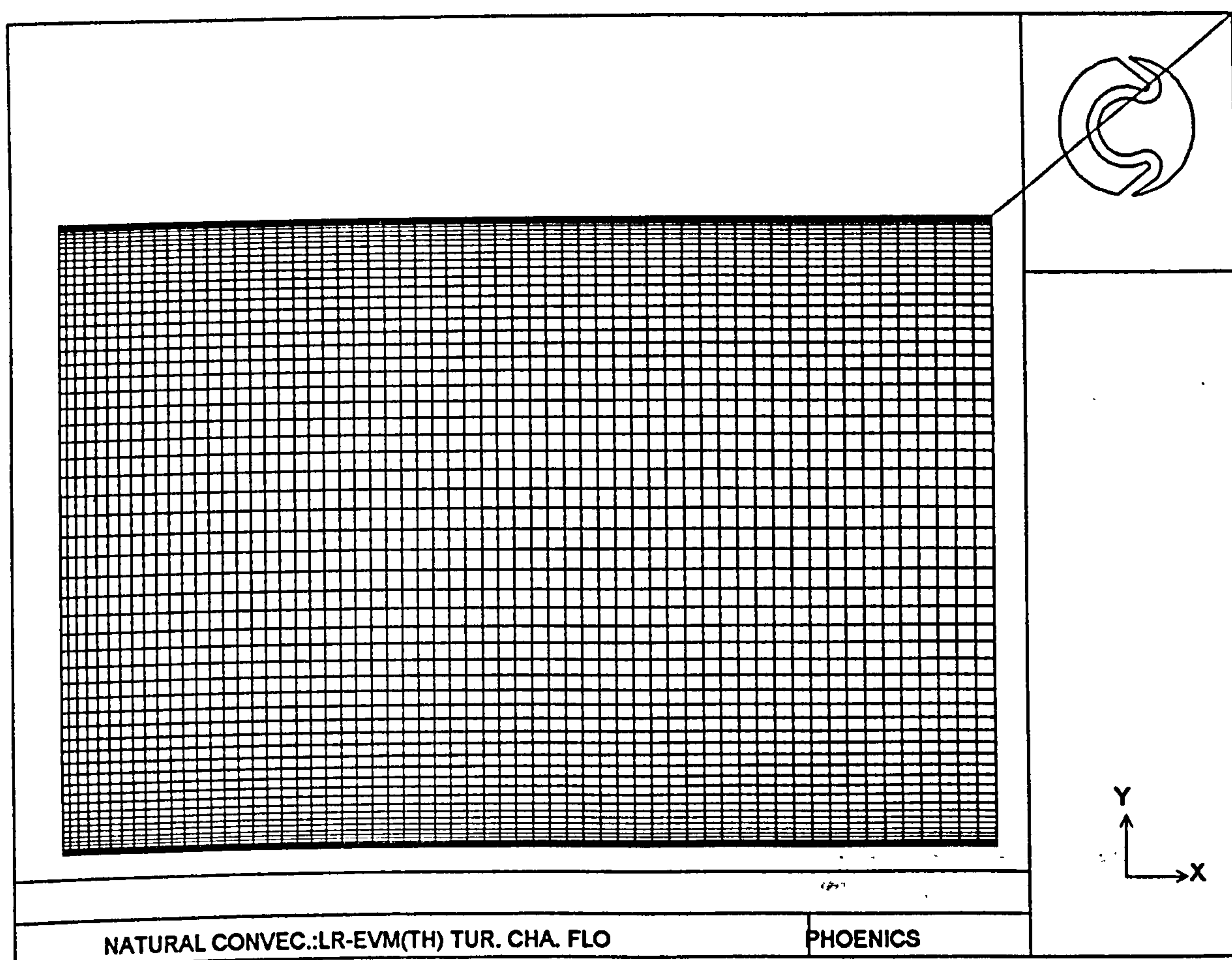


Figure 7.8 The grid used in turbulent natural convection calculations.

The results of the calculations indicated that all three models were insensitive to the number of grids in the x-direction within 2 per cent. As for the y-direction number of cells, the DA model was the only one found to be sensitive, producing results changing by as much as 13 %. For the model, the grid power was set to 3 which produced finer cells near the wall. Subsequent calculations for the model changing the number of cells in the y-direction by keeping the grid power as 3, indicated that a finer grid should be used. All of the models were insensitive to the grid power in x-direction. A grid of 60x60 with grid power of 1.2 in the x-direction and 2 in the y-direction was decided upon for further calculations. For the DA model however, a

grid power of 3 in y-direction was decided upon. The grid used in further calculations is given in Figure 7.8.

7.3.4 The Effect of the Turbulent Kinetic Energy Inlet Boundary Condition

In the numerical analyses in section 7.3.3 the inlet boundary condition of k was applied as the average of the measured values at the first elevation. Calculations were made using the TH and DA models to investigate the effect of k at the inlet. For this purpose calculations were made by applying a uniform k at the inlet of 0.5 and 0.25 of the measured average. A variable k at the inlet was also considered by applying the measured values of k at the first elevation as the inlet boundary condition of. Calculated heat transfer and mass flow rates are listed in Table 7.4. The values listed are normalised with respect to the experimental values.

The results indicate a strong dependence on the value of k at the inlet with the results changing by as much as 10 per cent for the TH model. The TH model produced the lowest numerical results for heat transfer and mass flow rates when using a variable k at the inlet. The DA model produced the lowest mass flow rate when using variable k and low heat transfer when $k=0.25 k_{exp,ave}$. Numerical solutions were more dependent on the inlet boundary condition than on grid size.

Table 7.4 The Effect of Inlet Boundary Condition of Turbulent kinetic energy.

The effect of k_0 (UWT, Case 4)				
	TH		DA	
k_0	$\frac{q_{c,num}}{q_{c,exp}}$	$\frac{\dot{m}_{num}}{\dot{m}_{exp}}$	$\frac{q_{c,num}}{q_{c,exp}}$	$\frac{\dot{m}_{num}}{\dot{m}_{exp}}$
$k_{exp,ave}$	1.16	1.04	1.03	0.99
0.5 $k_{exp,ave}$	1.10	1.00	0.99	0.96
0.25 $k_{exp,ave}$	1.07	0.98	0.98	0.94
$k_0=k_{exp}(y)$	1.05	0.96	1.00	0.92

7.3.5 Comparison of Numerical Solutions with Experimental Results

Calculations were performed for all the experimental cases of the UWT and UHF heating modes using a 60 x 60 grid by applying the average of the measured k at the first elevation as a uniform inlet boundary condition. The results of the numerical solutions are presented comparatively in the following sub-sections in respect of heat transfer, mass flow rates, velocity and temperature fields within the channels, the turbulent kinetic energy profiles and the wall temperature variations.

7.3.5.1 Comparisons of Experimental and Numerical Heat Transfer and Mass Flow rates

Calculated heat transfer and mass flow rates for all the cases of the UWT and the UHF experiments are listed in Table 7.5 as values normalised using the experimental values.

The predictions made by the DA model were in closest agreement with the experiments for the UWT heating mode.

For the UHF heating mode the TH model gave the closest predictions of mass flow rates.

For UWT the heat transfer rates were predicted within an accuracy of 18 percent and the mass flow rates within 13 percent depending upon the model. The TH model over estimated both heat transfer and mass flow rates whereas the LB model over predicted the mass flow rates while under estimating the heat transfer rates.

Table 7.5 Comparison of experimental results with numerical solutions.

UWT Heating Mode						
	TH		DA		LB	
Case	$\frac{Q_{c,num}}{Q_{c,exp}}$	$\frac{\dot{m}_{num}}{\dot{m}_{exp}}$	$\frac{Q_{c,num}}{Q_{c,exp}}$	$\frac{\dot{m}_{num}}{\dot{m}_{exp}}$	$\frac{Q_{c,num}}{Q_{c,exp}}$	$\frac{\dot{m}_{num}}{\dot{m}_{exp}}$
$T_w=60\text{ }^\circ\text{C}$	1.18	1.10	1.03	1.10	0.95	1.12
$T_w=75\text{ }^\circ\text{C}$	1.17	1.12	1.02	1.12	0.94	1.13
$T_w=90\text{ }^\circ\text{C}$	1.15	1.05	1.00	1.05	0.92	1.06
$T_w=100\text{ }^\circ\text{C}$	1.16	1.04	1.00	1.03	0.92	1.07
$T_w=130\text{ }^\circ\text{C}$	1.14	0.97	0.98	0.96	0.90	0.97
UHF Heating Mode						
1	1.0	1.46	1.0	1.50	1.0	1.58
2	1.0	1.44	1.0	1.48	1.0	1.55
3	1.0	1.33	1.0	1.37	1.0	1.44

7.3.5.2 Comparisons of Experimental Wall Temperatures with Numerical Predictions for UHF Heating Mode

Experimental and predicted wall temperatures for Case 3 of UHF heating mode case are depicted in Figure 7.9. As the figure indicates, all of the models closely captured the character of the wall temperature distribution. The predictions of the LB model were in very good agreement with experimental values over the first half of the channel while over predicting the values in the upper half. In contrast, the DA model under predicted the temperatures in the first half with very good prediction in the upper half. The TH model however, under predicted the wall temperatures throughout the channel.

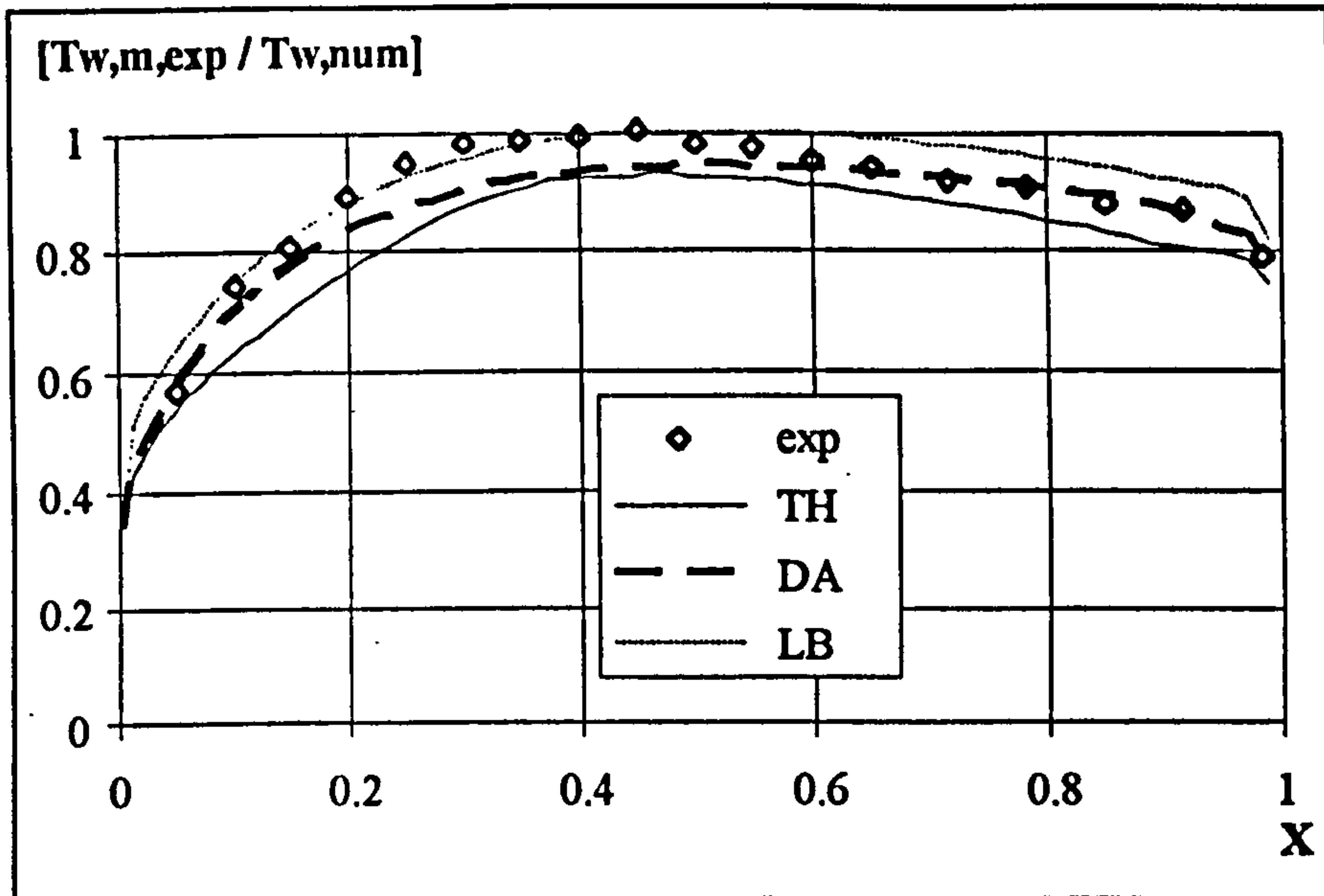


Figure 7.9 Experimental and numerical wall temperature distribution, UHF case 3.

7.3.5.3 Comparisons of Mean Velocity and Temperature Profiles for Selected Cases with Experimental Results

Numerical and experimental velocity and temperature profiles for Case 4 of UWT and Case 3 of UHF heating modes are presented in Figures 7.10 to 7.19. The axis shift method of plotting was again used. The velocity profiles were non-dimensionalised as before using the highest velocity as reference, whether experimental or numerical. Temperature was non-dimensionalised using equation (6.1). In the figures, numerical values are graphed using continuous lines.

Three turbulence models used predict the velocity profiles for the UWT heating mode very closely except for $X=0.5$ and 0.63 . However the LB model predicts the profiles at $X=0.5$ and 0.63 better than the other two models. The temperature profile near the exit of the channel is best predicted by the TH model, though it over-predicts the values in the core of the channel. The other two models under estimate the temperatures near the wall. The temperatures in the core of the channel are better predicted by the LB model.

The experimental velocity and temperature profiles for Case 3 of UHF heating mode are given in Figures 7.14 to 7.18 together with the predicted profiles. The velocity profiles clearly show over-prediction by all the models, although the predictions near the heated wall at the uppermost elevations agree with the measurements. The velocity profiles predicted by the TH model are better than the others. Temperature profiles up to the half height of the channel are well predicted by all the models. However the two profiles in the upper portion of the channel are under estimated by all the models. The best predictions of the temperature profiles, however, were made by the TH model. Temperatures in the core region of the channel were successfully predicted by all the models.

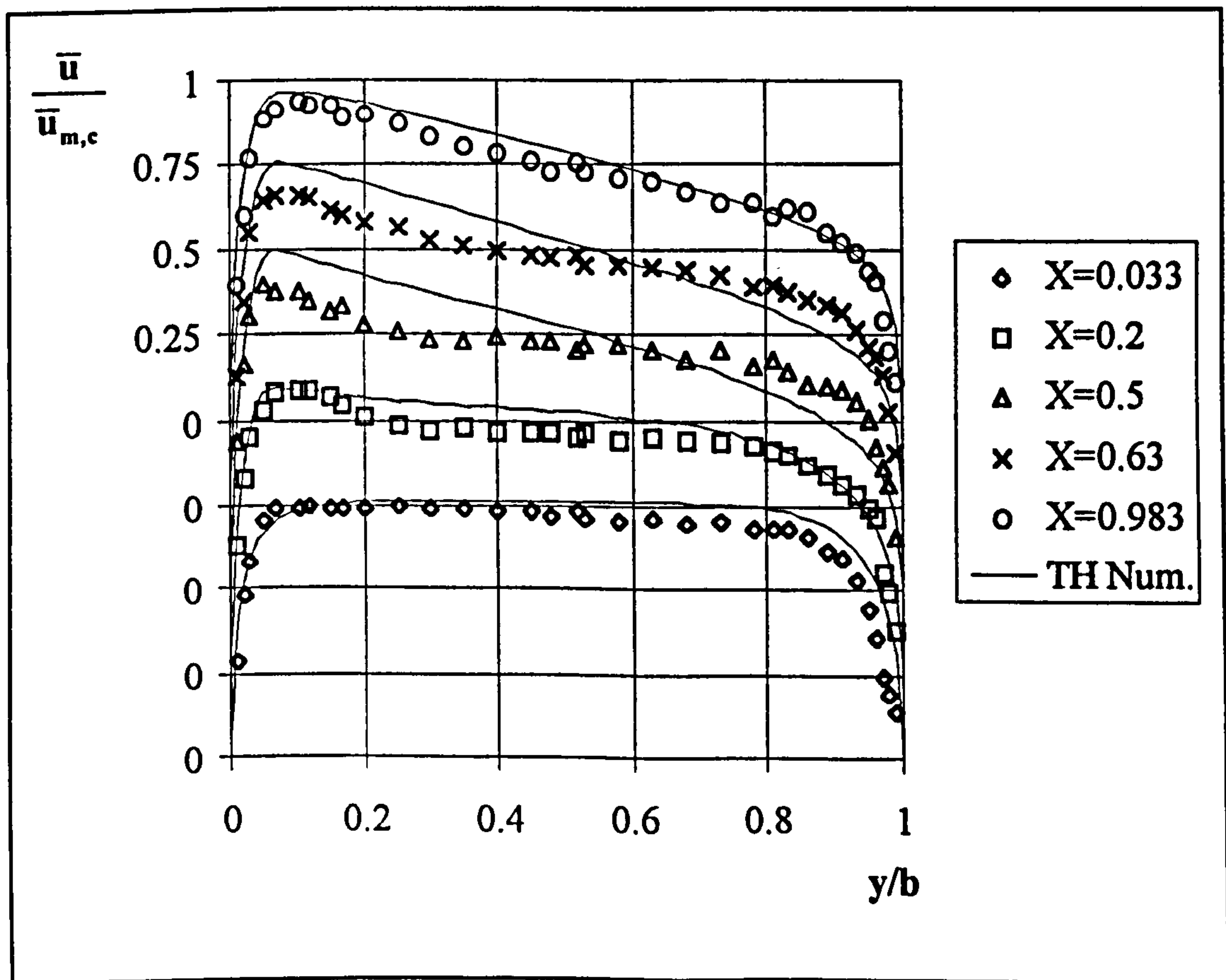


Figure 7.10 Experimental and numerical velocity profiles, UWT Case 4, TH model.

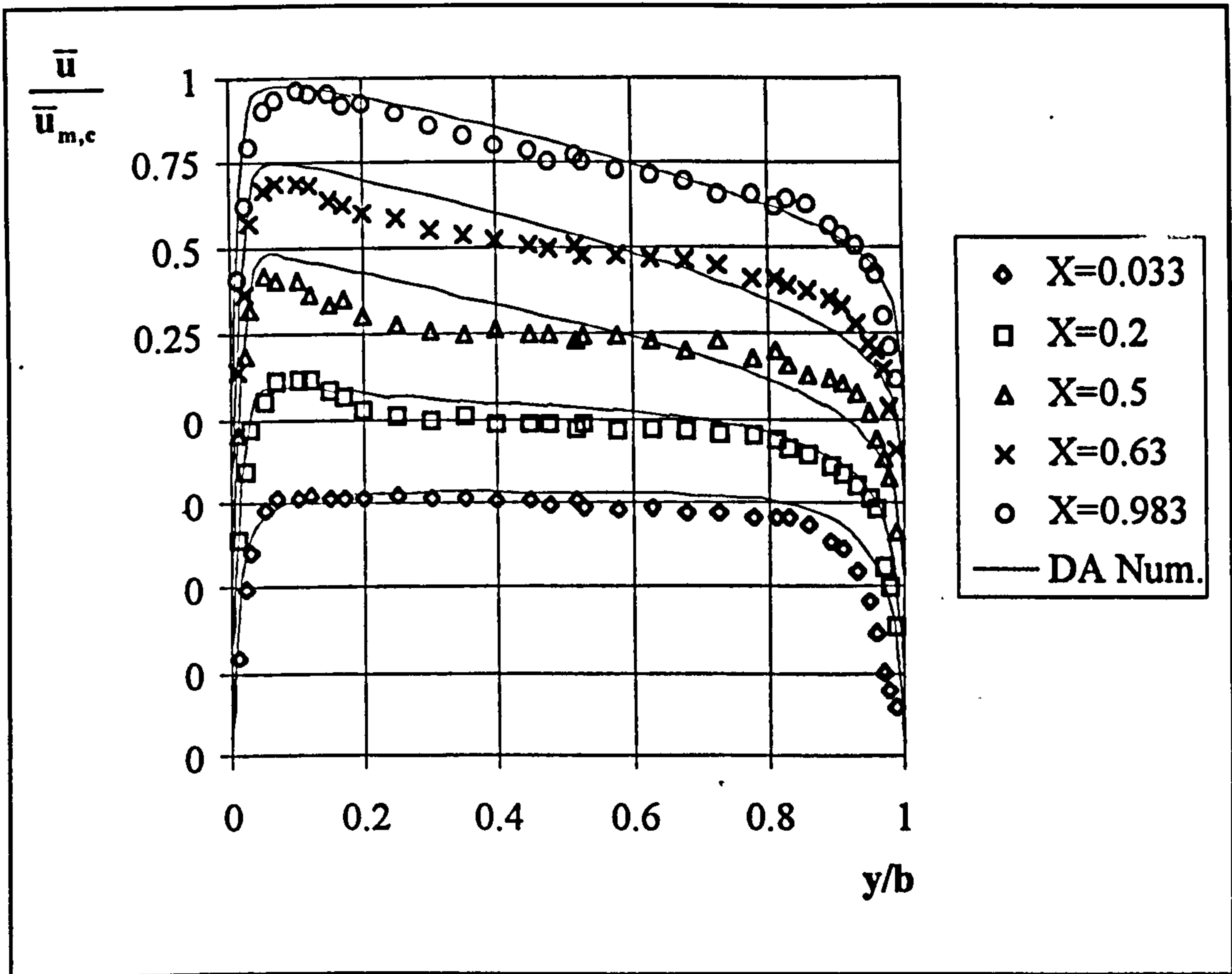


Figure 7.11 Experimental and numerical velocity profiles, UWT Case 4, DA model.

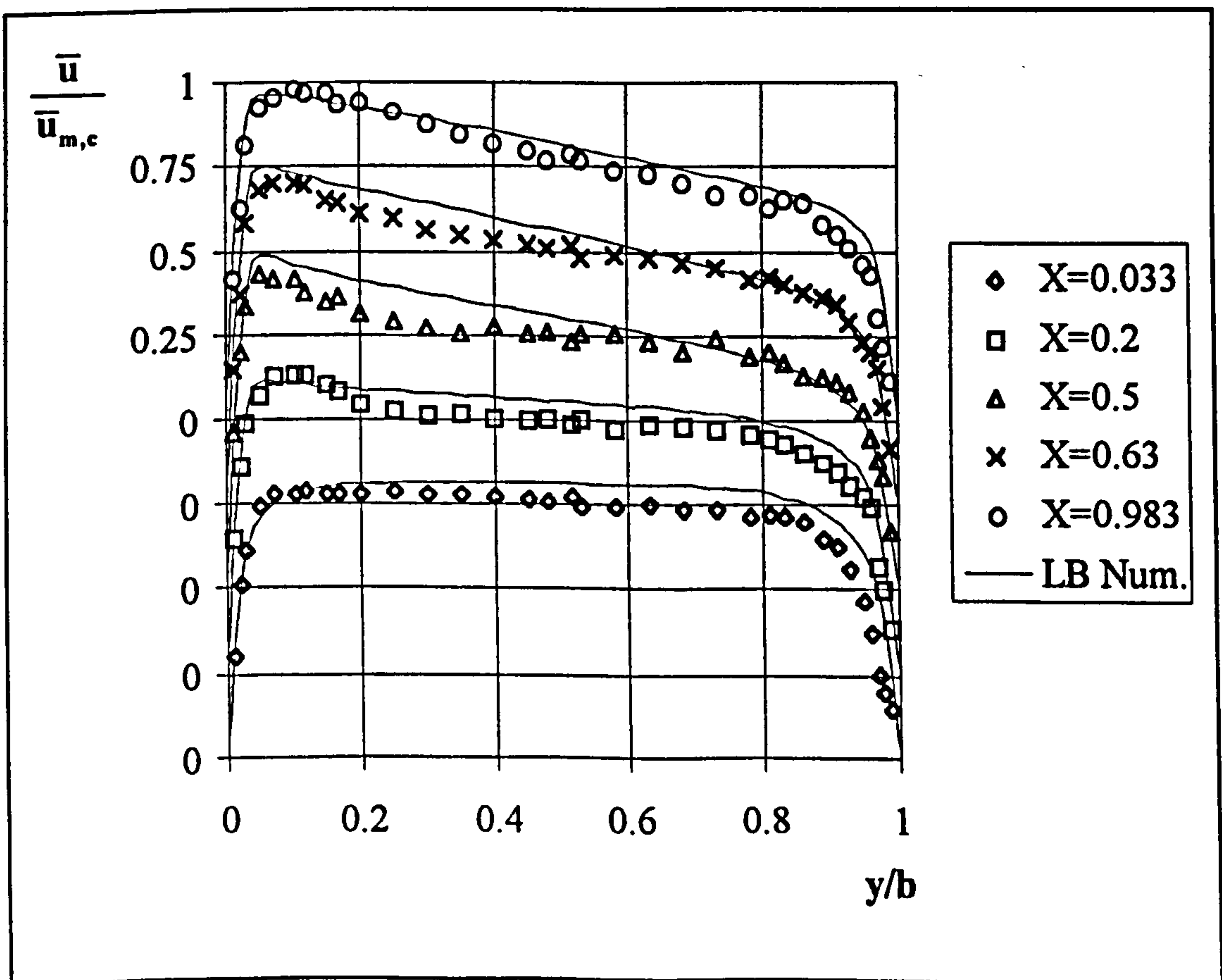


Figure 7.12 Experimental and numerical velocity profiles, UWT Case 4, LB model.

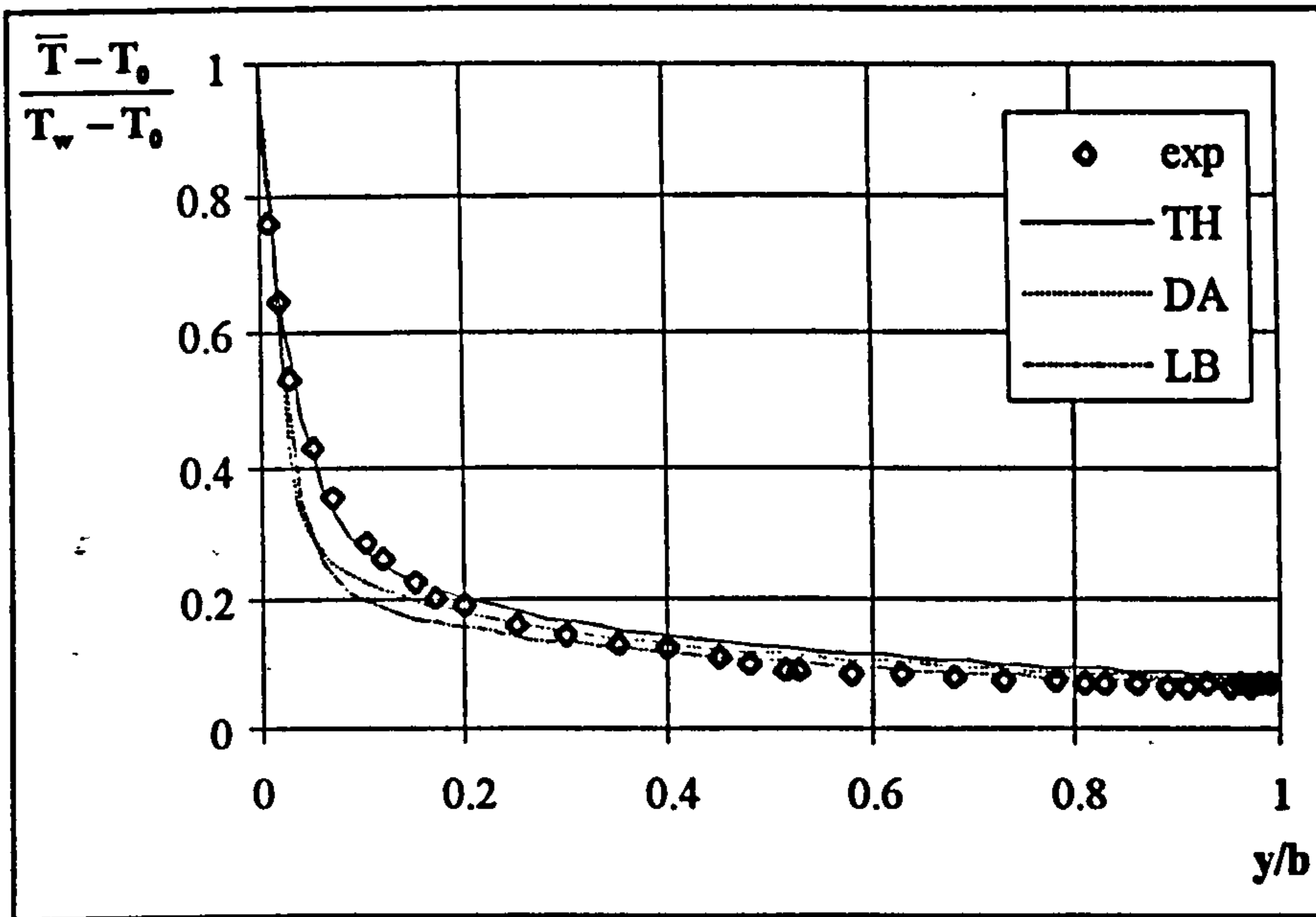


Figure 7.13 Experimental and numerical temperature profiles at exit, UWT Case 4.

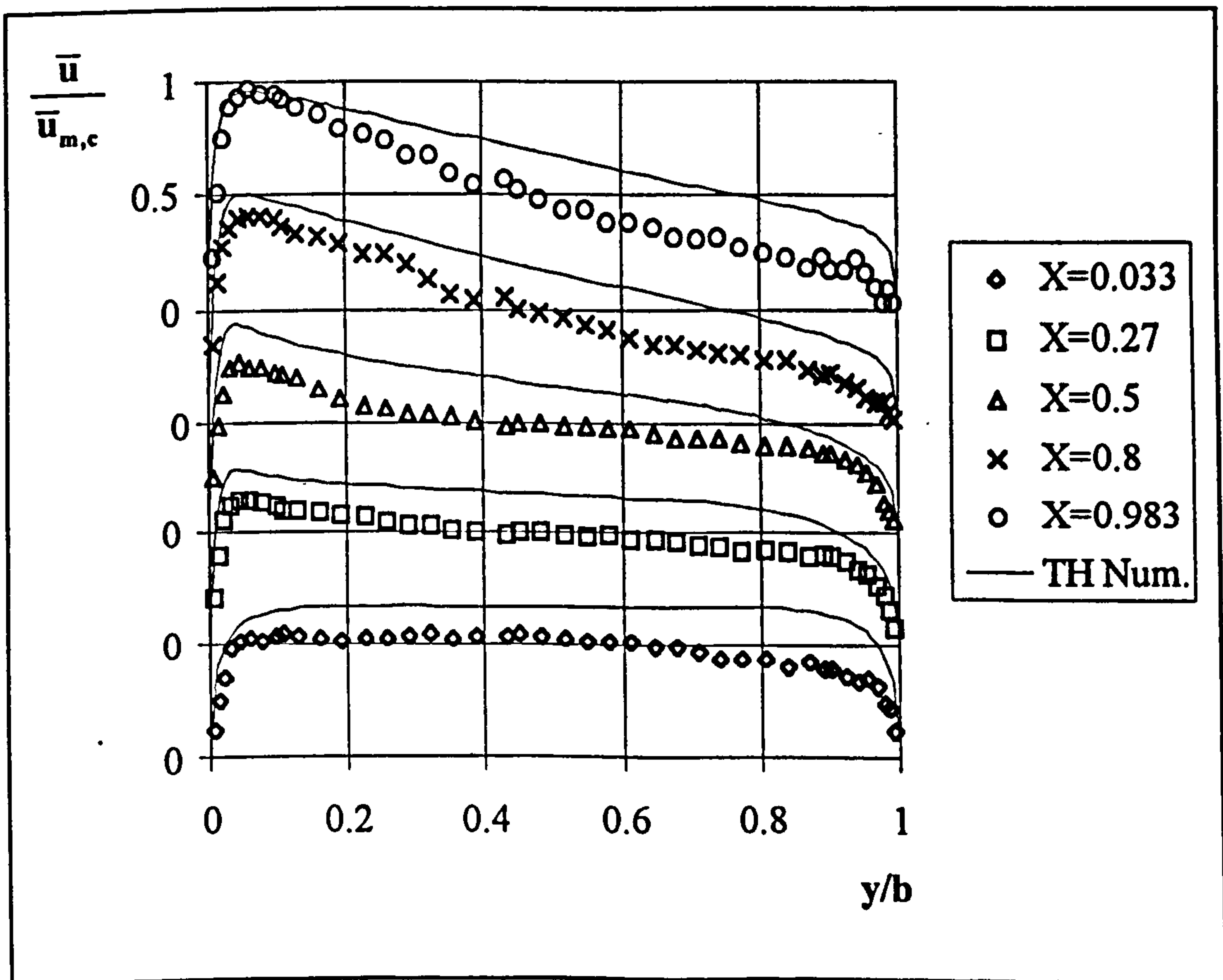


Figure 7.14 Experimental and numerical velocity profiles, UHF Case 3, TH model.

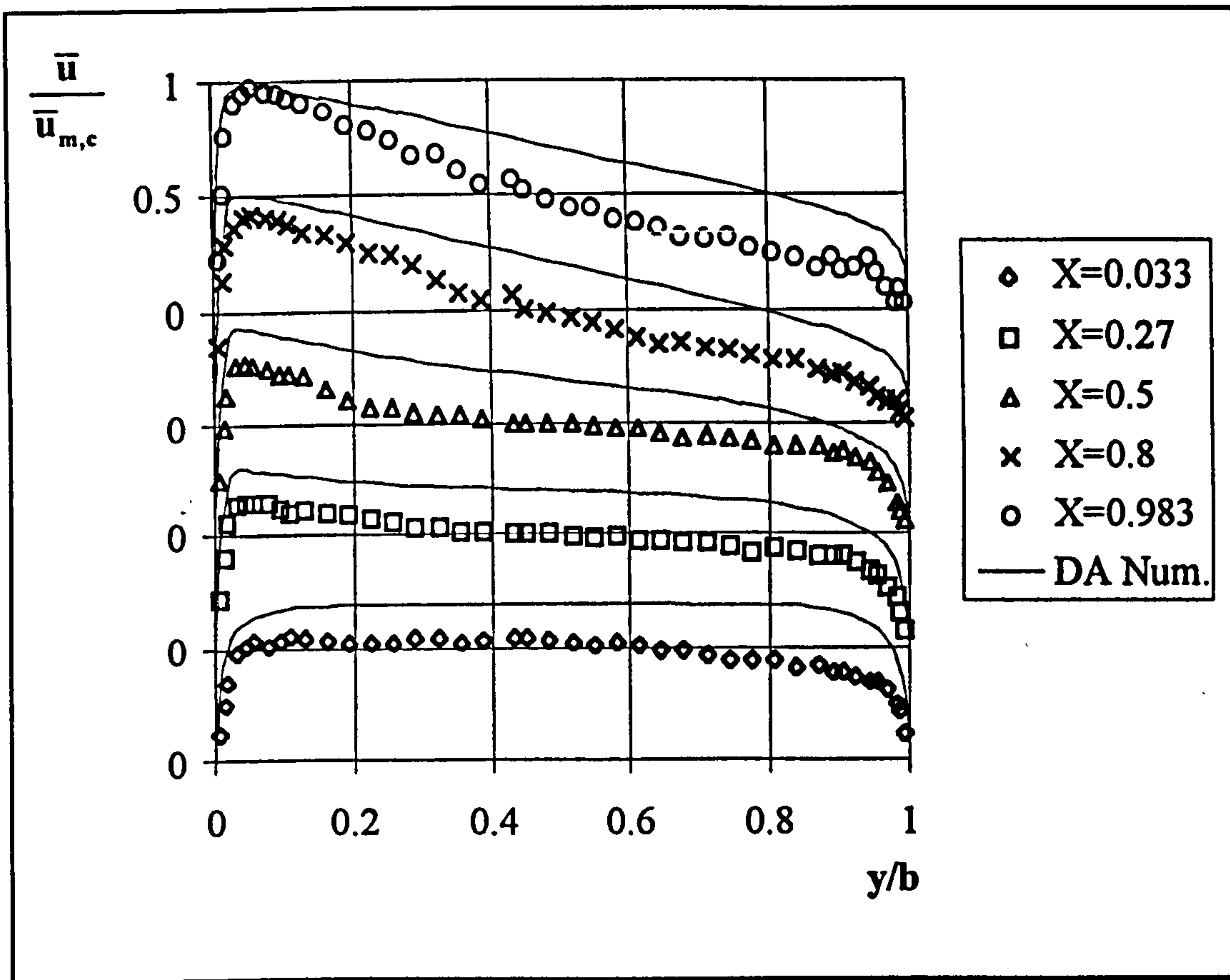


Figure 7.15 Experimental and numerical velocity profiles, UHF Case 3, DA model.

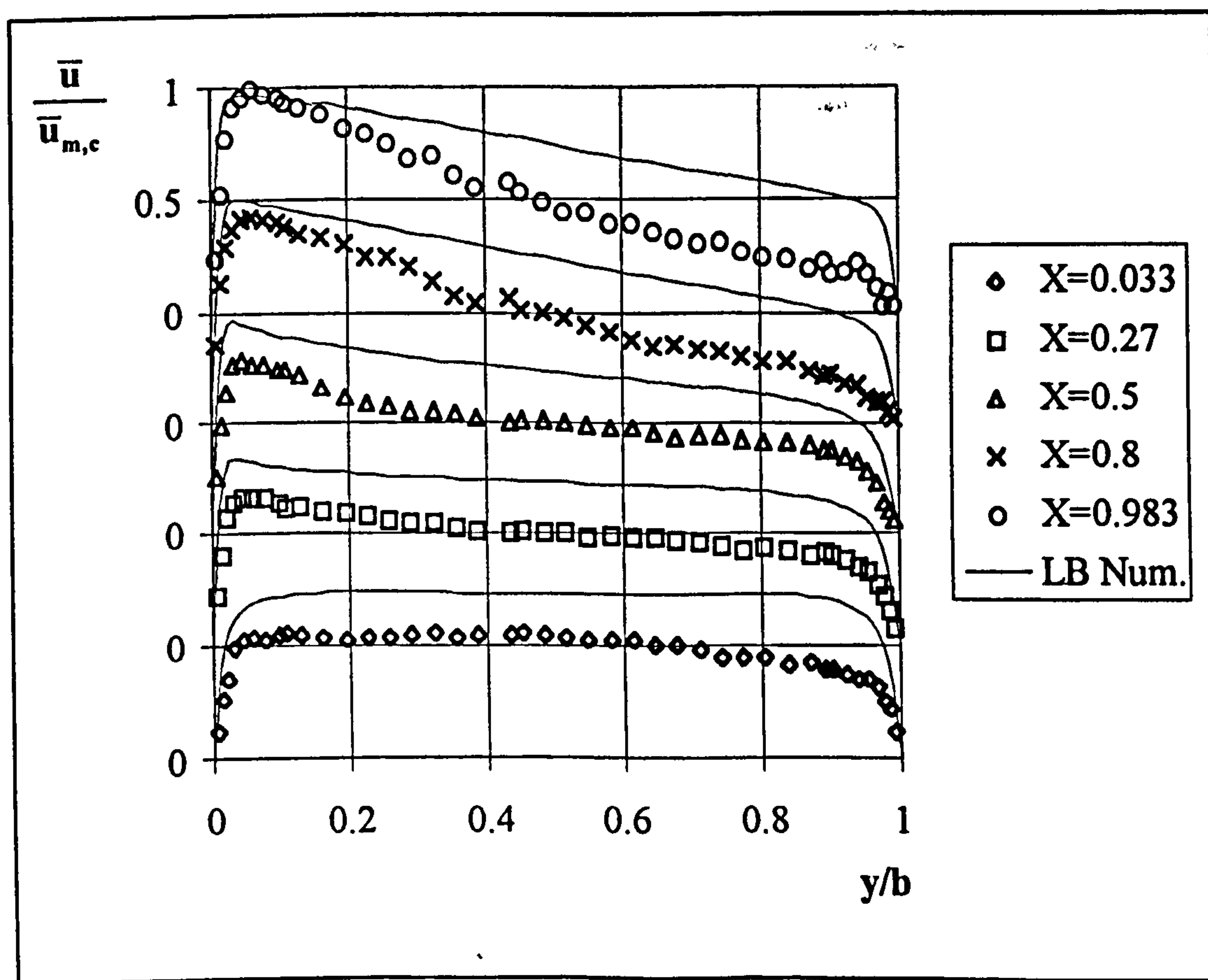


Figure 7.16 Experimental and numerical velocity profiles, UHF Case 3, LB model.

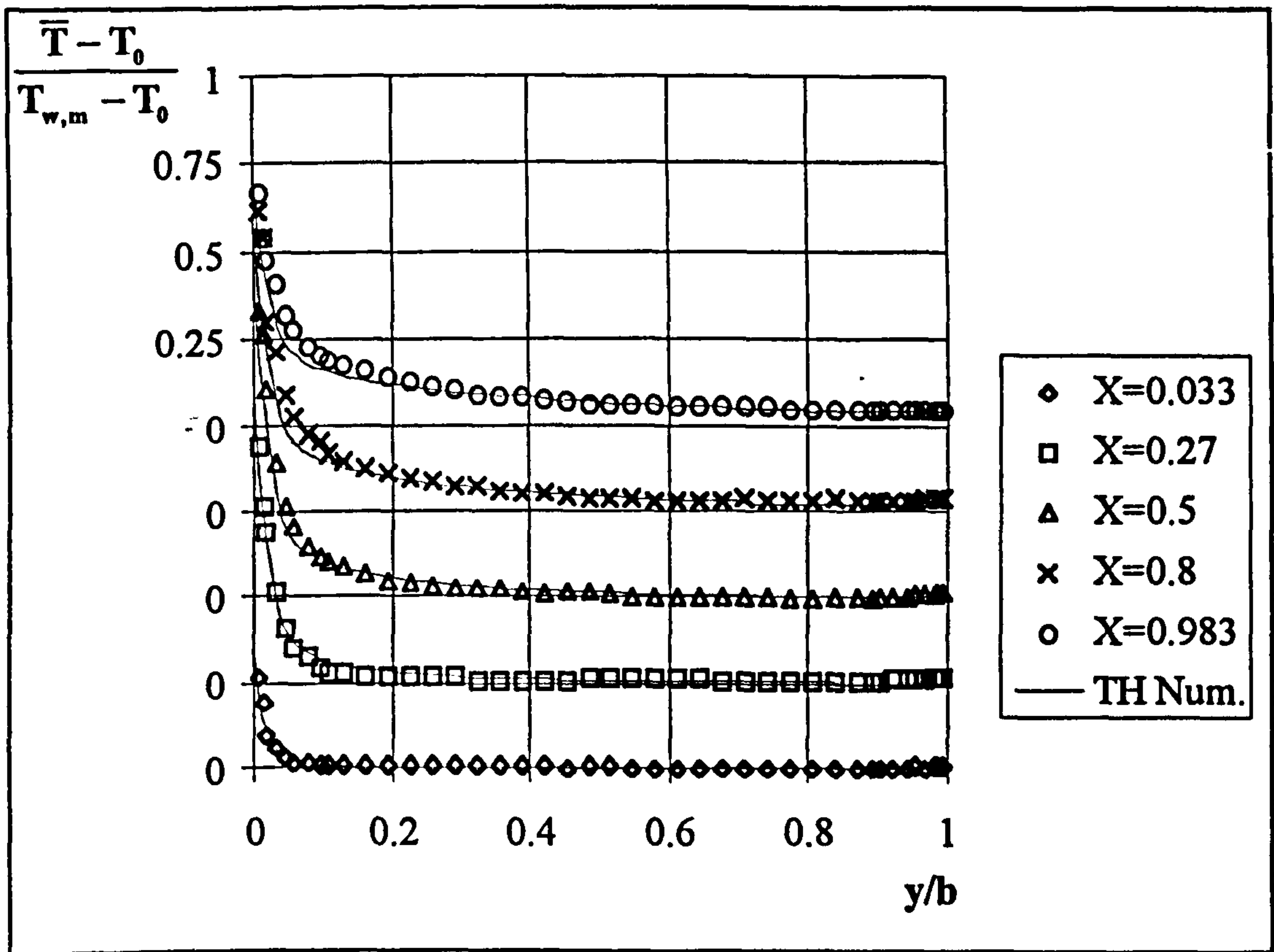


Figure 7.17 Experimental and numerical temp. profiles, UHF Case 3, TH model.

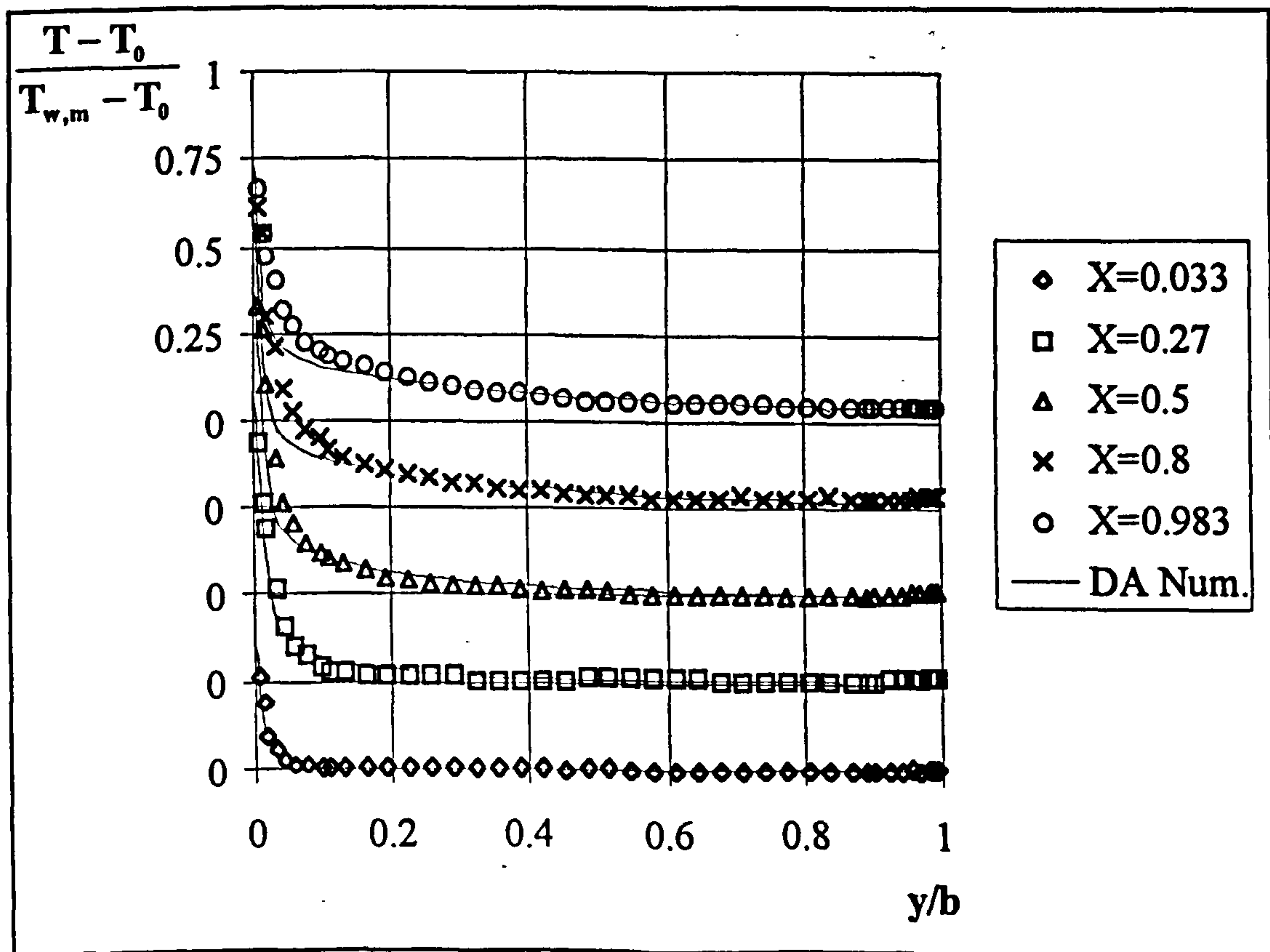


Figure 7.18 Experimental and numerical temp. profiles, UHF Case 3, DA model.

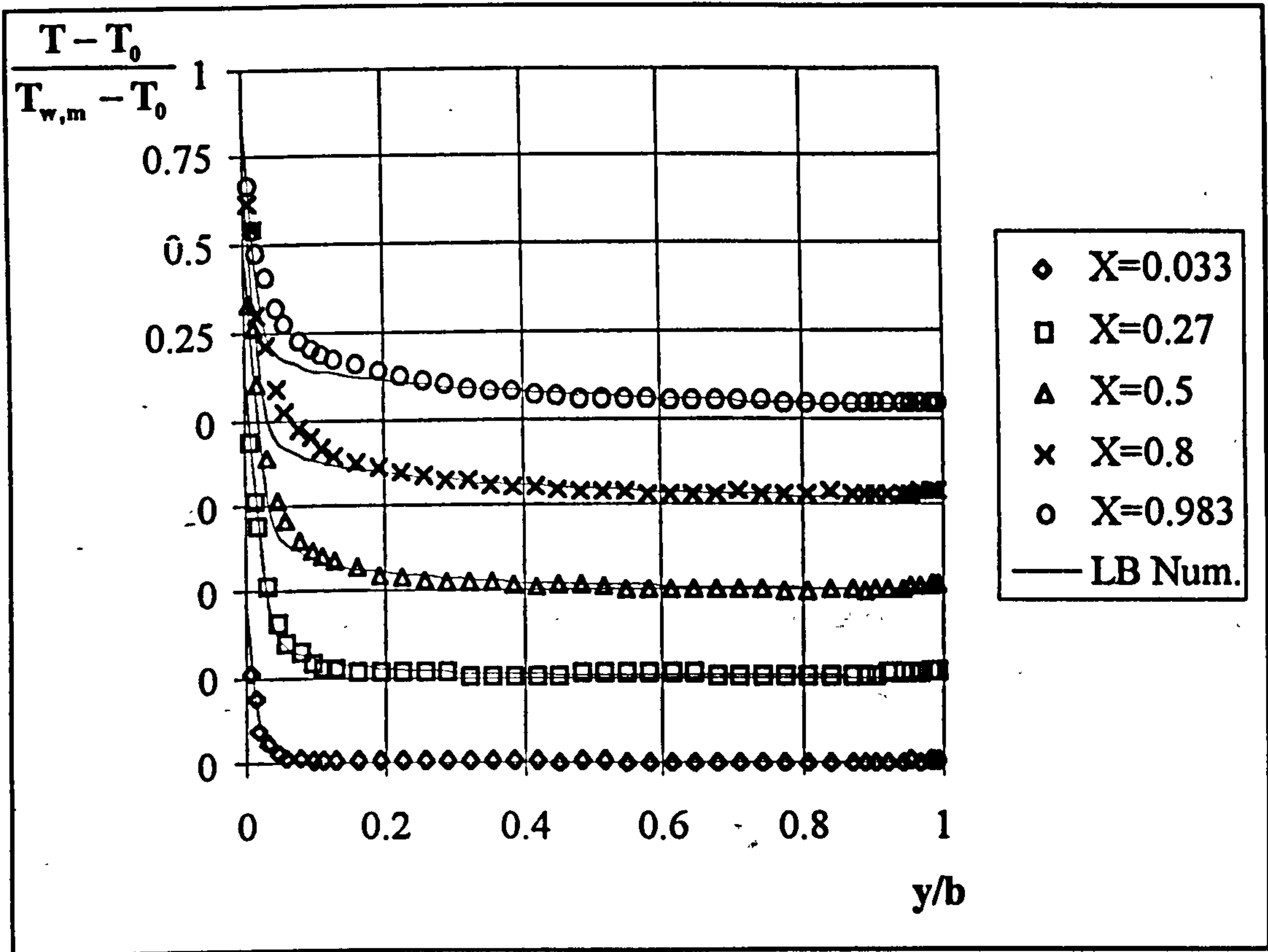


Figure 7.19 Experimental and numerical temp. profiles, UHF Case 3, LB model

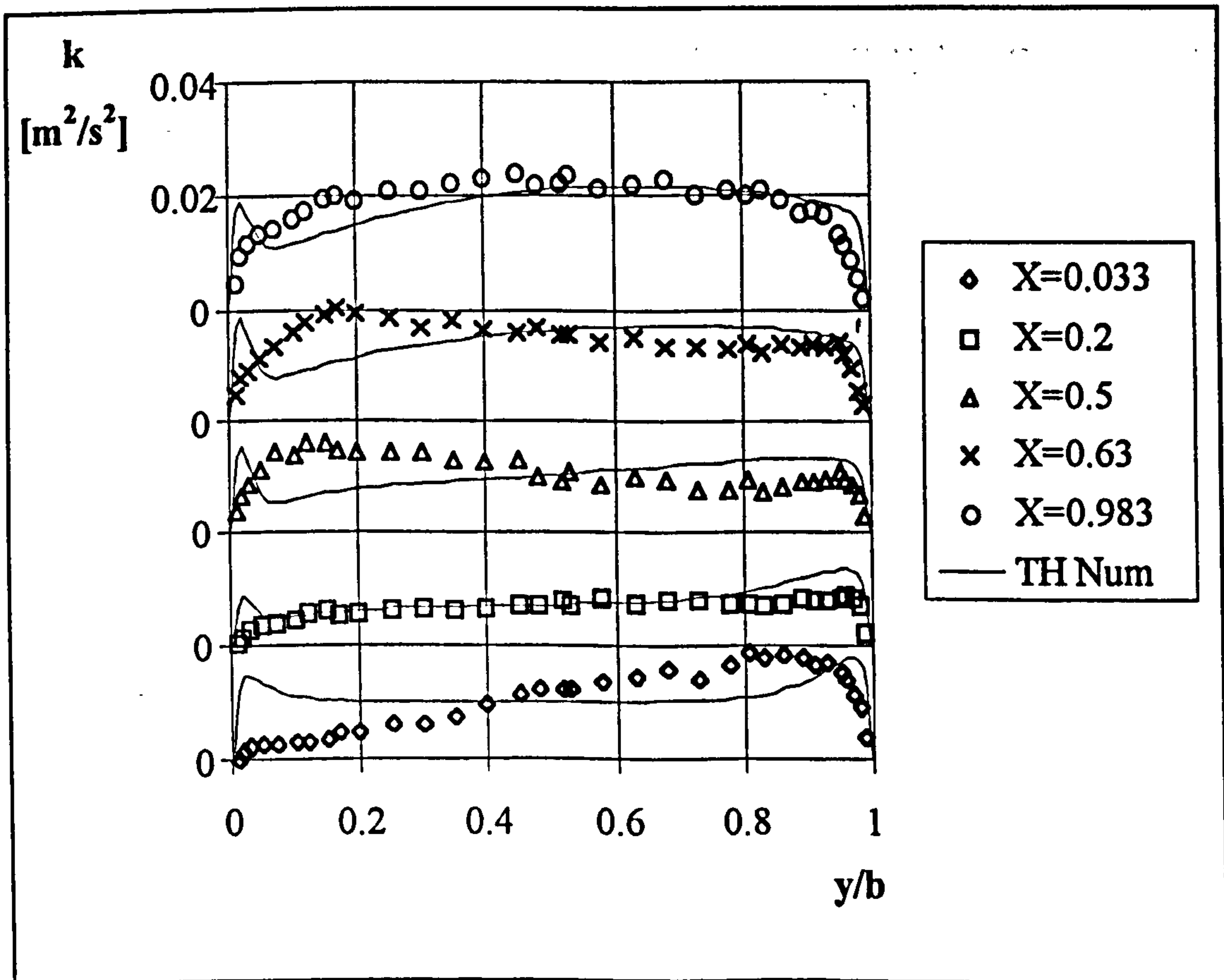


Figure 7.20 Experimental and numerical k profiles, UWT Case 4, TH model.

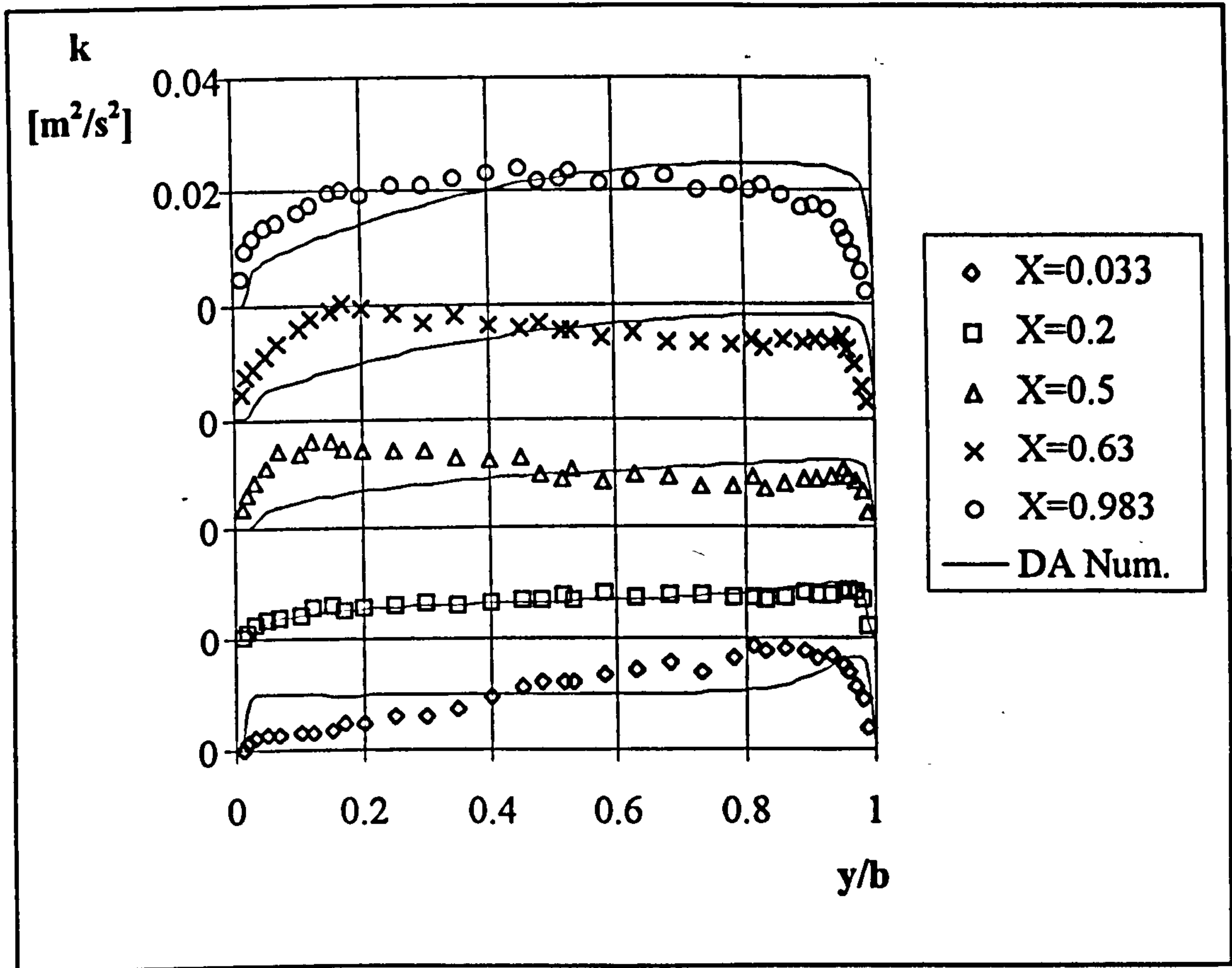


Figure 7.21 Experimental and numerical k profiles, UWT Case 4, DA model.

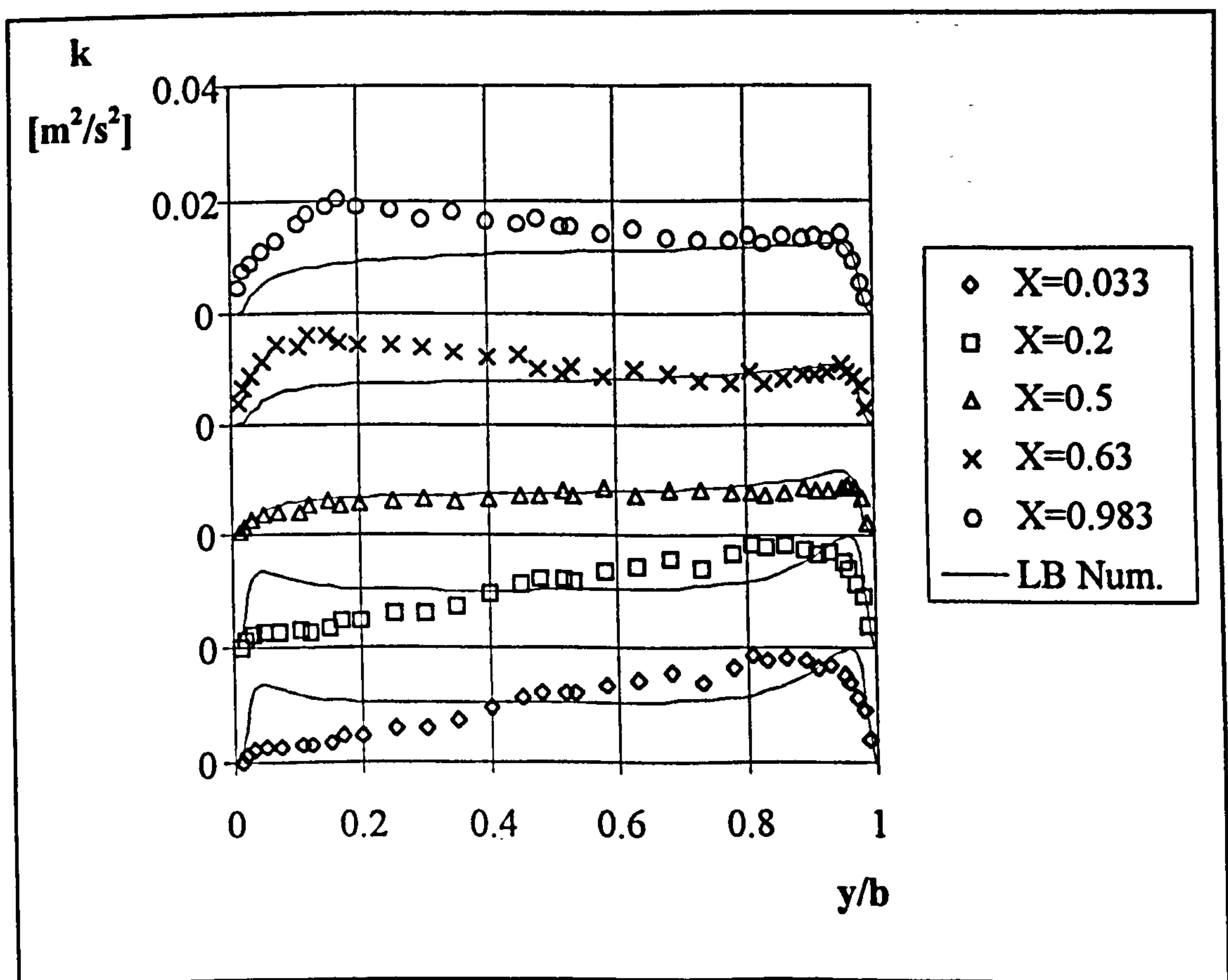


Figure 7.22 Experimental and numerical k profiles, UWT Case 4, LB model

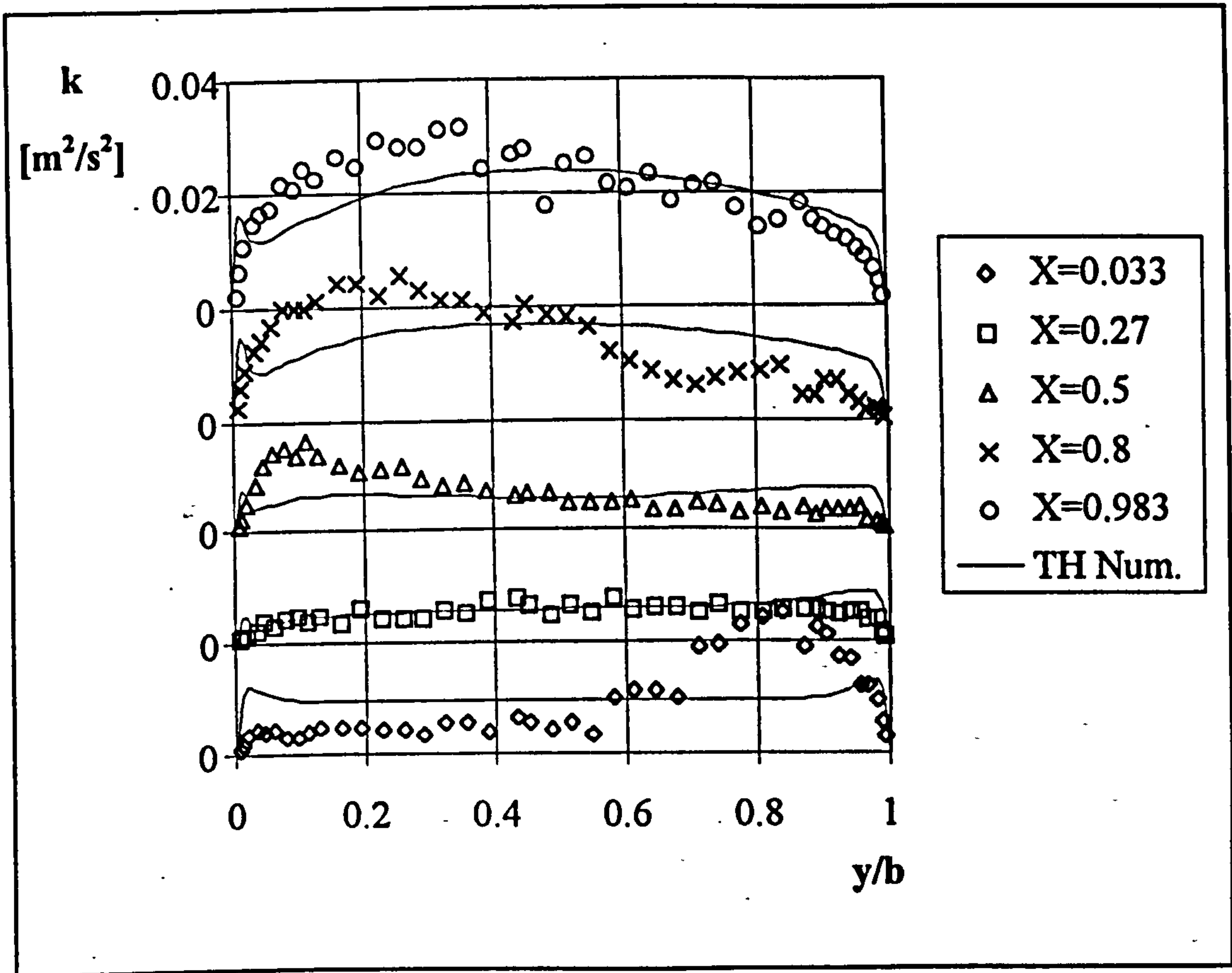


Figure 7.23 Experimental and numerical k profiles, UHF Case 3, TH model.

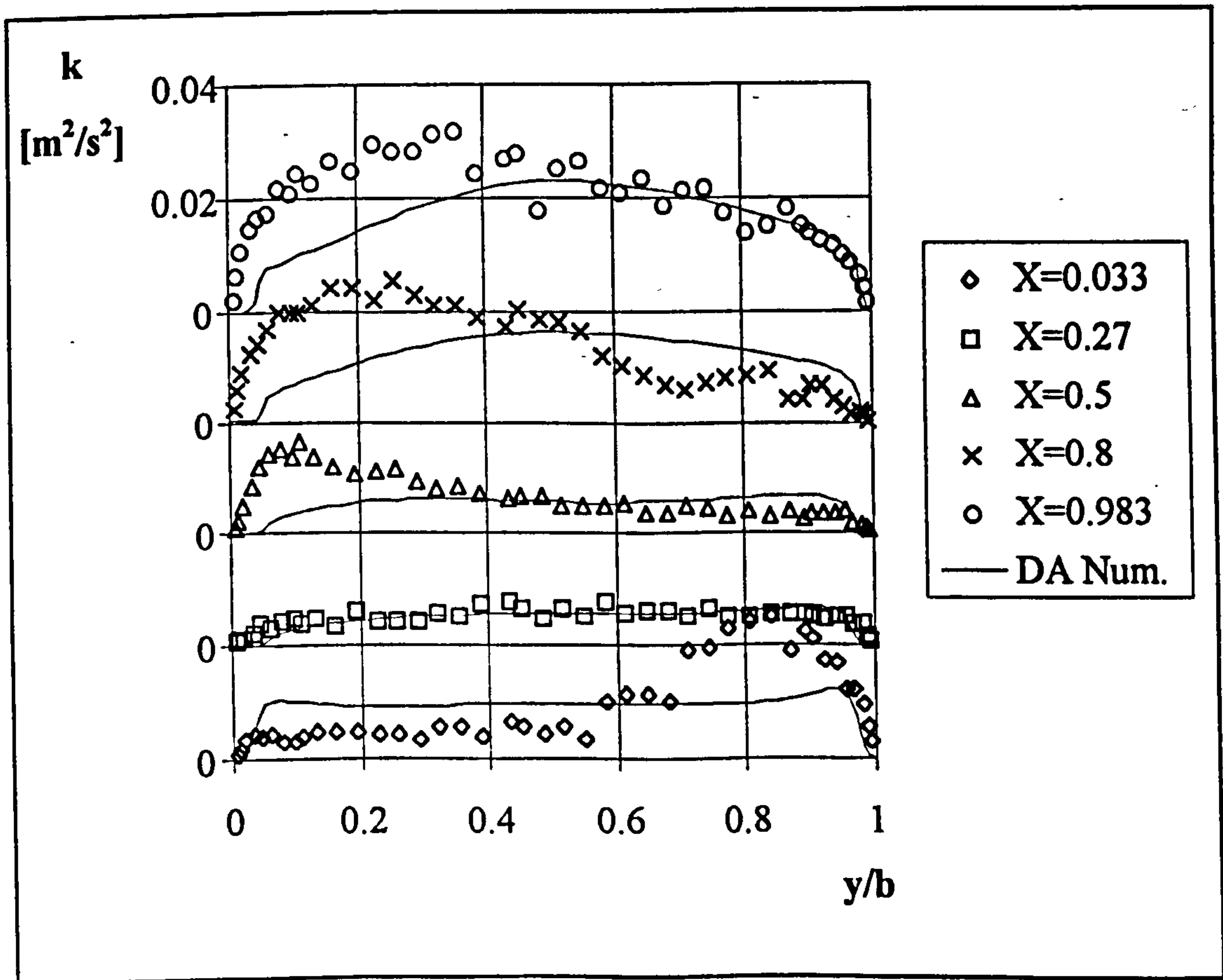


Figure 7.24 Experimental and numerical k profiles, UHF Case 3, DA model.

7.3.5.4 Comparisons of Turbulent Kinetic Energy Profiles of Selected Cases with Experimental Results

Experimental and numerical turbulent kinetic energy profiles of case 4 of UWT heating mode and case 3 of UHF heating mode are presented in Figures 7.20 to 7.24. In the numerical solutions, the inlet BC of turbulent kinetic energy was taken as the average of the measurement at the first elevation, $X=0.033$. The figures show that both DA and LB models produced similar profiles. The TH model has produced the best predictions for both UWT and UHF heating modes. It has predicted a sharp peak and drop near the heated wall. The profile at $X=0.2$ was perfectly captured by all the models for both heating mode. The profiles near the channel exit, the fully developed turbulent region has been captured correctly by the TH model only. The models of DA and LB has produced zero values near the heated wall whilst capturing the profile near the adiabatic wall correctly.

7.3.6 Summary and Conclusions

Numerical analysis of turbulent natural convection has been carried out for both UWT and UHF heating mode. Grid dependence of numerical solutions and the effect of inlet BC of k has been examined. Numerical solutions are found to be most sensitive to the inlet BC of k . Comparison of numerical solution results with the measurements were made. Among the models considered, DA has been found to be grid sensitive and needed very fine grid near the walls. The heat transfer and mass flow rates were best predicted by the model of DA, but the flow, temperature and kinetic energy fields best predicted by TH model. Numerical solutions have predicted excessively high mass flow rates for UHF heating mode by all the models. The method, and the tool of the numerical analysis considered in this study can be confidently used for UWT heating mode.

7.4 Correlating Equations

No correlations were sought for heat transfer and induced flow rates for the laminar channel flow . The results of this study indicated that, for the channel geometries similar to that of this study, numerical solutions will produce results with an accuracy better than 10 % of experiments as long as thermal BCs are exactly known.

The number of experiments for UHF heating mode was not adequate to produce correlating equations similar to those of UWT. Thus, no attempt was made to correlate induced mass flow rates.

Correlating equations were obtained for the Nusselt number and Reynolds number as functions of $GrPr(b/H)$ from the numerical solutions of UWT heating mode. Experiments of UWT heating mode covered five different wall temperatures for the channel aspect ratio of 1/30. Velocity measurements were also made for one wall temperature of aspect ratio $\approx 1/20$. That allowed the correlation UWF experimental values Re as function of $GrPr(b/H)$. However, when Re were plotted as a function of $GrPr(b/H)$ on a log-log plot, the data did not collapse on a straight line. Thus, Re/Gr vs $GrPr(b/H)$ was considered, equation (7.1). From the correlated values of Re , average inlet velocities were calculated for a wide range of $GrPr(b/H)$ which are not covered by the experiments. Using the calculated inlet velocities to determine average kinetic energies at the inlet for 10 % turbulence intensity at the inlet. Using this k value further cases were numerically calculated in order to cover a wide range of $GrPr(b/H)$.

From the results of the numerical analysis performed employing the models of TH and DA correlations of Nu and Re/Gr given in equations (7.2) to (7.5) are obtained.

$$(Re/Gr)_{exp} = 0.4691Gr Pr(b/H)^{-0.5396} \quad (7.1)$$

$$(\text{Re}/\text{Gr})_{\text{TH}} = 0.4691 \text{Gr Pr} (b/H)^{-0.5577} \quad (7.2)$$

$$(\text{Re}/\text{Gr})_{\text{DA}} = 0.4775 \text{Gr Pr} (b/H)^{-0.5595} \quad (7.3)$$

$$\text{Nu}_{\text{TH}} = 1.008 \text{Gr Pr} (b/H)^{0.2427} \quad (7.4)$$

$$\text{Nu}_{\text{DA}} = 0.5584 \text{Gr Pr} (b/H)^{0.2806} \quad (7.5)$$

The correlating equations for Re/Gr are presented in Figure 7.25. in graphical form. The figure shows that at low values of GrPr(b/h) numerical models over predict the mass flow rates and both models collapse on a single line.

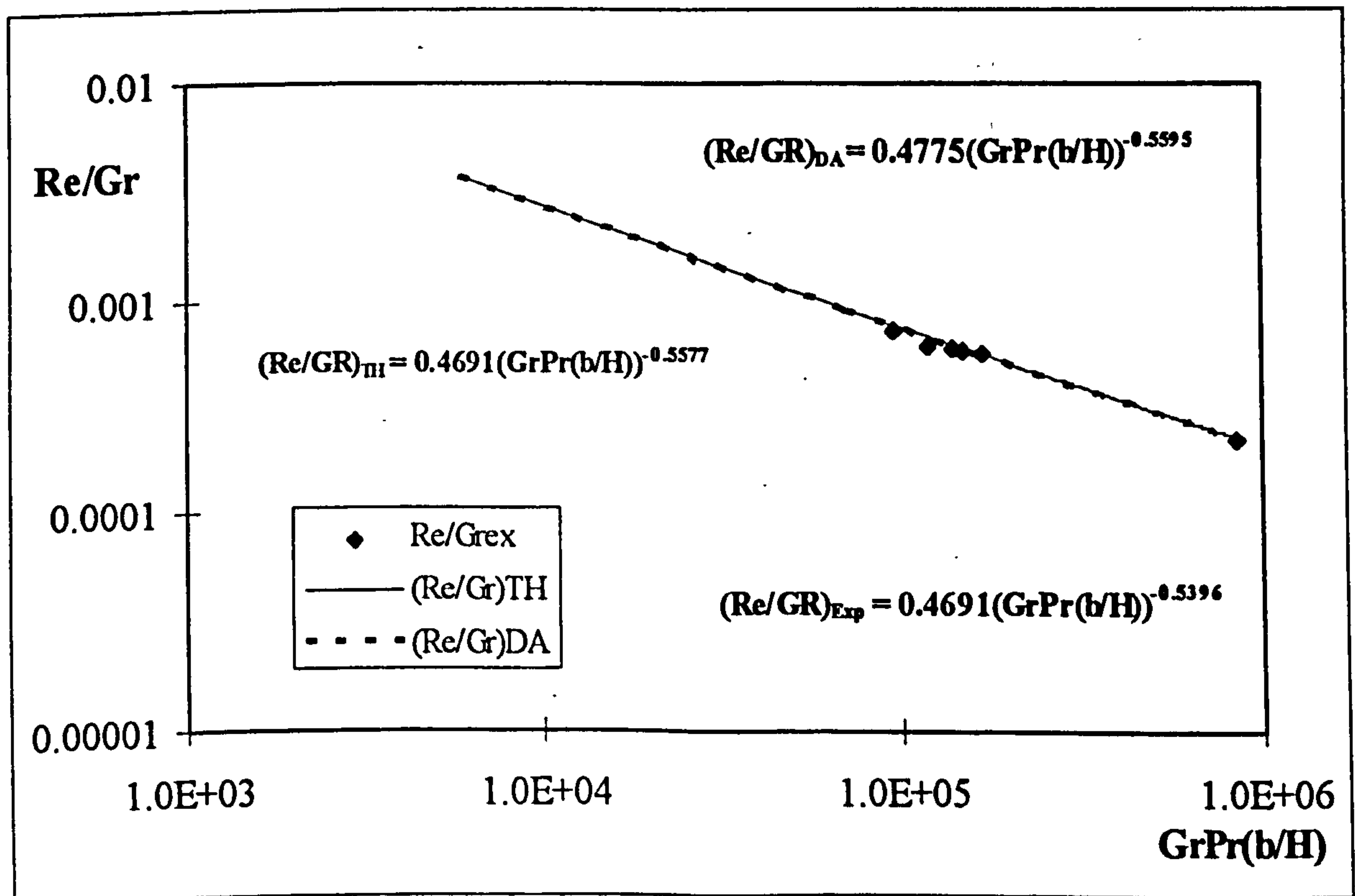


Figure 7.25 Experimental and numerical Re/GR as function of GrPr(b/H)

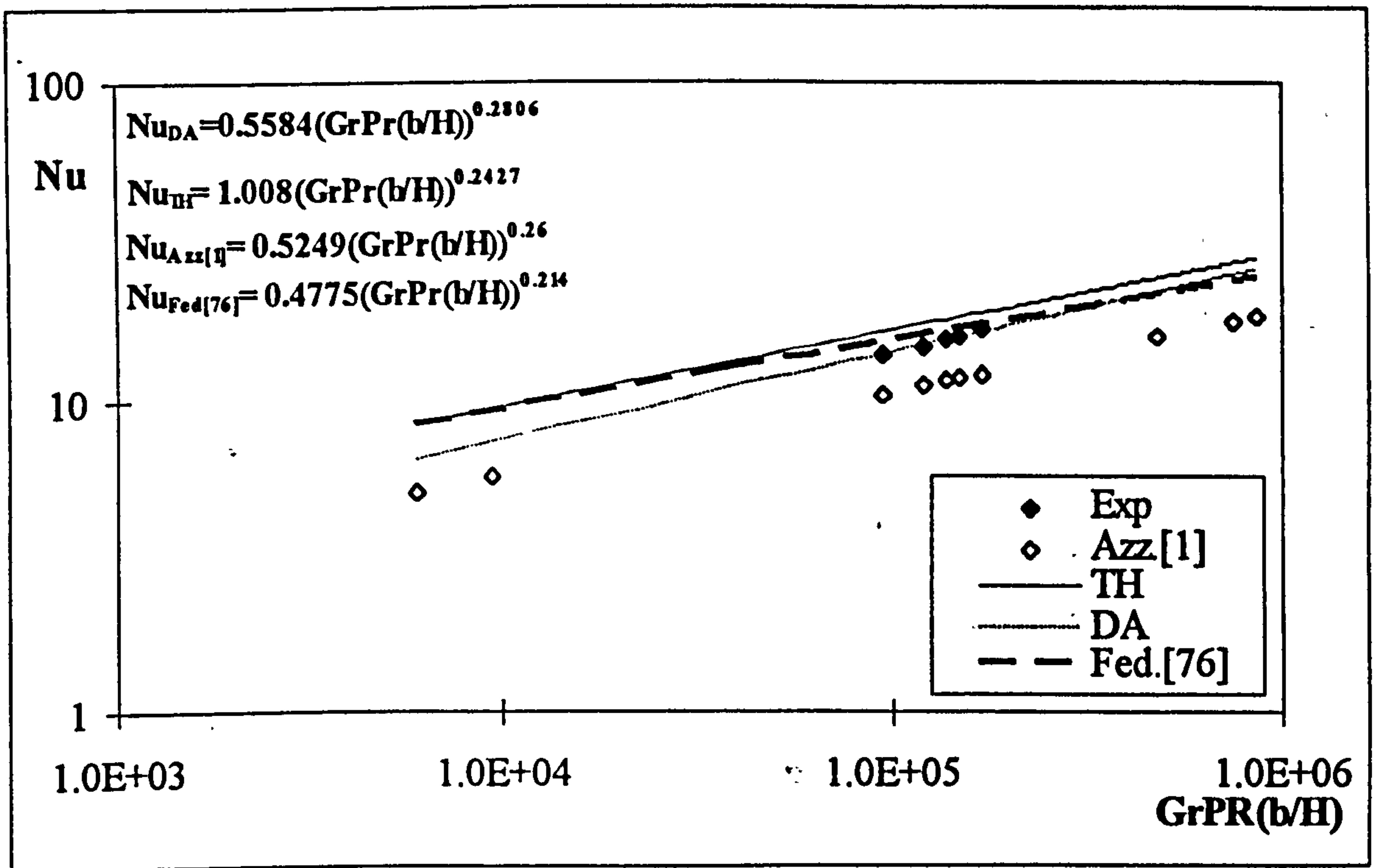


Figure 7.26 Numerical and experimental Nu as function of GrPr(b/H)

In Figure 7.26, numerically obtained correlations and experimental data are presented comparatively with the experimental results of Al Azzawi [1] and the numerical results of Fedorov and Viskanta [76]. The model of DA perfectly predicts the heat transfer in the present experimental range whereas The model of TH slightly over predicts the heat transfer. However, the predictions of both models remains almost within the experimental uncertainty limit. The difference between the predictions of the two models is large at low values of GrPr(b/H). Two lines converge as the value of GrPr(b/H) increases. The Fluid properties for the calculation of the dimensionless parameters were taken as the values at the average temperature of wall and inlet temperatures. The correlating equations can be confidently used within the GrPr(b/H) range of 10^5 and 10^6 . The inaccuracy at the low values of GrPr(b/H) should not be too much, but experimental data is needed to give the level of accuracy.

The results of Fedorov and Viskanta [76] do differ from the results of the model of TH obtained in this study although they used the same turbulence model. However,

they used a different definition for the value of k at the inlet of the channel. This may be the reason for the difference, particularly for the larger values of $GrPr(b/H)$.

Experimental results of Al Azzawi [1] are considerably lower than the experimental results of present study, although the trends of the results are very similar. The difference is attributed to the slightly different heating mode and measurement techniques used by Al Azzawi.

CHAPTER 8. CONCLUSIONS AND RECOMMENDATIONS FOR FUTURE STUDY

8.1 Conclusions

Laminar and turbulent natural convection heat transfer and fluid flow processes in asymmetrically heated vertical parallel flat plate channels have been investigated both experimentally and numerically. Three different experimental channels were built to carry out the experimental analysis. Air velocity and temperature measurements were made inside the channel. Turbulent kinetic energy profiles were calculated from the velocity data. A constant non-uniform wall heat flux BC was considered for the laminar natural convection. Turbulent natural convection was examined for both UHF and UWT BCs. Velocity measurements were made using LDA, and simultaneous temperature measurements for turbulent UHF BC were made using a Cr-Al thermocouple. The numerical analysis was carried out using the commercial CFD code of PHOENICS. Four different turbulence models were built into PHOENICS for the numerical analysis of turbulent natural convection. The results of experimental and numerical analysis have been presented and comparisons were made. Based upon the results following conclusions are made.

- 1) In laminar natural convection thermal radiation has plays an important role in heat transfer processes if the surface emissivities are high.
- 2) At high channel aspect ratios in laminar natural convection, flow reversals occur in the upper portion of the channel as deep as 1/3 of the channel height.
- 3) Numerical method and the code used in this study can predict overall heat transfer and mass flow rates, temperature and velocity fields of laminar natural convection with good accuracy if the BCs are known exactly.
- 4) At high channel aspect ratios the difference between the measured and calculated mass flow rates of laminar natural convection are the highest.
- 5) The flow in the channel starts laminar with some turbulence confined to half of the channel near the front wall, as the flow develops downstream, some of the

turbulence is destroyed, from the half height of the channel turbulence levels increase and fully developed turbulence is reached at the exit of the channel.

- 6) Heat transfer and mass flow rates are estimated with the considered turbulence models with good accuracy for UWT heating mode (BC).
- 7) The flow, temperature and turbulent kinetic energy field are best predicted by TH turbulence model.
- 8) Numerical prediction of mass flow rates for UHF heating mode was not as accurate.
- 9) Further experimental study is necessary in order to get data on the process of transition to turbulence.
- 10) Correlating equations produced for the UWT turbulent natural convection can be used confidently for the design purposes.

8.2 Recommendation for Future Study

The following items are recommended for future study.

- 1) The effect of radiation in the heat transfer processes can be experimentally investigated by changing the surface emissivities.
- 2) Numerical conjugate heat transfer analysis can be carried out to determine the front wall temperatures .
- 3) Flow visualisation can be used to study the flow reversals at high channel aspect ratios of laminar flow.
- 4) Experiments may be performed to collect heat transfer and mass flow rate data for a wide range of Ra in turbulent natural convection.
- 5) Flows visualisation can be employed to study transition to turbulence.
- 6) Reynolds stress model of turbulence can be used in the numerical calculations of turbulent natural convection.

REFERENCES

- [1]. Al-Azzawi, A.R.H., 'Natural Convection in a Vertical Channel Related to Passive Solar Systems,' Ph.D. Thesis, University of Strathclyde, Glasgow, UK, 1987.
- [2]. Sohn, D., 'A Numerical Study of Turbulent Natural Convection in a Vertical Parallel Plate Channel With Symmetric and Asymmetric Heating,' Ph.D. Thesis, Department of Mechanical Engineering, The Pennsylvania State University, USA, 1989.
- [3]. Carey, C., Gilchrist, A., and Yilmaz, T., 'Laminar Natural Convection in a Vertical Channel,' *Proceedings of the 3rd International Conference, LDA Applications & Advances*, Swansea, UK, 1989.
- [4]. Elenbaas, W., 'Heat Dissipation of Parallel Plates by Free Convection,' *Physica*, Vol. 9, pp. 1-28, 1942.
- [5]. Ostrach, S., 'Laminar Natural Convection Flow Heat Transfer of Fluids with and without Heat Sources in Channels with Constant Wall Temperatures,' *NACA Technical Note*, 2863, 1952.
- [6]. Bodoia, J.R., and Osterle, J.F., 'The Development of Free Convection Between Heated Vertical Plates,' *Journal of Heat Transfer*, Vol. 84, pp. 40-44, 1962.
- [7]. Engel, R.K., Mueller, W.K., 'An Analytical Investigation of Natural Convection in Vertical Channels,' *ASME Paper No. 67-ht-16*, 1967.
- [8]. Aung, W., Fletcher, L.S., Sernas, V., 'Developing Laminar Free Convection Between Vertical Flat Plates with Asymmetric Heating,' *Int. Journal of Heat & Mass Transfer*, Vol. 15, pp. 2293-2308, 1972.
- [9]. Aung, W., 'Fully Developed Laminar Free Convection Between Vertical Flat Plates Heated Asymmetrically,' *Int. Journal of Heat & Mass Transfer*, Vol. 15, pp. 1577-1580, 1972.
- [10]. Carpenter, J.R., Briggs, D.G., Sernas, V., 'Combined Radiation and Developing Laminar Free Convection Between Vertical Flat Plates with Asymmetric Heating,' *Journal of Heat Transfer*, Vol. 98, pp. 95-100, 1976.

- [11]. Sparrow, E.M., Shah, S., and Sernas, V., 'Natural Convection in a Vertical Channel: I. Interacting Convection and Radiation, II. The Vertical Plate with and without Shrouding,' *Numerical Heat Transfer*, Vol. 3, pp. 297-314, 1980.
- [12]. Dalbert, A.M., Penot, F., and Puebe, J.L., 'Convection Naturelle Laminaire dans un Canal Chauffe a Flux Constant,' *Int. Journal of Heat & Mass Transfer*, Vol. 24, pp. 1463-1473, 1981.
- [13]. Wirtz, R.A., and Stutzman, R.J., 'Experiments on Free Convection Between Vertical Plates with Symmetric Heating,' *Journal of Heat Transfer*, Vol. 104, pp. 501-507, 1982.
- [14]. Sparrow, E.M., Chrysler, G.M., and Azevedo, L.F., 'Observed Flow Reversals and Measured-Predicted Nusselt Numbers for Natural Convection in a One-Sided Heated Vertical Channel,' *Journal of Heat Transfer*, Vol. 106, pp. 325-332, 1984.
- [15]. Aung, W., and Worku, G., 'Developing Flow and Flow Reversal in a Vertical Channel with Asymmetric Wall Temperatures,' *Journal of Heat Transfer*, Vol. 108, pp. 299-304, 1986.
- [16]. Aung, W., and Worku, G., 'Theory of Fully Developed Combined Convection Including Flow Reversal,' *Journal of Heat Transfer*, Vol. 108, pp. 485-488, 1986.
- [17]. O'Meara, T., and Poulikakos, D., 'Experiments on the Cooling by Natural Convection of an Array of Vertical Heated Plates with Constant Heat Flux,' *Int. Journal of Heat and Fluid Flow*, Vol. 8, pp. 313-319, 1987.
- [18]. Sparrow, E.M., Bahrami, P.A., 'Experiments on Natural Convection from Vertical Parallel Plates with Either Open or Closed Edges,' *Journal of Heat Transfer*, Vol. 102, pp. 221-227, 1980.
- [19]. Sparrow, E.M., Azevedo, L.F.A., 'Vertical-Channel Natural Convection Spanning Between the Fully Developed Limit and Single-plate Boundary-Layer Limit,' *Int. Journal of Heat & Mass Transfer*, Vol. 28, pp. 1847-1857, 1985.

- [20]. Azevedo, L.F.A., and Sparrow, E.M., 'Natural Convection in Open-Ended Inclined Channels,' *Journal of Heat Transfer*, Vol. 107, pp. 893-901, 1985.
- [21]. Azevedo, L.F.A., and Sparrow, E.M., 'Natural Convection in a Vertical Channel Vented to the Ambient through an Aperture in the Channel Wall,' *Int. Journal of Heat & Mass Transfer*, Vol. 29, pp. 819-830, 1986.
- [22]. Papple, M.L.C., Tarasuk, J.D., 'Developing Natural Convective Flow in Vertical and Inclined Ducts,' *Proc. of the 1st Conference on Experimental Heat Transfer, Fluid Mechanics, and Thermodynamics*, pp. 433-440, Dubrovnik, 1988.
- [23]. Guo, Z., Song, Y.Z., Zhao, X.W., 'Experimental Investigation on Natural Convection in Channel by Laser Speckle Photography,' *Proc. of the 1st Conference on Experimental Heat Transfer, Fluid Mechanics, and Thermodynamics*, pp. 412-418, Dubrovnik, 1988.
- [24]. Li, Z., Gui, Y., Guo, Z., 'Experimental Investigation on the Edge Effect of Natural Convection Between Two Vertical Plates,' *Proc. of the 1st Conference on Experimental Heat Transfer, Fluid Mechanics, and Thermodynamics*, pp. 419-424, Dubrovnik, 1988.
- [25]. Webb, B.W., Hill, D.P., 'High Rayleigh Number Laminar Natural Convection in an Asymmetrically Heated Vertical Channel,' *Journal of Heat Transfer*, Vol. 111, pp. 649-656, 1989.
- [26]. Moutsoglou, A., Rhee, J.H. and Won, J.K., 'Natural Convection-Radiation Cooling of a Vented Channel,' *Int. Journal of Heat & Mass Transfer*, Vol. 35, pp. 2855-2863, 1992.
- [27]. Aihara, T., and Maruyama, S., 'Laminar Free Convective Heat Transfer in Vertical Uniform Heat Flux Ducts (Numerical Solution with Constant / Temperature-Dependent Fluid Properties),' *Heat Transfer-Japanese Res.*, Vol. 15, pp. 69-86, 1986.
- [28]. Sparrow, E.M., and Tao, W.Q., 'Buoyancy-Driven Fluid Flow and Heat Transfer in a Pair of Interacting Vertical Parallel Channels,' *Numerical Heat Transfer*, Vol. 5, pp. 39-58, 1982.

- [29]. Burch, T., Rhodes, T., and Acharya, S., 'Laminar Natural Convection Between Finitely Conducting Vertical Plates,' *Int. Journal of Heat & Mass Transfer*, Vol. 28, pp. 1173-1186, 1985.
- [30]. Kim, S., and Anand, N.K., and Aung, W., 'Effect of Wall Conduction on Free Convection Between Asymmetrically Heated Vertical Plates: Uniform Wall Heat Flux,' *Int. Journal of Heat & Mass Transfer*, Vol. 33, pp. 1013-1023, 1990.
- [31]. Chappidi, P.R., and Eno, B.E., 'Natural Convection in a Heated Parallel Plate Vertical Channel; Influence of Inlet Conditions,' *Proceedings of the 1988 National Heat Transfer Conference*, Vol. 2, pp. 135-143, ASME, New York 1988.
- [32]. Naylor, D., Floryan, J.M., Tarasuk, J.D., 'A Numerical Study of Developing Free Convection Between Isothermal Vertical Plates,' *Journal of Heat Transfer*, Vol. 113, pp. 620-626, 1991.
- [33]. Griffith, E., and Davies, A.H., 'The Transmission of Heat by Radiation and Convection,' DSIR-Br. Food Invest. Board, Special Report 9, 1922, 1931.
- [34]. Warner, C.Y., and Arpaci, V.S., 'An Experimental Investigation of Turbulent Natural Convection in Air along a Vertical Heated Flat Plate,' *Int. Journal of Heat & Mass Transfer*, Vol. 11, pp. 397-406, 1968.
- [35]. Cheesewright, R., 'Turbulent Natural Convection from a Vertical Plane Surface,' *Journal of Heat Transfer*, Vol. 90, pp. 1-8, 1968.
- [36]. Vliet, G.C., and Liu, C.K., 'An Experimental Study of Turbulent Natural Convection Boundary Layers,' *Journal of Heat Transfer*, Vol. 91, pp. 517-531, 1969.
- [37]. Smith, R.R., 'Characteristics of Turbulence in Free Convection Flow Past a Vertical Plate,' Ph.D. Thesis, Queen Mary College, University of London, UK, 1972.
- [38]. George, W.K., and Capp, S.P., 'A Theory for Natural Convection Turbulent Boundary Layers Next to Heated Vertical Surfaces,' *Int. Journal of Heat & Mass Transfer*, Vol. 22, pp. 813-826, 1979.

- [39]. Priestly, C.B.H., 'Turbulent Transfer in the Lower Atmosphere,' Chicago University Press, 1959.
- [40]. Elder, J.W., 'Turbulent Free Convection in a Vertical Slot,' *Journal of Fluid Mechanics*, Vol. 23, pp. 99-111, 1965.
- [41]. Cheesewright, R., Faculty of Engineering, Queen Mary College, University of London, Research Report (EP 5037), 1987.
- [42]. Cheesewright, R., and Mirzai, M.H., 'The Correlation of Experimental Velocity and Temperature Data for a Turbulent Natural Convection Boundary Layer,' *Proceedings of the 2nd National Heat Transfer Conference*, Glasgow, UK, 1988.
- [43]. Gebhart, B., Jaluria, Y., Mahajan, R.L., Sammakia, B., Buoyancy Induced Flows and Transport, Hemisphere Publishing Corporation, 1988.
- [44]. Miyamoto, M., Katoh, Y., Kurima, J., and Sasaki, H., 'Turbulent Free Convection Heat Transfer From Vertical Parallel Plates,' *Proc. of the 8th Int. Heat Transfer Conference*, Vol. 4, pp. 1593-1598, 1986.
- [45]. Pederson, D.R., Stewart, R.R., Tessier, J.H., Heineman, J.B., and Lottes, P.A., 'Experimental and Analytical Studies of Passive Shutdown Heat Removal Systems,' *AIChE Symp. Ser. No 257*, 83, 145, 1987.
- [46]. La Pica, A., Rodono, G., and Volpes, R., 'An Experimental Investigation on Natural Convection of Air in a Vertical Channel,' *Int. Journal of Heat & Mass Transfer*, Vol. 36, pp. 611-616, 1993.
- [47]. Jones, W.P., and Launder, B.E., 'The Prediction of Laminarization with a Two Equation Model of Turbulence,' *Int. Journal of Heat & Mass Transfer*, Vol. 15, pp. 301-314, 1972.
- [48]. Plumb, O.A., Kennedy, L.A., 'Application of a k- ϵ Turbulence Model to Natural Convection from a Vertical Isothermal Surface,' *Journal of Heat Transfer*, Vol. 99, pp. 79-85, 1977.
- [49]. Lin, S.J., and Churchill, S.W., 'Turbulent Free Convection from a Vertical Isothermal Plate,' *Numerical Heat Transfer*, Vol. 1, pp. 129-145, 1978.

- [50]. Launder, B.E., and Sharma, B.I., 'Application of the Energy Dissipation Model of Turbulence to the Calculation of Flow Near a Spinning Disk,' *Letters in Heat and Mass Transfer*, Vol. 1, pp. 131-138, 1974.
- [51]. Ince, E.Z., and Launder, B.E., 'On the Computation of Buoyancy-Driven Turbulent Flows in Rectangular Enclosures,' *Int. Journal of Heat and Fluid Flow*, Vol. 10, pp. 110-117, 1989.
- [52]. To, W.M., and Humphrey, J.A.C., 'Numerical Simulation of Buoyant Turbulent Flow-I. Free Convection along a Heated, Vertical, Flat Plate,' *Int. Journal of Heat & Mass Transfer*, Vol. 29, pp. 573-592, 1986.
- [53]. Davidson, L., 'Calculation of the Turbulent Buoyancy-Driven Flow in a Rectangular Cavity Using an Efficient Solver and Two Different k- ϵ Turbulence Models,' *Numerical Heat Transfer*, Vol. 18, pp. 129-147, 1990.
- [54]. Davidson, L., 'Second-Order Corrections of the k- ϵ Model to Account for Non-Isotropic Effects due to Buoyancy,' *Int. Journal of Heat & Mass Transfer*, Vol. 33, pp. 2599-2608, 1990.
- [55]. Patel, V.C., Rodi, W., and Scheurer, G., 'Turbulence Models for Near-Wall and Low Reynolds Number Flows: A Review,' *AIAA Journal*, Vol. 23, pp. 1308-1319, 1985.
- [56]. Lam, C.K., and Bremhorst, K., 'Modified Form of k- ϵ Model For Predicting Wall Turbulence,' *Journal of Fluid Eng.*, Vol. 103, pp. 456-460, 1981.
- [57]. Chien, K.Y., 'Predictions of Channel and Boundary-Layer Flows with a Low-Reynolds-Number Turbulence Model,' *AIAA Journal*, Vol. 20, pp. 33-38, 1982.
- [58]. Heiss, A., Straub, J., and Catton, I., 'Application of Turbulence Models to Natural Convection from a Vertical Isothermal Plate,' *Proceedings of the 1988 National Heat Transfer Conference*, Vol. 2, pp. 181-190, ASME, New York, 1988.
- [59]. Henkes, R.A.W.M., and Hoogendoorn, C.J., 'Comparison of Turbulence Models for the Natural Convection Boundary Layer along a Heated Vertical Plate,' *Int. Journal of Heat & Mass Transfer*, Vol. 32, pp. 157-169, 1989.

- [60]. Peeters, T.W.J., and Henkes, R.A.W.M., 'The Reynolds-Stress Model of Turbulence Applied to the Natural Convection Boundary Layer along a Heated Vertical Plate,' *Int. Journal of Heat & Mass Transfer*, Vol. 35, pp. 403-420, 1992.
- [61]. Schlichting, H., Boundary - Layer Theory, Sixth Edition, McGraw Hill Book Company, New York, 1968.
- [62]. Cebeci, T., Bradshaw, P., Physical and Computational Aspects of Convective Heat Transfer, Springer-Verlag, New York, 1984.
- [63]. Patankar, S.V., Numerical Heat Transfer and Fluid Flow, New York, Hemisphere, 1980.
- [64]. Leschziner, M.A., 'Modelling Turbulent Recirculating Flows by Finite-Volume Methods', *International Journal of Heat and Fluid Flow*, Vol. 10, pp. 186-202.
- [65]. Spalding, D.B., The PHOENICS Beginners Guide, CHAM TR/100, 1991.
- [66]. Ludwig, J.C., Qin, H.Q., Spalding, D.B., The PHOENICS Reference Manual, CHAM TR/200, 1989.
- [67]. Spalding, D.B., PHOENICS Instruction Courses, Course Notes, CHAM TR/300, 1989.
- [68]. DANTEC Elektronik, 'Burst Spectrum Analyzer User's Guide 57N10' Denmark, 1991.
- [69]. Moffat, R.J., 'Contributions to the Theory of Single-Sample Uncertainty Analysis', *Journal of Fluid Eng.*, Vol. 104, pp. 250-260, 1982.
- [70]. Moffat, R.J., 'Using Uncertainty Analysis in the Planning of an Experiment', *Journal of Fluid Eng.*, Vol. 107, pp. 173-178, 1985.
- [71]. Abernethy, R.B., Benedict, R.P. and Dowdell, R.B., ASME 'Measurement Uncertainty', *Journal of Fluid Eng.*, Vol. 107, pp. 161-164, 1985.
- [72]. Kline, S.J., 'The Purposes of Uncertainty Analysis', *Journal of Fluid Eng.*, Vol. 107, pp. 153-160, 1985.
- [73]. Smith, Jr. R.E. and Wehofer, S., 'From Measurement Uncertainty to Measurement Communications, Credibility, and Cost Control in Propulsion Ground Test Facilities', *Journal of Fluid Eng.*, Vol. 107, pp. 165-172, 1985.

- [74]. Dietrich, C.F., Uncertainty, Calibration and Probability - The Statistics of Scientific and Industrial Measurement, 2nd Ed., Bristol, Adam Hilger Pub., 1991.
- [75]. Holman, J.P., Experimental Methods for Engineers, 6th Ed., New York, McGraw-Hill, 1994.
- [76]. Fedorov, A.G., and Viskanta, R., 'Turbulent Natural Convection Heat Transfer in an Asymmetrically Heated, Vertical Parallel-Plate Channel,' *Int. Journal of Heat & Mass Transfer*, Vol. 40, pp. 3849-3860, 1997.

APPENDIX A
GOVERNING EQUATIONS

A.1 LAMINAR NATURAL CONVECTION FLOW EQUATIONS

A.1.1 General Equations of Fluid Flow and Heat Transfer

The conservation equations of mass, momentum and energy governing the variable property (with the exception of specific heat, c_p) non-isothermal unsteady flows in cartesian tensor notation are given below. These equations are derived by applying the conservation laws to an infinitesimal control volume of a Newtonian fluid in cartesian coordinates.

Conservation of Mass:

$$\frac{\partial \rho}{\partial t} + \frac{\partial}{\partial x_j} (\rho u_j) = 0 \quad (\text{A.1})$$

Conservation of Momentum:

$$\frac{\partial}{\partial t} (\rho u_i) + \frac{\partial}{\partial x_j} (\rho u_j u_i) = -\frac{\partial p}{\partial x_i} + \rho g_i + \frac{\partial}{\partial x_j} \left(\mu \left[\frac{\partial u_i}{\partial x_j} + \frac{\partial u_j}{\partial x_i} \right] + \left(\mu' - \frac{2}{3} \mu \right) \delta_{ij} \frac{\partial u_k}{\partial x_k} \right) \quad (\text{A.2})$$

Conservation of Energy:

$$\frac{\partial}{\partial t} (c_p \rho T) + \frac{\partial}{\partial x_j} (c_p u_j \rho T) = \frac{\partial}{\partial x_j} \left(\lambda \frac{\partial T}{\partial x_j} \right) + \left(\frac{\partial p}{\partial t} + u_j \frac{\partial p}{\partial x_j} \right) + \Phi + \ddot{q} \quad (\text{A.3})$$

where $i, j, k=1, \dots, 3$, δ_{ij} is the unit tensor and the dissipation term Φ is given as;

$$\Phi = \left\{ \frac{\partial}{\partial x_j} \left(\mu \left[\frac{\partial u_i}{\partial x_j} + \frac{\partial u_j}{\partial x_i} \right] \right) \left(\mu' - \frac{2}{3} \mu \right) \frac{\partial u_k}{\partial x_k} \right\} \frac{\partial u_i}{\partial x_j} \quad (\text{A.4})$$

In equation (A.1) the first term represents the net rate of increase of mass in the control volume, and the second the net influx of mass into the control volume.

The terms in equation (A.2) from left to right are the net rate of accumulation of momentum in the control volume, the influx of momentum into the control volume due to convection, force due to static pressure acting on the control volume, the body force, and the viscous forces. The second part of the viscous force term represents the effects of compressibility due to dilatation and normal stresses, μ' being the bulk viscosity. For incompressible flows this part becomes zero. Even in compressible flows μ' is negligible, and in natural convection flows since the density variation is fairly small the second part of the viscous force term can be neglected.

The terms on the left hand side of equation (A.3) are the net rate of accumulation of energy in the control volume and the net influx of energy into the control volume due to convection. As for the right hand side, the first term represents the net heat transfer to the control volume due to molecular diffusion and the second term the work done on the control volume by pressure. The third and fourth terms are the viscous dissipation and volumetric heat source respectively.

Equations (A.1) to (A.3) are applicable to natural convection flows as well as to forced convection flows. The main difference between natural convection flows and forced convection flows is the driving mechanism. Forced convection flows are driven by an imposed pressure or velocity level. Natural convection flows, however, are driven entirely by buoyancy force or the changing body force. Mixed convection flows occur where the imposed pressure force and the buoyancy force are comparable. The use of buoyancy force instead of the body force is advantageous in terms of numerical accuracy. Buoyancy force, however, does not appear in equation (A.2) explicitly. The buoyancy force acting on a fluid package of density ρ surrounded by an extensive quiescent ambient of density ρ_∞ is explained below.

A.1.2 The Buoyancy Force

Consider a fluid of density ρ_∞ which is a function of temperature, T_∞ , and static pressure, P_∞ , i.e. $\rho_\infty(T_\infty, P_\infty)$. In a quiescent ambient environment of such a fluid in a gravity field, a local region of lower density produces an upward buoyancy force which induces motion. This case is depicted in Figure A-1. As it can be seen from Figure A-1, the absolute value of pressure gradient in the ambient, equation (A.5), is bigger than that in the lower density region, equation (A.6). This results in an upward flow. If ambient density, ρ_∞ , is lower than local density, ρ , the flow will be downward.

$$\frac{dp_\infty}{dx} = -\rho_\infty g \quad (\text{A.5})$$

$$\frac{\partial p}{\partial x} = -\rho g \quad (\text{A.6})$$

The forces acting on the system shown in Figure A-1 can be represented by a single force which can be written as;

$$B(x,y) = (\rho_\infty - \rho)g \quad (\text{A.7.1})$$

where $g = -g$. In general the buoyancy force is

$$B_i = (\rho - \rho_\infty)g_i \quad (\text{A.7.2})$$

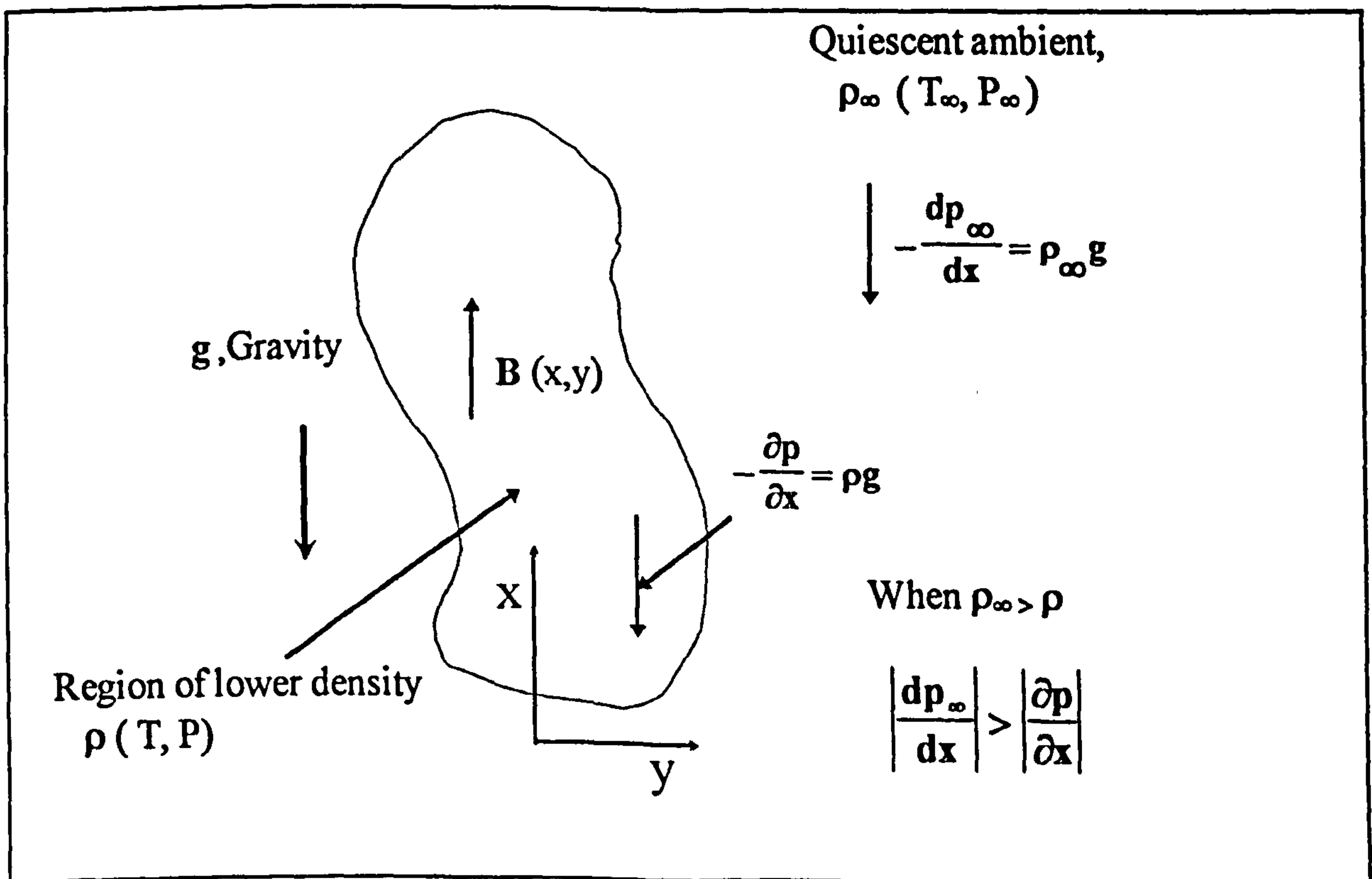


Figure A-1 The buoyancy force due to density variation in a quiescent ambient.

A.1.3 The Buoyancy Force and Motion Pressure

Some steps must be taken so that buoyancy force appears explicitly in the momentum equation (A.2). Now consider the pressure and body force terms in equation (A.2).

$$-\frac{\partial p}{\partial x_i} + \rho g_i \quad (\text{A.8})$$

where g is the gravity, and p is the static pressure which is the pressure that would be measured by a device moving with the fluid. Static pressure is related to the stagnation pressure by the dynamic pressure. Let us consider the hydrostatic pressure field that would occur in a fluid at rest but locally at reference density, ρ_∞ . The changes in this hydrostatic pressure field can be written as;

$$\frac{\partial p_h}{\partial x_i} = \rho_\infty g_i \quad (\text{A.9})$$

This is the result of equation (A.2) when velocity is taken zero. If the static pressure is decomposed into hydrostatic pressure, p_h , and motion pressure, p_m , as;

$$p = p_h + p_m \quad (\text{A.10})$$

the following relation can be written.

$$-\frac{\partial p}{\partial x_i} + \rho g_i = \rho g_i - \frac{\partial p_h}{\partial x_i} - \frac{\partial(p - p_h)}{\partial x_i} \quad (\text{A.11.1})$$

substituting equation (A.9) into equation (A.11.1) and considering equation (A.10), gives

$$-\frac{\partial p}{\partial x_i} + \rho g_i = -\frac{\partial p_m}{\partial x_i} + (\rho - \rho_\infty)g_i \quad (\text{A.11.2})$$

The second term on the right-hand side of equation (A.11.2) is the same as the buoyancy force of equation (A.7.2). Using equation (A.11.2), the conservation of momentum equation, (A.2), becomes;

$$\frac{\partial}{\partial t}(\rho u_i) + \frac{\partial}{\partial x_j}(\rho u_j u_i) = -\frac{\partial p_m}{\partial x_i} + (\rho - \rho_\infty)g_i + \frac{\partial}{\partial x_j}(\mu[\frac{\partial u_i}{\partial x_j} + \frac{\partial u_j}{\partial x_i}] + (\mu' - \frac{2}{3}\mu)\delta_{ij} \frac{\partial u_k}{\partial x_k}) \quad (\text{A.12})$$

Equations (A.2) and (A.12) differ from each other with the pressure term and the body force replaced by the motion pressure term and by the buoyancy term. Motion pressure is the result of the combined effects of acceleration, buoyancy and viscous forces. In analogy with forced flows, motion pressure can be considered as the impetus of the motion in buoyancy driven flows.

A.1.4 The Governing Equations of a Two Dimensional Natural Convection

Equations (A.1), (A.3), and (A.12) with the bulk viscosity, μ' , neglected can be rearranged in the following form.

Conservation of Mass:

$$\frac{\partial \rho}{\partial t} + \frac{\partial}{\partial x_j}(\rho u_j) = 0 \quad (\text{A.13})$$

Conservation of Momentum:

$$\frac{\partial}{\partial t}(\rho u_i) + (\rho u_j) \frac{\partial u_i}{\partial x_j} = -\frac{\partial p_m}{\partial x_i} + (\rho - \rho_\infty)g_i + \frac{\partial}{\partial x_j}(\mu[\frac{\partial u_i}{\partial x_j} + \frac{\partial u_j}{\partial x_i}] - \frac{2}{3}\mu\delta_{ij} \frac{\partial u_k}{\partial x_k}) \quad (\text{A.14})$$

Conservation of Energy:

$$\frac{\partial}{\partial t}(c_p \rho T) + (c_p \rho u_j) \frac{\partial T}{\partial x_j} = \frac{\partial}{\partial x_j}(\lambda \frac{\partial T}{\partial x_j}) + (\frac{\partial p}{\partial t} + u_j \frac{\partial p}{\partial x_j}) + \Phi + \ddot{q} \quad (\text{A.15})$$

where $i,j,k=1,\dots,3$, δ_{ij} is the unit tensor and the dissipation term Φ is given as;

$$\Phi = \left\{ \frac{\partial}{\partial x_j} \left(\mu \left[\frac{\partial u_i}{\partial x_j} + \frac{\partial u_j}{\partial x_i} \right] \right) - \frac{2}{3} \mu \frac{\partial u_k}{\partial x_k} \right\} \frac{\partial u_i}{\partial x_j} \quad (\text{A.16})$$

After expanding equations (A.13), (A.14), and (A.15) the governing equations of a two dimensional variable property laminar natural convection flow where the gravity field is aligned with the x direction are obtained as follows.

The continuity equation:

$$\frac{\partial(\rho u)}{\partial x} + \frac{\partial(\rho v)}{\partial y} = 0 \quad (\text{A.17})$$

X component of momentum equation:

$$\rho u \frac{\partial u}{\partial x} + \rho v \frac{\partial u}{\partial y} = -\frac{\partial p_m}{\partial x} + (\rho - \rho_\infty)g + \frac{\partial}{\partial x} \left[2\mu \frac{\partial u}{\partial x} - \frac{2}{3}\mu \left(\frac{\partial u}{\partial x} + \frac{\partial v}{\partial y} \right) \right] + \frac{\partial}{\partial y} \left[\mu \left(\frac{\partial v}{\partial x} + \frac{\partial u}{\partial y} \right) \right] \quad (\text{A.18})$$

Y component of momentum equation:

$$\rho u \frac{\partial v}{\partial x} + \rho v \frac{\partial v}{\partial y} = -\frac{\partial p_m}{\partial y} + \frac{\partial}{\partial x} \left[\mu \left(\frac{\partial v}{\partial x} + \frac{\partial u}{\partial y} \right) \right] + \frac{\partial}{\partial y} \left[2\mu \frac{\partial v}{\partial y} - \frac{2}{3}\mu \left(\frac{\partial u}{\partial x} + \frac{\partial v}{\partial y} \right) \right] \quad (\text{A.19})$$

The energy equation:

$$c_p \rho u \frac{\partial T}{\partial x} + c_p \rho v \frac{\partial T}{\partial y} = \frac{\partial}{\partial x} \left[\lambda \left(\frac{\partial T}{\partial x} \right) \right] + \frac{\partial}{\partial y} \left[\lambda \left(\frac{\partial T}{\partial y} \right) \right] + \left(u \frac{\partial p}{\partial x} + v \frac{\partial p}{\partial y} \right) + \Phi + \ddot{q} \quad (\text{A.20})$$

where Φ is given as;

$$\Phi = 2\mu \left(\frac{\partial u}{\partial x} \right)^2 + 2\mu \left(\frac{\partial v}{\partial y} \right)^2 + \mu \left(\frac{\partial u}{\partial y} + \frac{\partial v}{\partial x} \right)^2 - \frac{2}{3}\mu \left(\frac{\partial u}{\partial x} + \frac{\partial v}{\partial y} \right)^2 \quad (\text{A.21})$$

A.2 TURBULENT NATURAL CONVECTION FLOW EQUATIONS

A.2.1 General Turbulent Flow Equations of Variable Property Natural Convection

The mean flow equations of turbulent natural convection can be obtained by time averaging the instantaneous equations, equations (A.1), (A.3), and (A.12). The instantaneous variables are decomposed into a mean component denoted by an overbar, and a fluctuating component denoted by a prime with the usual Reynolds Decomposition Method as shown in equation (A.22).

$$\phi = \bar{\phi} + \phi' \quad (\text{A.22})$$

where ϕ is any of the flow variables such as x component of velocity, $u = \bar{u} + u'$. The average value of the variable, $\bar{\phi}$, is :

$$\bar{\phi} = \frac{1}{\Delta t} \int_{t_0}^{t_0 + \Delta t} \phi dt \quad (\text{A.23})$$

In equation (A.23) Δt is a time period such that it is larger than the typical time scale of turbulent fluctuations, yet smaller than the time scale of mean fluid motion if the flow is unsteady. The following rules apply for the time averaging process.

$$\overline{\phi\phi'} = 0 \quad (\text{A.24})$$

$$\frac{\partial \bar{\phi}}{\partial x_1} = \frac{\partial(\bar{\phi} + \phi')}{\partial x_1} = \frac{\partial \bar{\phi}}{\partial x_1} + \frac{\partial \phi'}{\partial x_1} = \frac{\partial \bar{\phi}}{\partial x_1} \quad (\text{A.25})$$

$$\frac{\partial \overline{\phi_1 \phi_2}}{\partial x_1} = \frac{\partial(\overline{(\phi_1 + \phi'_1)(\phi_2 + \phi'_2)})}{\partial x_1} = \frac{\partial(\overline{\phi_1 \phi_2 + \phi_1 \phi'_2 + \phi'_1 \phi_2 + \phi'_1 \phi'_2})}{\partial x_1} = \frac{\partial(\overline{\phi_1 \phi_2})}{\partial x_1} + \frac{\partial(\overline{\phi'_1 \phi'_2})}{\partial x_1} \quad (\text{A.26})$$

After applying the time averaging to equations (A.1), (A.3), (A.12) and neglecting triple correlations such as $\overline{\rho' u'_i u'_j}$, the governing equations of variable property steady turbulent natural convection flows are obtained as given below. It is assumed that the only fluctuating property is the density.

Conservation of Mass:

$$\frac{\partial}{\partial x_j} (\bar{\rho} \bar{u}_j + \overline{\rho' u'_j}) = 0 \quad (\text{A.27})$$

Conservation of Momentum:

$$\begin{aligned} & \frac{\partial}{\partial x_j} (\bar{\rho} \bar{u}_j \bar{u}_i) + \frac{\partial}{\partial x_j} (\overline{\rho' u'_j \bar{u}_i} + \overline{\rho' u'_i \bar{u}_j}) \\ &= -\frac{\partial \bar{p}_m}{\partial x_i} + (\bar{\rho} - \rho_\infty) g_i + \frac{\partial}{\partial x_j} \left[\mu \left(\frac{\partial \bar{u}_i}{\partial x_j} + \frac{\partial \bar{u}_j}{\partial x_i} \right) + \left(\mu' - \frac{2}{3} \mu \right) \delta_{ij} \frac{\partial \bar{u}_k}{\partial x_k} - \overline{\rho' u'_i u'_j} \right] \end{aligned} \quad (\text{A.28})$$

Conservation of Energy:

$$c_p \frac{\partial}{\partial x_j} (\bar{\rho} \bar{u}_j \bar{T} + \overline{\rho' u'_j \bar{T}} + \overline{\rho' \bar{T} u'_j}) = \frac{\partial}{\partial x_j} \left(\lambda \frac{\partial \bar{T}}{\partial x_j} - \overline{\rho' u'_j \bar{T}'} \right) + \bar{u}_j \frac{\partial \bar{p}}{\partial x_j} + \Phi + \rho \varepsilon + \ddot{q} \quad (\text{A.29})$$

where Φ is defined similarly to that in equation (A.4) with the velocity gradients being those of the mean flow, and ε is the dissipation rate of turbulent kinetic energy into thermal energy. The definition of ε is given by equation (A.30) where isotropic turbulence is assumed.

$$\varepsilon = \nu \overline{\frac{\partial u'_i}{\partial x_j} \frac{\partial u'_i}{\partial x_j}} \quad (\text{A.30})$$

Equations (A.27) to (A.29) differ from equations (A.1), (A.3), and (A.12) with terms such as $\overline{\rho u'_i u'_j}$, $\overline{\rho u'_j T'}$, etc, appearing which result from time averaging and known as Reynolds Stresses and turbulent heat flux respectively. In order that equations (A.27) to (A.29) can be solved these terms should be modelled.

In analogy with the laminar flow $\overline{\rho u'_i u'_j}$ and $\overline{\rho u'_j T'}$ can be modelled as;

$$\overline{\rho u'_i u'_j} = \mu_t \left(\frac{\partial \bar{u}_i}{\partial x_j} + \frac{\partial \bar{u}_j}{\partial x_i} \right) - \frac{2}{3} \bar{\rho} k \delta_{ij} \quad (\text{A.31})$$

$$\overline{\rho u'_j T'} = \frac{\mu_t}{\sigma_t} \frac{\partial \bar{T}}{\partial x_j} \quad (\text{A.32})$$

$$\mu_t = \bar{\rho} C_\mu f_\mu \frac{k^2}{\varepsilon} \quad (\text{A.33})$$

$$k = \frac{1}{2} \overline{u'_i u'_i} \quad (\text{A.34})$$

where μ_t and σ_t are the turbulent dynamic viscosity and the turbulent Prandtl number respectively. C_μ is an empirical constant, f_μ is a Low Reynolds Number model function, k and ε are the turbulent kinetic energy and its dissipation rate respectively which are obtained from the solution of their differential equations.

When density is taken as a function of temperature only, the following equations can be written from the ideal gas law.

$$\overline{\rho' u'_i T} + \bar{\rho} \overline{u'_i T'} = 0 \quad \Rightarrow \quad \overline{\rho' u'_i} = -\frac{\bar{\rho}}{\bar{T}} \overline{u'_i T'} \quad (\text{A.35})$$

$$\overline{\rho' T' T} + \bar{\rho} \overline{T'^2} = 0 \quad \Rightarrow \quad \overline{\rho' T'} = -\frac{\bar{\rho}}{\bar{T}} \overline{T'^2} \quad (\text{A.36})$$

From equations (A.32) and (A.35), $\overline{\rho'u'_j}$ can be modelled as;

$$\overline{\rho'u'_j} = \beta \frac{\mu_t}{\sigma_t} \frac{\partial \bar{T}}{\partial x_j} \quad (\text{A.37})$$

Equation (A.36) relates $\overline{\rho'T'}$ to $\overline{T'^2}$. To and Humphrey [52], referring to previous studies and using the exact transport equation of $\overline{T'^2}$ with simplifications, give the following equation.

$$\overline{\rho'T'} = 2R \frac{k}{\varepsilon} \frac{\bar{\rho}}{\bar{T}} \overline{u'_j T'} \frac{\partial \bar{T}}{\partial x_j} \quad (\text{A.38})$$

where R is a constant with the value of 0.8.

After neglecting μ' , substituting equations (A.31) and (A.32), and assuming that $\frac{2}{3} \bar{\rho} k \delta_{ij}$ is included in the pre-decomposed pressure term, equations (A.27) to (A.29) can be re-arranged as;

$$\frac{\partial}{\partial x_j} (\bar{\rho} \bar{u}_j + \overline{\rho'u'_j}) = 0 \quad (\text{A.39})$$

$$\begin{aligned} (\bar{\rho} \bar{u}_j + \overline{\rho'u'_j}) \frac{\partial \bar{u}_i}{\partial x_j} = & -\frac{\partial \bar{p}_m}{\partial x_i} + (\bar{\rho} - \rho_\infty) g_i \\ & + \frac{\partial}{\partial x_j} [(\mu + \mu_t) (\frac{\partial \bar{u}_i}{\partial x_j} + \frac{\partial \bar{u}_j}{\partial x_i}) + -\frac{2}{3} \mu \delta_{ij} \frac{\partial \bar{u}_k}{\partial x_k} - \overline{\rho'u'_i \bar{u}_j}] \end{aligned} \quad (\text{A.40})$$

$$c_p (\bar{\rho} \bar{u}_j + \overline{\rho'u'_j}) \frac{\partial \bar{T}}{\partial x_j} = \frac{\partial}{\partial x_j} [(\lambda + \frac{c_p \mu_t}{\sigma_t}) \frac{\partial \bar{T}}{\partial x_j} - c_p \overline{\rho'T' \bar{u}_j}] + \bar{u}_j \frac{\partial \bar{p}}{\partial x_j} + \Phi + \rho \varepsilon + \ddot{q} \quad (\text{A.41})$$

Equations (A.39) to (A.41), together with equations (A.33), (A.37), (A.38) and the respective differential equations for k and ε govern the steady turbulent natural convection flow of a variable property fluid.

APPENDIX B
TURBULENCE MODEL FILES

B.1 GROUND FILE of LRN k-ε TURBULENCE MODELS

C FILE NAME GROUND.FTN-----120392
CC--TY FILE NAME LRGRND.FOR-----120392
CC--TY
C
C THIS IS THE FILE LRGRND.FOR WHICH PROVIDES CODING FOR FOUR
DIFFERENT
C LOW REYNOLDS NUMBER KE-EP EDDY VISCOSITY TURBULENCE
MODELS (LR-EVM'S).
C THEY ARE:
C 1- LAUNDER & SHARMA (LS) LR-EVM
C 2-TO & HUMPHREY (TH) LR-EVM (VAR. OF JL MODEL FOR BUOYANCY
INDUCED FLOWS)
C 3-LAM & BREMHORST (LB) LR-EVM
C 4-L. DAVIDSON (DA) LR-EVM (A MODEL FOR BUOYANCY INDUCED
FLOWS)
C
CC--TY
C
C THIS IS THE MAIN PROGRAM OF EARTH
C
C (C) COPYRIGHT 1984, LAST REVISION 1992
C CONCENTRATION HEAT AND MOMENTUM LTD. ALL RIGHTS
RESERVED.
C This subroutine and the remainder of the PHOENICS code are
C proprietary software owned by Concentration Heat and Momentum
C Limited, 40 High Street, Wimbledon, London SW19 5AU, England.
C
C
PROGRAM MAIN
C
C 1 The following COMMON's, which appear identically in the
C satellite MAIN program, allow up to 50 dependent variables to
C be solved for (or their storage spaces to be occupied by
C other variables, such as density). If a larger number is
C required, the PARAMETER NUMPHI should be reset to the required
C larger number. Numbers less than 50 are not permitted.
C
PARAMETER (NUMPHI=50, NM=NUMPHI,NM4=NM*4)
C
COMMON/LGE4/L4(NM)

1/LDB1/L5(NM)/IDA1/I1(NM)/IDA2/I2(NM)/IDA3/I3(NM)/IDA4/I4(NM)
1/IDA5/I5(NM)/IDA6/I6(NM)/GI1/I7(NM)/GI2/I8(NM)/HDA1/IH1(NM)

1/GH1/IH2(NM)/RDA1/R1(NM)/RDA2/R2(NM)/RDA3/R3(NM)/RDA4/R4(NM)

1/RDA5/R5(NM)/RDA6/R6(NM)/RDA7/R7(NM)/RDA8/R8(NM)/RDA9/R9(NM)

1/RDA10/R10(NM)/RDA11/R11(NM)

1/GR1/R12(NM)/GR2/R13(NM)/GR3/R14(NM)/GR4/R15(NM)

1/IP1/IP1(NM)/HPIP2/IHP2(NM)/RPIP1/RVAL(NM)/LPIP1/LVAL(NM)

1/IFPL/IPL0(NM)/RFPL1/ORPRIN(NM)/RFPL2/ORMAX(NM)

1/RFPL3/ORMIN(NM)/IDA7/ID7(NM)/IDA8/ID8(NM)

LOGICAL L4,L5,DBGFIL,LVAL

CHARACTER*4 IH1,IH2,IHP2

C

COMMON/F01/I9(NM4)

COMMON/DISC/DBGFIL

COMMON/LUNITS/LUNIT(60)

C

EXTERNAL WAYOUT

C

C 2 Set dimensions of data-for-GROUND arrays here. WARNING: the

C corresponding arrays in the MAIN program of the satellite

C (see SATLIT) must have the same dimensions.

PARAMETER (NLG=20, NIG=20, NRG=100, NCG=10)

C

COMMON/LGRND/LG(NLG)/IGRND/IG(NIG)/RGRND/RG(NRG)/CGRND/CG(
NCG)

LOGICAL LG

CHARACTER*4 CG

C

C 3 Set dimensions of data-for-GREX arrays here. WARNING: the

C corresponding arrays in the MAIN program of the satellite

C (see SATLIT) must have the same dimensions.

PARAMETER(NLSG=20, NISG=20, NRSB=100,NCSG=10)

C

COMMON/LSG/LSGD(NLSG)/ISG/ISGD(NISG)/RSG/RSGD(NRSB)/CSG/CSGD
(NCSG)

LOGICAL LSGD

CHARACTER*4 CSGD

C

C 4 Set dimension of patch-name array here. WARNING: the array

C NAMPAT in the MAIN program of the satellite must have the

C same dimension.

PARAMETER (NPNAM=200)

C

```

COMMON/NPAT/NAMPAT(NPNAM)
COMMON/LWFUN1/DOSKIN(NPNAM)
COMMON/LWFUN2/DHCHKD(NPNAM)
CHARACTER*8 NAMPAT
LOGICAL DOSKIN,DHCHKD

```

```

C
C CONFIG FILE name declaration.
COMMON/CNFG/CNFIG
CHARACTER CNFIG*48

```

```

C
C 5 The numbers in the next statement indicates how much computer
C memory is to be set aside for storing the main and auxiliary
C variables. The user may alter them if he wishes, to accord
C with the number of grid nodes and dependent variables he is
C concerned with.
PARAMETER (NFDIM=800000)

```

```

C
COMMON F(NFDIM)

```

```

C
C 6 The following three statements concern storage for the PATCH-wise
C variables. If more than 30 PATCH-wise variables are required
C NPVDM should be increased and the common block /LBPV/ in the
C include file GRDLOC15 should be lengthened.

```

```

PARAMETER (NPVDM=30)
COMMON/INDPV/NPVMX,NIMAX,NITOT,L0PV(NPVDM)

```

```

C
CALL SUB2(NPVMX,NPVDM,NIMAX,NPVDM)

```

```

C
CALL CNFGZZ(2)
CALL EARSET(1)
CALL OPENFL(6)

```

```

C
CALL
MAIN1(NFDIM,NUMPHI,NLSG,NISG,NRSG,NCSG,NLG,NIG,NRG,NCG)
CALL WAYOUT(0)
STOP
END

```

```

C*****

```

```

SUBROUTINE GROSTA
INCLUDE 'd_phoe16\d_earth\SATEAR'
INCLUDE 'd_phoe16\d_earth\GRDLOC'
INCLUDE 'd_phoe16\d_earth\GRDEAR'

```

```

C
C... This subroutine acts as a junction-box, directing control to
C the GROUNDS selected by the SATELLITE settings of USEGRX,
C NAMGRD & USEGRD.

```

```

C

```


IF(USEGRX) CALL GREX3

C
C... SPECGR, SPC1GR, SPC2GR and SPC3GR are names which the user may
C give to "special GROUNDS" of his own.
C

```
IF(NAMGRD.NE.'NONE') THEN
  IF(NAMGRD.EQ.'SPEC') THEN
    CALL SPECGR
  ELSEIF(NAMGRD.EQ.'SPC1') THEN
    CALL SPC1GR
  ELSEIF(NAMGRD.EQ.'SPC2') THEN
    CALL SPC2GR
  ELSEIF(NAMGRD.EQ.'SPC3') THEN
    CALL SPC3GR
  ELSEIF(NAMGRD.EQ.'GHOL') THEN
    CALL HOLGR
  ELSEIF(NAMGRD.EQ.'RSTM') THEN
    CALL RSTMGR
  ELSEIF(NAMGRD.EQ.'COAL') THEN
    CALL COALGR
  ELSEIF(NAMGRD.EQ.'RSTR') THEN
    CALL RSTRGR
  ELSEIF(NAMGRD.EQ.'SURF') THEN
    CALL SURFGR
  ELSEIF(NAMGRD.EQ.'QUIK') THEN
    CALL QUIKGR
  ELSEIF(NAMGRD.EQ.'STRA') THEN
    CALL STRAGR
  ELSEIF(NAMGRD.EQ.'RADI') THEN
    CALL RADIGR
  ELSEIF(NAMGRD.EQ.'ESTR') THEN
    CALL ESTRGR
  ELSEIF(NAMGRD.EQ.'LINK') THEN
    CALL LINKGR
  ELSE
    CALL WRITBL
    CALL WRITST
    CALL WRIT40('NAMGRD set but no CALL made, ie.      ')
    CALL WRIT1A('NAMGRD ',NAMGRD)
    CALL WRIT40(' sections 9 and 10 added to Group 19  ')
    CALL WRIT40(' Permissible calls for this GROSTA are:-')
    CALL WRIT40(' SPEC, SPC1, SPC2, SPC3, GHOL, RSTM,  ')
    CALL WRIT40(' RST1, RST2, SURF, QUIK, STRA, LINK  ')
    CALL WRIT40(' Use upper-case names only      ')
    CALL WRITST
    CALL WRITBL
    CALL WAYOUT(2)
```


DATA CMULR,CE1LR,CE2LR,PRTT,TEXCO,CPLR/0.09,1.44,1.92,0.9,
13.333E-3,1004/

CC--TY

C

C 3 User places his data statements here, for example:

C DATA NXDIM,NYDIM/10,10/

C

C 4 Insert own coding below as desired, guided by GREX examples.

C Note that the satellite-to-GREX special data in the labelled
C COMMONs /RSG/, /ISG/, /LSG/ and /CSG/ can be included and
C used below but the user must check GREX for any conflicting
C uses. The same comment applies to the EARTH-spare working
C arrays EASP1, EASP2,...EASP20. In addition to the EASPs,
C there are 10 GRound-earth SPare arrays, GRSP1,...,GRSP10,
C supplied solely for the user, which are not used by GREX. If
C the call to GREX has been deactivated then all of the arrays
C may be used without reservation.

C

IXL=IABS(IXL)

IF(IGR.EQ.13) GO TO 13

IF(IGR.EQ.19) GO TO 19

GO TO (1,2,3,4,5,6,25,8,9,10,11,12,13,14,25,25,25,25,19,20,25,
125,23,24),IGR

25 CONTINUE

RETURN

C*****

C

C--- GROUP 1. Run title and other preliminaries

C

1 GO TO (1001,1002),ISC

1001 CONTINUE

C

C User may here change message transmitted to the VDU screen or
C batch-run log file.

IF(IGR.EQ.1.AND.ISC.EQ.1.AND..NOT.NULLPR) THEN

CC--TY CALL WRYT40('GROUND file is GROUND.FTN of: 120392')

CALL WRYT40('GROUND file is LRGRND.FOR by T.YILMAZ')

ENDIF

CC--TY PROVISION OF SPECIAL EARTH ARRAYS BY MEANS OF
STORAGE SETTING

C SUBROUTINE CALL MAKE(VARIABLE NAME) ARE MADE HERE IN
SEC.-1.

C

C PROVISION OF STORAGE FOR CELL CENTER DISTANCES FROM Y=0.0
PLANE

C FOR USE IN TURBULENT REYNOLDS NUMBER CALCULATIONS.

C-----YG2D

CALL MAKE(YG2D)
CALL MAKE(DXG2D)
CALL MAKE(DYG2D)
CALL MAKE(GRSP1)
CALL MAKE(GRSP2)
CALL MAKE(GRSP3)
CALL MAKE(GRSP4)
CALL MAKE(GRSP5)
CALL MAKE(GRSP6)
CALL MAKE(GRSP7)
CALL MAKE(GRSP8)
CALL MAKE(GRSP9)
CALL MAKE(GRSP10)

CC--TY
RETURN
1002 CONTINUE
RETURN

C*****

C

C--- GROUP 2. Transience; time-step specification

C

2 CONTINUE
RETURN

C*****

C

C--- GROUP 3. X-direction grid specification

C

3 CONTINUE
RETURN

C*****

C

C--- GROUP 4. Y-direction grid specification

C

4 CONTINUE
RETURN

C*****

C

C--- GROUP 5. Z-direction grid specification

C

5 CONTINUE
RETURN

C*****

C

C--- GROUP 6. Body-fitted coordinates or grid distortion

C

6 CONTINUE
RETURN


```

C*****
C * Make changes for this group only in group 19.
C--- GROUP 7. Variables stored, solved & named
C*****
C
C--- GROUP 8. Terms (in differential equations) & devices
C
  8 GO TO (81,82,83,84,85,86,87,88,89,810,811,812,813,814,815)
  1,ISC
  81 CONTINUE
C * ----- SECTION 1 -----
C For U1AD.LE.GRND--- phase 1 additional velocity. Index VELAD
  RETURN
  82 CONTINUE
C * ----- SECTION 2 -----
C For U2AD.LE.GRND--- phase 2 additional velocity. Index VELAD
  RETURN
  83 CONTINUE
C * ----- SECTION 3 -----
C For V1AD.LE.GRND--- phase 1 additional velocity. Index VELAD
  RETURN
  84 CONTINUE
C * ----- SECTION 4 -----
C For V2AD.LE.GRND--- phase 2 additional velocity. Index VELAD
  RETURN
  85 CONTINUE
C * ----- SECTION 5 -----
C For W1AD.LE.GRND--- phase 1 additional velocity. Index VELAD
  RETURN
  86 CONTINUE
C * ----- SECTION 6 -----
C For W2AD.LE.GRND--- phase 2 additional velocity. Index VELAD
  RETURN
  87 CONTINUE
C * ----- SECTION 7 ---- Volumetric source for gala
  RETURN
  88 CONTINUE
C * ----- SECTION 8 ---- Convection fluxes
  RETURN
  89 CONTINUE
C * ----- SECTION 9 ---- Diffusion coefficients
C--- Entered when UDIFF =.TRUE.; block-location indices are LAE
C for east, LAW for west, LAN for north, LAS for
C south, LD11 for high, and LD11 for low.
C User should provide INDVAR and NDIREC IF's as above.
C
  RETURN

```

```

810 CONTINUE
C * ----- SECTION 10 --- Convection neighbours
  RETURN
811 CONTINUE
C * ----- SECTION 11 --- Diffusion neighbours
  RETURN
812 CONTINUE
C * ----- SECTION 12 --- Linearised sources
  RETURN
813 CONTINUE
C * ----- SECTION 13 --- Correction coefficients
  RETURN
814 CONTINUE
C * ----- SECTION 14 --- User's solver
  RETURN
815 CONTINUE
C * ----- SECTION 15 --- Change solution
  RETURN
C
C * See the equivalent section in GREX for the indices to be
C   used in sections 7 - 15
C
C * Make all other group-8 changes in GROUP 19.
C*****
C
C--- GROUP 9. Properties of the medium (or media)
C
C The sections in this group are arranged sequentially in their
C order of calling from EARTH. Thus, as can be seen from below,
C the temperature sections (10 and 11) precede the density
C sections (1 and 3); so, density formulae can refer to
C temperature stores already set.
  9 GO TO (91,92,93,94,95,96,97,98,99,900,901,902,903,904,905),ISC
C*****
900 CONTINUE
C * ----- SECTION 10 -----
C For TMP1.LE.GRND----- phase-1 temperature Index TEMP1
  RETURN
901 CONTINUE
C * ----- SECTION 11 -----
C For TMP2.LE.GRND----- phase-2 temperature Index TEMP2
  RETURN
902 CONTINUE
C * ----- SECTION 12 -----
C For EL1.LE.GRND----- phase-1 length scale Index LEN1
  RETURN
903 CONTINUE

```

```

C * ----- SECTION 13 -----
C For EL2.LE.GRND----- phase-2 length scale Index LEN2
RETURN
904 CONTINUE
C * ----- SECTION 14 -----
C For SOLVE(TEMP1)----- phase-1 specic heat
RETURN
905 CONTINUE
C * ----- SECTION 15 -----
C For SOLVE(TEMP2)----- phase-2 specic heat
RETURN
91 CONTINUE
C * ----- SECTION 1 -----
C For RHO1.LE.GRND--- density for phase 1    Index DEN1
RETURN
92 CONTINUE
C * ----- SECTION 2 -----
C For DRH1DP.LE.GRND--- D(LN(DEN))/DP for phase 1
C                               Index D1DP
RETURN
93 CONTINUE
C * ----- SECTION 3 -----
C For RHO2.LE.GRND--- density for phase 2    Index DEN2
RETURN
94 CONTINUE
C * ----- SECTION 4 -----
C For DRH2DP.LE.GRND--- D(LN(DEN))/DP for phase 2
C                               Index D2DP
RETURN
CC--TY
95 IF(ENUT.EQ.GRND) THEN
CALL TYLRVT
ENDIF
CC--TY
C * ----- SECTION 5 -----
C For ENUT.LE.GRND--- reference turbulent kinematic viscosity
C                               Index VIST
RETURN
96 CONTINUE
C * ----- SECTION 6 -----
C For ENUL.LE.GRND--- reference laminar kinematic viscosity
C                               Index VISL
RETURN
97 CONTINUE
C * ----- SECTION 7 -----
C For PRNDTL( ).LE.GRND--- laminar PRANDTL nos., or diffusivity
C                               Index LAMPR

```



```

RETURN
98 CONTINUE
C * ----- SECTION 8 -----
C For PHINT( ).LE.GRND--- interface value of first phase
C                               Index FII1
RETURN
99 CONTINUE
C * ----- SECTION 9 -----
C For PHINT( ).LE.GRND--- interface value of second phase
C                               Index FII2
RETURN
C*****
C
C--- GROUP 10. Inter-phase-transfer processes and properties
C
10 GO TO (101,102,103,104),ISC
101 CONTINUE
C * ----- SECTION 1 -----
C For CFIPS.LE.GRND--- inter-phase friction coeff.
C                               Index INTFRC
RETURN
102 CONTINUE
C * ----- SECTION 2 -----
C For CMDOT.EQ.GRND- inter-phase mass transfer Index INTMDT
RETURN
103 CONTINUE
C * ----- SECTION 3 -----
C For CINT( ).EQ.GRND--- phase1-to-interface transfer coefficients
C                               Index COI1
RETURN
104 CONTINUE
C * ----- SECTION 4 -----
C For CINT( ).EQ.GRND--- phase2-to-interface transfer coefficients
C                               Index COI2
RETURN
C*****
C
C--- GROUP 11. Initialization of variable or porosity fields
C                               Index VAL
11 CONTINUE
RETURN
C*****
C
C--- GROUP 12. Convection and diffusion adjustments
C
12 CONTINUE
RETURN

```

```

C*****
C
C--- GROUP 13. Boundary conditions and special sources
C           Index for Coefficient - CO
C           Index for Value      - VAL
 13 CONTINUE
    NPAT=NPATCH(1:4)
    GO TO (130,131,132,133,134,135,136,137,138,139,1310,
    11311,1312,1313,1314,1315,1316,1317,1318,1319,1320,1321),ISC
 130 CONTINUE
C----- SECTION 1 ----- coefficient = GRND
CC--TY CACULATE THE CO OF LINEARIZED SOURCES OF KE & EP
    IF(INDVAR.EQ.12.OR.INDVAR.EQ.13) THEN
    IF(NPAT.EQ.'LRSO') THEN
    CALL TYLRSO
    ENDIF
    ENDIF

CC--TY
    RETURN
 131 CONTINUE
C----- SECTION 2 ----- coefficient = GRND1
    RETURN
 132 CONTINUE
C----- SECTION 3 ----- coefficient = GRND2
    RETURN
 133 CONTINUE
C----- SECTION 4 ----- coefficient = GRND3
    RETURN
 134 CONTINUE
C----- SECTION 5 ----- coefficient = GRND4
    RETURN
 135 CONTINUE
C----- SECTION 6 ----- coefficient = GRND5
    RETURN
 136 CONTINUE
C----- SECTION 7 ----- coefficient = GRND6
    RETURN
 137 CONTINUE
C----- SECTION 8 ----- coefficient = GRND7
    RETURN
 138 CONTINUE
C----- SECTION 9 ----- coefficient = GRND8
    RETURN
 139 CONTINUE
C----- SECTION 10 ----- coefficient = GRND9
    RETURN

```

```

1310 CONTINUE
C----- SECTION 11 ----- coefficient = GRND10
  RETURN
1311 CONTINUE
C----- SECTION 12 ----- value = GRND
CC--TY CACULATE THE VALUE PART OF LINEARIZED SOURCES OF KE &
EP
  IF(INDVAR.EQ.12.OR.INDVAR.EQ.13) THEN
  IF(NPAT.EQ.'LRSO') THEN
  CALL TYLRSO
  ENDIF
  ENDIF
CC--
  IF(INDVAR.EQ.12.OR.INDVAR.EQ.13) THEN
C-- IMPLEMENTATION OF VARIABLE KE&EP BOUND. CONDTIOONS AT
THE INLET
  IF(NPAT.EQ.'INLT') THEN
  IF(INDVAR.EQ.12) THEN
CC-- FNTYP(Y,X1,A,B,C,D,E,F,G) -- Y=A+B*X1+C*X1**2...+G*X1**6 -----
--
C-- (UWT Tw=100 C)

C  CALL FNTYP(VAL,YG2D,-0.0007,0.1054,-0.9905,4.442,-9.1342,
C  *8.7238,-3.1429)
C-- (UHF CASE -3)
  CALL FNTYP(VAL,YG2D,0.0022,0.0222,-0.0031,-0.2848,0.4562,
  *0.2123,-0.4037)
  ELSEIF(INDVAR.EQ.13) THEN
CC-- EPIN=(0.4/YVLAST)*KEIN**1.5 -----
  CTYY=0.4/YVLAST
  CALL FN8(VAL,KE,CTYY,0.0,1.5,0)
  ENDIF
  ENDIF
  ENDIF
CC--
  IF(WALLTY.AND.(INDVAR.EQ.EP)) THEN
  CALL TYLRWL
  ENDIF
C
CC--TY
  RETURN
1312 CONTINUE
C----- SECTION 13 ----- value = GRND1
  RETURN
1313 CONTINUE
C----- SECTION 14 ----- value = GRND2
  RETURN

```



```

1314 CONTINUE
C----- SECTION 15 ----- value = GRND3
  RETURN
1315 CONTINUE
C----- SECTION 16 ----- value = GRND4
  RETURN
1316 CONTINUE
C----- SECTION 17 ----- value = GRND5
  RETURN
1317 CONTINUE
C----- SECTION 18 ----- value = GRND6
  RETURN
1318 CONTINUE
C----- SECTION 19 ----- value = GRND7
  RETURN
1319 CONTINUE
C----- SECTION 20 ----- value = GRND8
  RETURN
1320 CONTINUE
C----- SECTION 21 ----- value = GRND9
  RETURN
1321 CONTINUE
C----- SECTION 22 ----- value = GRND10
  RETURN
C*****
C
C--- GROUP 14. Downstream pressure for PARAB=.TRUE.
C
  14 CONTINUE
  RETURN
C*****
C* Make changes for these groups only in GROUP 19.
C--- GROUP 15. Termination of sweeps
C--- GROUP 16. Termination of iterations
C--- GROUP 17. Under-relaxation devices
C--- GROUP 18. Limits on variables or increments to them
C*****
C
C--- GROUP 19. Special calls to GROUND from EARTH
C
  19 GO TO (191,192,193,194,195,196,197,198,199,1910),ISC
  191 CONTINUE
    IF(ISG1.GT.2) THEN
      CALL TYLRFN
    ENDIF
C * ----- SECTION 1 ---- Start of time step.
  RETURN

```

```

192 CONTINUE
C * ----- SECTION 2 ---- Start of sweep.
  RETURN
193 CONTINUE
C * ----- SECTION 3 ---- Start of iz slab.
  RETURN
194 CONTINUE
CC---TY -----
  IF(ISG1.EQ.1) THEN
  CALL FNSQRDUDY
  ENDIF
  IF(ISG1.LE.2) THEN
  CALL FNDSQRTKDY
  ENDIF
  CALL TYLRGN
CC---TY
C * ----- SECTION 4 ---- Start of iterations over slab.
  RETURN
199 CONTINUE

C * ----- SECTION 9 ---- Start of solution sequence for
C                               a variable
  RETURN
1910 CONTINUE
C * ----- SECTION 10---- Finish of solution sequence for
C                               a variable
  RETURN
195 CONTINUE
C * ----- SECTION 5 ---- Finish of iterations over slab.
  RETURN
196 CONTINUE
C * ----- SECTION 6 ---- Finish of iz slab.
  RETURN
197 CONTINUE
C * ----- SECTION 7 ---- Finish of sweep.
  RETURN
198 CONTINUE
C * ----- SECTION 8 ---- Finish of time step.
C--TY
  IF(ISWEEP.EQ.LSWEEP) THEN
  OPEN(7,FILE='PROFIL.PRN', STATUS = 'OLD')
  DO 3333 ITY=1,NY
  LLY=L0F(YG2D)
  LLU1=L0F(U1)
  RTY=F(LLY+ITY)/YVLAST
  RTU1=(F(LLU1+((IG(1)-1)*NY)+ITY))
  RTU2=(F(LLU1+((IG(2)-1)*NY)+ITY))

```

```

      RTU3=(F(LLU1+((IG(3)-1)*NY)+ITY))
      RTU4=(F(LLU1+((IG(4)-1)*NY)+ITY))
      RTU5=(F(LLU1+((IG(5)-1)*NY)+ITY))
      WRITE(7,333) RTY,RTU1,RTU2,RTU3,RTU4,RTU5
333  FORMAT(5X,E9.4,2X,E9.4,2X,E9.4,2X,E9.4,2X,E9.4,2X,E9.4)
3333 CONTINUE
      CLOSE(7)
      ENDIF
C--TY
      RETURN
C*****
C
C--- GROUP 20. Preliminary print-out
C
      20 CONTINUE
      RETURN
C*****
C* Make changes for these groups only in GROUP 19.
C--- GROUP 21. Print-out of variables
C--- GROUP 22. Spot-value print-out
C*****
C
C--- GROUP 23. Field print-out and plot control
      23 CONTINUE
      RETURN
C*****
C
C--- GROUP 24. Dumps for restarts
C
      24 CONTINUE
      END
C*****
      SUBROUTINE SPECGR
      CALL WRIT40('Dummy subroutine SPECGR called.   ')
      CALL WAYOUT(2)
      END
C*****
      SUBROUTINE SPC1GR
      CALL WRIT40('Dummy subroutine SPC1GR called.   ')
      CALL WAYOUT(2)
      END
C*****
      SUBROUTINE SPC2GR
      CALL WRIT40('Dummy subroutine SPC2GR called.   ')
      CALL WAYOUT(2)
      END
C*****

```



```

SUBROUTINE SPC3GR
CALL WRIT40('Dummy subroutine SPC3GR called.
CALL WAYOUT(2)
END
C*****
SUBROUTINE QUIZ
C--- This subroutine is used by CHAM for de-bugging
END
CC--TY
C
CC--TY THIS SUBROUTINE CALCULATES THE LR-EVM
FUNCTIONS,(Fm,F1,F2).
SUBROUTINE TYLRFN
C
INCLUDE 'd_phoe16\d_earth\GRDLOC'
INCLUDE 'd_phoe16\d_earth\GRDEAR'
INCLUDE 'd_phoe16\d_earth\SATEAR'
C
C
COMMON/NAMFN/NAMFUN,NAMSUB
CHARACTER*6 NAMFUN,NAMSUB
C
NAMSUB = 'TYLRFN'
IF(IGR.EQ.19) THEN
IF(ISG1.GT.2) THEN
C*****
C CALCULATE DISTANCES OF THE CELL CENTERS FROM THE WALL
FOR USE IN
C TURBULENT REYNOLDS NUMBER REy
LYF=L0F(YG2D)
LGF=L0F(GRSP1)
J=0
DO 110 IX=IXF,IXL
DO 110 IY=IYF,IYL
J=J+1
IF(F(LYF+J).LE.(YVLAST/2)) THEN
YL=F(LYF+J)
ELSE
YL=YVLAST - F(LYF+J)
ENDIF
C---DISTANCES OF THE CELL CENTERS FROM THE WALL ARE STORED
IN GRSP1-
F(LGF+J)=YL
110 CONTINUE
ENDIF
C*****
C----Group 9----Section 5-----

```

```

ELSEIF(IGR.EQ.9) THEN
C---CALCULATE TURBULENT REYNOLDS NUMBERS
C
  IF(ISG1.GT.2) THEN
C---REy=(Y*SQRT(KE))/VISL-----
CC-- FNTY7(Y,X1,X2,X3,A) -- Y=X1*(SQRT(X2)/(A*X3)
  CALL FNTY7(GRSP2,GRSP1,KE,VISL,1.0)
C---REy IS STORED IN GRSP2-----
C
  ENDIF
C---REt=KE**2/(VISL*EP)-----
  CALL FN8(GRSP3,KE,1.0,0.0,2.0,0.0)
  CALL FN21(GRSP10,VISL,EP,0.0,1.0)
C---REt IS STORED IN GRSP3-----
  CALL FN27(GRSP3,GRSP10)
C
C CALCULATE LR-EVM FUNCTIONS Fm,F1,F2 -----
  GO TO (951,952,953,954),ISG1
C
C 1- LAUNDER & SHARMA (LS) LR-EVM
C---Fm=EXP(-3.4/(1+0.02REt)) -----
C---F1=1.0 -----
C---F2=(1-0.3EXP(-REt**2)) -----
CC-- FNTY1(Y,X1,A,B,C,D) ---- Y=EXP(A/((B+C*X1)**D)) -----
CC-- FNTY5(Y,X1,A,B,C) ---- Y=A+B*EXP(C*(X1**D)) -----
C
  951 CONTINUE
  CALL FNTY1(GRSP4,GRSP3,-3.4,1.0,0.02,2.0)
  CALL FN1(GRSP5,1.0)
  CALL FNTY5(GRSP6,GRSP3,1.0,-0.3,-1.0,2.0)
  GO TO 955
C
C---Fm,F1 AND F2 ARE STORED IN GRSP4,GRSP5 AND GRSP6
RESPECTIVELY ----
C
C
C 2-TO & HUMPHREY (TH) LR-EVM (VAR. OF JL MODEL FOR BUOYANCY
INDUCED FLOWS)
C---Fm=EXP(-2.5/(1+0.02REt))-----
C---F1=1.0 -----
C---F2=(1-0.3EXP(-REt**2))*(1-EXP(-REt**2))-----
CC-- FNTY1(Y,X1,A,B,C,D) ---- Y=EXP(A/((B+C*X1)**D)) -----
CC-- FNTY4(Y,X1) - Y=(1-0.3*EXP(-X1**2))*(1-EXP(-X1**2)) -----
C
  952 CONTINUE
  CALL FNTY1(GRSP4,GRSP3,-2.5,1.0,0.02,1.0)
  CALL FN1(GRSP5,1.0)

```


CALL FNTY4(GRSP6,GRSP3)

GO TO 955

C

C---Fm,F1 AND F2 ARE STORED IN GRSP4,GRSP5 AND GRSP6
RESPECTIVELY ----

C

C

C 3-LAM & BREMHORST (LB) LR-EVM

C---Fm=(1-EXP(-0.0165REk))**2*(1+(20.5/REt))-----

C---F1=1+(0.05/Fm)**3 -----

C---F2=(1-EXP(-REt**2)) -----

CC-- FNTY2(Y,X1,X2,A,B,C,D,E) -- Y=((A-EXP(B*X1))**C)*(D+E/X2)-----

CC-- FNTY3(Y,X1,A,B,C) ---- Y=A+((B/X1)**C) -----

CC-- FNTY5(Y,X1,A,B,C) ---- Y=A+B*EXP(C*(X1**D)) -----

C

953 CONTINUE

CALL FNTY2(GRSP4,GRSP2,GRSP3,1.0,-0.0165,2.0,1.0,20.5)

CALL FNTY3(GRSP5,GRSP4,1.0,0.05,3.0)

CALL FNTY5(GRSP6,GRSP3,1.0,-1.0,-1.0,2.0)

GO TO 955

C

C---Fm,F1 AND F2 ARE STORED IN GRSP4,GRSP5 AND GRSP6
RESPECTIVELY ----

C

C 4-L. DAVIDSON (DA) LR-EVM (A MODEL FOR BUOYANCY INDUCED
FLOWS)

C---Fm=EXP(-3.4/((1+0.02REt)**2))-----

C---F1=1+(0.14/Fm)**3 -----

C---F2=(1-0.27EXP(-REt**2))*(1-EXP(-REk))-----

CC-- FNTY1(Y,X1,A,B,C,D) ---- Y=EXP(A/((B+C*X1)**D)) -----

CC-- FNTY3(Y,X1,A,B,C) ---- Y=A+((B/X1)**C) -----

CC-- FNTY6(Y,X1,X2) Y=(1-.27EXP(-(X1**2)))*(1-EXP(-(X2))) -----

C

954 CONTINUE

CALL FNTY1(GRSP4,GRSP3,-3.4,1.0,0.02,2.0)

CALL FNTY3(GRSP5,GRSP4,1.0,0.14,3.0)

CALL FNTY6(GRSP6,GRSP3,GRSP2)

C

C---Fm,F1 AND F2 ARE STORED IN GRSP4,GRSP5 AND GRSP6
RESPECTIVELY ----

C

C END OF SUBROUTINE TYLRFN

955 CONTINUE

ENDIF

END

CC--TY THIS SUBROUTINE CALCULATES THE LR-EVM TURBULENT
KINEMATIC VISC.

SUBROUTINE TYLRVT

C

C

INCLUDE 'd_phoe16\d_earth\GRDLOC'

INCLUDE 'd_phoe16\d_earth\GRDEAR'

INCLUDE 'd_phoe16\d_earth\SATEAR'

C

C

COMMON/TULRCS/CMULR,CE1LR,CE2LR,PRTT,TEXCO,CPLR

COMMON/NAMFN/NAMFUN,NAMSUB

CHARACTER*6 NAMFUN,NAMSUB

C

NAMSUB = 'TYLRVT'

C

CC-- CALCULATE THE THE TURBULENT KINEMATIC VISCOSITY

CC-- ENUT=CMULR*Fm*KE**2/EP

C

CALL TYLRFN

CALL FN0(GRSP10,KE)

CALL FN51(GRSP10,2.0)

CALL FN56(VIST,GRSP4,GRSP10,EP,CMULR)

C

C END OF SUBROUTINE TYLRVT

END

C

C

CC--TY THIS SUBROUTINE CALCULATES THE LR-EVM SOURCES OF KE
& EP

SUBROUTINE TYLRSO

C

C

INCLUDE 'd_phoe16\d_earth\GRDLOC'

INCLUDE 'd_phoe16\d_earth\GRDEAR'

INCLUDE 'd_phoe16\d_earth\SATEAR'

C

C

COMMON/TULRCS/CMULR,CE1LR,CE2LR,PRTT,TEXCO,CPLR

COMMON/NAMFN/NAMFUN,NAMSUB

CHARACTER*6 NAMFUN,NAMSUB

C

NAMSUB = 'TYLRSO'

C

IF(IGR.EQ.13.AND.ISC.EQ.1) THEN

CC-- CALCULATE THE COEFFICIENT PART OF LINEARIZED KE & EP
SOURCES--

```

C
C
  IF(INDVAR.EQ.KE) THEN
CC-- FN56(Y,X1,X2,X3,A) -- Y=A*X1*X2/X3 -----
  CALL FN56(CO,GRSP4,KE,VIST,CMULR)
  ELSEIF(INDVAR.EQ.EP) THEN
CC-- FN56(Y,X1,X2,X3,A) -- Y=A*X1*X2/X3 -----
  CALL FN56(CO,KE,GRSP6,VIST,CE2LR)
  CALL FN25(CO,CMULR)
  CALL FN26(CO,GRSP4)
  ENDIF
C
  ELSEIF(IGR.EQ.13.AND.ISC.EQ.12) THEN
CC-- CALCULATE THE VALUE PART OF LINEARIZED KE & EP SOURCES--
-----
C
  IF(INDVAR.EQ.KE) THEN
C
CC-- FNTY8A(Y,X1,X2,X3,X4,A) -----
C--- Y=X1**2*X2/A*X3*X4 -----
  CALL FNTY8A(VAL,VIST,GRSP7,GRSP4,KE,CMULR)
CC-- FNTY8B(Y,X1,X2,X3,X4,A,B,C,D) -----
C--- Y=Y+(A*B(X1**2)*X2/C*D*X3*X4) -----
  CALL FNTY8B(VAL,VIST,GRSP8,KE,GRSP4,TEXCO,-9.81,CMULR,PRTT)
C
  IF(ISG1.EQ.1) THEN
CC-- FNTY10(Y,X1,X2,X3,X4,X5,A) -----
C--- Y=Y-(2*X1*X2*X3**2/A*X4*X5) -----
  CALL FNTY10(VAL,VISL,VIST,GRSP9,GRSP4,KE,CMULR)
  ENDIF
  ELSEIF(INDVAR.EQ.EP) THEN
C
CC-- FNTY9A(Y,X1,X2,X3,X4,A,B) -----
C--- Y=(A*X1*X2*X3/B*X4) -----
  CALL FNTY9A(VAL,GRSP5,VIST,GRSP7,GRSP6,CE1LR,CE2LR)
CC-- FNTY9B(Y,X1,X2,X3,A,B,C,D,E) -----
C--- Y=Y+(A*B*C*X1*X2/D*E*X3) -----
  CALL FNTY9B(VAL,VIST,GRSP8,GRSP6,CE1LR,TEXCO,-
9.81,CE2LR,PRTT)
C
  IF(ISG1.EQ.1) THEN
  CALL FN51(GRSP1,2.0)
  CMULT=2.0/(CE2LR)
  CALL FN25(GRSP1,CMULT)
  CALL FN26(GRSP1,VISL)
  CALL FN26(GRSP1,VIST)
  CALL FN26(GRSP1,KE)

```

```

CALL FN27(GRSP1,GRSP6)
C CALL FN27(GRSP1,GRSP4)
CALL FN27(GRSP1,EP)
CALL FN34(VAL,GRSP1,1.0)
ENDIF
ENDIF
ENDIF
C END OF SUBROUTINE TYLRSO
END

C
C
CC--TY THIS SUBROUTINE CALCULATES THE GENERATION TERMS IN
THE CALCULATION
C OF THE PRODUCTION OF KE BY BOTH SHEARING AND BUOYANCY
C
SUBROUTINE TYLRGN
C
C
INCLUDE 'd_phoe16\d_earth\GRDLOC'
INCLUDE 'd_phoe16\d_earth\GRDEAR'
INCLUDE 'd_phoe16\d_earth\SATEAR'
C
C
COMMON/NAMFN/NAMFUN,NAMSUB
CHARACTER*6 NAMFUN,NAMSUB
C
NAMSUB = 'TYLRGN'
C
CC-- CALCULATE THE GENERATION DUE TO BUOYANCY -----
---
C
CALL FNDTDX
CC-- Y DERIVATIVES OF TEMP. PLACED IN GRSP8 -----
CC-- ----- DT/DX ----- CALCULATED AND PLACED IN GRSP8 -----
C
CC-- CALCULATE THE GENERATION DUE TO SHEARING -----
--
C  $Y=2*((dU_i/dX_i)**2)+(dU_i/dX_j + dU_j/dX_i)**2$ 
C
CC-----
CALL FNDUDX(GRSP2,U1)
CALL FN8(GRSP7,GRSP2,2.0,0.0,2.0,0.0)
CALL FNDVDY(GRSP2,V1)
CALL FN8(GRSP3,GRSP2,2.0,0.0,2.0,0.0)
CALL FN34(GRSP7,GRSP3,1.0)
CALL FNDUDY(GRSP2,U1)
CALL FNDVDX(GRSP3,V1)

```



```

CALL FN34(GRSP2,GRSP3,1.0)
CALL FN51(GRSP2,2.0)
CALL FN34(GRSP7,GRSP2,1.0)
C
C END OF SUBROUTINE TYLRGN
  END
C
C
CC--TY--USER CREATED FN SUBROUTINES-----
C
C
CC-- FNTY1(Y,X1,A,B,C,D) ---- Y=EXP(A/((B+C*X1)**D)) -----
  SUBROUTINE FNTY1(K1,K2,A,B,C,D)
    COMMON F(1)
    COMMON/IGE/IXF,IXL,IYF,IYL,IGFILL(21)
    IF(IXL.LT.0) RETURN
    CALL L0F2(K1,K2,I,I2M1,IADD,'FNTY1 ')
    DO 1 IX=IXF,IXL
      I=I+IADD
      DO 1 IY=IYF,IYL
        I=I+1
      1 F(I)=EXP(A/((B+C*F(I2M1+I))**D))
    END
C
C
CC-- FNTY2(Y,X1,X2,A,B,C,D,E) -- Y=((A-EXP(B*X1))**C)*(D+E/X2)-----
  SUBROUTINE FNTY2(K1,K2,K3,A,B,C,D,E)
    COMMON F(1)
    COMMON/IGE/IXF,IXL,IYF,IYL,IGFILL(21)
    IF(IXL.LT.0) RETURN
    CALL L0F3(K1,K2,K3,I,I2M1,I3M1,IADD,'FNTY2 ')
    DO 1 IX=IXF,IXL
      I=I+IADD
      DO 1 IY=IYF,IYL
        I=I+1
      1 F(I)=((A-EXP(B*F(I2M1+I))**C)*(D+E/F(I3M1+I))
    END
CC-- FNTY3(Y,X1,A,B,C) ---- Y=A+((B/X1)**C) -----
  SUBROUTINE FNTY3(K1,K2,A,B,C)
    COMMON F(1)
    COMMON/IGE/IXF,IXL,IYF,IYL,IGFILL(21)
    IF(IXL.LT.0) RETURN
    CALL L0F2(K1,K2,I,I2M1,IADD,'FNTY3 ')
    DO 1 IX=IXF,IXL
      I=I+IADD
      DO 1 IY=IYF,IYL
        I=I+1

```

```

1 F(I)=A+((B/F(I2M1+I))**C)
END
CC-- FNTY4(Y,X1) - Y=(1-0.3*EXP(-X1**2))*(1-EXP(-X1**2)) -----
SUBROUTINE FNTY4(K1,K2)
COMMON F(1)
COMMON/IGE/IXF,IXL,IYF,IYL,IGFILL(21)
IF(IXL.LT.0) RETURN
CALL L0F2(K1,K2,I,I2M1,IADD,'FNTY4 ')
DO 1 IX=IXF,IXL
I=I+IADD
DO 1 IY=IYF,IYL
I=I+1
1 F(I)=(1-0.3*EXP(-F(I2M1+I)**2))*(1-EXP(-F(I2M1+I)**2))
END
CC-- FNTY5(Y,X1,A,B,C) ----- Y=A+B*EXP(C*(X1**D)) -----
SUBROUTINE FNTY5(K1,K2,A,B,C,D)
COMMON F(1)
COMMON/IGE/IXF,IXL,IYF,IYL,IGFILL(21)
IF(IXL.LT.0) RETURN
CALL L0F2(K1,K2,I,I2M1,IADD,'FNTY5 ')
DO 1 IX=IXF,IXL
I=I+IADD
DO 1 IY=IYF,IYL
I=I+1
1 F(I)=A+B*EXP(C*(F(I2M1+I)**D))
END
CC-- FNTY6(Y,X1,X2,A,B,C,D,E) - Y=(1-.27EXP(-(X1**2)))*(1-EXP(-(X2)))
SUBROUTINE FNTY6(K1,K2,K3)
COMMON F(1)
COMMON/IGE/IXF,IXL,IYF,IYL,IGFILL(21)
IF(IXL.LT.0) RETURN
CALL L0F3(K1,K2,K3,I,I2M1,I3M1,IADD,'FNTY6 ')
DO 1 IX=IXF,IXL
I=I+IADD
DO 1 IY=IYF,IYL
I=I+1
1 F(I)=(1-0.27*EXP(-(F(I2M1+I)**2)))*(1-EXP(-F(I3M1+I)))
END
C
CC-- FNTY7(Y,X1,X2,X3,A) -- Y=X1*(SQRT(X2)/(A*X3)
SUBROUTINE FNTY7(K1,K2,K3,K4,A)
COMMON F(1)
COMMON/IGE/IXF,IXL,IYF,IYL,IGFILL(21)
IF(IXL.LT.0) RETURN
CALL L0F4(K1,K2,K3,K4,I,I2M1,I3M1,I4M1,IADD,'FNTY7 ')
DO 1 IX=IXF,IXL
I=I+IADD

```

```

    DO 1 IY=IYF,IYL
    I=I+1
    1 F(I)=F(I2M1+I)*SQRT(F(I3M1+I))/(A*F(I4M1+I))
    END
C
C
CC-- FNTY8A(Y,X1,X2,X3,X4,A) -----
C--- Y=X1**2*X2/A*X3*X4 -----
    SUBROUTINE FNTY8A(K1,K2,K3,K4,K5,A)
    COMMON F(1)
    COMMON/IGE/IXF,IXL,IYF,IYL,IGFILL(21)
    IF(IXL.LT.0) RETURN
    CALL L0F5(K1,K2,K3,K4,K5,I,I2M1,I3M1,I4M1,I5M1,IADD,'FNTY8A')
    DO 2 IX=IXF,IXL
    I=I+IADD
    DO 2 IY=IYF,IYL
    I=I+1
    2 F(I)=(F(I2M1+I)**2)*F(I3M1+I)/(A*F(I4M1+I)*F(I5M1+I))
    END
CC-- FNTY8B(Y,X1,X2,X3,X4,A,B,C,D) -----
C--- Y=Y+(A*B(X1**2)*X2/C*D*X3*X4) -----
    SUBROUTINE FNTY8B(K1,K2,K3,K4,K5,A,B,C,D)
    COMMON F(1)
    COMMON/IGE/IXF,IXL,IYF,IYL,IGFILL(21)
    IF(IXL.LT.0) RETURN
    CALL L0F5(K1,K2,K3,K4,K5,I,I2M1,I3M1,I4M1,I5M1,IADD,'FNTY8B')
    DO 2 IX=IXF,IXL
    I=I+IADD
    DO 2 IY=IYF,IYL
    I=I+1
    2 F(I)=F(I)+((A*B*(F(I2M1+I)**2)*F(I3M1+I))
    1/(C*D*F(I4M1+I)*F(I5M1+I)))
    END
C
CC-- FNTY9A(Y,X1,X2,X3,X4,A,B) -----
C--- Y=(A*X1*X2*X3/B*X4) -----
    SUBROUTINE FNTY9A(K1,K2,K3,K4,K5,A,B)
    COMMON F(1)
    COMMON/IGE/IXF,IXL,IYF,IYL,IGFILL(21)
    IF(IXL.LT.0) RETURN
    CALL L0F5(K1,K2,K3,K4,K5,I,I2M1,I3M1,I4M1,I5M1,IADD,'FNTY9A')
    DO 2 IX=IXF,IXL
    I=I+IADD
    DO 2 IY=IYF,IYL
    I=I+1
    2 F(I)=A*F(I2M1+I)*F(I3M1+I)*F(I4M1+I)/(B*F(I5M1+I))

```


END

C

CC-- FNTY9B(Y,X1,X2,X3,A,B,C,D,E) -----

C--- Y=Y+(*A*B*C*X1*X2/D*E*X3) -----

SUBROUTINE FNTY9B(K1,K2,K3,K4,A,B,C,D,E)

COMMON F(1)

COMMON/IGE/IXF,IXL,IYF,IYL,IGFILL(21)

IF(IXL.LT.0) RETURN

CALL L0F4(K1,K2,K3,K4,I,I2M1,I3M1,I4M1,IADD,'FNTY9B')

DO 2 IX=IXF,IXL

I=I+IADD

DO 2 IY=IYF,IYL

I=I+1

2 F(I)=F(I)+(A*B*C*F(I2M1+I)*F(I3M1+I)/(D*E*F(I4M1+I)))

END

C

C

CC-- FNTY10(Y,X1,X2,X3,X4,X5,A) -----

C--- Y=Y-2*X1*X2*X3**2/A*X4*X5 -----

SUBROUTINE FNTY10(K1,K2,K3,K4,K5,K6,A)

COMMON F(1)

COMMON/IGE/IXF,IXL,IYF,IYL,IGFILL(21)

IF(IXL.LT.0) RETURN

CALL L0F6(K1,K2,K3,K4,K5,K6,I,I2M1,I3M1,I4M1,I5M1,I6M1,
IADD,'FNTY10')

DO 2 IX=IXF,IXL

I=I+IADD

DO 2 IY=IYF,IYL

I=I+1

2 F(I)=F(I)-(2*F(I2M1+I)*F(I3M1+I)*(F(I4M1+I)**2)

1/(A*F(I5M1+I)*F(I6M1+I)))

END

C

CC-- FNTYP(Y,X1,A,B,C,D,E,F,G) -- Y=A+B*X1+C*X2**2...+G*X**6 -----

SUBROUTINE FNTYP(K1,K2,A,B,C,D,E,FT,G)

COMMON F(1)

COMMON/IGE/IXF,IXL,IYF,IYL,IGFILL(21)

IF(IXL.LT.0) RETURN

CALL L0F2(K1,K2,I,I2M1,IADD,'FNTYP')

DO 1 IX=IXF,IXL

I=I+IADD

DO 1 IY=IYF,IYL

I=I+1

1 F(I)=A+B*F(I2M1+I)+C*F(I2M1+I)**2+D*F(I2M1+I)**3+E*F(I2M1+I)**4
*+FT*F(I2M1+I)**5+G*F(I2M1+I)**6

END

CC-- FNDTDX-----Y=dT/dX-----

C-- DERIVATIVES ARE CALCULATED WITH A FIRST DEGREE APPR. OF
FUNCTION---

SUBROUTINE FNDTDX

C

INCLUDE 'd_phoe16\d_earth\GRDLOC'

INCLUDE 'd_phoe16\d_earth\GRDEAR'

INCLUDE 'd_phoe16\d_earth\SATEAR'

C

COMMON/TULRCS/CMULR,CE1LR,CE2LR,PRTT,TEXCO,CPLR

COMMON/NAMFN/NAMFUN,NAMSUB

CHARACTER*6 NAMFUN,NAMSUB

C

NAMSUB = 'FNDTDX'

C

LOTE=L0F(H1)

L0DX=L0F(DXG2D)

L0ST=L0F(GRSP8)

I=0

DO 1 IX=IXF,IXL

DO 1 IY=IYF,IYL

I=I+1

KI=I+IYL

KJ=I-IYL

IF(IX.LT.IXL)THEN

F(L0ST+I)=(F(LOTE+KI)/CPLR-F(LOTE+I)/CPLR)/F(L0DX+I)

ELSE

F(L0ST+I)=(F(LOTE+I)/CPLR-F(LOTE+KJ)/CPLR)/F(L0DX+I)

ENDIF

1 CONTINUE

END

CC-- FNDTDY -- Y=dT/dY -----

C-- DERIVATIVES ARE CALCULATED WITH A FIRST DEGREE APPR. OF
FUNCTION---

SUBROUTINE FNDTDY

C

INCLUDE 'd_phoe16\d_earth\GRDLOC'

INCLUDE 'd_phoe16\d_earth\GRDEAR'

INCLUDE 'd_phoe16\d_earth\SATEAR'

C

COMMON/TULRCS/CMULR,CE1LR,CE2LR,PRTT,TEXCO,CPLR

COMMON/NAMFN/NAMFUN,NAMSUB

CHARACTER*6 NAMFUN,NAMSUB

C

NAMSUB = 'FNDTDY'

C

```
LOTE=L0F(H1)
LODY=L0F(DYG2D)
LOST=L0F(GRSP3)
I=0
  DO 1 IX=IXF,IXL
  DO 1 IY=IYF,IYL
I=I+1
KI=I+1
KJ=I-1
IF(IY.LT.IYL) THEN
F(LOST+I)=(F(LOTE+KI)/CPLR-F(LOTE+I)/CPLR)/F(LODY+I)
ELSE
F(LOST+I)=(F(LOTE+I)/CPLR-F(LOTE+KJ)/CPLR)/F(LODY+I)
ENDIF
1 CONTINUE
END
```

C

C

```
CC-- FNDSQRTKDY --  $Y=d(K)**0.5/dY$  -----
C-- DERIVATIVES ARE CALCULATED WITH A FIRST DEGREE APPR. OF
FUNCTION---
```

```
  SUBROUTINE FNDSQRTKDY
```

C

```
  INCLUDE 'd_phoe16\d_earth\GRDLOC'
  INCLUDE 'd_phoe16\d_earth\GRDEAR'
  INCLUDE 'd_phoe16\d_earth\SATEAR'
```

C

```
  COMMON/NAMFN/NAMFUN,NAMSUB
  CHARACTER*6 NAMFUN,NAMSUB
```

C

```
  NAMSUB = 'FNDSQRTKDY'
```

C

```
LOKE=L0F(KE)
LODY=L0F(DYG2D)
LOST=L0F(GRSP9)
I=0
  DO 1 IX=IXF,IXL
  DO 1 IY=IYF,IYL
I=I+1
KI=I+1
KJ=I-1
IF(IY.LT.IYL) THEN
F(LOST+I)=(SQRT(F(LOKE+KI))-SQRT(F(LOKE+I)))/F(LODY+I)
ELSE
F(LOST+I)=(SQRT(F(LOKE+I))-SQRT(F(LOKE+KJ)))/F(LODY+I)
ENDIF
```



```

1 CONTINUE
  END
CC-- FNSQRDUDY --  $Y=d^{**2}Y/d(Y^{**2})$  -----
C-- DERIVATIVES ARE CALCULATED WITH A SECOND DEGREE APPR.
OF FUNCTION---
C
  SUBROUTINE FNSQRDUDY
C
  INCLUDE 'd_phoe16\d_earth\GRDLOC'
  INCLUDE 'd_phoe16\d_earth\GRDEAR'
  INCLUDE 'd_phoe16\d_earth\SATEAR'
C
  COMMON/NAMFN/NAMFUN,NAMSUB
  CHARACTER*6 NAMFUN,NAMSUB
C
  NAMSUB = 'FNSQRDUDY'
C
  LOV=LOF(U1)
  LODY=LOF(DYG2D)
  LOST=LOF(GRSP1)
  I=0
    DO 2 IX=IXF,IXL
      DO 2 IY=IYF,IYL
        I=I+1
        KI=I+2
        KA=I+1
        KJ=I-2
        KB=I-1
        IF(IY.LE.(IYL-2)) THEN
          F(LOST+I)=2*((F(LOV+KI)-F(LOV+I))/((F(LODY+I)+F(LODY+KA))
1 *F(LODY+KA))-((F(LOV+KA)-F(LOV+I))/(F(LODY+I)*F(LODY+KA))))
        ELSE
          F(LOST+I)=2*((F(LOV+I)-F(LOV+KJ))/((F(LODY+KJ)+F(LODY+KB))
1 *F(LODY+KB))-((F(LOV+KB)-F(LOV+KJ))/(F(LODY+KJ)*F(LODY+KB))))
        ENDIF
      2 CONTINUE
    END
C
C
CC---TY THIS SUBROUTINE CALCULATES THE VAL OF KE AT THE WALL
FOR THE -----
CC  TH LR-EVM
  SUBROUTINE TYLRWL
C
  INCLUDE 'd_phoe16\d_earth\GRDLOC'
  INCLUDE 'd_phoe16\d_earth\GRDEAR'
  INCLUDE 'd_phoe16\d_earth\SATEAR'

```

```
C
COMMON/NAMFN/NAMFUN,NAMSUB
CHARACTER*6 NAMFUN,NAMSUB
C
NAMSUB = 'TYLRWL'
C
C
IF(INDVAR.EQ.EP) THEN
CALL FN31(VAL,VISL,GRSP9,2.0,1.0,2.0)
ENDIF
END
CC---TY END OF SUBROUTINE TYLRWL -----
```

B.2 Q1 FILE of LRN k-ε TURBULENCE MODELS

TALK=T;RUN(1, 1);VDU=VGACURSR

REAL(CP,HIN,PBOT,RHOIN,KEIN,EPIN)

CP=1004.5;HIN=22.5*CP;PBOT=0.0;

GROUP 1. Run title and other preliminaries

TEXT(NATURAL CONVEC.:LR-EVM(TH) TUR. CHA. FLOW)

GROUP 2. Transience; time-step specification

GROUP 3. X-direction grid specification

GRDPWR(X,60,3,1.2)

GROUP 4. Y-direction grid specification

GRDPWR(Y,-60,.1,2)

GROUP 5. Z-direction grid specification

GROUP 6. Body-fitted coordinates or grid distortion

GROUP 7. Variables stored, solved & named

SOLVE(P1,U1,V1,H1,KE,EP);SOLUTN(P1,Y,Y,Y,P,P,P)

STORE(ENUT,ENUL,RHO1)

GROUP 8. Terms (in differential equations) & devices

GROUP 9. Properties of the medium (or media)

ENUL=1.5E-5;PRNDTL(H1)=0.71;PRT(H1)=0.9

ENUT=GRND;

RHO1=GRND2;RHO1A=287.0*273.0/1.E5;RHO1B=287.0/(1E5*CP)

GROUP 10. Inter-phase-transfer processes and properties

GROUP 11. Initialization of variable or porosity fields

RHOIN=1.0/(RHO1A+RHO1B*HIN);FIINIT(ENUT)=1.5E-3

KEIN=0.018*0.25*0.5**2;

*** EXP. VALUE OF KE

KEIN=1.06E-2

EPIN=(0.4/YVLAST)*KEIN**1.5

FIINIT(ENUL)=1.5E-5;FIINIT(RHO1)=RHOIN

FIINIT(H1)=HIN;FIINIT(KE)=KEIN;FIINIT(EP)=EPIN;

GROUP 12. Patchwise adjustment of terms (in differential equatio

GROUP 13. Boundary conditions and special sources

PATCH(BUOYANCY,PHASEM,1,NX,1,NY,1,1,1,1)

COVAL(BUOYANCY,U1,FIXFLU,GRND2)

RSG1=RHOIN;RSG8=-9.81

PATCH(LRSOURCE,PHASEM,1,NX,1,NY,1,1,1,1)

COVAL(LRSOURCE,KE,GRND,GRND)

COVAL(LRSOURCE,EP,GRND,GRND)

PATCH(INLET,EAST,1,1,1,NY,1,1,1,1)

COVAL(INLET,P1,-2*RHOIN,PBOT)

COVAL(INLET,U1,ONLYMS,SAME)

COVAL(INLET,V1,ONLYMS,SAME)

COVAL(INLET,H1,ONLYMS,HIN)

COVAL(INLET,KE,ONLYMS,KEIN)

COVAL(INLET,EP,ONLYMS,EPIN)

PATCH(OUTLET,WEST,NX,NX,1,NY,1,1,1,1)

COVAL(OUTLET,P1,1.0E3,PBOT)

COVAL(OUTLET,U1,ONLYMS,SAME)

COVAL(OUTLET,V1,ONLYMS,SAME)

COVAL(OUTLET,H1,ONLYMS,SAME)

COVAL(OUTLET,KE,ONLYMS,SAME)

COVAL(OUTLET,EP,ONLYMS,SAME)

PATCH(HOTWALL,SWALL,1,NX,1,1,1,1,1,1)

COVAL(HOTWALL,U1,1.0,0.0)

COVAL(HOTWALL,KE,1.0,0.0)

COVAL(HOTWALL,EP,1.0/PRT(EP),GRND)

COVAL(HOTWALL,H1,1.0/PRNDTL(H1),100.0*CP)

PATCH(COLDWALL,NWALL,1,NX,NY,NY,1,1,1,1)

COVAL(COLDWALL,U1,1.0,0.0)

COVAL(COLDWALL,KE,1.0,0.0)

COVAL(COLDWALL,EP,1.0/PRT(EP),GRND)

GROUP 14. Downstream pressure for PARAB=.TRUE.

GROUP 15. Termination of sweeps

LSWEEP=400

GROUP 16. Termination of iterations

GROUP 17. Under-relaxation devices

RELAX(P1,LINRLX,0.4)
RELAX(U1,FALSDT,0.2)
RELAX(V1,FALSDT,0.2)
RELAX(H1,FALSDT,0.2)
RELAX(KE,FALSDT,0.2)
RELAX(EP,FALSDT,0.2)
RELAX(ENUT,FALSDT,0.2)

GROUP 18. Limits on variables or increments to them

VARMIN(KE)=1.0E-25
VARMIN(EP)=1.0E-25
VARMIN(U1)=-1E5
VARMIN(V1)=-1E5
VARMIN(P1)=-1E10
VARMAX(KE)=1E5
VARMAX(EP)=1E5
VARMAX(U1)=1E5
VARMAX(V1)=1E5
VARMAX(P1)=0
VARMAX(ENUT)=.1

GROUP 19. Data communicated by satellite to GROUND

ISG1=2

PROFILE LOCATIONS

IG(1)=4
IG(2)=16
IG(3)=34
IG(4)=42
IG(5)=59

GROUP 20. Preliminary print-out

ECHO=F

GROUP 21. Print-out of variables

GROUP 22. Spot-value print-out

IXMON=40;IYMON=20

GROUP 23. Field print-out and plot control

NXPRIN=1;NYPRIN=1;

ITABL=1

I PROF=3

PATCH(X.1,PROFIL,IG(1),IG(1),1,NY,1,1,1,1)

PLOT(X.1,U1,0.0,0.0)

PATCH(X.6,PROFIL,IG(2),IG(2),1,NY,1,1,1,1)

PLOT(X.6,U1,0.0,0.0)

PATCH(X1.5,PROFIL,IG(3),IG(3),1,NY,1,1,1,1)

```
PLOT(X1.5,U1,0.0,0.0)
PATCH(X1.9,PROFIL,IG(4),IG(4),1,NY,1,1,1,1)
PLOT(X1.9,U1,0.0,0.0)
PATCH(X2.95,PROFIL,IG(5),IG(5),1,NY,1,1,1,1)
PLOT(X2.95,U1,0.0,0.0)
```

```
GROUP 24. Dumps for restarts
STOP
```



```

C
C 4 Insert own coding below as desired, guided by GREX examples.
C Note that the satellite-to-GREX special data in the labelled
C COMMONs /RSG/, /ISG/, /LSG/ and /CSG/ can be included and
C used below but the user must check GREX for any conflicting
C uses. The same comment applies to the EARTH-spare working
C arrays EASP1, EASP2,...EASP20. In addition to the EASPs,
C there are 10 GRound-earth SPare arrays, GRSP1,...,GRSP10,
C supplied solely for the user, which are not used by GREX. If
C the call to GREX has been deactivated then all of the arrays
C may be used without reservation.
C
  IXL=IABS(IXL)
  IF(IGR.EQ.13) GO TO 13
  IF(IGR.EQ.19) GO TO 19
  GO TO (1,2,3,4,5,6,25,8,9,10,11,12,13,14,25,25,25,25,19,20,25,
  125,23,24),IGR
  25 CONTINUE
  RETURN
C*****
C
C--- GROUP 1. Run title and other preliminaries
C
  1 GO TO (1001,1002),ISC
  1001 CONTINUE
C
C User may here change message transmitted to the VDU screen or
C batch-run log file.
  IF(IGR.EQ.1.AND.ISC.EQ.1.AND..NOT.NULLPR) THEN
c   CALL WRYT40('GROUND file is GROUND.FTN of: 120392 ')
  CALL WRYT40('GROUND file is lmgnd.for by T. YILMAZ ')
  ENDIF
C
C PROVISION OF STORAGE FOR CELL CENTER DISTANCES FROM X=0.0
C PLANE
C FOR USE IN VARIABLE WALL TEMP. BC CALCULATIONS.
C-----XG2D
  CALL MAKE(XG2D)
  CALL MAKE(DXG2D)
  CALL MAKE(YG2D)
  CALL MAKE(GRSP1)
  CALL MAKE(GRSP2)
CC--TY
  RETURN
  1002 CONTINUE
  RETURN

```


{----- DATA OMITTED -----}

```
C*****
C
C--- GROUP 13. Boundary conditions and special sources
C           Index for Coefficient - CO
C           Index for Value      - VAL
  13 CONTINUE
    NPAT=NPATCH(1:4)
    GO TO (130,131,132,133,134,135,136,137,138,139,1310,
    11311,1312,1313,1314,1315,1316,1317,1318,1319,1320,1321),ISC
  130 CONTINUE
C----- SECTION 1 ----- coefficient = GRND
    RETURN
  131 CONTINUE
C----- SECTION 2 ----- coefficient = GRND1
    RETURN
  132 CONTINUE
C----- SECTION 3 ----- coefficient = GRND2
    RETURN
  133 CONTINUE
C----- SECTION 4 ----- coefficient = GRND3
    RETURN
  134 CONTINUE
C----- SECTION 5 ----- coefficient = GRND4
    RETURN
  135 CONTINUE
C----- SECTION 6 ----- coefficient = GRND5
    RETURN
  136 CONTINUE
C----- SECTION 7 ----- coefficient = GRND6
    RETURN
  137 CONTINUE
C----- SECTION 8 ----- coefficient = GRND7
    RETURN
  138 CONTINUE
C----- SECTION 9 ----- coefficient = GRND8
    RETURN
  139 CONTINUE
C----- SECTION 10 ----- coefficient = GRND9
    RETURN
  1310 CONTINUE
C----- SECTION 11 ----- coefficient = GRND10
    RETURN
  1311 CONTINUE
C----- SECTION 12 ----- value = GRND
```


{ -- CODING TO IMPLEMENT VARIABLE WALL TEMPERATURE BC -- }

```
CC--TY CACULATE THE VALUE PART OF VARIABLE WALL TEMP. BC
  IF(INDVAR.EQ.H1) THEN
C   CALCULATE TEMPERATURE-----
  IF(NPAT.EQ.'VRTH') THEN
C   WRITE(*,*)'HOT WALL VALUES BEING CALCULATED
  CALL FN3(VAL,XG2D,RSG30,RSG29,RSG28)
C   CALL PRN(VRTEVAL,VAL)
  CALL FN25(VAL,RSG24)
  ELSEIF(NPAT.EQ.'VRTC') THEN
C   WRITE(*,*)'COLD WALL VALUES BEING CALCULATED
  CALL FN3(VAL,XG2D,RSG27,RSG26,RSG25)
  CALL FN25(VAL,RSG24)
  ENDIF
  ENDIF
CC--TY
  RETURN
1312 CONTINUE
C----- SECTION 13 ----- value = GRND1
  RETURN
1313 CONTINUE
C----- SECTION 14 ----- value = GRND2
  RETURN
1314 CONTINUE
C----- SECTION 15 ----- value = GRND3
  RETURN
1315 CONTINUE
C----- SECTION 16 ----- value = GRND4
  RETURN
1316 CONTINUE
C----- SECTION 17 ----- value = GRND5
  RETURN
1317 CONTINUE
C----- SECTION 18 ----- value = GRND6
  RETURN
1318 CONTINUE
C----- SECTION 19 ----- value = GRND7
  RETURN
1319 CONTINUE
C----- SECTION 20 ----- value = GRND8
  RETURN
1320 CONTINUE
C----- SECTION 21 ----- value = GRND9
  RETURN
1321 CONTINUE
```

```

C----- SECTION 22 ----- value = GRND10
  RETURN
C*****
C
C--- GROUP 14. Downstream pressure for PARAB=.TRUE.
C
  14 CONTINUE
  RETURN
C*****
C* Make changes for these groups only in GROUP 19.
C--- GROUP 15. Termination of sweeps
C--- GROUP 16. Termination of iterations
C--- GROUP 17. Under-relaxation devices
C--- GROUP 18. Limits on variables or increments to them
C*****
C
C--- GROUP 19. Special calls to GROUND from EARTH
C
  19 GO TO (191,192,193,194,195,196,197,198,199,1910),ISC
  191 CONTINUE
C * ----- SECTION 1 ---- Start of time step.
  RETURN
  192 CONTINUE
C * ----- SECTION 2 ---- Start of sweep.
  RETURN
  193 CONTINUE
C * ----- SECTION 3 ---- Start of iz slab.
  RETURN
  194 CONTINUE
C * ----- SECTION 4 ---- Start of iterations over slab.
  RETURN
  199 CONTINUE
C * ----- SECTION 9 ---- Start of solution sequence for
C                               a variable
  RETURN
  1910 CONTINUE
C * ----- SECTION 10---- Finish of solution sequence for
C                               a variable
  RETURN
  195 CONTINUE
C * ----- SECTION 5 ---- Finish of iterations over slab.
  RETURN
  196 CONTINUE
C * ----- SECTION 6 ---- Finish of iz slab.
  RETURN
  197 CONTINUE
C * ----- SECTION 7 ---- Finish of sweep.

```

```

RETURN
198 CONTINUE
C * ----- SECTION 8 ---- Finish of time step.
C

```

```

{-- CODING TO WRITE U1 AND H1 PROFILES OF DESIRED
ELEVATION INTO A FILE CALLED 'PROFIL.PRN' --}

```

```

C--TY
c IF(ISWEEP.EQ.LSWEEP) THEN
c CALL PRN('DXG2D',DXG2D)
c OPEN(7,FILE='PROFIL.PRN', STATUS = 'OLD')
c DO 3333 ITY=6,NY
c LLY=L0F(YG2D)
c LLU1=L0F(u1)
c RTY=((F(LLY+ITY)-.003))/(YVLAST-.003)
c RTU1=(F(LLU1+((IG(1)-1)*NY)+ITY))*1000.0
c RTU2=(F(LLU1+((IG(2)-1)*NY)+ITY))*1000.0
c RTU3=(F(LLU1+((IG(3)-1)*NY)+ITY))*1000.0
c RTU4=(F(LLU1+((IG(4)-1)*NY)+ITY))*1000.0
c RTU5=(F(LLU1+((IG(5)-1)*NY)+ITY))*1000.0
c WRITE(7,333) RTY,RTU1,RTU2,RTU3,RTU4,RTU5
c333 FORMAT(5X,E9.4,2X,E9.4,2X,E9.4,2X,E9.4,2X,E9.4,2X,E9.4)
c3333 CONTINUE
c CLOSE(7)
c ENDIF

```

```

C--TY

```

```

C--TY
IF(ISWEEP.EQ.LSWEEP) THEN
CALL PRN('DXG2D',DXG2D)
OPEN(7,FILE='PROFIL.PRN', STATUS = 'OLD')
DO 3333 ITY=6,NY
LLY=L0F(YG2D)
LLU1=L0F(H1)
RTY=((F(LLY+ITY)-.003))/(YVLAST-.003)
RTU1=(F(LLU1+((IG(1)-1)*NY)+ITY))/1004.5
RTU2=(F(LLU1+((IG(2)-1)*NY)+ITY))/1004.5
RTU3=(F(LLU1+((IG(3)-1)*NY)+ITY))/1004.5
RTU4=(F(LLU1+((IG(4)-1)*NY)+ITY))/1004.5
RTU5=(F(LLU1+((IG(5)-1)*NY)+ITY))/1004.5
WRITE(7,333) RTY,RTU1,RTU2,RTU3,RTU4,RTU5
333 FORMAT(5X,E9.4,2X,E9.4,2X,E9.4,2X,E9.4,2X,E9.4,2X,E9.4)
3333 CONTINUE
CLOSE(7)
ENDIF

```

```

C--TY
RETURN

```



```

C*****
C
C--- GROUP 20. Preliminary print-out
C
  20 CONTINUE
  RETURN
C*****
C* Make changes for these groups only in GROUP 19.
C--- GROUP 21. Print-out of variables
C--- GROUP 22. Spot-value print-out
C*****
C
C--- GROUP 23. Field print-out and plot control
  23 CONTINUE
  RETURN
C*****
C
C--- GROUP 24. Dumps for restarts
C
  24 CONTINUE
  END
C*****
  SUBROUTINE SPECGR
  CALL WRIT40('Dummy subroutine SPECGR called.  ')
  CALL WAYOUT(2)
  END
C*****
  SUBROUTINE SPC1GR
  CALL WRIT40('Dummy subroutine SPC1GR called.  ')
  CALL WAYOUT(2)
  END
C*****
  SUBROUTINE SPC2GR
  CALL WRIT40('Dummy subroutine SPC2GR called.  ')
  CALL WAYOUT(2)
  END
C*****
  SUBROUTINE SPC3GR
  CALL WRIT40('Dummy subroutine SPC3GR called.  ')
  CALL WAYOUT(2)
  END
C*****
  SUBROUTINE QUIZ
C--- This subroutine is used by CHAM for de-bugging
  END

```

B.4 Q1 File of LAMINAR FLOW (Case 5)

```
TALK=T;RUN( 1, 1);VDU=VGACURSR
****
REAL(CP,HIN,PBOT,RHOIN,KEIN,EPIN)
CP=1004.5;HIN=21.5*CP;PBOT=0.0;
****
GROUP 1. Run title and other preliminaries
****
TEXT(LAMINAR CHAN FLOW CASE-5)
****
GROUP 2. Transience; time-step specification
GROUP 3. X-direction grid specification
****
NREGX=2
IREGX=1;GRDPWR(X,-18,0.18,1.2)
IREGX=2;GRDPWR(X,64,0.32,1.2)
****
GROUP 4. Y-direction grid specification
****
NREGY=2
IREGY=1;GRDPWR(Y,5,0.003,-1.2)
IREGY=2;GRDPWR(Y,-30,0.02,1.2)
****
GROUP 5. Z-direction grid specification
GROUP 6. Body-fitted coordinates or grid distortion
GROUP 7. Variables stored, solved & named
****
SOLVE(P1,U1,V1,H1);SOLUTN(P1,Y,Y,Y,P,P,P)
STORE(RHO1)
****
GROUP 8. Terms (in differential equations) & devices
GROUP 9. Properties of the medium (or media)
****
ENUL=1.65E-5;PRNDTL(H1)=0.71
RHO1=GRND2;RHO1A=287.0*273.0/1.E5;RHO1B=287.0/(1E5*CP)
****
GROUP 10. Inter-phase-transfer processes and properties
GROUP 11. Initialization of variable or porosity fields
****
CONPOR(ALPLT,0.0,CELL,-19,-NX,1,5,1,1)
RHOIN=1.0/(RHO1A+RHO1B*HIN)
FIINIT(RHO1)=RHOIN
FIINIT(H1)=HIN
****
```

GROUP 12. Patchwise adjustment of terms (in differential equatio

GROUP 13. Boundary conditions and special sources

PATCH(BUOYANCY,PHASEM,1,NX,1,NY,1,1,1,1)

COVAL(BUOYANCY,U1,FIXFLU,GRND2)

RSG1=RHOIN;RSG8=-9.81

PATCH(INLET,EAST,1,1,1,NY,1,1,1,1)

COVAL(INLET,P1,-2*RHOIN,PBOT)

COVAL(INLET,U1,ONLYMS,SAME)

COVAL(INLET,V1,ONLYMS,SAME)

COVAL(INLET,H1,ONLYMS,HIN)

PATCH(OUTLET,WEST,NX,NX,6,NY,1,1,1,1)

COVAL(OUTLET,P1,1.0E3,PBOT)

COVAL(OUTLET,U1,ONLYMS,SAME)

COVAL(OUTLET,V1,ONLYMS,SAME)

COVAL(OUTLET,H1,ONLYMS,SAME)

PATCH(VRTH,SWALL,19,NX,6,6,1,1,1,1)

COVAL(VRTH,U1,1.0,0.0)

COVAL(VRTH,H1,1.0/PRNDTL(H1),GRND)

PATCH(COLDWAL,NWALL,1,NX,NY,NY,1,1,1,1)

COVAL(COLDWAL,U1,1.0,0.0)

PATCH(VRTC,NWALL,19,NX,NY,NY,1,1,1,1)

COVAL(VRTC,H1,1.0/PRNDTL(H1),GRND)

GROUP 14. Downstream pressure for PARAB=.TRUE.

GROUP 15. Termination of sweeps

LSWEEP=100

GROUP 16. Termination of iterations

GROUP 17. Under-relaxation devices

RELAX(P1,LINRLX,0.4)

RELAX(U1,FALSDT,0.2)

RELAX(V1,FALSDT,0.2)

RELAX(H1,FALSDT,0.2)

GROUP 18. Limits on variables or increments to them

GROUP 19. Data communicated by satellite to GROUND

** MULTIPLIERS OF TEMP. FUNCTION $T=A+BX+CX**2$ **

* HOT WALL A,B,C

RSG30=47.929


```

RSG29=56.106
RSG28=-61.8
  * COLD WALL A,B,C
RSG27=6.4845
RSG26=140.84
RSG25=-168.51
  **
RSG24=CP
  ****
  PROFILE LOCATIONS
IG(1)=22
IG(2)=47
IG(3)=56
IG(4)=66
IG(5)=81
  GROUP 20. Preliminary print-out
  ****
ECHO=F
  ****
  GROUP 21. Print-out of variables
  GROUP 22. Spot-value print-out
IXMON=40;IYMON=15
  GROUP 23. Field print-out and plot control
  ****
  NXPRIN=1;
  NYPRIN=1;
  ITABL=3
IPROF=3
PATCH(c11,PROFIL,IG(1),IG(1),6,NY,1,1,1,1)
PLOT(c11,U1,0.0,0.0)
PATCH(c12,PROFIL, IG(2),IG(2),NY,1,1,1,1)
PLOT(c12,U1,0.0,0.0)
PATCH(c13,PROFIL, IG(3),IG(3),6,NY,1,1,1,1)
PLOT(c13,U1,0.0,0.0)
PATCH(c14,PROFIL, IG(4),IG(4),6,NY,1,1,1,1)
PLOT(c14,U1,0.0,0.0)
PATCH(c15,PROFIL, IG(5),IG(5),6,NY,1,1,1,1)
PLOT(c15,U1,0.0,0.0)
  ****
  GROUP 24. Dumps for restarts
STOP

```

APPENDIX C

CALIBRATION DATA AND UNCERTAINTY ANALYSIS OF EXPERIMENTAL DATA

C.1 GENERAL

The accuracy of experimental results has always been the concern of the experimentalist. The experimentalist should always know the validity and quality of data. There has been controversy and confusion about the subject for many decades. Within the last two decades, however, the formulation of national and international standards on the subject has brought clarity to the uncertainty analysis. Today there are several standards available on uncertainty analysis, such as ANSI/ASME MFC-2M-1983 (R 1988), ANSI/ASME PTC-19.1-1985 (R 1990), ISO/DIS 7066-1.2 and BS 5844:1980 (ISO 5168-1978). The theory and practice of uncertainty analysis has been the focus of many research papers [69, 70, 71, 72, 73]. There are also books sometimes devoting whole chapters to the subject [74, 75]. In spite of the large amount of research work on uncertainty analysis, some aspects of the subject are still in dispute.

In this study end-to-end calibration was carried out for all the thermocouples (TCs) used in the measurement of surface and air flow temperatures. Before presenting the analysis some definitions on the subject are given below.

End-to-end calibration: A standard or a known value of the quantity to be measured is applied to a transducer and the system response through the data acquisition and data reduction systems is recorded.

Bias: The difference between the average of all possible measured values and the true value. It is also called the systematic error or fixed error that characterises every member of a set of measurements.

Degrees of freedom (n): A sample of n values is said to have n-k degrees of freedom, where k is the number of functions of the sample values which are held constant. Hence, the statistic calculated from it is also said to have n-k degrees of freedom.

Precision error: The random error observed in a set of repeated measurements. Also known as repeatability error and sampling error.

Measurement error: The collective term meaning the difference between the true value and the measured value. This includes both the bias and precision error.

Precision index (s): The precision index s defined as the computed standard deviation of the measurements.

$$s = \sqrt{\frac{1}{n-1} \sum_{i=1}^n (x_i - \bar{x})^2} \quad (\text{C.1})$$

Standard error of estimate (residual standard deviation): The measure of dispersion of the dependent variable about the least-squares line in curve fitting or regression analysis. It is the precision index of the output for any fixed level of the independent variable input. The formula for calculating this is

$$s_e = \sqrt{\frac{1}{n-k} \sum_{i=1}^n (y_{ob} - y_c)^2} \quad (\text{C.2})$$

for a curve fit of n data points in which k constants are estimated for the curve. Here y_{ob} is the observed value and y_c is the calibration value.

Student's t distribution : The ratio of the difference between the population mean and the sample mean to a sample standard deviation multiplied by a constant (t) in samples from a normal population. It is used to set confidence limits for the population mean for small number of samples (as low as 10 or below). The constant (t) is obtained from tables entered with degrees of freedom and confidence level.

Uncertainty interval (U): An estimate of the error band, centred about the measurement, within which the true value must fall with high probability. This can be written for the 95% confidence level as

$$U_{95} = \sqrt{B^2 + (t_{95} s_e)^2} \quad (\text{C.3})$$

where B stands for the bias error.

In the following subsections calibration procedures and data are given about the calibrations made to the TCs and the method of determining the uncertainty of LDA velocity measurements for both laminar and turbulent channel flows. Ultimately, the uncertainty in the calculated results of mass flow rate and heat flow rates from the channels are determined.

C.2 CALIBRATION OF THERMOCOUPLES

A total of 67 TCs have been manufactured and attached to different locations on the three experimental rigs. Cu-Const. (Type T) TCs with Teflon coated wire diameters of 76.2 μm and 200 μm were used, except for a Chromel-Alumel (Type K) thermocouple of 25 μm in diameter that was used for the temperature measurement probe for the turbulent flow experiments. The temperature probe used for the laminar flow air temperature measurements was fabricated using a 76.2 μm Cu-Const. thermocouple. Thermocouple locations on the three experimental rigs are marked with a + sign and the corresponding TC numbers are shown schematically in Figures C.1, C.3, C.5 for the laminar, turbulent UWT heating mode and turbulent UHF heating mode rigs respectively. Numbers 14 to 19 for UWT and 25 to 30 for UHF refer to same TCs. The TCs marked outside the channels are those used to monitor ambient temperature at different levels next to the channels.

Preliminary calibrations of some TCs were performed using an ISOTECH R Range metal block calibration system available in the laboratory. The system had a temperature read-out unit of ± 0.1 C accuracy, and allowed full control of the heating rate by a potentiometer to set the desired temperature. The calibration data, which is not presented here, indicated very good linear behaviour of the TCs. Consequently, all TCs used in the experiments were calibrated at two temperatures, viz. triple point and boiling point of pure water. The triple-point of water was realised inside a sealed flask containing crushed ice made from distilled water and liquid distilled water. The boiling point was achieved by boiling a large volume of distilled water exposed to the atmosphere under continuous heating by a Bunsen burner. For every thermocouple, calibrations were repeated 10 times, 5 at triple-point and 5 at boiling-point. Linear least squares regression analysis was applied to all the data using the commercial spreadsheet computer software Excel so as to determine

calibration lines and Standard error of estimate statistically . The calibration curve from the linear least squares fit is obtained as

$$y = ax + b \tag{C.4}$$

where y is the desired parameter, a is the gradient, x is the calibration data and b is the intercept.

Calibration of the laminar flow channel air temperature probe was performed as for those TCs used for surface temperature measurement. Calibration of the turbulent flow channel air temperature probe, however, was made using the data acquisition system detailed in Chapter 5. End-to-end calibration was employed as previously mentioned. The software was written to read in the calibration data at the two temperatures considered. The data were read in as numbers between 0 and 4096 and were converted to temperatures by the calibration curve given in Figure C.8. The calibration curve is the result of the average of five readings at each temperature.

The results of the uncertainty analysis are presented in Tables C.1 to C.4 and the calibration curves(lines) in Figures C.2, C.4, C.6, C.7 and C.8. Uncertainty of temperature measurements might be presumed to depend mainly on the calibration accuracy, thus, bias and other effects can be taken as negligible. The uncertainty analysis was carried out for the confidence level of 95 %.

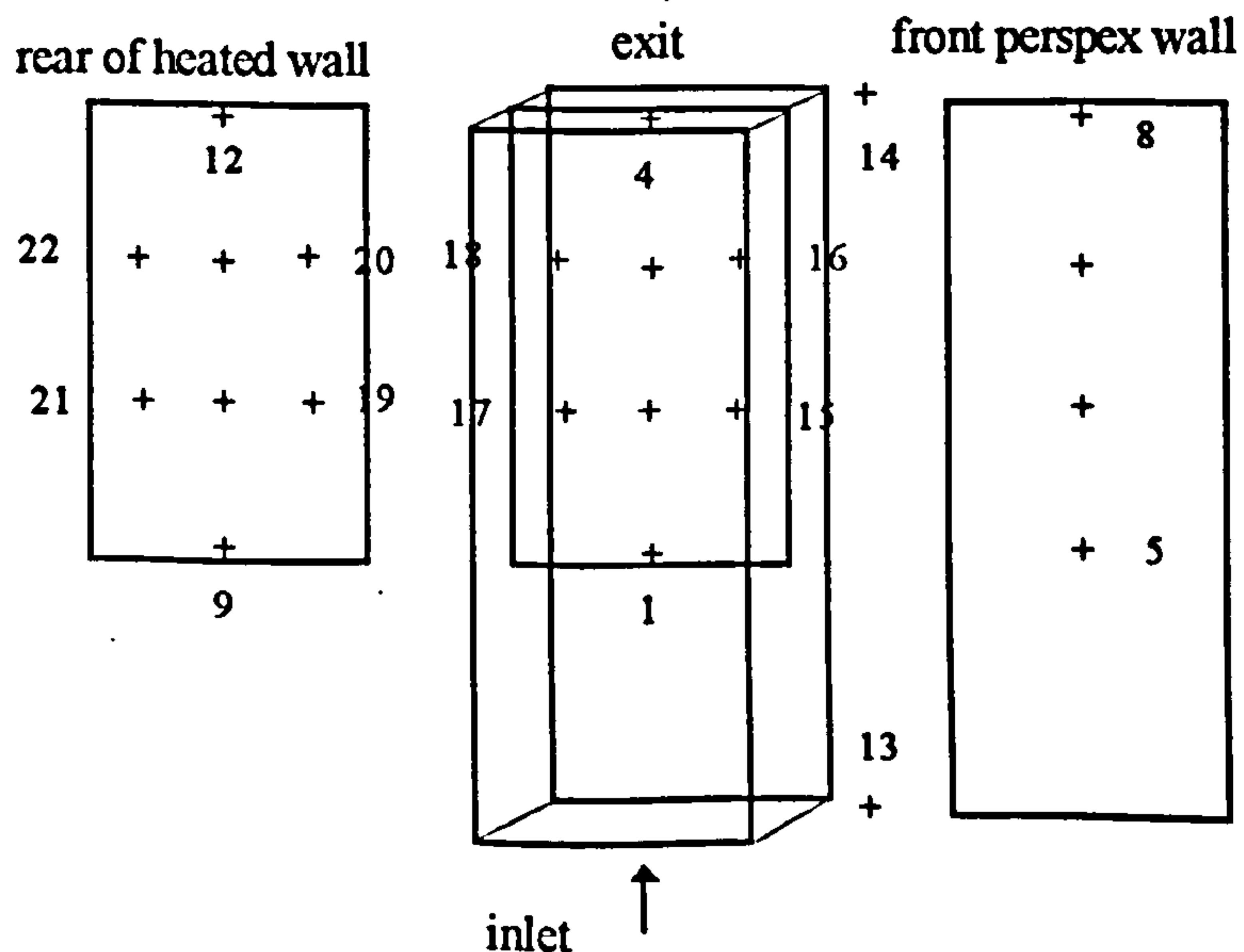


Figure C.1 Thermocouple locations on the laminar flow channel.

Table C.1 Results of uncertainty analysis from the calibration data of TCs attached to laminar flow channel

TC Number	Gradient a	Intercept b	Precision Index S_e	Degree of Freedom ν	Uncertainty $\pm U$ [C]	Operating Range [C]	Relative Error Range [%]
1	1.0045	0.6804	0.422	8	0.973	20 - 70	4.87 - 1.39
2	1.0124	0.7052	0.488	8	1.125	20 - 70	5.63 - 1.161
3	1.0068	0.8106	0.322	8	0.743	20 - 70	3.71 - 1.06
4	1.0024	0.6165	0.356	8	0.821	20 - 70	4.10 - 1.17
5	1.0086	0.7563	0.406	8	0.936	20 - 70	4.68 - 1.34
6	1.0108	0.8064	0.294	8	0.678	20 - 70	3.39 - 0.97
7	1.0086	0.7563	0.366	8	0.844	20 - 70	4.22 - 1.21
8	1.002	0.8766	0.232	8	0.535	20 - 70	2.67 - 0.76
9	1.0105	0.9895	0.302	8	0.696	20 - 70	3.48 - 0.99
10	0.9998	0.105	0.194	8	0.447	20 - 70	2.24 - 0.64
11	1.0076	0.7008	0.264	8	0.609	20 - 70	3.04 - 0.87
12	1.0005	0.1505	0.445	8	1.026	20 - 70	5.13 - 1.47
13	0.9988	0.199	0.209	8	0.482	20 - 70	2.41 - 0.69
14	1.0065	0.7808	0.344	8	0.793	20 - 70	3.97 - 1.13
15	1.0014	0.6876	0.398	8	0.918	20 - 70	4.59 - 1.31
16	1.0008	0.1806	0.418	8	0.964	20 - 70	4.82 - 1.38
17	0.9986	0.186	0.186	8	0.429	20 - 70	2.14 - 0.61
18	1.006	0.6806	0.311	8	0.717	20 - 70	3.59 - 1.02
19	1.003	0.6508	0.268	8	0.618	20 - 70	3.09 - 0.88
20	1.013	0.9056	0.377	8	0.869	20 - 70	4.35 - 1.24
21	1.008	0.8004	0.324	8	0.747	20 - 70	3.74 - 1.07
22	1.0106	0.9086	0.388	8	0.8951	20 - 70	4.47 - 1.28

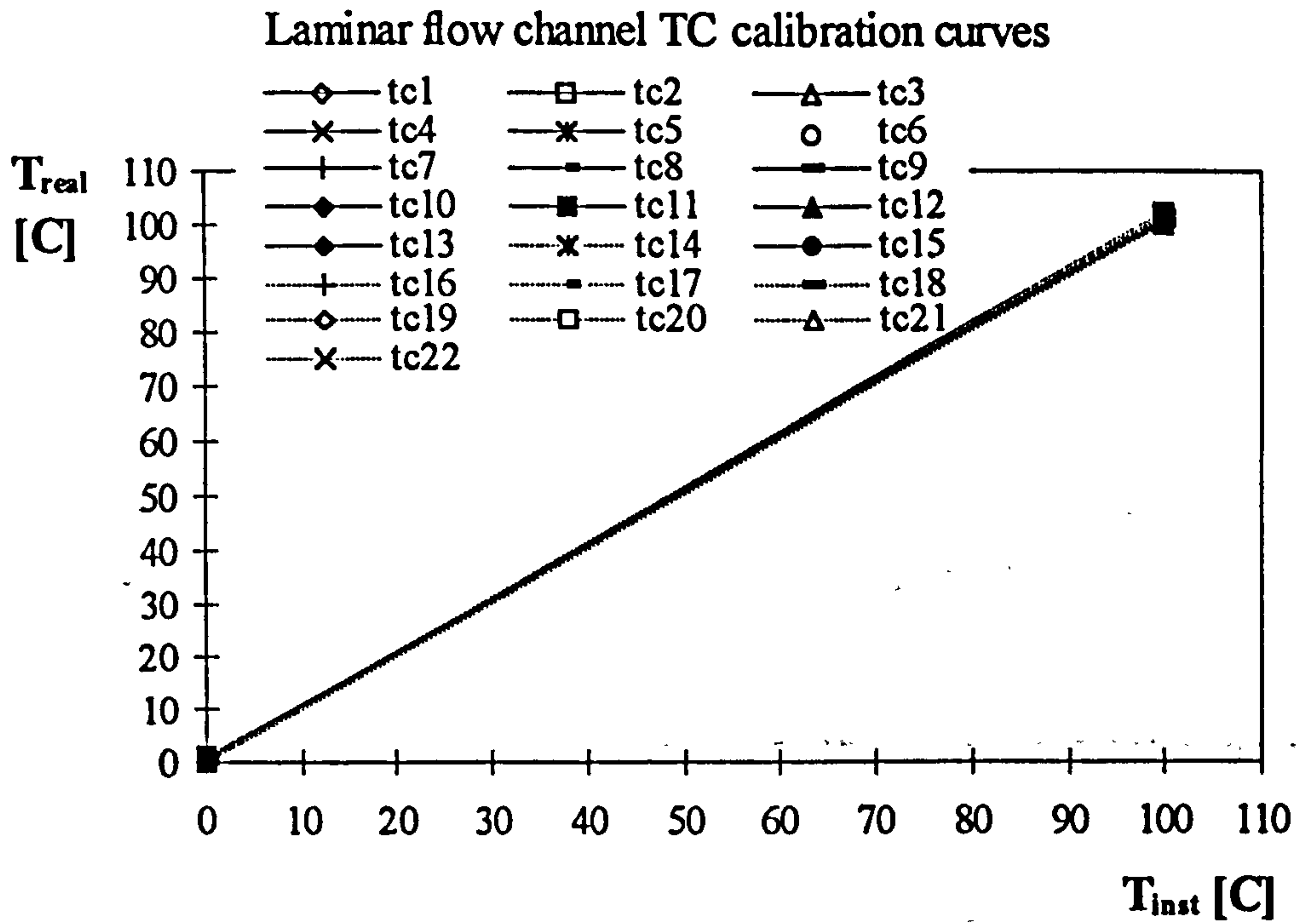


Figure C.2 Calibration curves of TCs attached to laminar flow channel

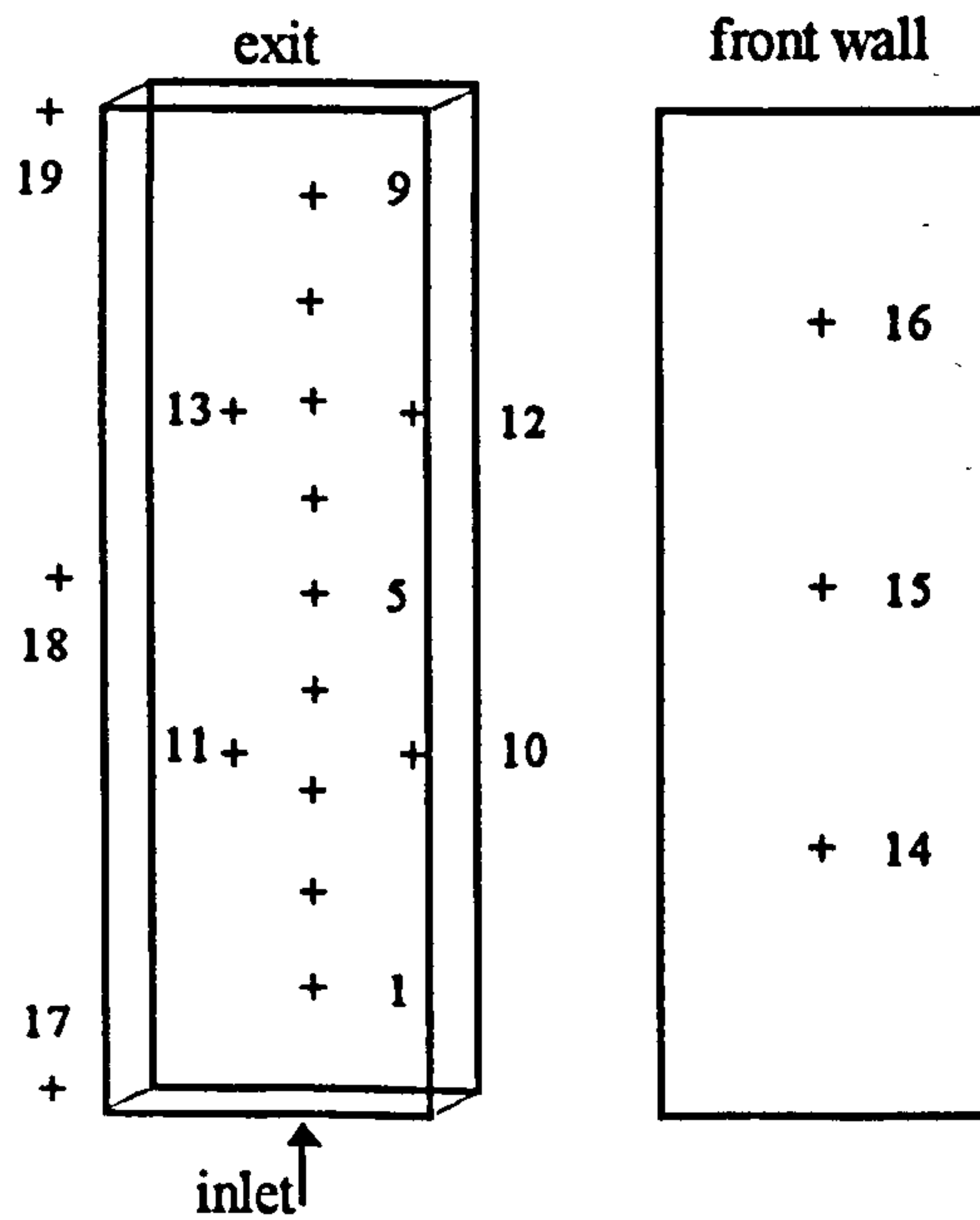


Figure C.3 Thermocouple locations on the turbulent flow channel, UWT heating mode.

Table C.2 Results of uncertainty analysis from the calibration data of TCs attached to turbulent flow channel, UWT heating mode

TC Number	Gradient a	Intercept b	Precision Index S_e	Degr. of Freedom ν	Uncertainty $\pm U$ [C]	Operating Range [C]	Relative Error Range [%]
1	1.0077	0.6906	0.357	8	0.823	20 - 140	4.12 - 0.59
2	1.0118	0.7652	0.458	8	1.056	20 - 140	5.28 - 0.75
3	1.0039	0.8204	0.313	8	0.722	20 - 140	3.61 - 0.52
4	1.0092	0.6573	0.344	8	0.793	20 - 140	3.97 - 0.57
5	1.0118	0.8004	0.401	8	0.925	20 - 140	4.62 - 0.66
6	1.0066	0.7664	0.299	8	0.689	20 - 140	3.45 - 0.49
7	1.0108	0.8896	0.385	8	0.888	20 - 140	4.44 - 0.63
8	0.9998	0.1344	0.217	8	0.500	20 - 140	2.50 - 0.36
9	1.0082	0.8068	0.341	8	0.786	20 - 140	3.93 - 0.56
10	1.0002	0.1205	0.204	8	0.470	20 - 140	2.35 - 0.34
11	0.9988	0.1896	0.182	8	0.420	20 - 140	2.10 - 0.30
12	1.0044	0.7509	0.425	8	0.980	20 - 140	4.90 - 0.70
13	1.0102	0.3806	0.411	8	0.948	20 - 140	4.74 - 0.68
14	0.9986	0.1786	0.224	8	0.517	20 - 140	2.58 - 0.37
15	1.0068	0.7805	0.366	8	0.844	20 - 140	4.22 - 0.60
16	1.0030	0.6855	0.347	8	0.800	20 - 140	4.00 - 0.57
17	1.0126	0.9122	0.334	8	0.770	20 - 140	3.85 - 0.55
18	1.0068	0.8034	0.359	8	0.828	20 - 140	4.14 - 0.59
19	1.0048	0.7118	0.289	8	0.666	20 - 140	3.33 - 0.48

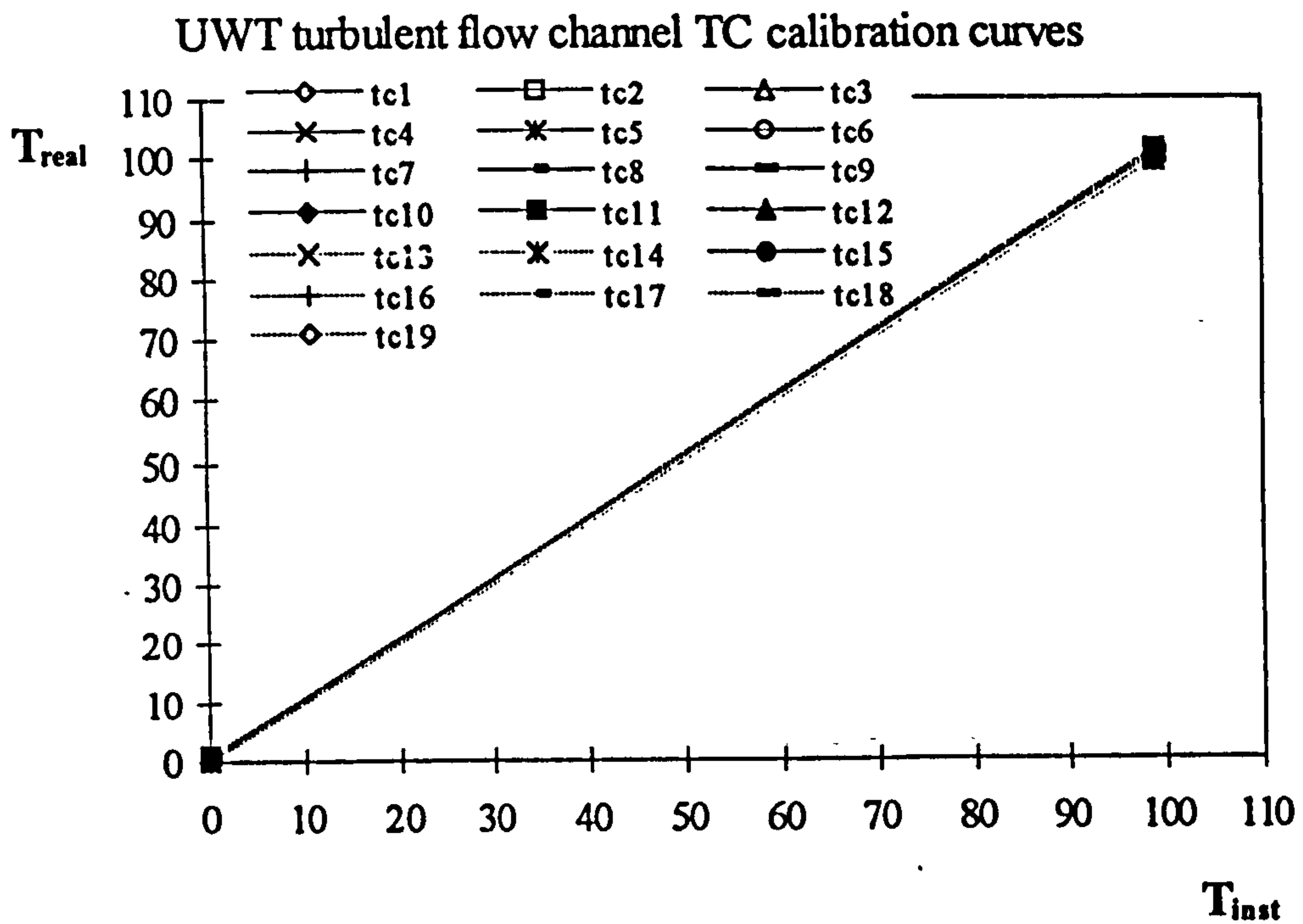


Figure C.4 Calibration curves of TCs attached to turbulentflow channel, UWT heating mode.

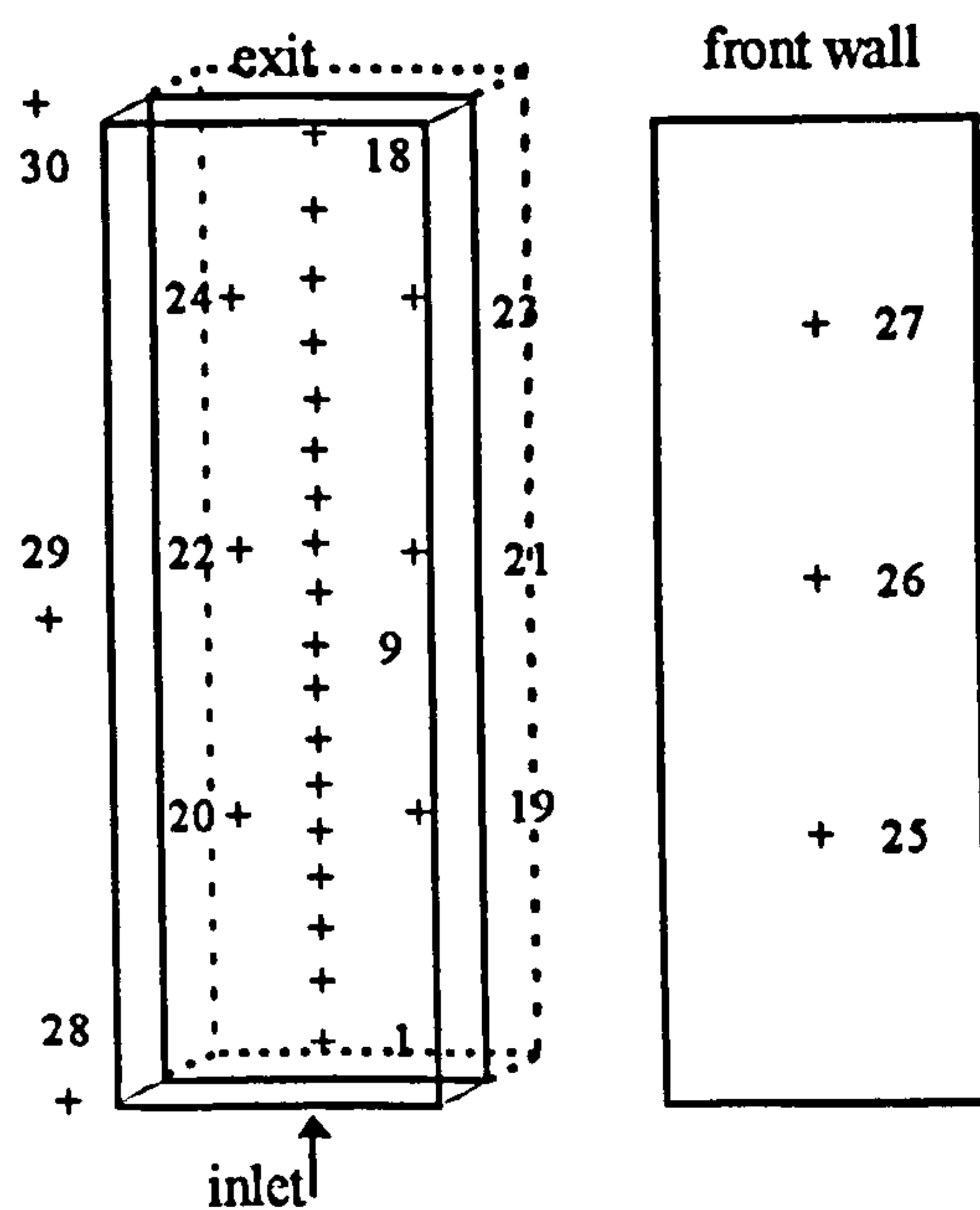


Figure C.5 Thermocouple locations on the turbulent flow channel, UHF heating mode.

Table C.3 Results of uncertainty analysis from the calibration data of TCs attached to turbulent flow channel, UHF heating mode

TC Number	Gradient a	Intercept b	Precision Index S_e	Degr. of Freedom ν	Uncertainty $\pm U$ [C]	Operating Range [C]	Relative Error Range [%]
1	0.9986	0.8804	0.312	8	0.719	20 - 120	3.60 - 0.60
2	1.0101	0.7077	0.418	8	0.964	20 - 120	4.82 - 0.80
3	0.9996	0.6406	0.222	8	0.512	20 - 120	2.56 - 0.43
4	1.0022	0.6844	0.255	8	0.588	20 - 120	2.94 - 0.49
5	1.0099	0.5544	0.406	8	0.936	20 - 120	4.68 - 0.78
6	1.0188	0.9022	0.442	8	1.019	20 - 120	5.10 - 0.85
7	0.9991	0.7233	0.266	8	0.613	20 - 120	3.07 - 0.51
8	1.0029	0.8116	0.255	8	0.588	20 - 120	2.94 - 0.49
9	1.0105	0.9833	0.332	8	0.766	20 - 120	3.83 - 0.64
10	0.9998	0.3054	0.242	8	0.558	20 - 120	2.79 - 0.49
11	1.0077	0.5008	0.364	8	0.839	20 - 120	4.20 - 0.70
12	1.0008	0.2246	0.402	8	0.927	20 - 120	4.64 - 0.77
13	0.9989	0.2990	0.188	8	0.434	20 - 120	2.17 - 0.36
14	1.0165	0.6402	0.344	8	0.793	20 - 120	3.97 - 0.66
15	1.0012	0.6269	0.373	8	0.860	20 - 120	4.30 - 0.72
16	1.0118	0.6220	0.382	8	0.881	20 - 120	4.40 - 0.73
17	0.9986	0.2144	0.164	8	0.378	20 - 120	1.89 - 0.32
18	1.0060	0.7844	0.317	8	0.731	20 - 120	3.66 - 0.61
19	1.0030	0.6533	0.251	8	0.579	20 - 120	2.89 - 0.48
20	1.0130	0.8052	0.368	8	0.849	20 - 120	4.24 - 0.71
21	1.0082	0.8094	0.336	8	0.775	20 - 120	3.87 - 0.65
22	1.0100	0.6337	0.411	8	0.948	20 - 120	4.74 - 0.79
23	0.9990	0.1846	0.253	8	0.583	20 - 120	2.92 - 0.49
24	1.0156	0.6086	0.428	8	0.987	20 - 120	4.93 - 0.82

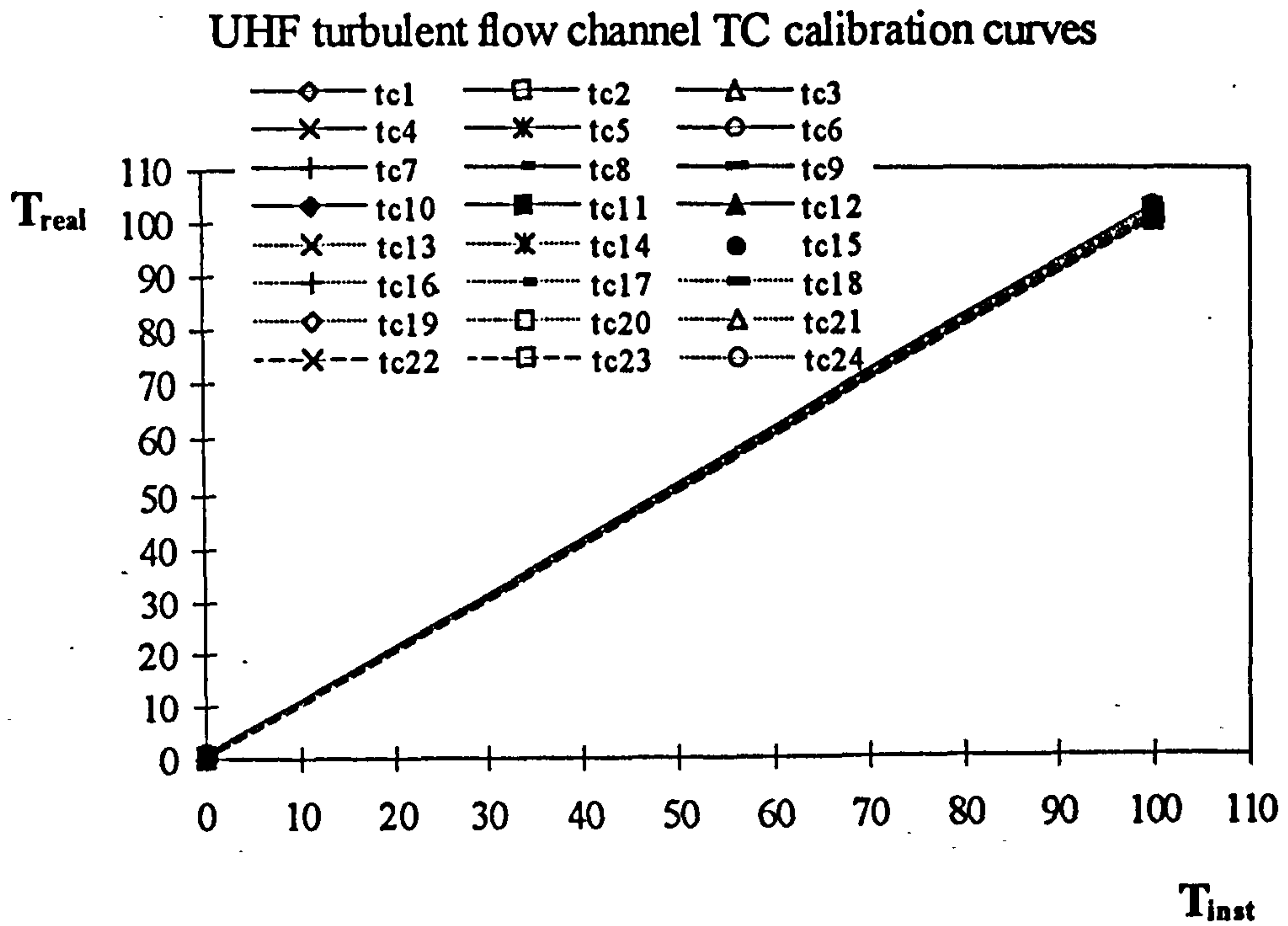


Figure C.6 Calibration curves of TCs attached to turbulentflow channel, UHFheating mode.

Table C.4 Results of uncertainty analysis from the calibration data of air temperature measurement probes.

Air Temperature Measurement Probe	Gradient a	Intercept b	Precision Index S_e	Degr. of Freedom ν	Uncertainty $\pm U$ [C]	Operating Range [C]	Relative Error Range [%]
Laminar Flow Channel	1.0015	0.1804	0.155	8	0.357	20-70	1.79 - 0.51
Turbulent Flow Chan. (UWT and UHF)	0.03305	-0.5	0.087	8	0.201	20-135	1.00 - 0.15

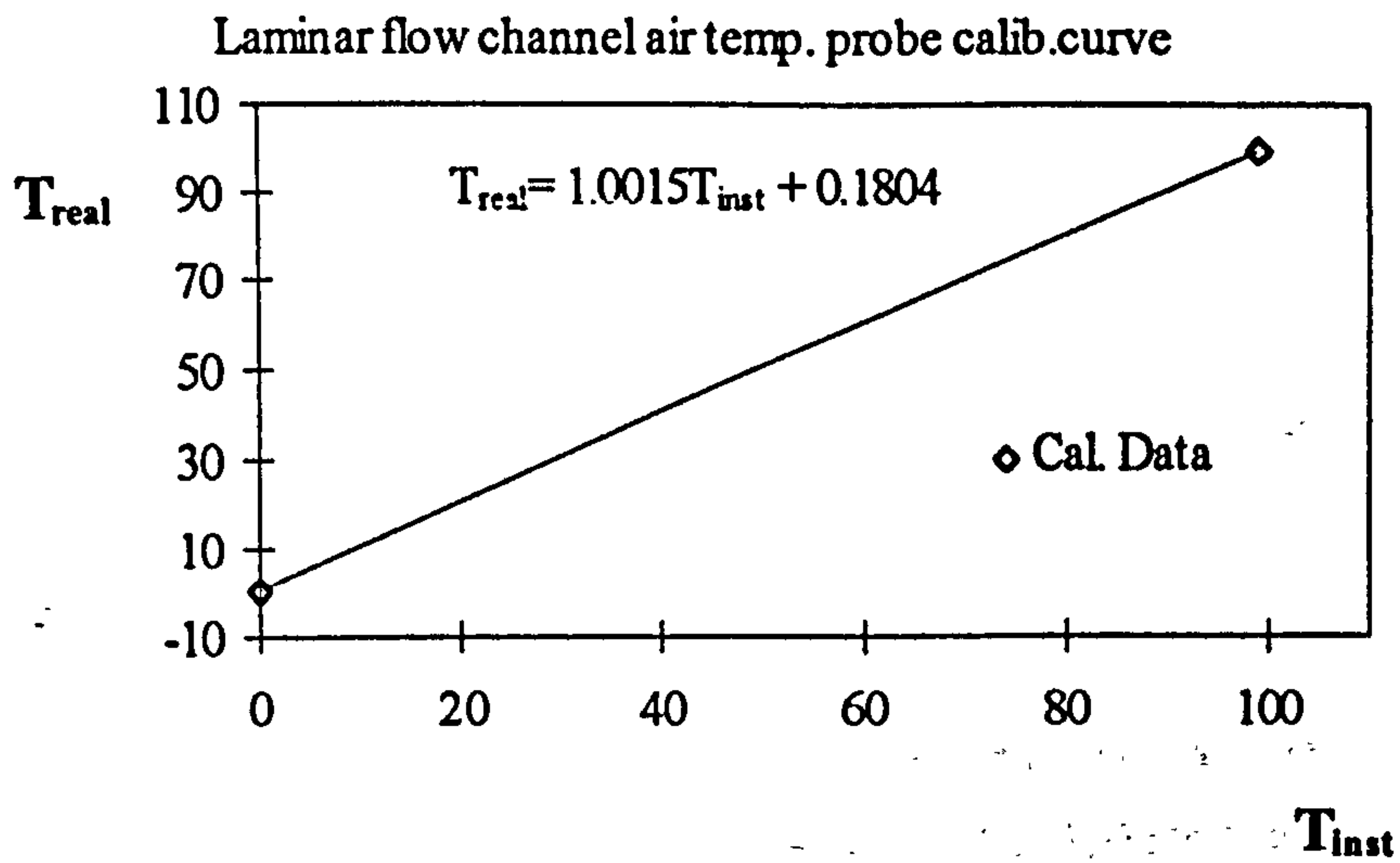


Figure C.7 Calibration curve of air temperature measurement probe, laminar flow.

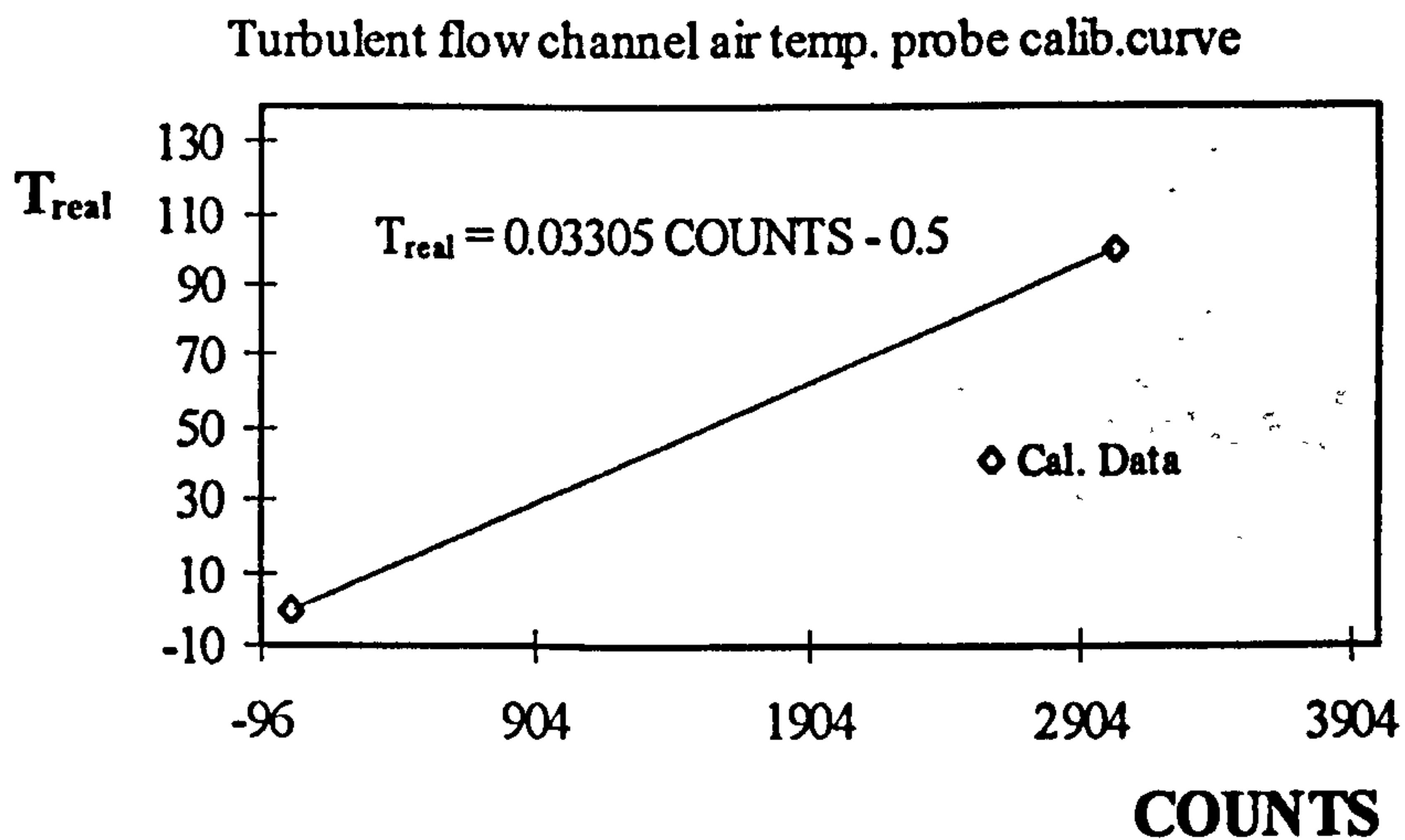


Figure C.8 Calibration curve of air temperature measurement probe, turbulent flow.

C.3 UNCERTAINTY OF LDA VELOCITY MEASUREMENTS

Uncertainty analysis of the velocity measurements by LDA has been the interest of many researchers and the subject is well established. Uncertainty interval of velocity, E , can be predicted using the root-sum-square method given by Eq. (C.5).

$$E^2 = \left(\frac{tu'}{\sqrt{n}}\right)^2 + \left(\left(\frac{u'}{U}\right)^2 U\right)^2 + (0.004(U + U_0))^2 + (0.01(U + U_0))^2 \quad (C.5)$$

In the equation u' stands for rms of velocity, U the mean velocity, U_0 effective fringe velocity due to frequency shift, n the sample size and t the constant from Student's t distribution table which is taken 2 (Taylor [76]). The first term represents errors due to turbulence, effects of unsteadiness in the flow, velocity variations resulting from drift in operating conditions, velocity gradients within the optical probe volume and random noise in the signals. In the second term effect of velocity bias was represented by the square of turbulence intensity, details are given by Durao et.al. [77], McLaughlin and Tiederman [78]. The third term represents error resulting from uncertainty in the beam angle determination. The final term accounts for the error due to frequency output from the BSA that is rated by manufacturer to be app. %1. The method described above is given by Carey [79] in detail.

Table C.5 Results of uncertainty analysis of velocity measurements.

Laminar Flow Channel Measurements					
	Mean Velocity U [mm/s]	rms of Velocity [mm/s]	Sample size n	Uncertainty E [mm/s]	Relative Error [%]
Typical	332	5.3	> 500	7.2	2.2
Worst	88.6	17.7	> 500	4.3	4.9
Turbulent Flow Channel Measurements UWT Heating Mode					
	Mean Velocity U [m/s]	rms of Velocity [m/s]	Sample size n	Uncertainty E [m/s]	Relative Error [%]
Typical	0.760	0.103	> 5000	0.022	2.8
Worst	0.646	0.166	> 5000	0.047	4.9
Turbulent Flow Channel Measurements UHF Heating Mode					
Flow Channel	Mean Velocity U [m/s]	rms of Velocity [m/s]	Sample size n	Uncertainty E [m/s]	Relative Error [%]
Typical	0.509	0.099	> 5000	0.022	4.4
Worst	0.570	0.182	> 5000	0.060	10.5

Uncertainties of velocity measurements made in the three experimental channels employed in this study have been determined for a typical velocity and for the worst case. The results are presented in Table C.5.

C.4 UNCERTAINTY OF CALCULATED RESULTS

The quantities calculated from experimental measurements of this study are the heat and mass flow rates from the channel outlet. For a calculated result of $R = R(x_1, x_2, \dots, x_m)$, Holman[75] gives a relation for the uncertainty of result as;

$$u_r = \left[\left(\frac{\partial R}{\partial x_1} u_1 \right)^2 + \left(\frac{\partial R}{\partial x_2} u_2 \right)^2 + \dots + \left(\frac{\partial R}{\partial x_m} u_m \right)^2 \right]^{1/2} \quad (\text{C.6})$$

where u_r is the uncertainty of the results and $u_{1\dots m}$ uncertainties of individual variables. Experimental results of heat and mass flow rates were calculated using equations (C.7) and (C.8) respectively.

$$Q = \rho c_p A u_{ave} (T_b - T_0) \quad (\text{C.7})$$

$$\dot{m} = \rho A u_{ave} \quad (\text{C.8})$$

$$u_{ave} = \frac{1}{A} \int_0^b u dy \quad \text{or} \quad \bar{u}_{ave} = \frac{1}{A} \int_0^b \bar{u} dy \quad (\text{C.9})$$

$$T_b = \frac{1}{A u_{ave}} \int_0^b u T dy \quad \text{or} \quad \bar{T}_b = \frac{1}{A u_{ave}} \int_0^b \bar{u} \bar{T} dy \quad (\text{C.10})$$

Table C.6 Results of uncertainty analysis heat and mass flow rates.

Laminar Flow Channel Measurements						
Case No.	Heat Flow Rate, q_c			Mass Flow Rate, \dot{m}		
	Mean [w/m ²]	Uncertainty [w/m ²]	Relative Error [%]	Mean [g/s]	Uncertainty [g/s]	Relative Error [%]
1	128.6	2.077	1.61	1.89	0.0895	4.73
2	206.6	2.817	1.36	2.36	0.0952	4.03
3	139.2	1.720	0.91	3.88	0.1815	4.68
4	172.5	1.40	0.84	4.35	0.1891	4.35
5	215.4	1.581	0.73	4.52	0.1761	3.90
6	126.48	1.274	1.01	3.63	0.5172	14.25
7	195.51	1.460	0.75	4.82	0.5180	10.75
Turbulent Flow Channel Measurements, UWT Heating Mode						
	Heat Flow Rate, q_c			Mass Flow Rate, \dot{m}		
T_w [°C]	Mean [w/m ²]	Uncertainty [w/m ²]	Relative Error [%]	Mean [g/s]	Uncertainty [g/s]	Relative Error [%]
60	139.43	14.58	10.46	60.16	5.377	8.94
75	212.44	21.09	9.93	67.78	4.836	7.13
90	294.17	29.06	9.88	79.74	6.145	7.71
100	350.00	39.55	11.30	85.56	4.966	5.80
130	540.67	63.21	11.69	106.23	6.651	6.26
Turbulent Flow Channel Measurements, UHF Heating Mode						
	Heat Flow Rate, q_c			Mass Flow Rate, \dot{m}		
Case No.	Mean [w/m ²]	Uncertainty [w/m ²]	Relative Error [%]	Mean [g/s]	Uncertainty [g/s]	Relative Error [%]
1	190.8	28.54	14.96	64.1	8.690	13.56
2	280.4	41.85	14.93	73.83	10.566	14.31
3	322.3	46.00	14.27	82.97	11.045	13.31

In the above equations, Q is the heat flow rate from the channel, \dot{m} the mass flow rate, c_p the air specific heat and ρ the density of air calculated at the bulk temperature ideal gas relation, u_{ave} average experimental velocity at the channel outlet calculated

from the curve fit average of measurements, equation (C.9), A the channel area, T_0 air temp at the inlet and T_b the bulk temperature of air calculated from the curve fit of measurements at the outlet of the channel, equation (C.10). The uncertainties of heat and mass flow rates for all the cases were calculated using the method described above. The uncertainties of average temperature (T_b) and average velocity were taken as the square-root-sum of measurement uncertainty and residual standard deviation of the curve fit from which averages were computed. In the calculations, the uncertainties resulting from the density, specific heat and area calculations were neglected and only those relating to average velocity, bulk and inlet temperatures were considered. The results of the analysis are presented in Table C.6.

APPENDIX D

SPECIFICATIONS of TEMPERATURE MEASURING DEVICE

2. SPECIFICATION

Conditions

Ambient Temperature 25 degC and rated power supplies

ACCURACY	Millivolt input	$\pm (0.006\% + 1 \text{ digit})$
	Voltage input	$\pm (0.006\% + 1 \text{ digit})$
	Thermocouple input	$\pm 5 \mu\text{V}$ e.g. Typically Type K $\pm (0.1 \text{ degC} + 1 \text{ digit})$ Type S $\pm (1.0 \text{ degC} + 1 \text{ digit})$
	Strain Gauges	$\pm 10 \text{ microStrain}$
	Millivolt output	$\pm 10 \text{ microVolt}$
	Voltage output	$\pm 1 \text{ millivolt}$
INPUT IMPEDANCE	Millivolt input	$> 1 \text{ Mohm}$
	Voltage input	$> 1 \text{ Mohm}$
OUTPUT IMPEDANCE	$< 0.1 \text{ ohm}$ (10V range) $< 20 \text{ ohm}$ (100mV range) $> 10 \text{ Mohm}$ (20mA range)	
A to D RESOLUTION	16 Bits (0.0015%)	
RANGES	Millivolt input	$\pm 100 \text{ mV}$
	Voltage input	$\pm 10 \text{ V}$
	Strain Gauge input	$\pm 19999 \text{ microStrain}$
	Thermocouple	J -210 to +750 C K -270 to +1050 C T -270 to +400 C E 0 to 860 C R -50 to +1650 C S -50 to +1650 C B 0 to 1810 C
STABILITY	Input Zero	$\pm 0.25 \mu\text{V} / \text{deg C}$
	Input Range	$< \pm 50 \text{ ppm} / \text{deg C}$
	Long Term	$\pm 1 \mu\text{V} / \text{year}$
	Output Zero	$< \pm 100 \text{ ppm} / \text{deg C}$
	Output Range	$< \pm 100 \text{ ppm} / \text{deg C}$
	Input Noise	$< 5 \mu\text{V P-P}$
	Output Noise (100mV)	$< 10 \mu\text{V P-P}$
	Output Noise (10V)	$< 10 \text{ mV P-P}$
	Cold Junction	Ratio 50:1 (10-30 C) Ratio 30:1 (0-60 C)
COMMON MODE REJECTION	Millivolt input	110dB
	Voltage input	Referred to ground
	Millivolt output	Referred to ground
	Voltage output	Referred to ground
WARM UP	10 minutes to rated specification	
AMBIENT TEMPERATURE	-5 to 55 C operating	
	-25 to 80 C storage	
POWER SUPPLY	TAB80	220 to 240V $\pm 10\%$ 50 to 60 Hz
	TAB81	110 to 120V $\pm 10\%$ 50 to 60 Hz

APPENDIX E

SPECIFICATIONS of DATA ACQUISITION BOARD

THE PC - 30 ANALOG MULTIFUNCTION BOARD

1. INTRODUCTION

The PC-30 card is a plug in A/D, D/A multi-function board for the IBM PC and compatible PC's. The PC-30 board includes the Analog Devices A/D converter AD 574 with a typical conversion time of 25 μ s, and a 16 channel multiplexer. Typical conversion time for the whole system (Multiplexer, Sample & Hold, AD 574) is 35 μ s.

The sample rate can be determined by software (using a software clock) or by the onboard programmable timer. The sampling software which is included with the PC-30 board allows the user to sample any of the 16 input channels with a sampling rate of 6000 Hz (Turbo Pascal) or 200 Hz (BASIC).

For full use of the PC-30 board an additional software package (written in TURBO PASCAL and ASSEMBLER) is available. Using the software clock mode, sampling rates of up to 30 000 samples a second are possible (depending on speed of the PC used). The sampled data can be viewed on the screen (only with Graphics Monitor), and stored on disc for further analysis. A LOTUS 1-2-3 compatible file mode is also provided.

Additionally the PC-30 board provides two 12 bit D/A converters, two 8 bit D/A converters and 24 digital I/O lines. Typical conversion time of the D/A converters is less than 1 μ s.

2. SPECIFICATIONS

2.1 A/D Converter AD 574 AJD (AKD):

Resolution	:	12 bit
Conversion time	:	25 μ s (AD 574)
	:	35 μ s (Multiplexer + S&H, AD 574)
Input voltage	:	- 5V to + 5V
	:	- 10V to + 10V
	:	0V to + 10V
Linearity	:	11 bit (AD 574 AJD)
	:	12 bit (AD 574 AKD)
Offset	:	adjustable to zero
Linearity drift	:	0.5 (0.5) ppm/C
Offset drift	:	10 (5) ppm/C
Gain drift	:	50 (27) ppm/C

2.2 Sample & Hold LF 398:

settling time	:	< 8 μ s
Sample & Hold error	:	< 0.005 %

2.3 Multiplexer M6116:

settling time	:	< 1 μ s
input impedance	:	22 K Ohms

Note that the output impedance of the signal sources connected to the inputs of the multiplexer must be less than 5 Ohms to keep the full scale error to less than 1 LSB. We therefore recommend the use of a noninverting operational amplifier as buffer amplifier. Unused inputs should be tied to ground.

2.4 12-bit Digital To Analog Converters:

Resolution	:	12-bit
Linearity	:	13 bit
Settling time	:	< 1 μ s
gain drift	:	6 ppm (C)
Output range	:	bipolar : -10 to +10 V
	:	monopolar : 0 to +10 V

(offset and gain errors adjustable to zero)

2.5 8-bit Digital To Analog Converters:

Resolution	:	8-bit
Linearity	:	8-bit (ie 0.38%)
Settling time	:	< 1 μ s

(gain error adjustable to zero)

APPENDIX F

DATA ACQUISTION and TRAVERSING SOFTWARE

F.1 DATA ACQUISTION SOFTWARE

```
PROGRAM Temp_login;  
USES CRT,DOS;
```

```
VAR  
  COUNT,CHA,CHAN,OUTCHAN,SAMP,WASTE,ns,nf:INTEGER;  
  TAIR:ARRAY [1..10000] OF real;  
  tairave,tairaver:real;  
  choice:CHAR;  
  FLNAME1:STRING[10];  
  FILEVAR1:text;  
  quit:boolean;
```

```
procedure wait1;  
{This proc. creates the 40 micro s wait state for the end of conversion  
on a philips p3202 pc without co-processor}
```

```
var r:integer;
```

```
begin
```

```
  for r:=1 to 11 do
```

```
    begin
```

```
      end;
```

```
    end;
```

```
procedure wait;
```

```
var s:integer;
```

```
begin
```

```
  for s:=1 to 265 do
```

```
    begin
```

```
      end;
```

```
    end;
```

```
procedure convert_to_TEMP_sy;
```

```
const a=-0.5;
```

```
      b=0.03305;
```

```
VAR M:INTEGER;
```

```
  BEGIN
```

```
    tairave:=0;
```

```
    BEGIN
```

```
      FOR M:=1 TO (COUNT) DO
```

```
        BEGIN
```

```
          TAIR[M]:=A+B*TAIR[M];
```

```
          tairave:=tairave+tair[m];
```

```

    END;
    TAIRAVR:=TAIRAVE/COUNT;
END;
END;
PROCEDURE write_to_file;
VAR
    P:INTEGER;

    BEGIN
        ASSIGN(FILEVAR1,FLNAME1);
        REWRITE(FILEVAR1);
        WRITELN(FILEVAR1,'FILENAME ',FLNAME1:10,' NUMBER OF DATA =
',(COUNT):5);
        writeln('AVERAGE FLOV TEMP = ',TAIRAVR:10);
        APPEND(FILEVAR1);
        for P:=1 to (count) do
            begin
                WRITE(FILEVAR1,TAIR[P]:10);
                END;
                WRITELN;
                writeln('AVERAGE FLOV TEMP = ',TAIRAVR:10);
                CLOSE(FILEVAR1);
            END;
        PROCEDURE synchro_scan;
            var SYNCHSAMP:integer;
            tairAD,z:integer;

            BEGIN
                WRITELN('ENTER THE NO OF SAMPLES TO BE TAKEN');
                READLN(NF);
                WRITELN('ENTER THE FILE NAME FOR FLOW TEMP. (10 CHAR.
MAX.)');
                READLN(FLNAME1);
                PORT[$703]:=$92;
                delay(1);
                PORT[$702]:=(1 SHL 4) + 2;
                delay(1);
                PORT[$702]:=(1 SHL 4) + 3;
                wait1;
                waste:=((PORT[$701] AND $0F) SHL 8) +PORT[$700];

                REPEAT
                    PORT[$702]:=(1 SHL 4) + 2;
                    delay(1);
                    PORT[$702]:=(1 SHL 4) + 3;
                    wait1;
                    SYNCHSAMP:=((PORT[$701] AND $0F) SHL 8) +PORT[$700];

```

```

UNTIL SYNCHSAMP < 2000;
writeln('SYNCH. RES. SIGNAL DETECTED & FLOW TEMP. BEING
READ');
COUNT:=0;
repeat
count:=count+1;
PORT[$702]:= 2;
delay(8);
PORT[$702]:= 3;
wait1;
TAIRAD:=((PORT[$701] AND $0F) SHL 8) +PORT[$700];
tair[count]:=tairAD;
delay(1);
wait;
UNTIL COUNT >=nf;
writeln(' ,(count):10,'  SAMPLES HAVE BEEN TAKEN' );
CONVERT_TO_TEMP_sy;
write_to_file;
END;

```

```

PROCEDURE MENU;
BEGIN
clrscr;
quit:=false;
REPEAT
WRITELN('1 - SCAN FLOW TEMP. CHANNEL ( 0 ) AT 100 Hz &
RECORD');
WRITELN('2 - QUIT');
writeln;
writeln;
repeat
choice:=readkey;
until choice in['1'..'2'];
case choice of
'1' : synchro_scan;
'2' : quit:=true;
end;{case}
UNTIL quit;
END;

```

```
{MAIN PROGRAM}
```

```

BEGIN
PORT[$703]:=$92;
NS:=10;
MENU;
END.

```


F.2 TRAVERSING SOFTWARE

```
program port_control;
```

```
uses crt,graph,dos,dataglob,wimpsimp;
```

```
var
```

```
    select,i,j,k,code,inc_step    :integer;  
    counter,stepx,stepy,Vi: real;
```

```
PROCEDURE rpoint(var i:integer;r:real);
```

```
var s : string[10];
```

```
begin
```

```
str(r:10:0,s);
```

```
val(s,i,code);
```

```
end;
```

```
PROCEDURE step_x_rev;
```

```
begin
```

```
for i := 1 to inc_step do
```

```
begin
```

```
    PORT[$708] := $2;
```

```
    delay(1);
```

```
    PORT[$708] := $0;
```

```
    delay(1);
```

```
end; { of for loop }
```

```
end; { of procedure }
```

```
PROCEDURE step_x_for;
```

```
begin
```

```
for i := 1 to inc_step do
```

```
begin
```

```
    PORT[$708] := $3;
```

```
    delay(1);
```

```
    PORT[$708] := $1;
```

```
    delay(1);
```

```
end; { of for loop }
```

```
end; { of procedure }
```

```
PROCEDURE step_y_rev;
```

```
begin
```

```
for i := 1 to inc_step do
```

```
begin
```

```
    PORT[$708] := $8;
```

```
    delay(1);
```

```
    PORT[$708] := $0;
```

```

        delay(1);
end; { of for loop}
end; {of procedure}

```

```

PROCEDURE step_y_for;
begin
for i := 1 to inc_step do
begin
        PORT[$708] := $C;
        delay(1);
        PORT[$708] := $4;
        delay(1);
end; { of for loop}
end; {of procedure}

```

```

Procedure Outvalxy(x,y : integer; value : real);
begin
str(value:10:3,labl);
outtextxy(x,y,labl);
end;{ of outvalxy}
Procedure Outintxy(x,y : integer; value : real);
begin
str(value:10:0,labl);
outtextxy(x,y,labl);
end;{ of outintxy}

```

```

PROCEDURE set_port;
begin
        PORT[$703] := $92;
        PORT[$70B] := $80;
end;

```

```

PROCEDURE set_x;
begin
setviewport(0,0,xm,ym,clipon);
setcolor(4);
setbkcolor(4);
clrscr;
outtextxy(xm div 4,ym div 20 * 19,'Enter x-traverse movement in mm (+/-)');
value:= "";
        setfillstyle(1,11);
        bar(xm div 4,ym div 2-20, xm div 4 * 3,ym div 4 * 3);
        outtextxy(xm div 4 + 5,ym div 2 + 40,'Current position in mm = ');
        outvalxy(xm div 4 + 200,ym div 2 + 40,stepx/200);
repeat
        bar(xm div 4,ym div 2, xm div 4 * 3,ym div 16 * 9);
        outtextxy(xm div 4 + 10,ym div 2 + 5,concat('value in mm =' + value));

```

```

    ch := readkey;
if (ch<>#27) and (ch<>#13) and (ch<>#8) and (ch in ['0'..'9','-','.']) then
    value:= CONCAT(value,ch);
    if ch = #8 then value:= copy(value,1,length(value)-1);
until ((ch= #27) and (value<> "")) or ((ch = #13) and (value<> ""));
val(copy(value,1,length(value)),Vi,code);
stepx := stepx + vi*200;
if vi >= 0 then
begin
rtoint(inc_step, vi *400);
step_x_rev;
end
else
begin
rtoint(inc_step, -vi *400);
step_x_for;
end;

```

```

bar(xm div 4,ym div 16 * 9, xm div 4 * 3,ym div 4 * 3);
outtextxy(xm div 4 + 10,ym div 2 + 40,'Current position in mm = ');
outvalxy(xm div 4 + 200,ym div 2 + 40,stepx/200);
outtextxy(xm div 4 +10,ym div 2 + 60,'Press ANY key to continue');
ch := readkey;
end;

```

PROCEDURE set_y;

```

begin
setviewport(0,0,xm,ym,clipon);
setcolor(4);
setbkcolor(4);
clrscr;
outtextxy(xm div 4,ym div 20 * 19,'Enter y-traverse movement in mm (+/-)');
value:="";
    setfillstyle(1,11);
    bar(xm div 4,ym div 2+20, xm div 4 * 3,ym div 4 * 3);
    outtextxy(xm div 4 + 5,ym div 2 + 40,'Current position in mm = ');
    outvalxy(xm div 4 + 200,ym div 2 + 40,stepy/200);
repeat
    bar(xm div 4,ym div 2-20, xm div 4 * 3,ym div 16 * 9);
    outtextxy(xm div 4 + 10,ym div 2 + 5,concat('value in mm =' +
value));
    ch := readkey;
if (ch<>#27) and (ch<>#13) and (ch<>#8) and (ch in ['0'..'9','-','.']) then
    value:= CONCAT(value,ch);
    if ch = #8 then value:= copy(value,1,length(value)-1);

```



```

until ((ch= #27) and (value<> "")) or ((ch = #13) and (value<> ""));
val(copy(value,1,length(value)),Vi,code);
stepy := stepy + vi*200;

if vi >= 0 then
begin
rtoint(inc_step, vi *400);
step_y_rev;
end
else
begin
rtoint(inc_step, -vi *400);
step_y_for;
end;
bar(xm div 4,ym div 16 * 9, xm div 4 * 3,ym div 4 * 3);
outtextxy(xm div 4 + 10,ym div 2 + 40,'Current position in mm = ');
outvalxy(xm div 4 + 200,ym div 2 + 40,stepy/200);
outtextxy(xm div 4 +10,ym div 2 + 60,'Press ANY key to continue');
ch := readkey;
end;

```

```

PROCEDURE input_steps;

```

```

CONST

```

```

    enter = #13;
    esc = #27;
    curu = 'H';
    curd = 'P';
    curl = 'K';
    curr = 'M';

```

```

VAR

```

```

    traverse : char;
    KEY      : CHAR;
    position : real;
begin
    clrscr;
    setbkcolor(12);
    setcolor(1);
    outtextxy(xm div 4,ym - 80,'Use the arrow cursor keys to move
traverse ');
    outtextxy(xm div 4, ym -60,'ESC or RETURN key  to finish');
    setfillstyle(1,9);
    bar(xm div 20,ym div 5,xm div 2- 20,ym div 12*5);
    bar(xm div 2,ym div 5,xm - 20,ym div 12*5);
    setcolor(14);
    outtextxy(xm div 20 + 5,ym div 5 +15,'STEPX');
    outtextxy(xm div 20+5,ym div 5 + 45,'Position (mm)');

```

```

        outintxy(xm div 4+5,ym div 5+15,stepx);
        outvalxy(xm div 4+5,ym div 5+45,stepx/200);
        outtextxy(xm div 2+5,ym div 5+15,'STEPY');
        outtextxy(xm div 2+5,ym div 5+45,'Position (mm)');
        outintxy(xm div 8*6,ym div 5+15,stepy);
        outvalxy(xm div 8*6,ym div 5+45,stepy/200);
repeat
  begin
    KEY := READKEY;
    if key = #0 then key :=readkey;
    inc_step := 2;
    case key of
      curu :begin
        stepy := stepy - 1;
        step_y_for;
      end;
      curd : begin
        stepy := stepy + 1;
        step_y_rev;
      end;
      curl : begin
        stepx :=stepx -1;
        step_x_for;
      end;
      curr : begin
        stepx := stepx + 1;
        step_x_rev;
      end;
    end;
    if (key = curl) or (key = curr) then
      begin
        bar(xm div 4,ym div 5,xm div 2- 20,ym div 12*5);
        outintxy(xm div 4+5,ym div 5+15,stepx);
        outvalxy(xm div 4+5,ym div 5+45,stepx/200);
      end;
    if (key = curu) or (key = curd) then
      begin
        bar(xm div 4* 3,ym div 5,xm - 20,ym div 12*5);
        outintxy(xm div 8*6,ym div 5+15,stepy);
        outvalxy(xm div 8*6,ym div 5+45,stepy/200);
      end;
    end; {of repeat}
    until (KEY = ESC) or (key = #13) ;
  end;
end;

PROCEDURE menu;
begin

```

```

quit := false;
repeat
    setbkcolor(4);
    clrscr;
    setfillstyle(1,11);
    setcolor(0);

    bar(xm div 4, ym div 5, xm div 4 *3,ym div 4 * 3);
    outtextxy(xm div 4 + 5,ym div 4,' 1. Move X traverse');
    outtextxy(xm div 4 + 5,ym div 3,' 2. Move Y traverse');
    outtextxy(xm div 4 + 5,ym div 3+30,' 3. Move by CURSOR');
    outtextxy(xm div 4 + 5,ym div 2,' 4. QUIT Program');
    outtextxy( xm div 4+10,ym div 4 * 3 -15,'Select 1 - 4');
    ch := readkey;
    val(ch,select,code);
    case select of

        1: set_x;
        2: set_y;
        3: input_steps;
        4: quit := true
    END ; {Case}

UNTIL Quit ;
end;

```

```

BEGIN
    stepx := 0;stepy := 0;
    xm := getmaxx; ym:= getmaxy;
    bar(0,0,xm,ym);
    clrscr;
    set_port;
    menu;
    restorecrtmode;
end.

```


APPENDIX G

LAMINAR FLOW CHANNEL SURFACE TEMPERATURES

	Case 1			Case No: 2			Case No: 3		
	$T_{w,h}$	$T_{w,uh}$	r_T	$T_{w,h}$	$T_{w,uh}$	r_T	$T_{w,h}$	$T_{w,uh}$	r_T
	50.90	35.90	0.705	63.61	41.60	0.654	47.96	30.76	0.641
	50.77	36.14	0.712	63.30	41.90	0.662	47.85	31.06	0.649
	49.32	33.06	0.670	61.05	37.43	0.613	47.05	29.77	0.533
	47.42	26.66	0.562	58.21	29.03	0.499	45.40	25.80	0.568
STD [C]	± 0.64			± 0.73			± 0.62		
T_{amb} [C]	21.45 ± 0.4			21.35 ± 0.5			21.3 ± 0.55		
	Case No: 4			Case No: 5			Case No: 6		
X	$T_{w,h}$	$T_{w,uh}$	r_T	$T_{w,h}$	$T_{w,uh}$	r_T	$T_{w,h}$	$T_{w,uh}$	r_T
0.96	53.91	33.26	0.580	60.59	35.38	0.584	45.91	26.59	0.579
0.8	53.91	33.61	0.623	60.56	35.57	0.584	46.00	26.89	0.585
0.6	52.93	32.10	0.606	59.13	33.83	0.572	45.27	26.01	0.574
0.4	50.95	27.30	0.536	56.70	27.83	0.491	44.46	22.60	0.508
STD [C]	± 0.66			± 0.71			± 0.67		
T_{amb} [C]	21.4 ± 0.6			21.5 ± 0.7			21.34 ± 0.6		
	Case No: 7								
X	$T_{w,h}$	$T_{w,uh}$	r_T						
0.96	58.25	31.5	0.540						
0.8	58.37	31.71	0.543						
0.6	57.37	30.66	0.534						
0.4	55.81	25.77	0.462						
STD [C]	± 0.75								
T_{amb} [C]	21.3 ± 0.65								

Table - D.1 List of Surface temperatures of the laminar flow channel.

STD is the standard deviation of the average of temperature readings during the completion of case at the respective points.